LBL-16347 2/2
SAC-45
UC-70

SWEDISH-AMERICAN COOPERATIVE PROGRAM ON RADIOACTIVE WASTE STORAGE IN MINED CAVERNS IN CRYSTALLINE ROCK

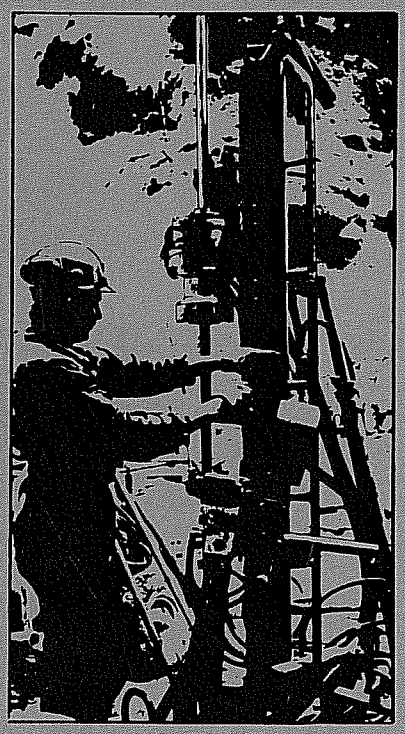

Technical Information Report No. 45

FRACTURE DETECTION IN CRYSTALLINE ROCK USING ULTRASONIC REFLECTION TECHNIQUES

Volume II

S.P. Palmer
Lawrence Berkeley Laboratory
University of California
Berkeley, California 94720

November 1982

A Joint Project of

Swedish Nuclear Fuel Supply Co.
Fack 10240 Stockholm, Sweden

Operated for the Swedish
Nuclear Power Utility Industry

Lawrence Berkeley Laboratory
Earth Sciences Division
University of California
Berkeley, California 94720, USA

Operated for the U.S. Department of
Energy under Contract DE-AC03-76SF00098

Printed in the United States of America
Available from
National Technical Information Service
U.S. Department of Commerce
5285 Port Royal Road
Springfield, VA 22161
Price Code: A09

LBL-16347 2/2
SAC-45
UC-70

FRACTURE DETECTION IN CRYSTALLINE ROCK USING ULTRASONIC REFLECTION TECHNIQUES
Volume II

Stephen P. Palmer

Lawrence Berkeley Laboratory
University of California
Berkeley, California 94720

November 1982

This work was supported, in part, by the Assistant Secretary for Nuclear Energy, Office of Waste Isolation of the U.S. Department of Energy under Contract Number DE-AC03-76SF00098. Funding for this project is administered by the Office of Nuclear Waste Isolation at Battelle Memorial Institute.

Fracture Detection in Crystalline Rock
Using Ultrasonic Reflection Techniques

by

Stephen Philip Palmer

Table of Contents

		pages
Acknowledgements		ii-iii
Chapter I	Introduction	1-4
References		5-6
Chapter II		
Section 1	Preliminary Theoretical Considerations	7-24
Section 2	Description of the Experimental System	25-39
Section 3	Initial SH Experiments	40-80
Section 4	Initial P Experiments	81-96
Section 5	Conclusions	97-98
References		99-100
Chapter III		
Section 1	Introduction	101-116
Section 2	Field Experiments at the Shaw Quarry	117-152
Section 3	Conclusions	153-155
References		156
Chapter IV		
Section 1	Introduction	157-158
Section 2	P and S Velocities of Raymond Granite	159-169
Section 3	Water Gap Experiment #1	170-195
Section 4	Water Gap Experiment #2	196-257
Section 5	Phase Spectra and Arrival Time Analysis	258-284
Section 6	Conclusions	285-288
References		289
Chapter V		
Section 1	Reexamination of the Field Work at the Shaw Quarry	290-308
Section 2	Final Statements	309-317
References		318
Appendix I		319-321
Appendix II		322-337
References		338

CHAPTER IV

Section 1

Introduction

In the last chapter the SH field data recorded at the Shaw quarry was interpreted using a model that assumed:

1) SH reflection from a horizontal, air or water-filled fracture was total, and,
2) the S velocity at the quarry site was very homogeneous beneath each source location.

A number of experiments was performed in an attempt to test the validity of these two assumptions, and the results of these studies will be presented in this chapter. In Section 2 the P and S velocities of small samples of Raymond granite were measured using a pulse transmission/timing method. The velocities were measured with the specimens in both dry and water-saturated conditions. It was found that the P velocity could increase 5-30% after saturating the specimen, and the S velocity also showed an increase of 10-20% after saturation.

In a series of experiments discussed in Sections 3, 4, and 5, a planar, air gap was created by separating two granite slabs with thin metal shins. The air gap was sealed at the edges with caulk and the gap filled with water. Evidently water was then absorbed into the granite slabs from the gap, causing the arrival time of the SH reflection from the water gap to decrease approximately 5% in one week. A drastic decrease in the amplitude of this event was also observed during this period.

In these sections attempts are made to quantify the thickness of the layer saturated by the absorbed water, and the value of the shear attenuation constant at ambient laboratory conditions (Q_{Sd}) and after saturation (Q_{Ss}). The results of these experiments suggest that the homogeneous S velocity assumption may not be particularly valid, as the S velocity of Raymond granite varies greatly with the degree of saturation. Also, the sharp decrease in Q_S with saturation may have important implications regarding detection of SH reflection events at the quarry site.

CHAPTER IV

Section 2

P and S Velocities of Raymond Granite

In this section the results of experiments are presented in which the P and S velocities of small specimens of Raymond granite were measured using a pulse transmission technique. Specimens of Raymond granite were cored from a block of granite acquired at the Shaw quarry, and one of the granite slabs used as a laboratory model. Velocity measurements were made with the specimens in both dry and water-saturated conditions.

These velocity measurements were made using a pulse transmission technique in which the transit time of a P or S elastic pulse through a cylindrical rock sample of known length is measured. The elastic pulse generally is band-limited in the frequency range of 50-750 kHz. The velocity is then determined by dividing the sample length by the one-way transmit time. Typically, the P and S velocities are measured as the axial stress along the cylindrical specimen is increased from zero to a predetermined load limit. The results of these transient time experiments yield measurements of the P and S velocities of a specimen as a function of the applied uniaxial stress.

Three cylindrical specimens (57 mm long × 35 mm diameter) of Raymond granite obtained at the Shaw quarry were tested in this manner by Dr. M. S. King. These measurements were made with the specimens in dry and water-saturated conditions, and the average values obtained from these three samples are given in Table IV-2-1 (M. King, personal commu-

Table IV-2-1

Axial Stress (MPa)	V_P Dry (m/s)	V_P Saturated (m/s)	% Difference $\frac{V_P Wet}{V_P Dry}$ - 100%	V_S Dry (m/s)	V_S Saturated (m/s)	% Difference $\frac{V_S Wet}{V_S Dry}$ - 100%
0	2980	Not Measurable	——	1700	Not Measurable	——
4.8	3650	4770	30.7	2080	2500	20.2
9.5	4020	5010	24.6	2230	2620	17.5
14.2	4250	5130	20.7	2360	2690	14.0
23.7	4540	5330	17.4	2490	2780	11.6
33.2	4710	5420	15.1	2580	2830	9.7

Measurements courtesy of Dr. M. S. King.

nication). The results of the P wave measurements are published in King and Paulsson, 1981, and included in this paper is the laboratory technique used in drying the specimens. Quoting from their work:

> "...the former (dry) condition being obtained by placing the specimens in a vacuum oven maintained at 105° C for 12 hours."

Also reported in this paper are the average saturated density (2658 kg/m^3) and porosity (1.2%) of the Shaw quarry samples. The average P and S velocities (dry and water-saturated) for the three Shaw quarry samples as a function of uniaxial stress are shown in Figure IV-2-1.

The notable feature of the measurements summarized in Table IV-2-1 is that the S velocity of the Shaw quarry granite increase 10-20% when going from a dry to water-saturated condition. Also the value of the dry S velocity (2080 m/s) at low stress (4.8 MPa) is typical of the S velocities estimated at the Shaw quarry using the direct SH event. In fact, these S velocity measurements require that the quarry granite be in a relatively dry condition and at a low stress state.

Similar P and S velocity measurements were made on a cylindrical specimen of Raymond granite (79 mm long × 44 mm diameter) cored from one of the granite slabs used as a laboratory model. Again, these measurements were performed with the specimen under a variable uniaxial stress, and with the sample in dry and water-saturated conditions. The "dry" velocity measurements were made after the core sample had attained equilibrium with the ambient temperature and humidity conditions of the laboratory. After the "dry" velocities were measured, the sample was placed under water for a month prior to the water-saturated velocity determinations.

The measured P and S velocity values for the laboratory model sample of Raymond granite are presented in Table IV-2-2, and these results are shown graphically in Figure IV-2-2. Again, the S velocities measured in the water-saturated specimen were 11-16% higher (at the same uniaxial stress) than the measured velocities of the dry specimen. The dry S velocity (2600 m/s) measured at the lowest non-zero stress level (3.22 MPa) corresponds well with the value quoted in Chapter II, Section 4 (2610 m/s).

The results of this experiment shed an interesting light on the much-used assumption that an even-grained, visually homogeneous granitic rock mass will have a very constant P and S velocity. This assumption may be valid if the saturation of the granite is constant, but the results of the pulse transit-time study clearly demonstrate that large velocity variations are possible in a granitic rock mass if the saturation varies spatially.

The results of these velocity measurements seem to contradict the results of Nur and Simmons, 1969, in which:

"...V_S is unaffected by the presence of fluid (water)."

However, closer examination of Table 2 of Nur and Simmons, 1969, shows that at low uniaxial pressures (less than 300 bars) the saturated shear velocity increases 1-7% over the dry V_S for the Casco and Westerly granites. Only the Troy granite shows no increase in V_S with saturation over the entire range of uniaxial pressures. The data of Nur and Simmons, 1969, then indicates that a 1-7% increase in V_S with saturation is reasonable at uniaxial stresses below 30 MPa (1 bar = 0.1 MPa). Thus the increase in the shear velocity of the Raymond granite with

Table IV-2-2

Axial Stress (MPa)	Dry P Velocity (m/s)	Wet P Velocity (m/s)	% Difference V_{Wet}/V_P - 100%	Dry S Velocity (m/s)	Wet S Velocity (m/s)	% Difference V_{Wet}/V_P - 100%
0	3933.1	4773.3	21.4	2491.4	2901.7	16.5
3.22	4451.9	4825.1	8.4	2599.9	2944.4	13.3
6.44	4563.6	4884.0	7.0	2649.0	2995.1	13.1
9.68	4608.3	4902.0	6.4	2687.3	3007.5	11.9
12.88	4653.9	4953.6	6.4	2707.3	3023.4	11.7
16.10	4711.4	4978.2	5.7	2736.9	3044.1	11.2
19.32	4725.3	4984.4	5.5	2746.3	3058.1	11.4
22.54	4753.4	5034.6	5.9	2759.6	3065.1	11.1

saturation measured at axial stresses ranging from 0-30 MPa is basically consistent with the results of Nur and Simmons, 1969. The conclusion of the authors that V_S is unaffected by the presence of water is entirely valid only at uniaxial stresses over 200 bars.

The P and S velocity values quoted in Nur and Simmons, 1969, for the Casco and Westerly granites at uniaxial stresses below 200 bars (20 MPa) are graphed in Figure IV-2-3. It should also be noted that in Table 3 of Nur and Simmons, 1969, the columns corresponding to the dry and saturated shear modulus μ of the Casco granite have been erroneously reversed.

Figure Captions

Figure IV-2-1
Graph of experimental measurements of P and S velocities on a Raymond granite sample acquired at the Shaw quarry. Measurements courtesy of Dr. M. S. King.

Figure IV-2-2
Graph of experimental measurements of P and S velocities on a Raymond granite sample acquired from a laboratory slab.

Figure IV-2-3
Graph of experimental measurements of P and S velocities presented in Nur and Simmons, 1969.
a) Velocities measured in Casco granite specimens
b) Velocities measured in Westerly granite specimens

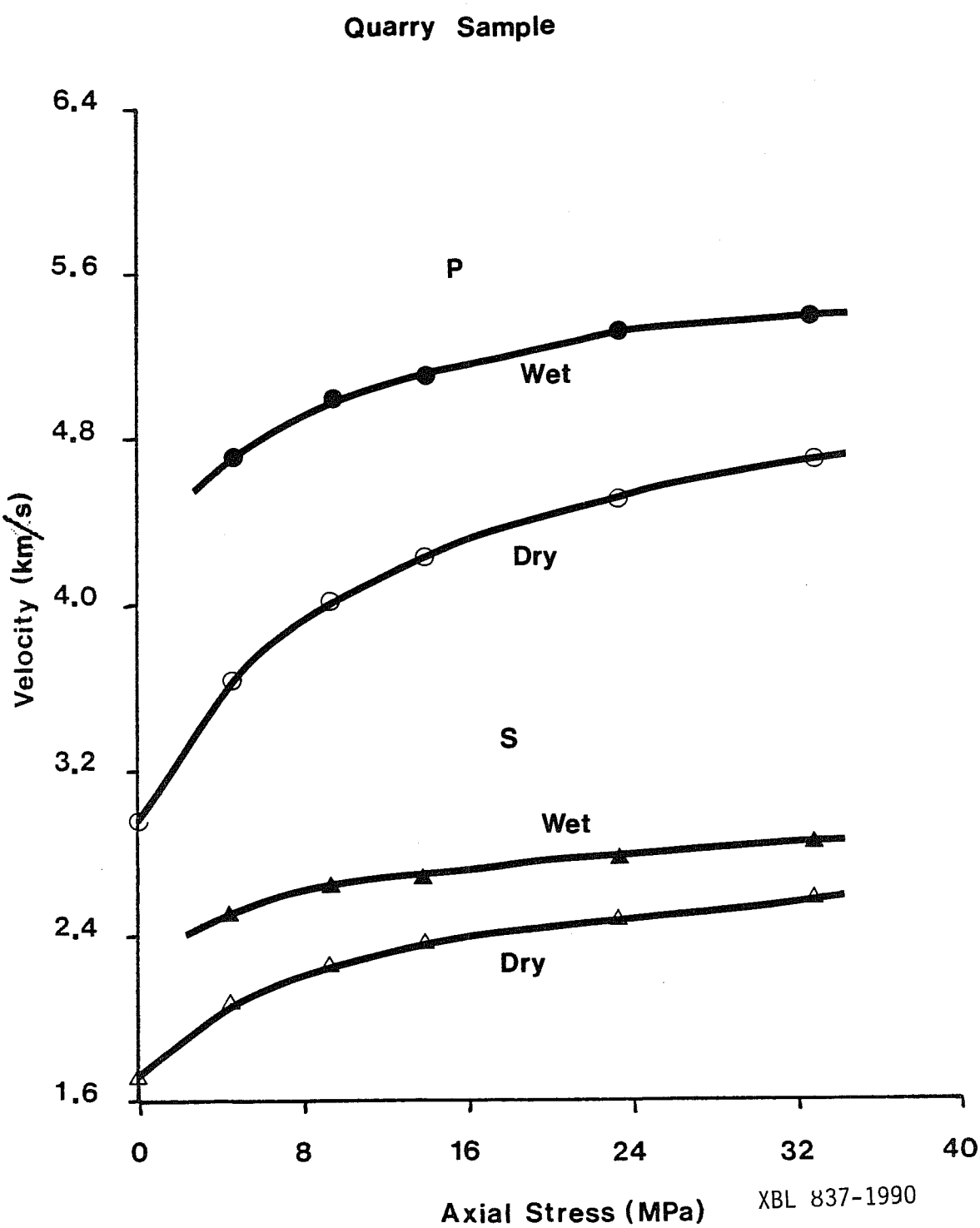
Quarry Sample
6.4
5.6
4.8
4.0
3.2
2.4
1.6
Velocity (km/s)
P
Wet
Dry
S
Wet
Dry
0
8
16
24
32
40
Axial Stress (MPa)
XBL 837-1990

Figure IV-2-1

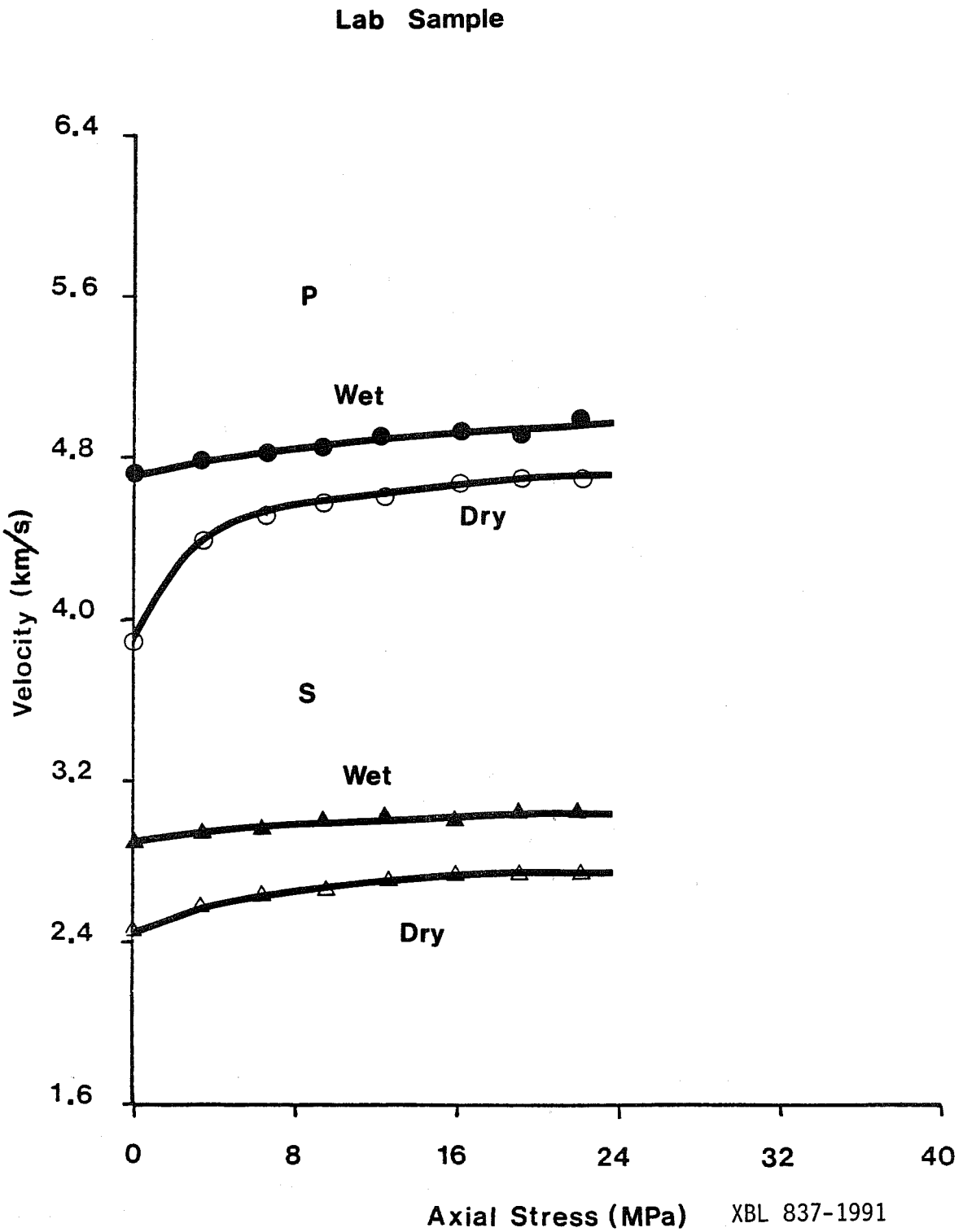
Lab Sample
6.4
5.6
4.8
4.0
3.2
2.4
1.6
Velocity (km/s)
P
Wet
Dry
S
Wet
Dry
0
8
16
24
32
40
Axial Stress (MPa)
XBL 837-1991

Figure IV-2-2

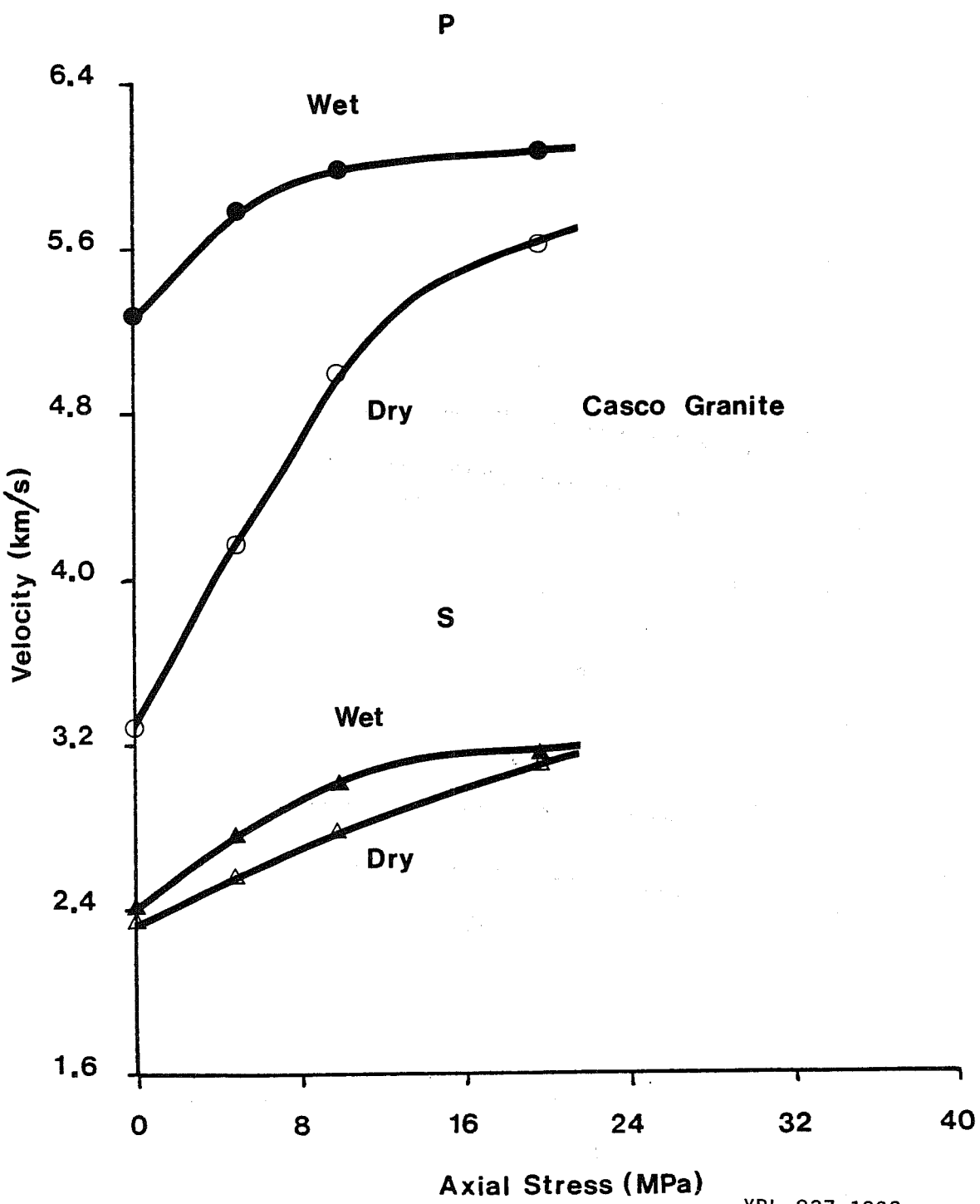

XBL 837-1992

Figure IV-23a

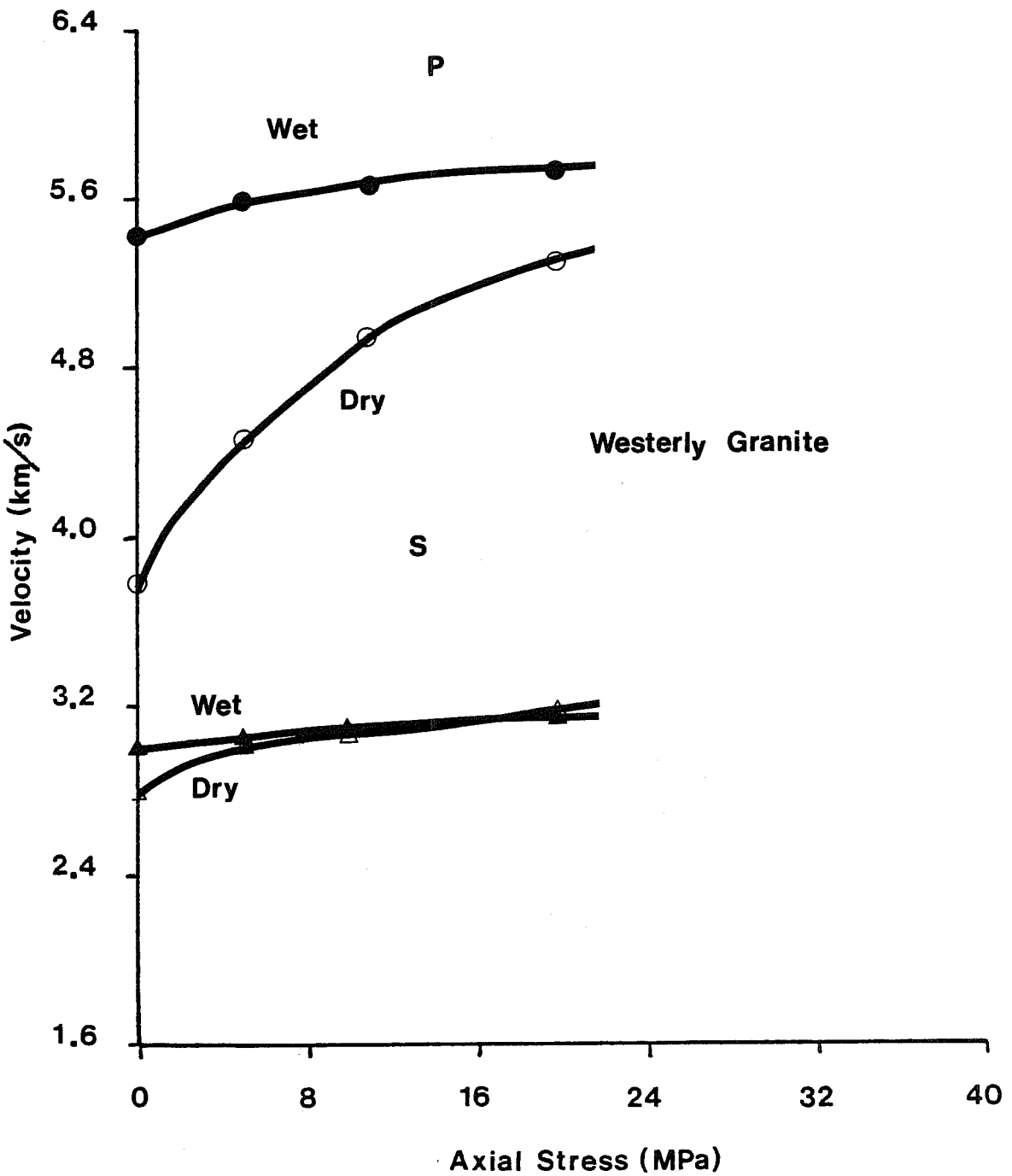

XBL 837-1993

Figure IV-2-3b

CHAPTER IV

Section 3

Water Gap Experiment #1

This section will describe the unexpected results of an experiment performed in the summer and fall of 1980. The original purpose of this experiment was to study the change in the SH reflection coefficient of a water-filled planar gap. However, the observed changes in the SH reflection event during this experiment were deduced to be due to absorption of water from the gap into the granite slabs used in forming the gap.

An air-filled planar gap 1.5 mm thick was created by shimming two 0.91 m × 0.91 m × 0.30 m Raymond granite slabs. Since the large faces of both of these slabs are highly polished and are very flat, the gap is fairly even in thickness. The location of SH traverse S2 is shown in Figure IV-3-1, along with the other SH traverses used in this experiment. An unprocessed SH traverse recorded along S2 on July 6, 1981 is presented in Figure IV-3-2. The S velocity estimated from the direct SH event in this data is 2585 m/s ± 10 m/s. The moveout velocity of the SH reflection event is 2650 m/s ± 20 m/s, the zero offset arrival time is 224.8 μs ± 10 μs, and the calculated depth to the air gap is 29.8 cm ± 1.3 cm.

The original intent of this experiment was to fill the air gap with water and repeat the SH traverse at locations S1 to S4. It was expected that little change in the SH wavefield would occur, because SH

reflection from either an air or water-filled gap in this situation should be total. This experiment would then confirm the assumption of total SH reflection from a fluid-filled fracture.

The next step in this experiment was to seal the exterior of the gap with caulking compound. Small sections of 1 mm diameter plastic tubing were extended through the caulk every 30 cm to provide escape and entry passages for air and water. Water was added through the tube with the highest elevation until water ran from all of the lower tubes. These tubes were sealed, presumably insuring that the gap was completely water-filled. The drained water was captured and measured so that the total volume of water filling the gap could be estimated.

This procedure was followed on July 11, 1981, and was completed in the late afternoon. Since this day was a Saturday, thin tissue paper was taped below the caulkline in order to detect any major leak of water. Tuesday, July 14, 1981 was the next time the tissue paper was inspected, and no water markings were detected. However, it was noticed that an amount of water (perhaps 500 cm^3) had to be added to again completely fill the gap. Since no leaks of this size had occurred over the weekend, the need for this additional amount of water was at first ascribed to slow migration of trapped air bubbles to the uphill end of the gap.

A SH traverse at position S2 was recorded on Wednesday, July 15, 1982 with the gap filled with water, and this data is shown in Figure IV-3-3. This SH profile is remarkable because of the severe attenuation of the arrival events occurring after 150 μs, causing the SH reflection event to be almost indistinguishable from the background noise.

Indeed, the only event unchanged in the profiles shown in Figures IV-3-(2 and 3) was the direct SH body wave event.

Needless to say, the results seen in these profiles suggested a possible instrumentation malfunction, but similar effects were obtained along the three other SH traverses, S1, S3, and S4. The SH profiles recorded at these positions for both the air and water-filled gaps are shown in Figures IV-3-(4, 5, and 6), and these data corroborate the results obtained at position S2. It was proposed that if this effect was due to the presence of water in the gap causing a consequent sharp decrease in the SH reflection coefficient, then draining the water from the gap could restore the previous total SH reflection from the air-filled gap.

The water was drained on August 12, 1981, with a SH receiver fixed at an 8 cm offset from source S2. The SH data from this receiver were continuously monitored during the draining of the water, but no detectable change in the SH waveform was observed before and after drainage (see Figure IV-3-7). This result was most peculiar, and demanded rethinking of the problem.

Figure IV-3-8 shows the SH trace recorded at 8 cm offset at S2 when the gap was originally air-filled (July 6, 1981), and the SH trace recorded on August 12, 1981 after draining the water. The differences in these two waveforms cannot be due to the presence of air or water in the gap. The advanced arrival time of the attenuated SH reflection event recorded on August 12 suggests that the average S velocity of the upper granite slab must have increased in the previous month. From the laboratory measurements presented in Section 2 of this chapter, we

concluded that water had been absorbed from the gap into the granite slabs. This increased moisture content would cause the apparent increase in S velocity of the granite slab. If this is the case, it also appears that the increase in moisture content causes an increase in the S wave anelastic attenuation (decrease in Q_S). However, this experiment was not designed to measure changes in Q_S, and only qualitative statements can be made about S wave attenuation in the saturated granite from these results.

If water was absorbed into the granite, then presumably this process could be reversed and the granite dried to its original condition. The fixed receiver at S2 was monitored during August 12 to October 7, 1981, and the data recorded during this period are shown in Figure IV-3-9. Indeed the SH reflection event increased in amplitude and arrival time as the upper granite slab dried. Note the consistent waveform exhibited by the direct SH event during this period, indicating that these changes are not due to varying source effects. The results of this experiment indicate that water is quickly absorbed when placed in contact with dry granite. This absorption explains the necessity of adding water to the gap three days after the initial filling.

A simple experiment that clearly shows the effect of moisture on the P velocity of a Chelmford granite is presented in Nur and Simmons, 1969. In this study a fully-saturated granite specimen was allowed to dry while subject to normal room temperature, pressure, and humidity. The compressional wave velocity (V_P) of the sample was measured during this eighty hour drying period, and was found to decrease smoothly from an initial fully-saturated value of V_P = 5400 m/s to a final value of

V_p = 4100 m/s. In fact V_p was found to decrease 10% (from 5400 m/s to 4900 m/s) during the first six hours of drying. However, no measurements of the shear wave velocity (V_S) were performed by Nur and Simmons during this drying experiment. This published experiment tends to corroborate our conclusion that water absorbed into the granite slab from the water gap was responsible for the changes in arrival time of the SH reflection event.

The time window between 180-300 μs of the two SH traces recorded on July 6 and August 12 is shown in Figure IV-3-10 (the full traces were shown in Figure IV-3-8). The primary SH reflection from the top surface of the gap is clearly visible in this figure, and the advanced arrival time and attenuated amplitude of the trace recorded on August 12 is apparent. The arrival times of the SH reflection are marked on this figure, and are 218.75 μs (July 6) and 207.03 μs (August 12). During this month long period the arrival time of the primary SH reflection advanced 5% (11.72 μs) and the amplitude decreased by a factor of three.

Since water in the gap appears to have been absorbed into the overlying granite slab, it would be worthwhile to estimate the approximate thickness of the zone of water saturated rock from the observed SH arrival time advance. To perform this calculation exactly, it is necessary to know:

1) the exact saturation distribution due to the absorbed water,
2) the exact constituative relationship between the S velocity and the degree of water saturation for the Raymond granite used in the laboratory models.

Since neither of these quantities are easily measured, two simple models of the S velocity distribution within the saturated granite slabs were investigated. It was assumed in this analysis that the increase of S velocity with increasing saturation is linear, so that the velocity distributions used in these two models can be related to the degree of saturation of the granite. Recent experiments by Paulsson suggest that the S velocity of a Stripa granite increases very linearly with increasing degree of water saturation (B. Paulsson, personal communication).

The first of these velocity models, shown in Figure IV-3-11a, is a simple step at depth z_1 from the top surface between the reference dry (β_d) and wet S velocity (β_s). Reflection of the downgoing SH waves at this step velocity transition is incorrectly ignored, although the calculated reflection coefficient from at 10% velocity increase at the step is small ($R_{SH} \cong 0.05$). Since a decrease in the primary SH reflection by a factor of three made it difficult to detect, an amplitude decrease of a factor of 20 would make the SH reflection from the step velocity transition virtually undetectable in the unprocessed SH data. Most of the downgoing SH energy would pass through this step to be completely reflected at the water gap, resulting in the primary SH reflection observed during the drying experiment shown in Figure IV-3-9.

Relevant parameters used in the velocity model of Figure IV-3-11a are:

β_d = S velocity at standard laboratory conditions (temperature, humidity, atmospheric pressure)

β_s = S velocity at total saturation (sample submerged in water for one month)

t_d = arrival time of the reflected SH event prior to filling the gap with water (July 6)

t_s = arrival time of the reflected SH event after filling the gap with water and waiting one month (August 12)

d = thickness of the granite slab

z_1 = depth from top surface to step velocity transition.

Relationships between the parameters are:

$$\Delta\beta = \beta_s - \beta_d \qquad [IV.3.1]$$

$$\Delta t = t_s - t_d \qquad [IV.3.2]$$

$$\beta_d = 2d/t_d \qquad [IV.3.3]$$

$$z_1 = \left(\frac{\beta_d^2}{2}\right)\left[\frac{\Delta t}{\Delta\beta} + \frac{t_s}{\beta_d}\right] \qquad [IV.3.4]$$

The last of these equations (IV.3.4) relates the advance in SH reflection arrival time to the thickness of the water-saturated zone $(d - z_1)$. It is derived using the one-dimensional travel time integral, where the travel time $t(a,b)$ for a wave to go from $z = a$ to $z = b$ is:

$$t(a,b) = \int_a^b \frac{dz}{V(z)} \qquad [IV.3.5]$$

where $V(z)$ is the velocity distribution in the interval $a \leq z \leq b$. The arrival times t_d and t_s are obtained from the values given in Figure IV-3-10, i.e., t_d = 218.75 μs and t_s = 207.03 μs. The thickness of the

slab d = 30.1 cm is easily measured. The dry reference velocity β_d = 2750 m/s is derived using Equation IV.3.3.

In order to get a value for the saturated wet velocity β_s, we must refer to the S wave velocity measurements presented in Section 2 of this chapter. In this previous section the S velocity of a sample obtained from one of the laboratory slabs was measured. This sample was initially tested a few months after being cored from the slab, which allowed sufficient time for the sample to obtain equilibrium with the ambient laboratory humidity. The velocity results of this initial test, because of the laboratory equilibrium saturation, will correspond to the dry reference velocity β_d. For a given value of β_d, a corresponding value of β_s can be obtained from Figure IV-2-2 (Section 2). Since we have an independent measure of β_d (obtained from t_d), then a specific value of β_s can be obtained from Figure IV-2-2.

In this particular case at location S2 the reference velocity is β_d = 2750 m/s. Referring to Figure IV-2-2, this ambient dry S velocity occurs at a stress of about 21 MPa. It is believed that this large stress must be applied in order to close microfracture damage caused during the coring of the specimen. The corresponding water-saturated S velocity at the 21 MPa stress level is β_s = 3060 m/s, which will be the value used in the calculation of z_1.

At location S2, the following values are used to calculate z_1:

d = 30.1 cm

β_d = 2750 m/s

t_s = 207.03 μs

Δt = -11.72 μs

$\Delta\beta$ = 310 m/s, and

z_1 = 14.3 cm

This result implies that the absorbed water fully saturated the granite in a layer extending 15.8 cm above the top of the water gap.

The second velocity model shown in Figure IV-3-11b is a simple linear increase in S velocity with depth under a layer of constant reference velocity β_d. By performing the travel time integration given in Equation IV.3.5, the height of the saturated zone (linear velocity transition) from the water gap is given by:

$$d - z_2 = \frac{\Delta\beta\Delta t}{(2)\,[\ell n(\beta_s/\beta_d)-(\Delta\beta/\beta_d)]} \qquad [IV.3.6]$$

where all other parameters are defined as before. By using the same values for these variables as was done in calculating z_1, the height $d - z_2$ = 30.57 cm. This result indicates that the linear transformation extended just beyond the top surface of the slab.

The final effort in this analysis will attempt to quantify the errors in calculating depths to the saturated zone for these two velocity models. The algebraic form of Equations IV.3.(4 and 6) was chosen to simplify the error analysis by using the terms $\Delta\beta$ and Δt in these expressions. The major errors in this experiment involve the estimation of the advance of the arrival time (Δt) and the change in S velocity of the granite when going from ambient dry to water-saturated conditions ($\Delta\beta$). The other parameters (t_d, t_s, and d) are relatively well determined, with maximum errors of ±1%. The value t = -11.72 μs

has an error associated with the digitization interval of 1 μs. We assign Δt a maximum error of 5% since the SH reflection arrival times determined from Figure IV-3-10 can be measured to one-half digitization interval. Observation of the curves in Figure IV-2-2 (Section 2) show that the difference $\Delta\beta$ between the S velocities measured at ambient dry and water-saturated conditions is very constant at uniaxial stresses above 5 MPa. Thus we feel that $\Delta\beta$ can be estimated to ±1.5% ($\Delta\beta$ = 310 m/s ± 5 m/s) with reasonable confidence. These error estimates can then be propagated through Equations IV.3.(4 and 6) to give the estimated error on the calculated depths z_1 and z_2.

Performing this error analysis on Equation IV.3.4 suggests that the depth z_1 can be estimated with a maximum error of 15%, so that the calculated depth at location S2 is z_1 = 14.3 cm ± 2.2 cm. This suggests that the granite is completely saturated in a layer that extends between 13.6-18.0 cm above the water gap.

When a similar analysis is performed on Equation IV.3.6, a larger error results because of the denominator term $\beta_d \ell n\left(\frac{\beta_s}{\beta_d}\right) - \Delta\beta$. Because the value obtained by performing this difference is small (~16 m/s) compared to the error on this term (±8 m/s), then the denominator term has a large resulting uncertainty of ±50%. Completion of the error propagation in this equation suggests that the calculated height z_2 has an associated uncertainty of ±51%. Then the height of the linear velocity transition ($d - z_2$) is calculated to be 30.6 cm ± 15.6 cm.

The two significant effects observed in the SH data recorded before and after filling the gap with water were the decrease in the arrival time of the primary SH reflection and the increased attenuation of this

event. The advance in SH reflection arrival time, coupled with the S velocity measurements presented in Section 2 made on dry and saturated granite specimens, was used to estimate the height of the zone of saturation. This was estimated for both of the velocity distribution models shown in Figure IV-3-11, and the errors expected on these height calculations were estimated for both models.

The primary conclusion of this experiment is that water is quickly absorbed into a dry granite specimen, and that the saturation front can penetrate a fair distance into the granite (a minimum of 13.5 cm in a month). The absorption process is reversible, so that the granite can be dried, but the amount of time required to dry the saturated granite is considerably longer than the time required to saturate the dry granite. This observation supports the hypothesis that the absorption of the water into the upper slab is due to capillary flow through the microfractures in the granite.

Because of the significance of this experiment in understanding the results of the field study, it was decided to repeat this experiment in the winter of 1981-82. This second experiment was designed to study the water uptake as well as the drying of the granite slab. Also, the P and SH reflection response was recorded immediately after filling the gap with water, which was an original purpose of the July-October experiment. Finally, an attempt was made in this repeated experiment to quantify the decrease in Q_S with the increasing water saturation of a granite specimen. The description and results of this experiment will be presented in Section 4 of this chapter.

Figure Captions

Figure IV-3-1
Locations of SH traverses on the granite slab model for experiments performed between July to October, 1981.

Figure IV-3-2
Unprocessed SH traverse recorded at position S2 on July 6, 1981. Gap is air-filled.

Figure IV-3-3
Unprocessed SH traverse recorded at position S2 on July 15, 1981. Gap is water-filled.

Figure IV-3-4
Unprocessed SH traverses recorded at position S1.
a) Recorded July 6, air-filled gap
b) Recorded July 15, water-filled gap

Figure IV-3-5
Unprocessed SH traverse recorded at position S3.
a) Recorded July 6, air-filled gap
b) Recorded July 15, water-filled gap

Figure IV-3-6
Unprocessed SH traverses recorded at position S4.
a) Recorded July 6, air-filled gap
b) Recorded July 15, water-filled gap

Figure IV-3-7
SH data recorded on August 13, 1981, with a fixed receiver at an 8 cm offset from source S2. Traces recorded just prior to and after draining the water-filled gap.

Figure IV-3-8
SH data recorded at 8 cm offset from S2 on July 6, and August 12, 1981. Gap is air-filled in both cases. Note increased attenuation of the SH reflection during this 5 week period.

Figure IV-3-9
SH data recorded at 8 cm offset from source S2 during August 12-October 7, 1981. Note increase of amplitude and arrival time of SH reflection during this period.

Figure IV-3-10
SH traces windowed between 180-330 μs recorded on July 6, and August 12, 1981.

Figure IV-3-11
Velocity models used to estimate thickness of the water saturated zone in the granite slab from the SH arrival time advance.
a) Step velocity transition model
b) Linear velocity transition model

EXPERIMENT #1

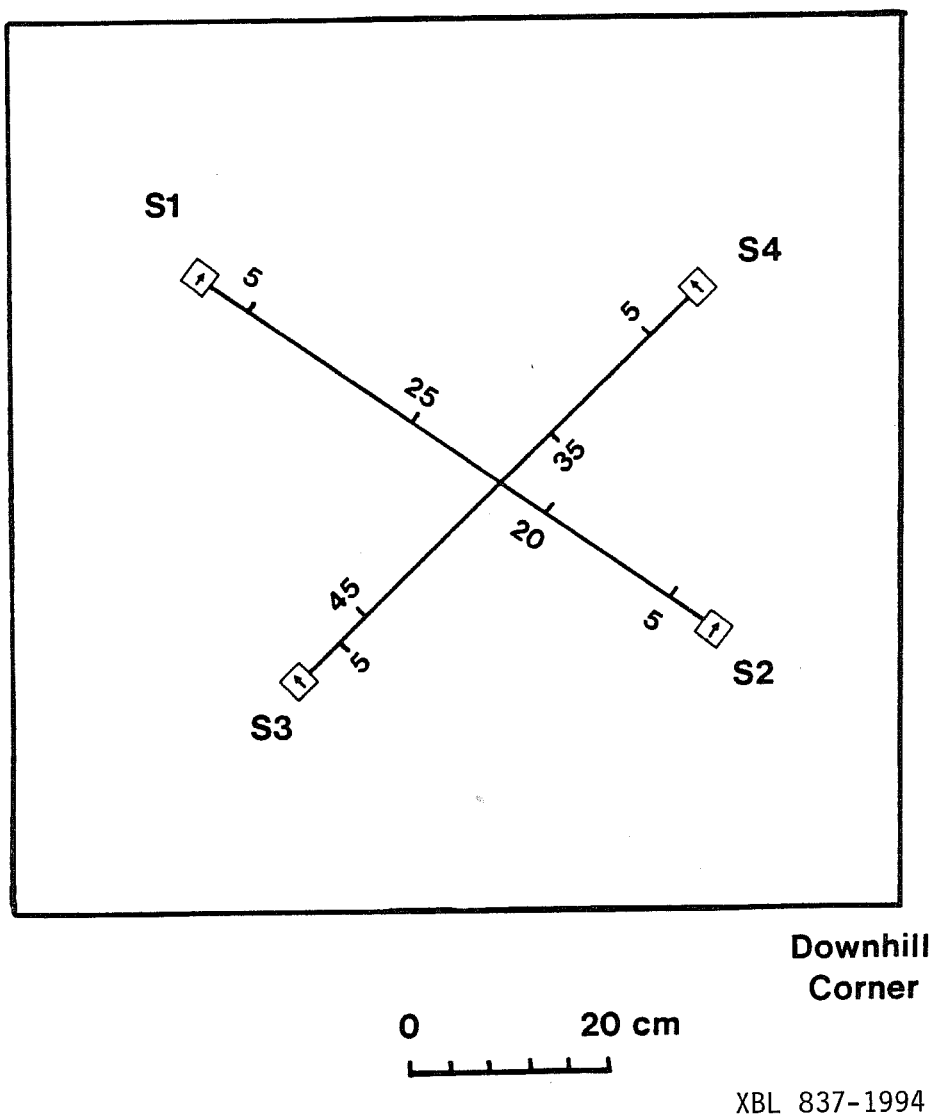

Figure IV-3-1

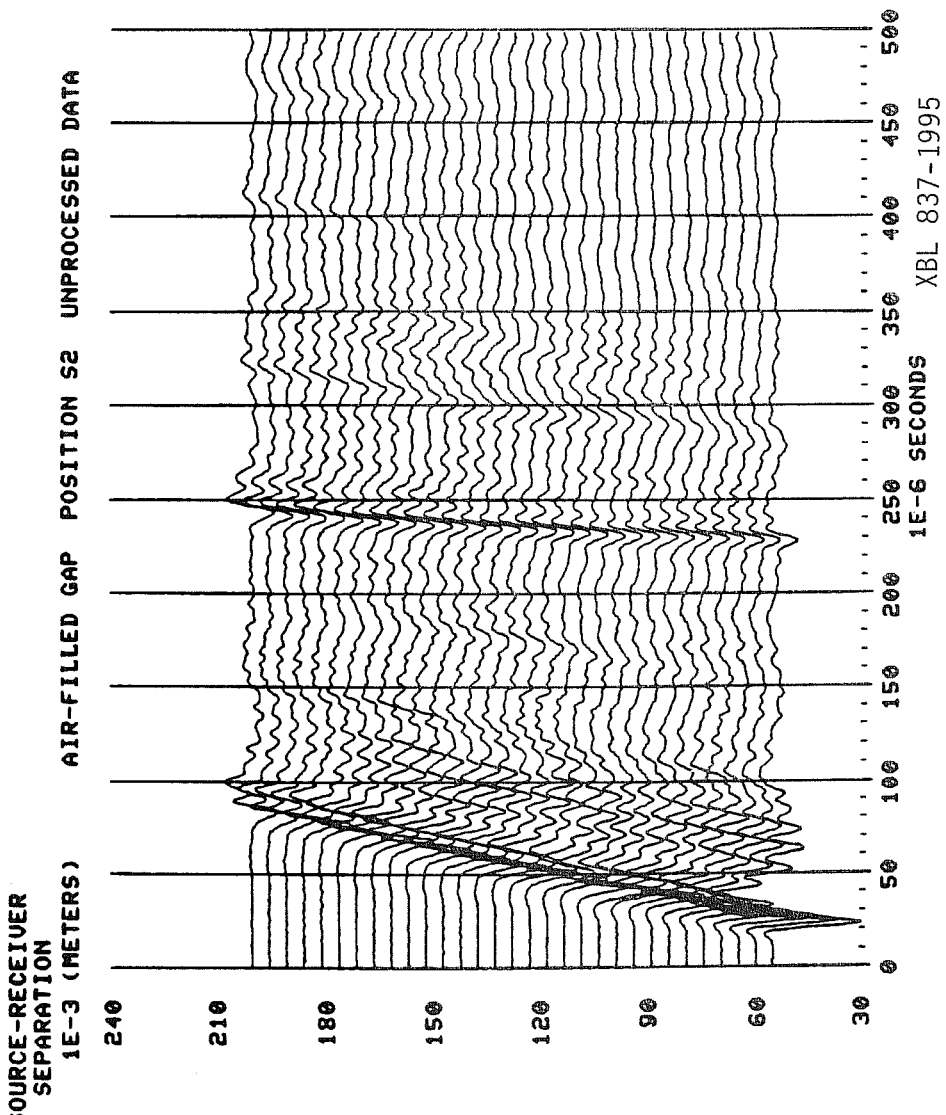
SOURCE-RECEIVER SEPARATION 1E-3 (METERS)
AIR-FILLED GAP POSITION S2 UNPROCESSED DATA
240
210
180
150
120
90
60
30
0
50
100
150
200
250
300
350
400
450
500
1E-6 SECONDS
XBL 837-1995

Figure IV-3-2

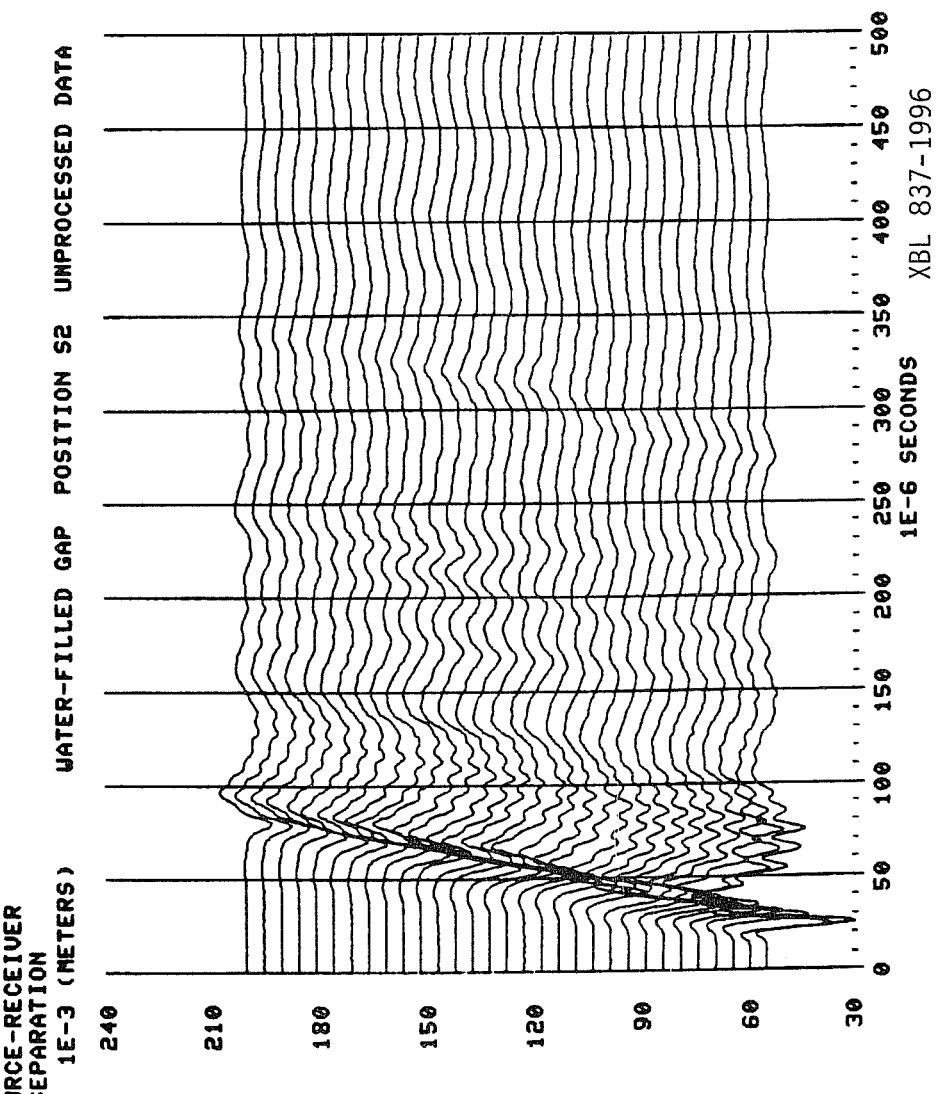
SOURCE-RECEIVER SEPARATION 1E-3 (METERS)
WATER-FILLED GAP POSITION S2 UNPROCESSED DATA
240
210
180
150
120
90
60
30
0
50
100
150
200
250
300
350
400
450
500
1E-6 SECONDS
XBL 837-1996

Figure IV-3-3

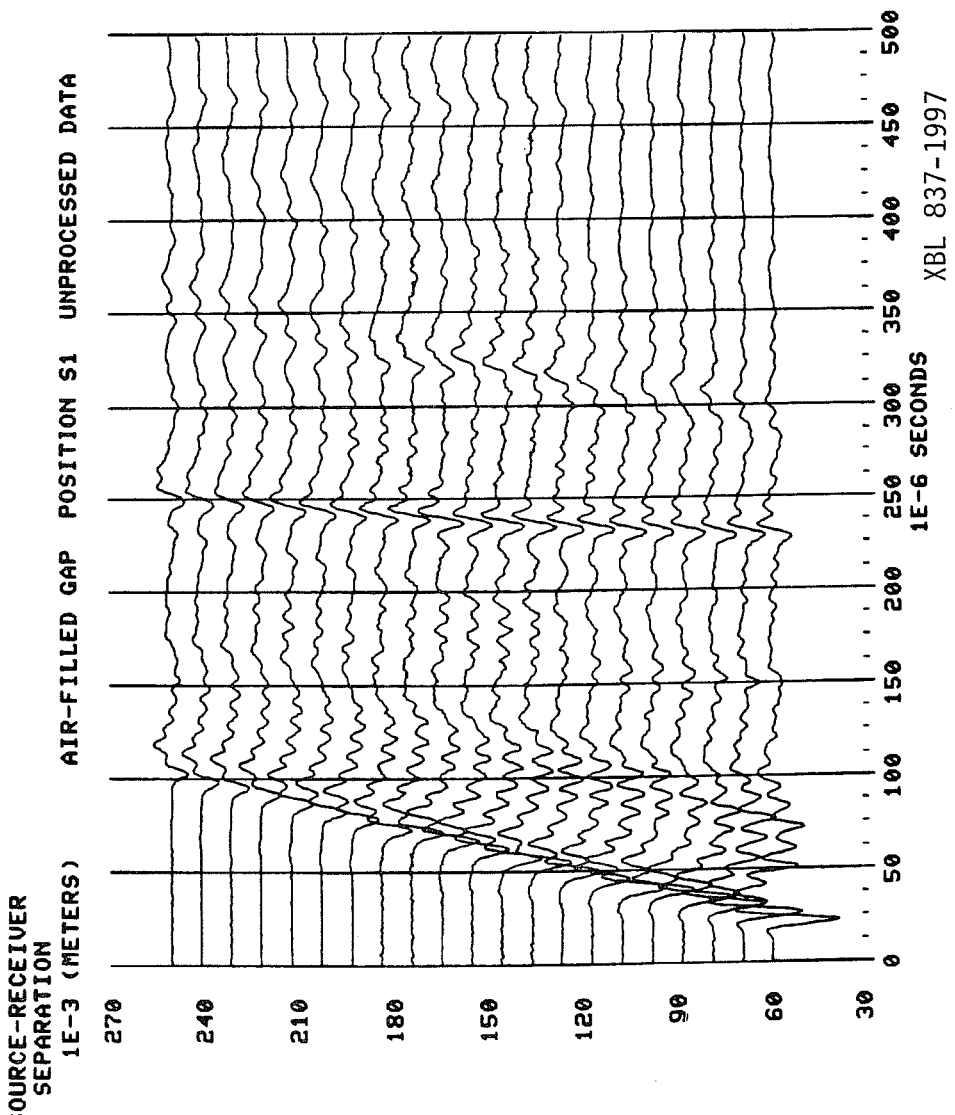

Figure IV-3-4a

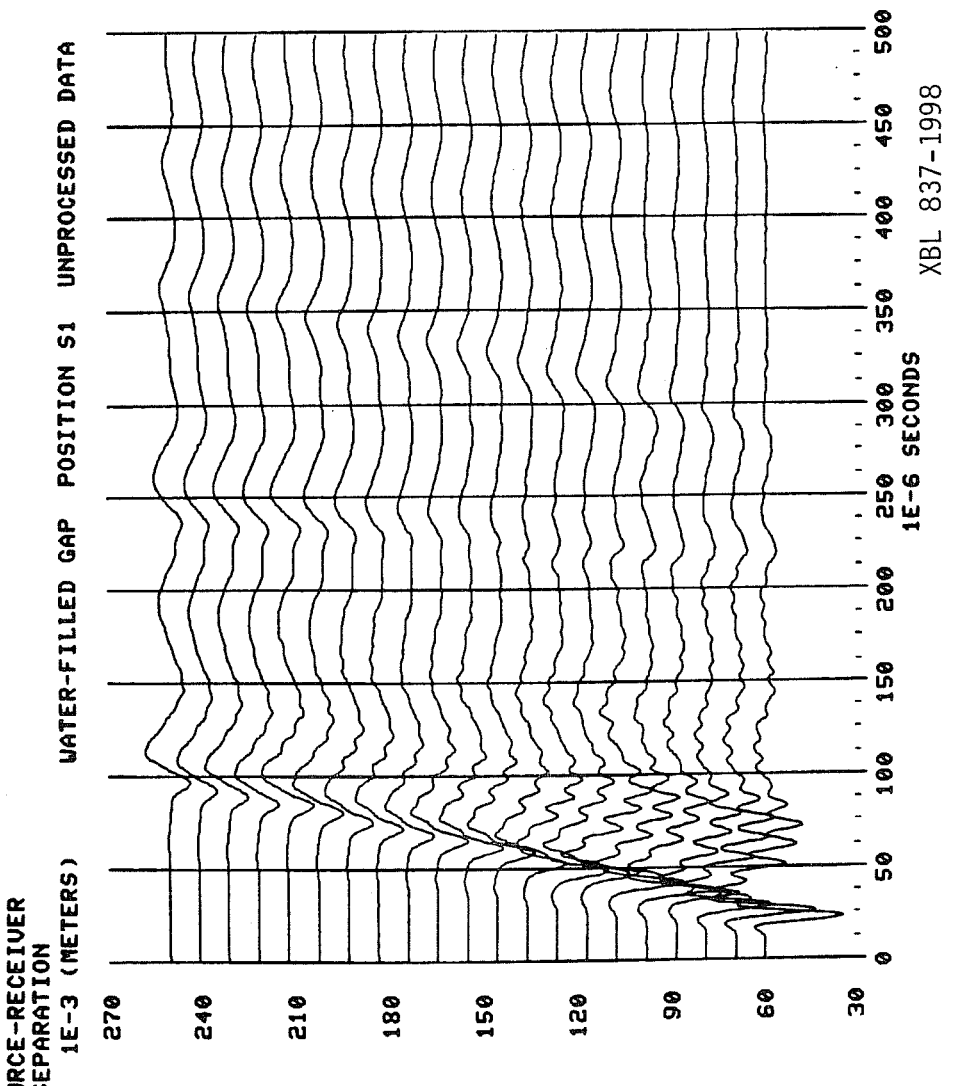

Figure IV-3-4b

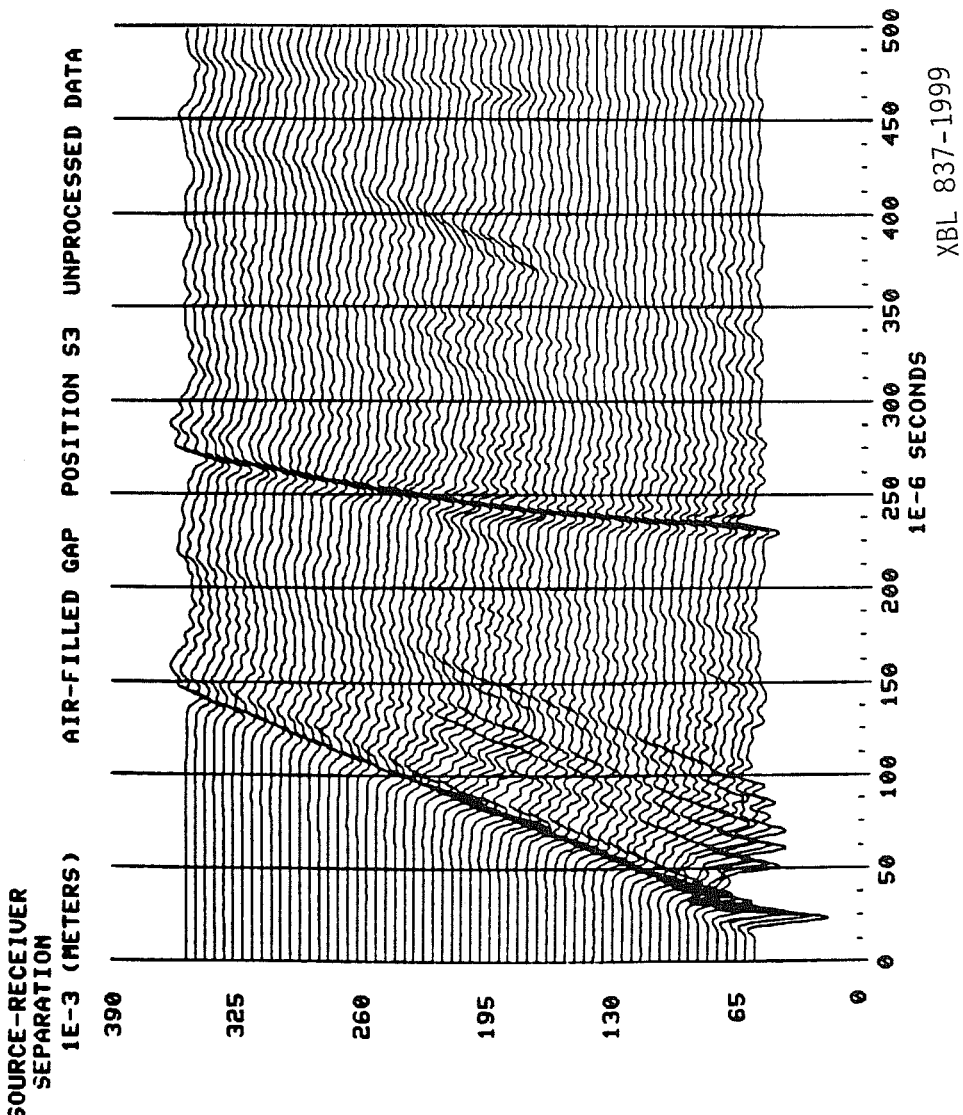

Figure IV-3-5a

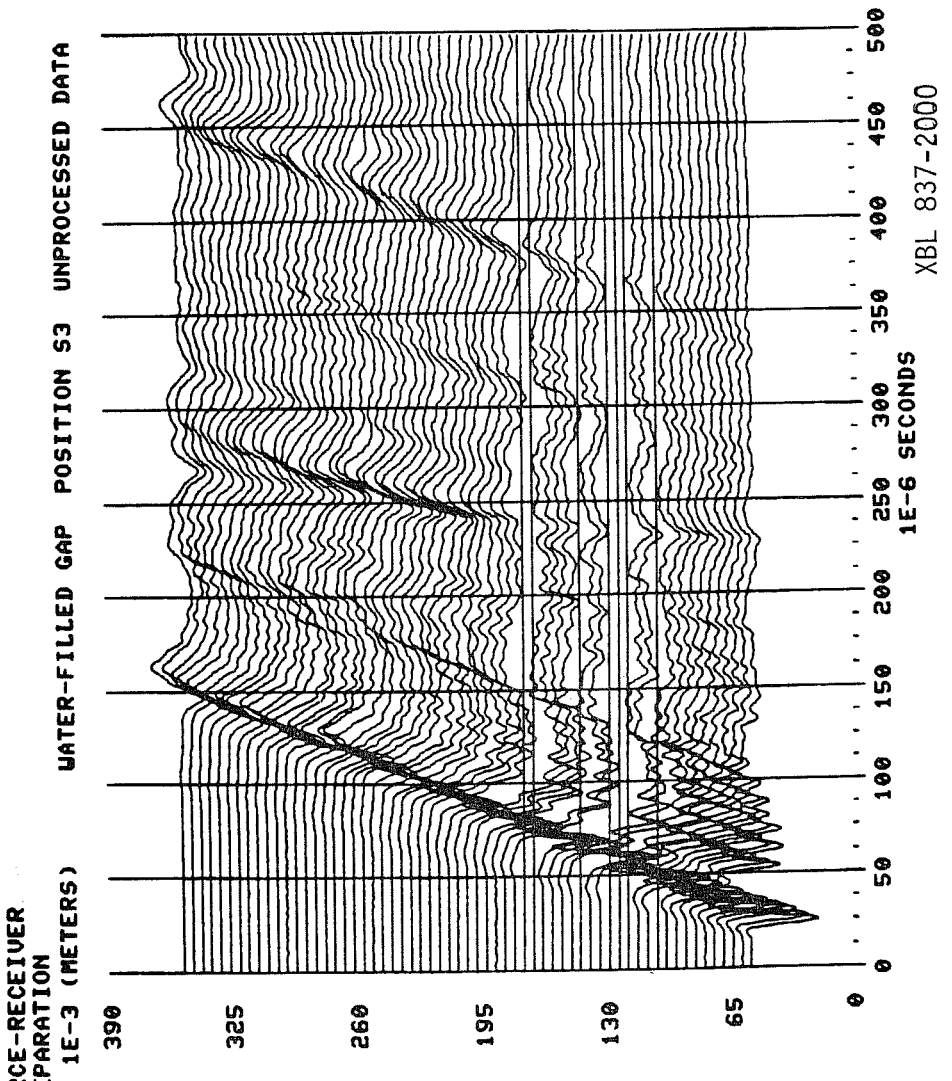

Figure IV-3-5b

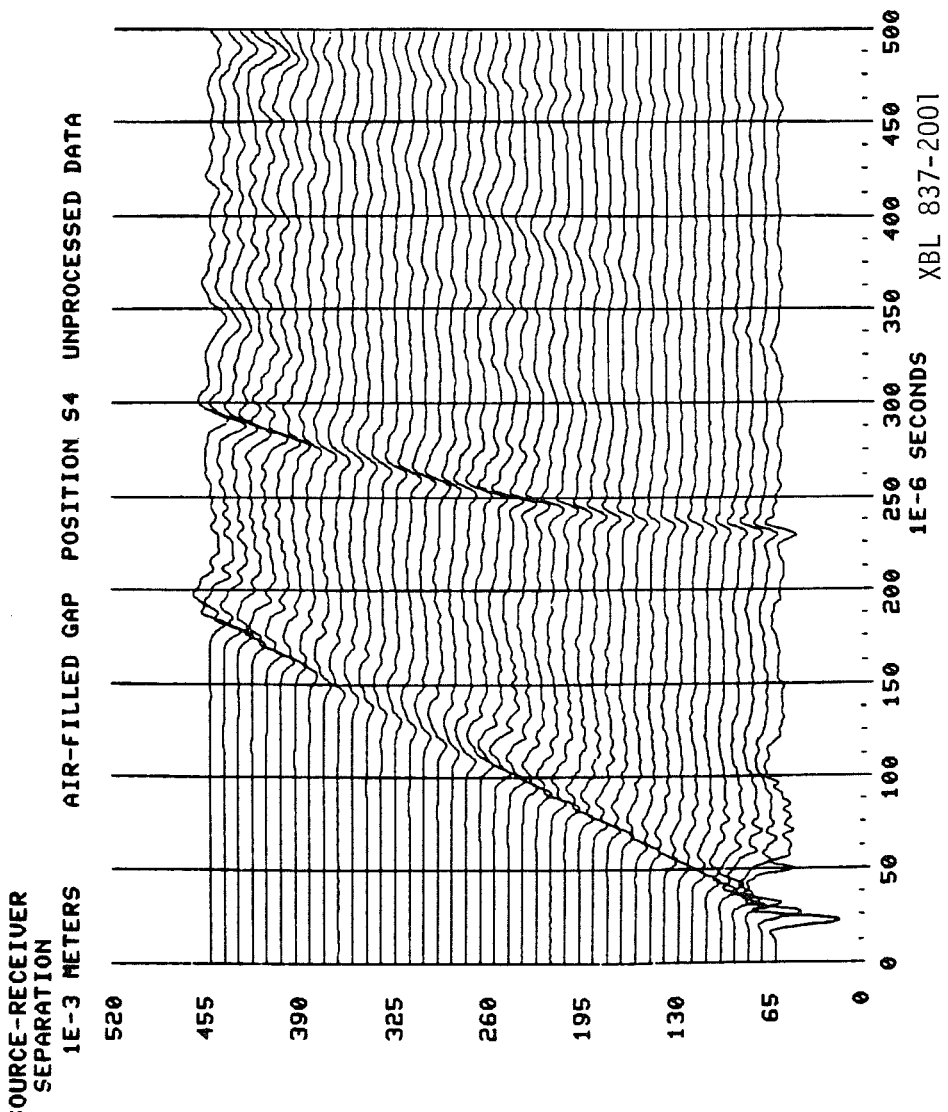

Figure IV-3-6a

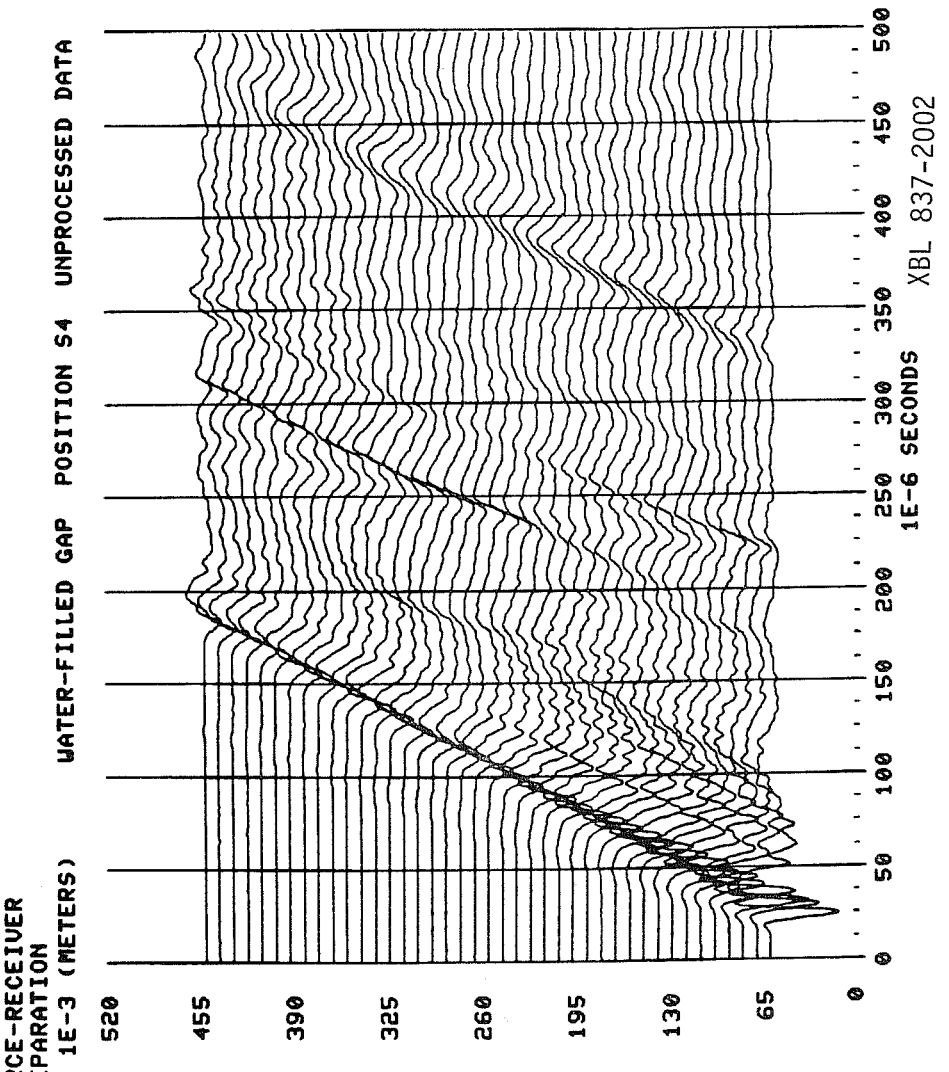

Figure IV-3-6b

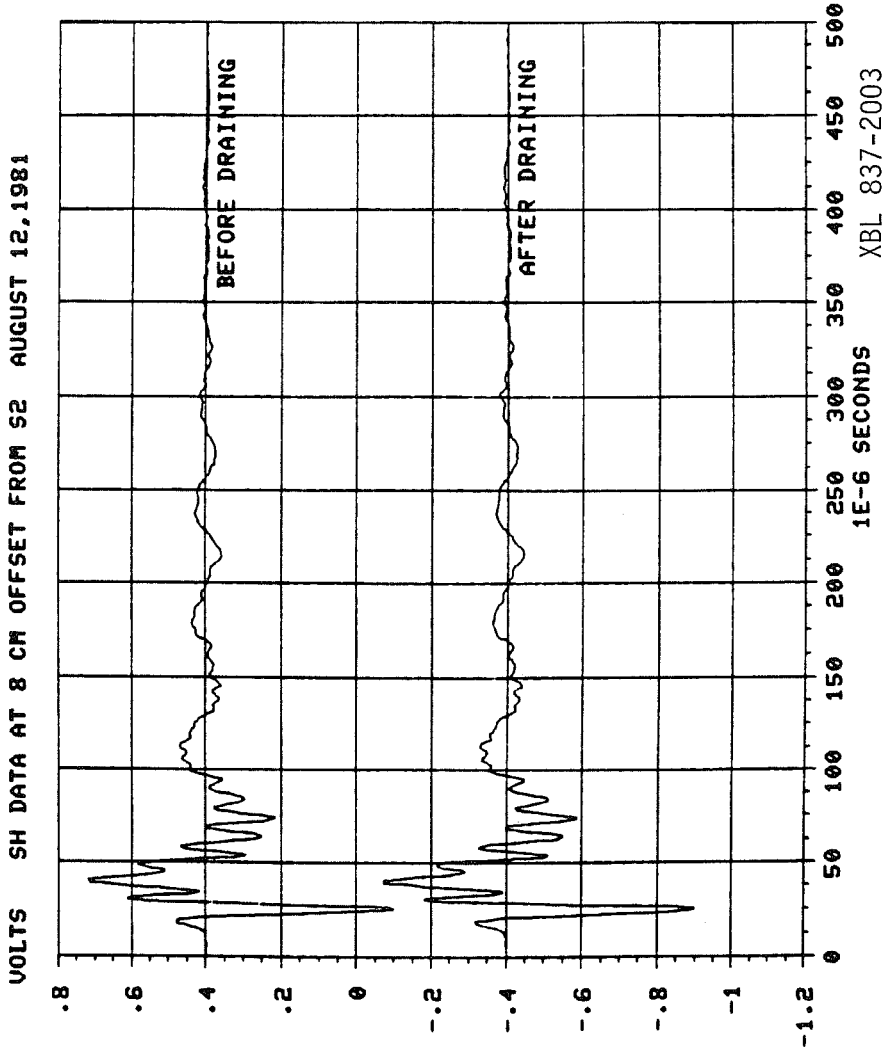
VOLTS SH DATA AT 8 CM OFFSET FROM S2 AUGUST 12,1981
BEFORE DRAINING
AFTER DRAINING
.8
.6
.4
.2
0
-.2
-.4
-.6
-.8
-1
-1.2
0
50
100
150
200
250
300
350
400
450
500
1E-6 SECONDS
XBL 837-2003

Figure IV-3-7

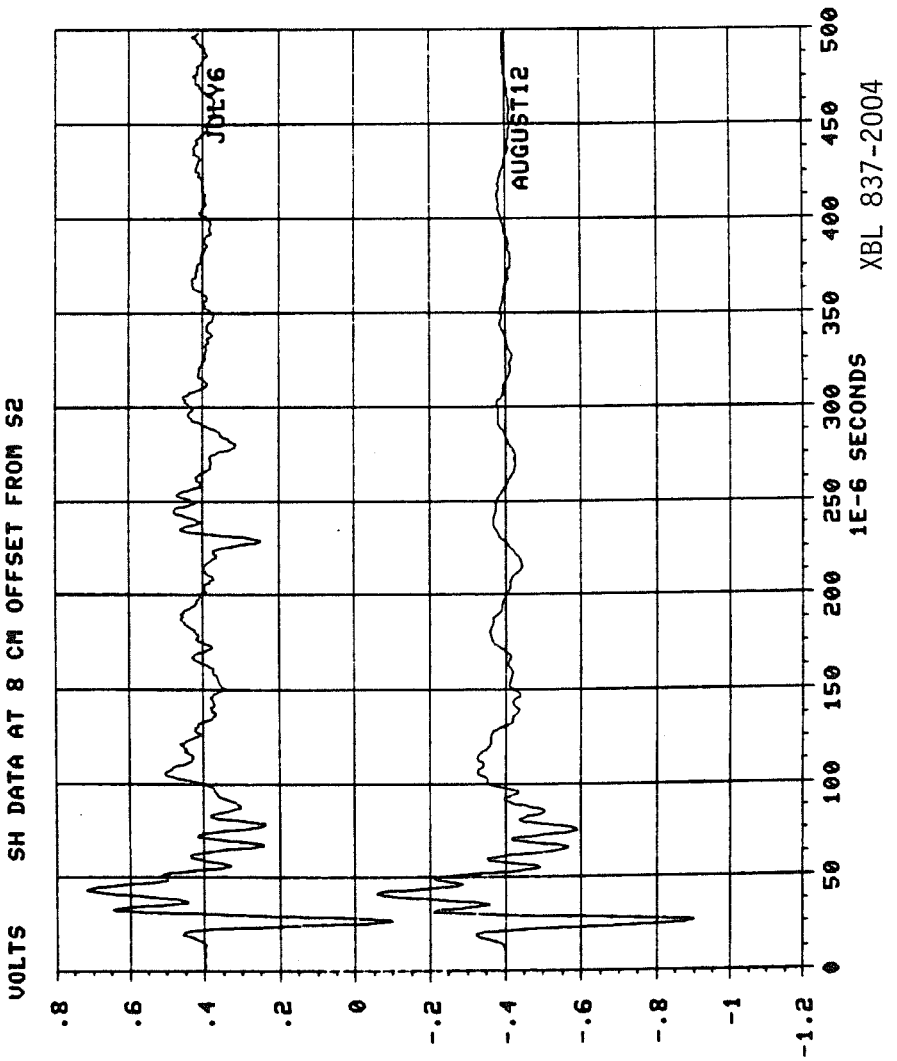
VOLTS SH DATA AT 8 CM OFFSET FROM S2
.8
.6
.4
.2
0
-.2
-.4
-.6
-.8
-1
-1.2
0
50
100
150
200
250
300
350
400
450
500
1E-6 SECONDS
JULY6
AUGUST12
XBL 837-2004

Figure IV-3-8

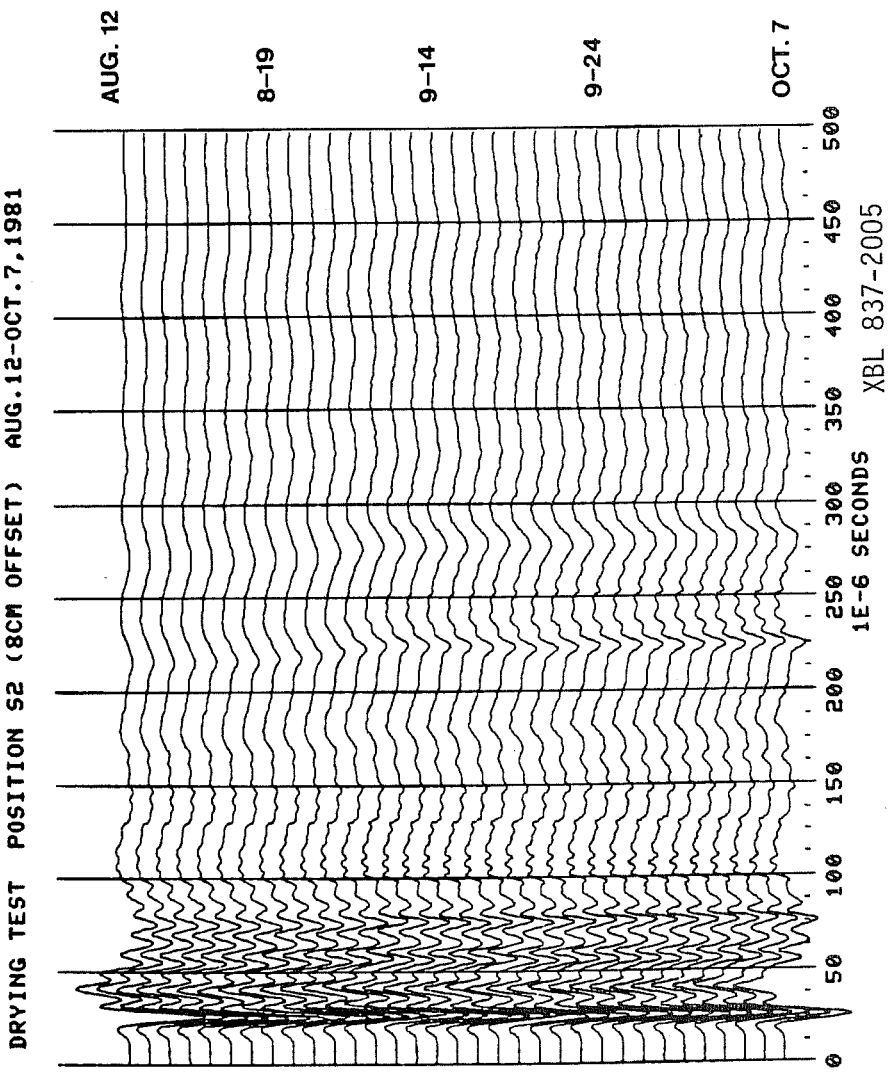
DRYING TEST POSITION S2 (8CM OFFSET) AUG.12-OCT.7,1981
AUG. 12
8-19
9-14
9-24
OCT. 7
0
50
100
150
200
250
300
350
400
450
500
1E-6 SECONDS
XBL 837-2005

Figure IV-3-9

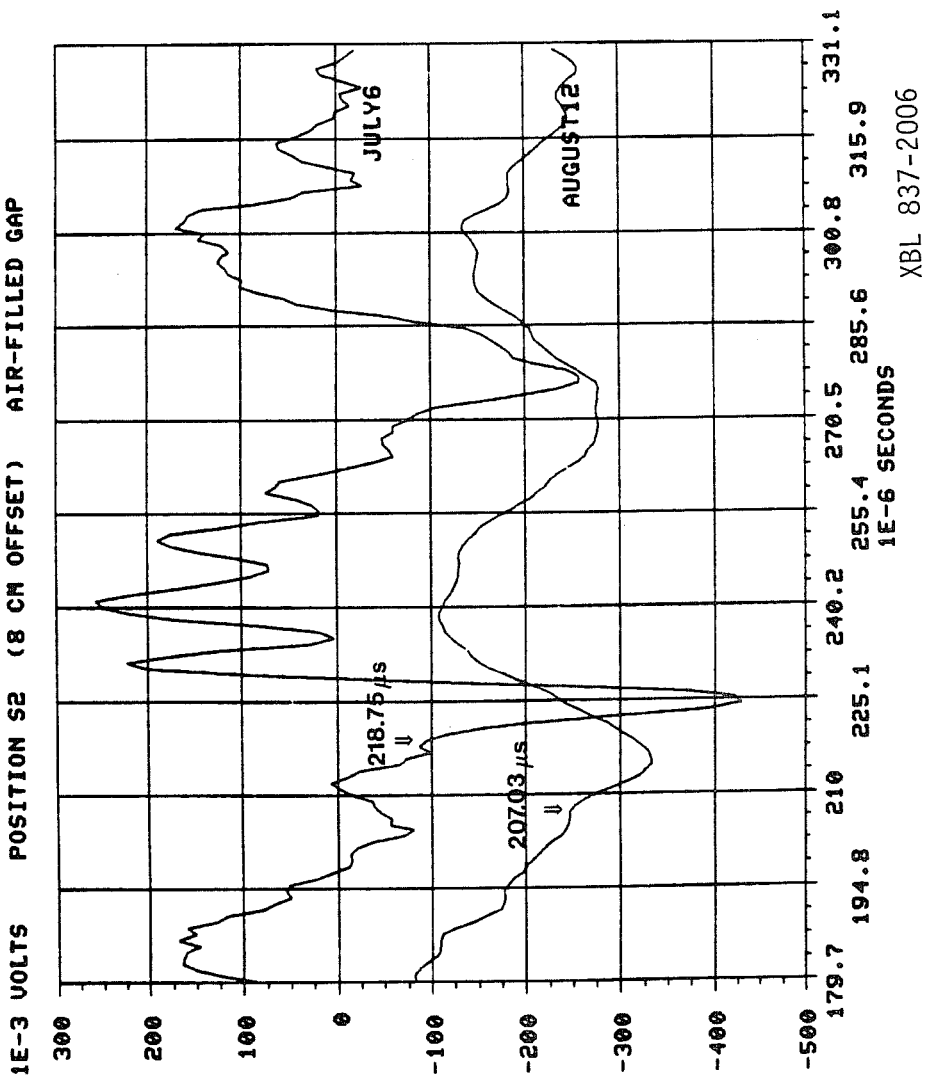

Figure IV-3-10

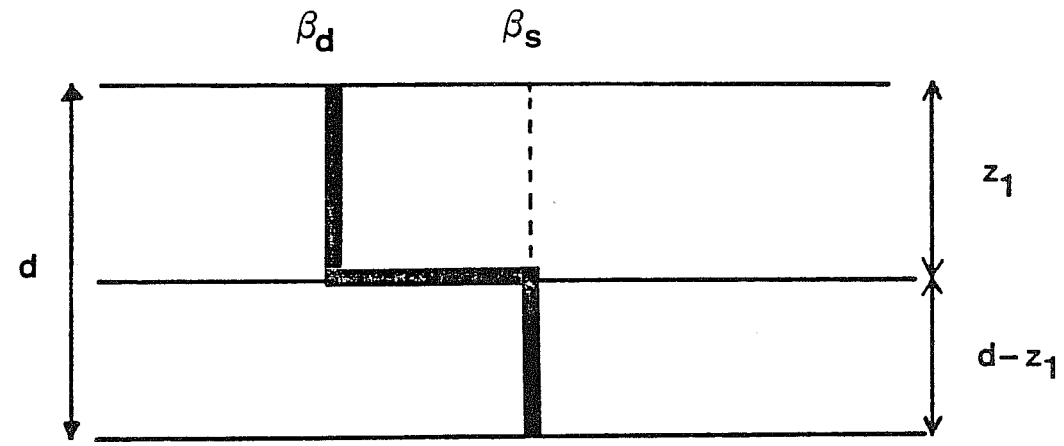

MODEL #1

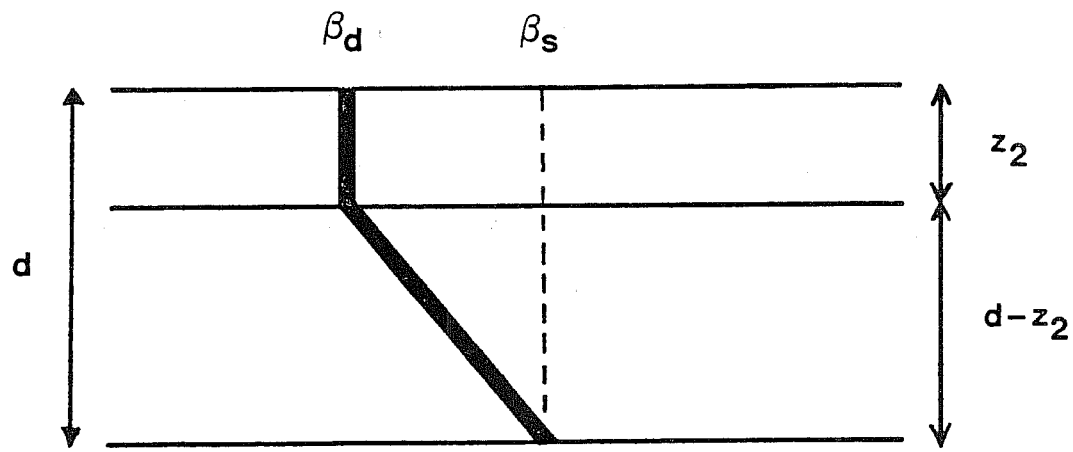

MODEL #2

XBL 837-2007

Figure IV-3-11

CHAPTER IV

Section 4

Water Gap Experiment #2

The results of the experiment presented in the previous section of this chapter were unexpected, to say the least. Because of this lack of foresight, many factors in this study had poor experimental control, most notably, the lack of fixed SH receiver data recorded prior to the initial filling of the gap with water. Thus, it was decided to repeat this experiment in the winter of 1982 in order to provide improved measurement of the phenomena observed in the original test. This second experiment, performed during January to March, 1982, will be described in this section.

A 1.5 mm planar air gap was created by shimming two granite slabs, as was done in the experiment performed during August to October, 1981. Two SH sources (S1 and S2) and one P source (P1) were fixed with epoxy cement to the top surface of the upper granite slab at locations shown in Figure IV-4-1. During the first week of January reflection profiles were recorded at each source location with the gap air-filled. The unprocessed SH profiles at locations S1 and S2 are shown in Figure IV-4-2, and the large amplitude primary SH reflection from the air gap (occurring from 220-270 μs) is quite prominent. The unprocessed P reflection profile at location P1 is shown in Figure IV-4-3a, and the results of summing this data to produce the response of a 2 cm array are presented in Figure IV-4-3b. The primary P reflection from the air

gap (occurring between 135-160 μs) is best seen in the summed data, but this event is also clearly visible at small offset distances in the unprocessed P data. P and S velocities estimated using the moveout (X^2-T^2) velocities of the P and SH reflection events are summarized in Table IV-4-1. These velocity values indicate that the saturation effects created during the previous experiment have substantially disappeared.

On January 12, 1982, single fixed receivers were positioned at a very small offset (< 3 cm) from the P and S sources, as shown in Figure IV-4-1. The P and SH traces recorded at these fixed receivers prior to filling the gap with water were used to determine the S velocity (β_d) and attenuation constant (Q_S) of the granite slab at ambient laboratory (dry) conditions. The fixed receiver data recorded with the gap air-filled (January 12) are shown in Figure IV-4-4, and the primary P and SH reflections from the air gap are clearly visible in this figure. All of the P and SH data obtained from these fixed receivers are normalized so that the minimum amplitude of the surface-propagating event (either the direct body SH wave for SH source-receiver pairs, or the Rayleigh wave for P source-receiver pairs) has a value of -1. Thus these surface-propagating events must maintain a constant waveform during any monitoring experiments if this method of normalization is used.

The gap was filled with water on January 13 in a forty minute procedure that was started at 2:40 PM. A total amount of 1300 cm^3 of water was added to the gap during this period. By dividing this volume by the area of the gap (8281 cm^2) one obtains the average thickness of the water-filled gap (1.57 mm).

The traces in Figure IV-4-5 were recorded on January 13 at the fixed receiver locations at 1:00 PM (prior to filling the gap with water), and at 3:30 PM (as quickly as possible after filling the gap). Comparison of the traces recorded before and just after filling the gap will give a relative measure of the P and SH reflection coefficients of the water-filled gap. By assuming that P and SH reflection from the air-filled gap is total, then an absolute measure of the reflection coefficients of the water-filled gap can be obtained.

Close examination of Figure IV-4-5 shows that the peak-to-peak amplitude of the P and SH reflection events decreased by approximately 3% after the gap was filled with water. The small decrease in the P reflection amplitude was consistent with the predicted amplitude response shown in Figure II-1-3 (Chapter II). The decrease in the SH reflection amplitude suggested that the assumption of total SH reflection at a horizontal, water-filled fracture is not exact. However, since it took almost an hour to fill the gap with water and record the fixed receiver data, the possibility exists that some water was absorbed into the granite slab during this procedure. Thus, the 3% decrease in amplitude of the P and SH reflection events could have resulted from an increased anelastic loss due to increased saturation of the granite. This experiment does verify that SH reflection coefficient of a horizontal, planar, water-filled gap with a thickness ranging from 1-2 mm is nearly unity (to within 3% or better).

The gap was kept filled with water for 289.5 hours until January 25 at 3:00 PM, when it was drained. During this time it was necessary to add a total of 1430 cm^3 of water to replace the volume absorbed into

the granite. If 715 cm^3 of water was absorbed into the upper slab and the porosity of the slab is assumed as 1% then the volume of the absorbed water was sufficient to fully saturate a layer with dimensions 91 cm × 91 cm × 8.6 cm. The thickness of this saturated zone (8.6 cm) is in good agreement with the thickness determined in the saturation experiment discussed in Section 3 (14.3 cm ± 2.2 cm). This evidence strongly supports our conclusion that the observed changes in the SH reflection arrival time result from absorption of water into the granite slab.

Figure IV-4-6 presents the fixed SH receiver traces recorded at S1 and S2 from 1:00 PM January 13 (just prior to filling the gap) to 3:00 PM January 25 (just after the gap was drained). During this period there was a noticeable decrease in the SH reflection arrival time, as well as a sharp decrease in the amplitude of this event. This confirmed that the phenomena observed in the previous water gap experiment could be repeated. The waveform of the direct SH event remained quite constant during this period, indicating that the observed changes in the SH reflection waveform were not due to varying source effects.

The traces recorded at the fixed P receiver during the period January 13-25 are presented in Figure IV-4-7. Examination of these data shows that the arrival time and amplitude of the P reflection from the water gap also decreased with increasing saturation of the granite. The decrease in arrival time is consistent with the increase of P velocity with saturation discussed in Section 2 of this chapter. The decreased amplitude of the P reflection indicates that Q_P of the granite must decrease for increasing water saturation. However, the increased atten-

uation of the P reflection quickly decreased the amplitude of this event below the background noise level of this source-receiver pair. Thus, no quantitative analysis using the increased P reflection arrival time or decreased amplitude was attempted. However, it appears likely that any decrease in the P reflection arrival time was due to an increase in the P velocity of the granite, and that this velocity increase is caused by water absorbed into the granite.

The SH reflection events observed at locations S1 and S2 just before filling the gap (1 PM, January 13) and just before draining the gap (2 PM, January 25) are shown in Figure IV-4-8. The arrival times of the SH reflection event obtained from this figure are summarized in Table IV-4-2. These arrival times will be used to calculate the thickness of the saturated zone using the two velocity models developed in Section 3 of this chapter. The relevant expressions used to calculate the saturated zone thickness for the two models are given in Equation IV.3.(4 and 6) of the previous section. Table IV-4-2 also presents (besides the arrival time data t_d and Δt) the dry reference S velocity β_d (calculated using d = 30.2 cm), the assumed differential velocity $\Delta\beta$, and the calculated saturated zone thicknesses ($d-z_1$ and $d-z_2$) for the two velocity models.

The results of the analysis using the step velocity transition model suggested that the thickness of the water saturated layer was 12.5 cm ± 2.0 cm. This value compares favorably with the saturated layer thickness estimated from the volume of the absorbed water (8.6 cm). The results using the linear velocity model suggested that the saturation zone was 24.0 cm ± 10 cm thick.

Table IV-4-1

Source Position	Reflection Moveout Velocity (m/s)	Zero-Offset Arrival Time (μs)	Depth to Reflector (cm)
S1	2490 ± 3.4%	221.1 ± 3.8%	27.5 ± 5.1%
S2	2695 ± 5.0%	224.4 ± 4.1%	30.2 ± 6.5%
P1	4330 ± 7.8%	139.5 ± 4.2%	30.2 ± 8.9%

Table IV-4-2

Location S1	Location S2	
215.82 μs ± 1%	219.73 μs ± 1%	t_d
-8.79 μs ± 5.6%	-9.76 μs ± 5.1%	Δt
2795 m/s ± 1%	2735 m/s ± 1%	β_d
315 m/s ± 1.5%	315 m/s ± 1.5%	$\Delta\beta$
12.2 cm	13.0 cm	$d - z_1$ (Model #1)
±1.8 cm (±14.8%)	±1.7 cm (±13.1%)	Error on $d - z_1$
23.3 cm	24.8 cm	$d - z_2$ (Model #2)
±9.1 cm (±39.1%)	±9.3 cm (±37.5%)	Error on $d - z_2$

The SH reflection data recorded at the fixed receivers during the water gap experiment were used to estimate the S wave attenuation constant Q_S for a saturated granite slab. This value must be less than the Q_S of the granite at ambient dry conditions to account for the drastic decrease in the SH reflection amplitude observed in Figure IV-4-6. Because the S velocity and Q_S of the granite slab both depend on saturation, these variations are, in a sense, coupled. Since the S velocity and Q_S must both vary with depth in the saturated granite slab, an account must be made for the spatial variation of these quantities in the equations governing anelastic attenuation.

Referring to Aki and Richards, 1980, if the shear velocity β and attenuation constant Q_S vary with depth z, then the linear first order differential equation governing plane wave anelastic loss is:

$$\frac{dA(z,f)}{dz} + \left[\frac{\pi f}{Q_S(z)\beta(z)}\right]A(z,f) = 0 \qquad \text{[IV.4.1]}$$

where, $A(z,f)$ = the amplitude of the plane SH wave as a function of spatial coordinate z and frequency f

$\beta(z)$ = S wave velocity as a function of z

$Q_S(z)$ = S wave attenuation constant as a function of z.

Solution of Equation IV.4.1 using the initial condition

$$A(0,f) = A_o \qquad \text{[IV.4.2]}$$

gives the following equation valid at $z = z_1 \geq 0$:

$$A(z_1,f) = A_o \exp\left[-\int_0^{z_1} \gamma(z,f)dz\right] \qquad [IV.4.3]$$

where:

$$\gamma(z,f) = \frac{\pi f}{Q_S(z)\beta(z)} \qquad [IV.4.4]$$

An estimate of the change in Q_S during the water gap experiment was obtained using a step transition model between the dry and saturated values of Q_S and β, as shown in Figure IV-4-9. The thickness of the saturated layer was determined from the travel-time advance of the SH reflection from the water gap. The dry and saturated values of β correspond to those used in the step-transition velocity model previously discussed in this section. Using this spatial distribution of β and Q_S, the attenuation of the SH reflection event along its two-way travel path can be calulated using Equation IV.4.3, and is given by:

$$A_s(2d,f) = A_o \exp -\left[\int_0^d \gamma(z,f)dz + \int_d^0 \gamma(z,f)dz\right] \qquad [IV.4.5]$$

where,

$$\gamma(z,f) = \begin{cases} \dfrac{\pi f}{\beta_d Q_{Sd}} & 0 \le z \le z_1 \\ \dfrac{\pi f}{\beta_s Q_{Ss}} & z_1 \le z \le d \end{cases} \qquad [IV.4.6]$$

In these equations

β_d = the S velocity at ambient dry conditions

β_s = the saturated S velocity

Q_{Sd} = the shear attenuation constant at ambient dry conditions

Q_{Ss} = the saturated shear attention constant.

Completing the integral in Equation IV.4.5, then,

$$A_s(2d,f) = A_o \exp\left[(-2\pi f)\left[\frac{z_1}{\beta_d Q_{Sd}} + \frac{(d-z_1)}{\beta_s Q_{Ss}}\right]\right] \qquad [IV.4.7]$$

The attenuation for the granite slab at ambient dry conditions is easily calculated:

$$A_d(2d,f) = A_o \exp\left[\frac{-2\pi f d}{\beta_d Q_{Sd}}\right] \qquad [IV.4.8]$$

The fixed receiver data recorded at position S2 prior to filling the gap with water were used in estimating the change of Q_S with increased saturation. The SH reflection was windowed from 200-275 μs, as shown in Figure IV-4-10, with the amplitude spectrum of this wavelet presented in Figure IV-4-10. Since anelastic loss is basically a filtering operation, the spectrum shown in Figure IV-4-10 actually combines the response of the SH source spectrum and the effect of the anelastic filtering. This is expressed as the spectral product:

$$\tilde{R}(f) = \tilde{S}(f)\tilde{f}(f) \qquad [IV.4.9]$$

where, $\tilde{R}(f)$ = the amplitude spectrum of the SH reflection wavelet

$\tilde{S}(f)$ = the amplitude spectrum of the SH source function

$\tilde{f}(f)$ = the amplitude spectrum of the anelastic loss filter

Suppose the spectra of the SH reflection are measured at ambient dry and saturated conditions, $\tilde{R}_d(f)$ and $\tilde{R}_s(f)$ respectively. By taking the ratio of these two quantities, the expression in Equation IV.4.9 implies:

$$\frac{\tilde{R}_s(f)}{\tilde{R}_d(f)} = \frac{\tilde{S}(f)\tilde{f}_s(f)}{\tilde{S}(f)\tilde{f}_d(f)} = \frac{\tilde{f}_s(f)}{\tilde{f}_d(f)} \qquad \text{[IV.4.10]}$$

This result assumes that the SH source spectrum $\tilde{S}(f)$ remains unchanged during the measurement of $\tilde{R}_d(f)$ and $\tilde{R}_s(f)$.

Expressions for $\tilde{R}_d(f)$ and $\tilde{R}_s(f)$ for the step transition model shown in Figure IV-4-9 were derived in Equation IV.4.(7 and 8), respectively. Then:

$$\frac{\tilde{R}_s(f)}{\tilde{R}_d(f)} = \frac{A_s(2d,f)}{A_d(2d,f)} = \exp\left[-(2\pi f)(d-z_1)\left[\frac{\beta_d Q_{Sd} - \beta_s Q_{Ss}}{\beta_d \beta_s Q_{Sd} Q_{Ss}}\right]\right] \qquad \text{[IV.4.11]}$$

Rewriting this expression, then

$$\ell n\left[\frac{A_s(2d,f)}{A_d(2d,f)}\right] = f\left[(2\pi)(d-z_1)\left[\frac{\beta_s Q_{Ss} - \beta_d Q_{Sd}}{\beta_d \beta_s Q_{Sd} Q_{Ss}}\right]\right] \qquad \text{[IV.4.12]}$$

The amplitude spectrum shown in Figure IV-4-10 was then used as an estimate of $R_d(2d,f)$. The SH reflection event was windowed from the fixed receiver traces recorded at S2 after the gap was filled with water. The amplitude spectra of each of these windowed events would provide a separate estimate of $R_s(2d,f)$. Each of these estimates of $R_s(2d,f)$ will have an associated estimate of the saturated layer thickness $d - z_1$ obtained from the arrival time of the SH reflection. The

ratio $\frac{\tilde{R}_s(f)}{\tilde{R}_d(f)}$ was used to estimate $\frac{A_s(2d,f)}{A_d(2d,f)}$ under the assumption that the source input $\tilde{S}(f)$ remains unchanged. Since β_d and β_s were used in the estimation of $d - z_1$, the only unknown quantities in Equation IV.4.12 are Q_{Sd} and Q_{Ss}. A spectral ratio method described in Appendix II was employed on the spectra of the primary and first multiple SH reflections from the air gap recorded with the slab at ambient dry conditions. The results of estimates at locations S1 and S2 suggest that $Q_{Sd} = 50$ is a reasonable estimate for the granite slab.

Equation IV.4.12 is a linear equation of the form $y = bx$ where

$$y = \ln\left[\frac{A_s(2d,f)}{A_d(2d,f)}\right] \quad \text{and} \quad x = f \ .$$

We then used a least-squares best fit of the measured spectral data to obtain the value of the slope b. Referring again to Equation IV.4.12, the best-fit slope is then:

$$b = (2\pi)(d-z_1)\left[\frac{\beta_s Q_{Ss} - \beta_d Q_{Sd}}{\beta_d \beta_s Q_{Sd} Q_{Ss}}\right] \qquad [IV.4.13]$$

Solving this equation for Q_{Ss}, we obtain,

$$Q_{Ss} = \frac{2\pi\beta_d Q_{Sd}(d-z_1)}{\beta_s [2\pi(d-z_1) - b\beta_d Q_{Sd}]} \qquad [IV.4.14]$$

This log spectral method of estimating Q in rock specimens is discussed in detail in Johnson and Toksoz, 1980. In our particular case the Q value of the standard specimen corresponds to Q_{Sd} (estimated in

in Appendix II). The problem of the dependence of Q with frequency is somewhat answered by the uncertainty in the best-fit slope b. If Q varies greatly over the frequency band used in the best-fit analysis, then this variation will be reflected as a large uncertainty in the linear slope b. In a sense this method itself tests the assumption of Q being constant over the frequency band of the measurement.

In actuality, Equation IV.4.12 is a linear equation in frequency only if the shear attenuation constant Q_S is not dependent on frequency. Theoretical analyses by Nur, 1971, and O'Connell and Budiansky, 1977, suggest that the shear attenuation constant may indeed be strongly dependent on frequency in a fluid-saturated rock under certain conditions. Referring to Figure 7 of O'Connell and Budiansky, 1977, which tabulates the theoretical behavior of V_P, V_S, Q_P, and Q_S for a water-saturated rock over a range of frequencies from 1-10^8 Hz and for three values of crack density ε, we quote:

> "Note that Q can be relatively independent of frequency over a wide range of frequencies. From 1 to 10^6 Hz, dissipation is due to fluid flow between cracks; this range includes most laboratory measurements and seismic measurements. The velocity dispersion between laboratory and seismic frequencies can be appreciable."

Thus, our assumption that Q_S is independent of frequency in the band 10^4-10^5 Hz seems entirely consistent with the O'Connell-Budiansky analysis. Indeed, no measurements of the variation of Q_S with increased water saturation for a granitic rock similar to the Raymond granite are available in the published literature. Thus our assumption that Q_S

is independent of frequency does not appear to violate the results of previously published experimental or theoretical work. Also, as previously stated, the log spectral ratio method will itself provide a test of the constant Q assumption.

It would seem that this procedure for calculating Q_{Ss} could be successfully employed for all of the traces recorded with the gap water-filled. However, the amplitude spectra of these windowed traces have a certain noise level that is due to the arrival of elastic wave energy unrelated to the SH reflection during the 200-275 μs time window. When the amplitude of the SH reflection is severely reduced, the background noise contribution to the amplitude spectra of the windowed trace becomes significant. Thus, this method of calculating Q_{Ss} could only be applied in the cases where the attenuation of the SH reflection was relatively small. As it turned out, only data recorded within the first 24 hours after filling the gap with water could be used in the estimate of Q_{Ss}. After this time the SH reflection was so severely attenuated that the best-fit estimates of the slope b were unreliable.

Figure IV-4-11a shows the windowed SH reflection recorded at location S2 during the first 63.5 hours after filling the water gap, and the amplitude spectra of these traces are shown in Figure IV-4-11b. The continual decrease in amplitude in the higher frequency spectral components (> 60 kHz) occurs only during the first 41.5 hours of saturation. However, the decrease in the lower frequency components (< 60 kHz) is noticeable during the entire 63.5 hours of measurements, as shown in Figure IV-4-11c. This suggests that the higher frequency components that remain constant after 40-45 hours are due to elastic

wave energy unrelated in travel path with the SH reflection from the water gap. If this is the case, then this background spectrum will represent some form of "noise" to the simple one dimensional Q analysis previously described. This possibly explains the fact that the best-fit slope estimates become unreliable as the attenuation of the SH reflection increased.

The windowed SH reflection event recorded at S2 on January 13, 4.5 hours after filling the gap with water, is shown in Figure IV-4-12a. Comparison of the amplitude spectrum shown in this figure with the spectrum of the dry reference trace at S2 (shown in Figure IV-4-10) shows that noticeable attenuation has occurred in the 10-120 kHz frequency band at 4.5 hours. Spectral division is performed to yield the quotient $\tilde{R}_s(f)/\tilde{R}_d(f)$, where $\tilde{R}_s(f)$ is the saturated spectrum shown in Figure IV-4-12a, and $\tilde{R}_d(f)$ is the dry reference spectrum given in Figure IV-4-10. The logarithm of this spectral ratio in the frequency band 20-120 kHz is shown in Figure IV-4-12b, and the best-fit line with slope b to the log spectral ratio data is included in this figure. The value of the slope b and its corresponding uncertainty are given in Table IV-4-3, as is the differential arrival time $\Delta t = -0.98\ \mu s \pm 51\%$ for the 4.5 hour data. The dry reference arrival time at S2 is $t_d = 219.73\ \mu s \pm 0.5\%$, so that $\beta_d = 2735$ m/s $\pm$ 1% for d = 30.2 cm $\pm$ 0.5%. The corresponding value of the saturated shear velocity is estimated as $\beta_s = 3050$ m/s $\pm$ 1% using the results of Section 2 of this chapter. The thickness of the saturated zone $d - z_1$, derived using these values of β_d and $\Delta\beta$, is also presented in Table IV-4-3. These values were used with $Q_{Sd} = 50 \pm 30\%$ in Equation IV.4.12 to yield a calculated value of $Q_{Ss} = 3.8 \pm 80\%$.

Table IV-4-3

Hours After Filling Gap With Water	Differential Arrival Δt Time (μs)	Saturated Layer Thickness $d - z_1$ (cm)	Slope of Spectral Ratio (Hz^{-1})	Calculated Q_{Ss} for $Q_{Sd} = 50$
4.5	-0.98 ± 51%	1.45 ± 56%	-7.284×10^{-6} ±10.2%	3.8 ± 80%
7.0	-1.96 ± 25.5%	2.75 ± 30%	-1.332×10^{-5} ±12.4%	3.9 ± 53%
9.5	-2.93 ± 17.1%	4.03 ± 22%	-1.672×10^{-5} ± 9.3%	4.5 ± 48%
17.0	-4.89 ± 10.2%	6.63 ± 16%	-2.988×10^{-5} ± 8.9%	4.1 ± 45%

Position S2 (20-120 kHz)

The log spectral ratio shown in Figure IV-4-12b has a very deep "hole" centered between 90-100 kHz. This spectral hole implies that Q_S decreases sharply in this band when compared to the background attenuation in the 10-80 kHz band. Indeed, this sort of dependence of Q_S with frequency is consistent with the theoretical predictions of Nur, 1971, and O'Connell and Budiansky, 1977. Both of these theoretical models suggest the presence of such spectral "holes" resulting from a strong decrease in Q_S within a narrow frequency band. The presence of this spectral hole causes the best-fit slope b to have a fairly large uncertainty (± 10%), especially since the sample size of the data set is large (N = 101 in Equation II.3.8). Thus the assumption that Q_S is frequency independent may not be valid in the 20-120 kHz band.

Figure IV-4-12c shows the log spectral ratio and best-fit line obtained in the 10-60 kHz band for the 4.5 hour data at S2. Using the same values of β_d, $\Delta\beta$, Q_{Sd} and $d - z_1$ as before, then $Q_{Ss} = 3.2 \pm 89\%$ is calculated from the best-fit slope $b = -8.728 \times 10^{-6} Hz^{-1} \pm 8.3\%$ (as tabulated in Table IV-4-4). This result shows that attenuation is indeed occurring in the 10-60 kHz band, as was previously observed in the amplitude spectrum shown in Figure IV-4-12a. The uncertainty of the slope b is smaller in the 10-60 kHz band (± 8%) than that obtained in the 20-120 kHz band (± 10%) even though the sample size of the 10-60 kHz data (N = 51) is half that of the 20-120 kHz data. These results suggest that the presence of the 90-100 kHz spectral "hole" does not cause serious errors in the estimate of the slope b in the 20-120 kHz band, and that attenuation occurs in the 10-60 kHz band as well as at higher frequencies. The windowed SH events recorded at S2 at 7.0, 9.5,

Table IV-4-4

Hours After Filling Gap With Water	Differential Arrival Δt Time (μs)	Saturated Layer Thickness $d - z_1$ (cm)	Slope of Spectral Ratio (Hz^{-1})	Calculated Q_{Ss} for $Q_{Sd} = 50$
4.5	-0.98 ± 51%	1.45 ± 56%	-8.728×10^{-6} ± 8.3%	3.2 ± 89%
7.0	-1.96 ± 25.5%	2.75 ± 30%	-1.273×10^{-5} ± 8.0%	4.0 ± 59%
9.5	-2.93 ± 17.1%	4.03 ± 22%	-1.300×10^{-5} ± 8.3%	5.6 ± 51%
17.0	-4.89 ± 10.2%	6.63 ± 16%	-1.547×10^{-5} ± 9.3%	7.4 ± 45%

Position S2 (10-60 kHz)

and 17.0 hours after filling the gap are shown correspondingly in Figures IV-4-(13a to 15a). Likewise the log spectral ratios for the two frequency bands (20-120 kHz and 10-60 kHz) are shown in Figures IV-4-(13b,c to 15b,c). The best-fit slopes b and corresponding Q_{Ss} for the data at S2 are tabulated in Table IV-4-3 for the 20-120 kHz band.

The results presented in Tables IV-4-(3 and 4) suggest that Q_{Ss} has a value of 7 ± 4. Although Q_{Ss} is not well determined statistically, this value represents nearly an order of magnitude decrease in Q_S with saturation. This is a rather large decrease in Q_S, but a similar decrease in Q_S with saturation in a Bedford limestone is given in Nur, 1971. In Figure 3 of this paper, the relative attentuation Q_S^{-1} is seen to increase over a factor of 10 as the viscosity of the fluid phase in the rock is increased from air (10^{-4} poise) to water (10^{-2} poise). This figure also shows an increase in Q_P^{-1} with saturation, although the effect is not as large as the change in Q_S^{-1}.

Similar calculations of Q_{Ss} were performed using SH data recorded at location S1. The dry reference SH reflection and its amplitude spectrum are shown in Figure IV-4-16, with t_d = 215.82 μs ± 0.5% and β_d = 2795 m/s ± 1%. The value $\Delta\beta$ = 315 m/s ± 1.5% obtained using the experimental results of Section 2, and Q_{Sd} = 50 ± 30% from Appendix II. The windowed SH reflection events recorded at 4.5, 7.0, 9.5, and 17.0 hours after filling the gap are shown correspondingly in Figures IV-4-(17a to 20a). The log spectral ratios in the 20-120 kHz and 10-60 kHz bands are likewise shown in Figures IV-4-(17b,c to 20b,c). The best-fit slopes b obtained from the 20-120 kHz and 10-60 kHz spectral ratio data are given in Table IV-4-(5 and 6), respectively.

Table IV-4-5

Hours After Filling Gap With Water	Arrival Time (μs)	Saturated Layer Thickness $d - z_1$ (cm)	Slope of Spectral Ratio (Hz^{-1})	Calculated Q_{Ss} for $Q_{Sd} = 50$
4.5	-1.95 ± 25.6%	2.73 ± 30.6%	-1.538×10^{-6} ±23.3%	20.1 ± 56%
7.0	-1.95 ± 25.6%	2.73 ± 30.6%	-2.195×10^{-6} ±21.0%	16.2 ± 55%
9.5	-2.93 ± 17.1%	4.08 ± 22.3%	-3.157×10^{-6} ±15.9%	16.5 ± 48%
17.0	-5.19 ± 9.6%	7.20 ± 15.4%	-6.67×10^{-6} ±11.2%	14.7 ± 43%

Position S1 (20-120 kHz)

Table IV-4-6

Hours After Filling Gap With Water	Arrival Time (μs)	Saturated Layer Thickness $d - z_1$ (cm)	Slope of Spectral Ratio (Hz^{-1})	Calculated Q_{Ss} for $Q_{Sd} = 50$
4.5	-1.95 ± 25.6%	2.73 ± 30.6%	-3.408×10^{-6} ±10.5%	11.9 ± 53%
7.0	-1.95 ± 25.6%	2.73 ± 30.6%	-2.118×10^{-6} ±25.2%	16.5 ± 56%
9.5	-2.93 ± 17.1%	4.08 ± 22.3%	-2.088×10^{-6} ±30.5%	21.0 ± 50%
17.0	-5.19 ± 9.6%	7.20 ± 15.4%	-2.025×10^{-6} ±47.4%	27.6 ± 46%

Position S1 (10-60 kHz)

The uncertainty on the best-fit slope b is fairly large at position S1, in the range of 15-40%. Although the log spectral ratios shown in Figure IV-4-(17b to 20b) indicate that there is no definite spectral "hole" in the 90-100 kHz band as was found at S2, there is considerable irregular curvature in the log spectral data. The appearance of the log spectral curves at S1 indicates that the noise level of this data is large, and this is also reflected in the large uncertainties on the slope b (± 15-40%). Thus the appearance of the spectral "hole" in the data recorded at S2 might represent noise in the spectral ratio technique, rather than the implied strong decrease of Q_S with frequency in this notch. It appears that the assumption of a frequency independent Q_S is valid within the uncertainties of the log spectral ratio used in this application.

The values of $d - z_1$ and Q_{Ss} are calculated at S1 using β_d = 2795 m/s ± 1%, $\Delta\beta$ = 315 m/s ± 1.5%, and Q_{Sd} = 50 ± 30%, and the results are given in Tables IV-4-(5 and 6) for each best-fit slope b. These results suggest that Q_{Ss} ranges from 12-28 at S1, which is a much larger value than the calculated Q_{Ss} at location S2. The error on Q_{Ss} will again be on the order of 50%.

The results presented in Tables IV-4-(3 to 6) suggest that Q_{Ss} may range in value from 3-30. Even though these values are rather poorly determined statistically, the reliability of these estimates yet depends on the validity of the assumption that the absorbed water creates a sharply defined layer of constant saturation. Indeed, if absorption of the water is due to capillary forces, then a gradient of saturation would exist with the layer affected by the absorbed water.

Then a linear transition velocity/attenuation model would more adequately represent this zone of variable saturation. However, the large error on the layer thickness $d - z_2$ estimated in Section 3 from the linear velocity transition model would cause very large errors on Q_{Ss} estimated using such a model. Thus, only the step velocity/attenuation model shown in Figure IV-4-9 was used to quantify the attenuation effects observed in this experiment.

Another assumption fundamental to this analysis of Q_{Ss} is that Q_S decrease monototically when going from an ambient dry to saturated state. In fact, recent work by Frisillo and Stewart, 1980, and Winkler and Nur, 1982, report that Q_P in partially saturated Berea and Massilon sandstones is less than Q_P measured in dry or fully-saturated specimens of the sandstones. These authors also found that Q_P of the dry sandstones was larger than the fully saturated Q_P. Also, Winkler and Nur, 1982, report that Q_S of a Massilon sandstone decreases monototically in going from dry to fully saturated conditions. Unfortunately, no measurements of the variation in Q_S with saturation for a low permeability granitic rock were found by the author in the published literature.

Because the actual distribution of saturation, shear velocity β and shear attenuation Q_S are not known within the granite slab, the values of Q_{Ss} determined using the step transition model represent only an approximation of the actual behavior of Q_S within the slab. Importantly, the step-velocity model results in a minimum estimate for the thickness of the saturated layer when compared to any other one dimensional geometry used in modeling a velocity transition from β_d to β_s. Thus, the minimum thickness layer used in the step velocity/attenuation

model will require the maximum change between Q_{Sd} and Q_{Ss} to account for the observed decrease in amplitude. This suggests that the use of this step Q_S transition model will result in Q_{Ss} being underestimated, which might suggest that the values given in Tables IV-4-(3 to 6) represent a lower bound on the actual decrease in Q_S with saturation.

The final phase of this experiment was to repeat the drying of the granite slab. The SH traces shown in Figure 21 were recorded at positions S1 and S2 between January 25 (after draining the water gap) and March 16, 1982. Once again, as the granite dried out the SH reflection increased in amplitude and arrival time. Since the waveform of the direct SH event remained fairly constant during this period, the changes in the SH reflection cannot be due to varying source effects. This experiment again corroborates the conclusion that water absorbed from the gap was responsible for the observed changes in the shear velocity and attenuation of the granite slab.

The results of the experiment presented in this section confirmed that water could be quickly absorbed into a dry granite slab. The absorbed water causes the S velocity of the granite to increase, and also results in a substantial decrease in the shear attenuation constant (Q_S) of the granite. The increased velocity and attenuation that occur in a Raymond granite with increased saturation have important implications with regard to the interpretation of the SH field data obtained at the Shaw quarry which will be discussed further in Chapter V.

To this point the arrival time of the SH reflection have been picked manually. Because the increase in average shear velocity of the granite slab with saturation is inferred from these arrival times, it

would be desirable to quantify these changes in arrival time solely from the SH waveform data. In the next section a method is described in which the change of arrival time of the windowed SH reflection events are estimated from the phase spectra of these data.

Figure Captions

Figure IV-4-1
Locations of SH traverses on the granite slab model for experiments performed between January to March, 1982.

Figure IV-4-2
Unprocessed SH profiles recorded during the first week of January, 1982, at locations:
a) S1
b) S2

Figure IV-4-3
P reflection profile recorded during the first week of January, 1982, at location P1.
a) Unprocessed data
b) Unprocessed data summed to give response of a 2 cm linear array

Figure IV-4-4
Data recorded at fixed receiver on January 12, 1982, at positions S1, S2, and P1. Gap is air-filled.

Figure IV-4-5
Fixed receiver data recorded on January 13, 1982, from both air and water-filled gaps.
a) Position S1
b) Position S2
c) Position P1

Figure IV-4-6
SH data recorded during January 13-25, 1982, showing advance in arrival times and decrease in amplitude of the SH reflection from the water-filled gap.
a) Position S1
b) Position S2

Figure IV-4-7
P data recorded during January 13-25, 1982, at position P1.

Figure IV-4-8
Fixed SH receiver data recorded just prior to filling gap with water (January 13), and just prior to draining gap (January 25).
a) Position S1
b) Position S2

Figure IV-4-9
Step shear velocity/attenuation model used in estimating the change in Q_S during the saturation of the granite slab.

Figure IV-4-10
Windowed SH reflection at S2 recorded on January 13, 1982, prior to filling the gap with water. The amplitude spectrum shown in this figure will be used as the reference spectrum.

Figure IV-4-11
SH data recorded at location S2 during the first 63.5 hours after filling the gap with water.
a) Windowed SH data
b) Amplitude spectra of windowed SH data (0-200 kHz)
c) Amplitude spectra of windowed SH data (10-70 kHz)

Figure IV-4-12
SH reflection data recorded at S2 on January 13, 4.5 hours after filling gap with water.
a) Windowed SH reflection and amplitude spectrum
b) Log spectral ratio between 20-120 kHz
c) Log spectral ratio between 10-60 kHz

Figure IV-4-13
SH reflection data recorded at S2 on January 13, 7.0 hours after filling gap with water.
a) Windowed SH reflection and amplitude spectrum
b) Log spectral ratio between 20-120 kHz
c) Log spectral ratio betwen 10-60 kHz

Figure IV-4-14
SH reflection data recorded at S2 on January 13, 9.5 hours after filling gap with water.
a) Windowed SH reflection and amplitude spectrum
b) Log spectral ratio between 20-120 kHz
c) Log spectral ratio between 10-60 kHz

Figure IV-4-15
SH reflection data recorded at S2 on January 13, 17.0 hours after filling gap with water.
a) Windowed SH reflection and amplitude spectrum
b) Log spectral ratio between 20-120 kHz
c) Log spectral ratio between 10-60 kHz

Figure IV-4-16
Windowed SH reflection at S1 recorded on January 13, 1982, prior to filling the gap with water. The amplitude spectrum shown in this figure will be used as the reference spectrum.

Figure IV-4-17
SH reflection data recorded at S1 on January 13, 4.5 hours after filling gap with water.
a) Windowed SH reflection and amplitude spectrum
b) Log spectral ratio between 20-120 kHz
c) Log spectral ratio between 10-60 kHz

Figure IV-4-18
SH reflection data recorded at S1 on January 13, 7.0 hours after filling gap with water.
a) Windowed SH reflection and amplitude spectrum
b) Log spectral ratio between 20-120 kHz
c) Log spectral ratio between 10-60 kHz

Figure IV-4-19
SH reflection data recorded at S1 on January 13, 9.5 hours after filling gap with water.
a) Windowed SH reflection and amplitude spectrum
b) Log spectral ratio between 20-120 kHz
c) Log spectral ratio between 10-60 kHz

Figure IV-4-20
SH reflection data recorded at S1 on January 13, 17.0 hours after filling gap with water.
a) Windowed SH reflection and amplitude spectrum
b) Log spectral ratio between 20-120 kHz
c) Log spectral ratio between 10-60 kHz

Figure IV-4-21
SH data recorded at fixed receiver from January 25 to March 16, 1982. Note increase in amplitude and arrival time of SH reflection during this period.
a) Receiver at position S1
b) Receiver at position S2

EXPERIMENT #2

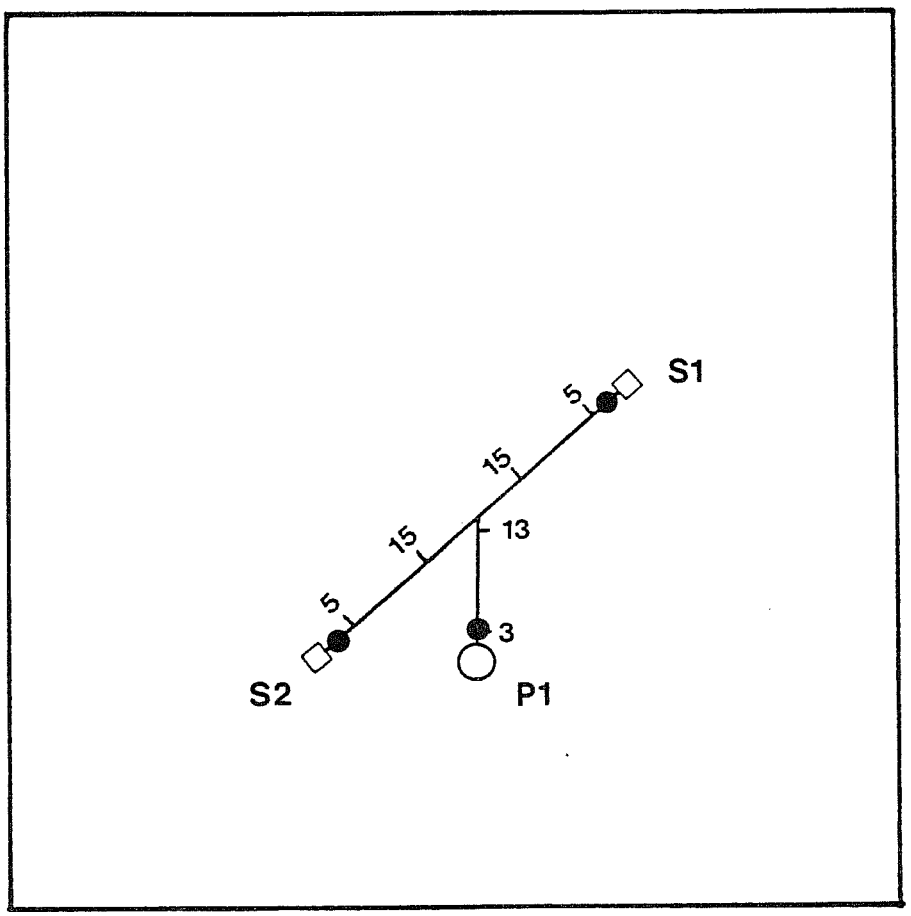

● Fixed receiver position

0 20 cm

XBL 837-2008

Figure IV-4-1

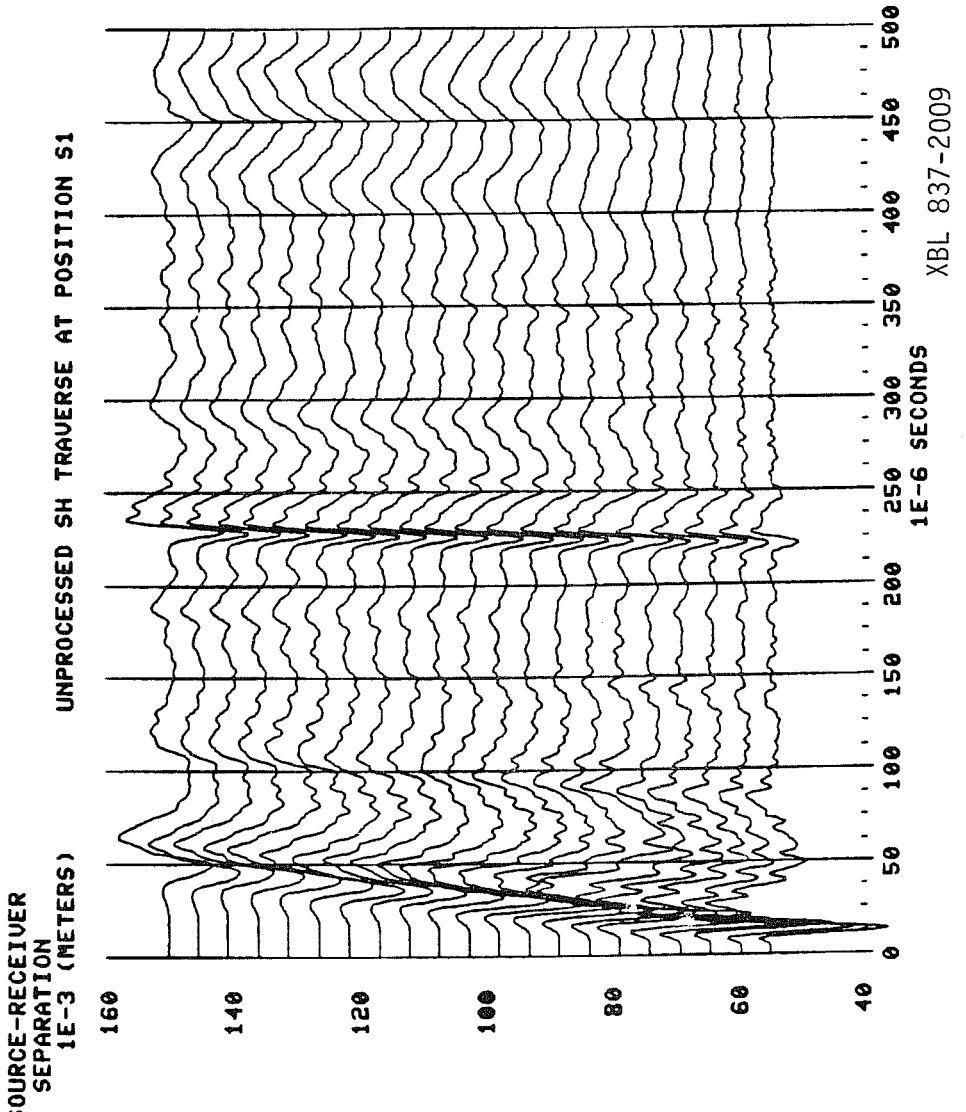

Figure IV-4-2a

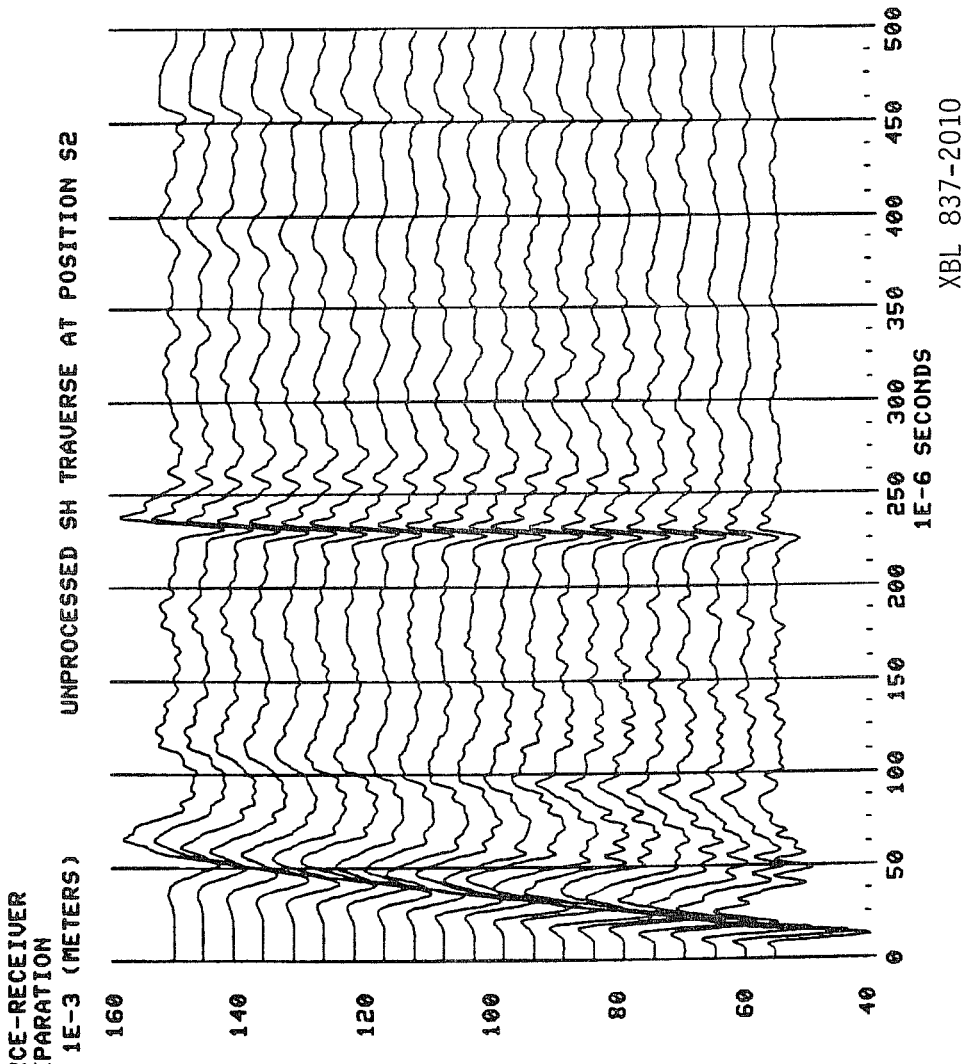

Figure IV-4-2b

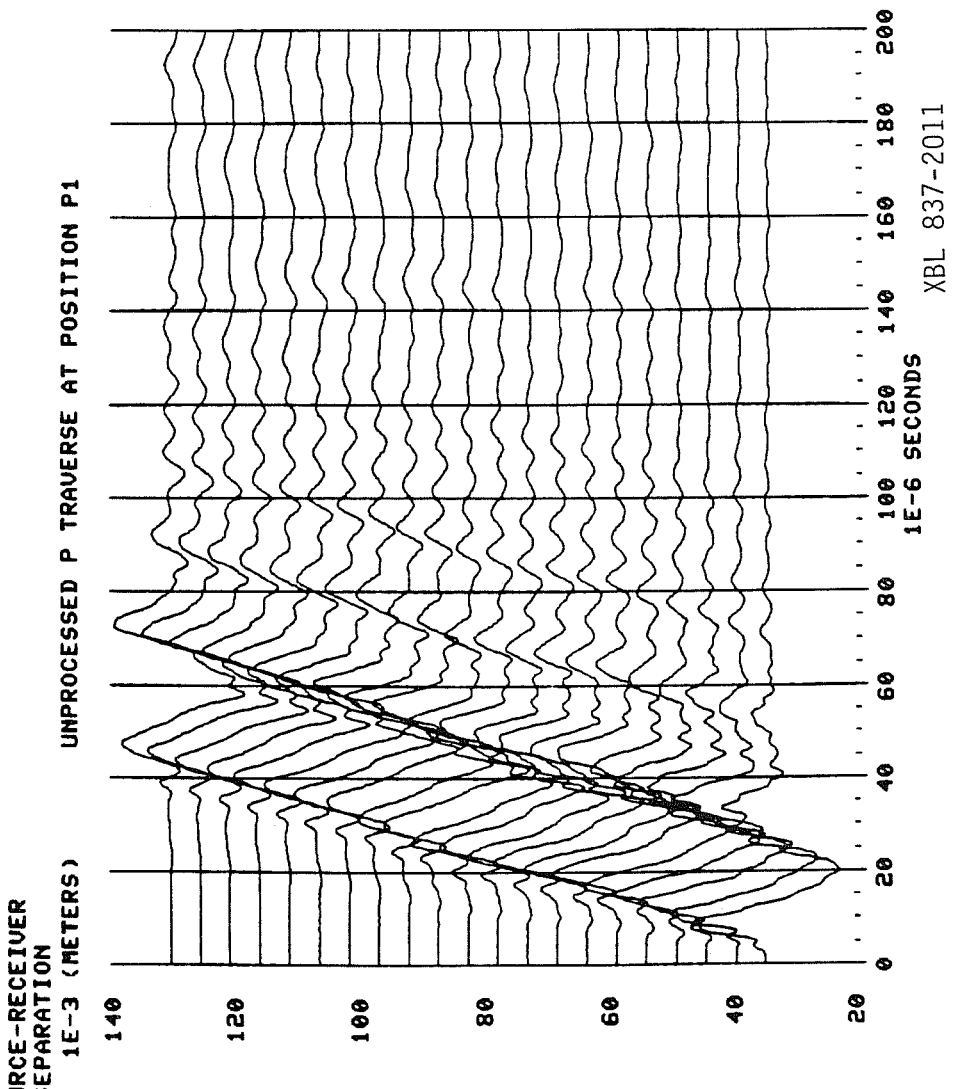

Figure IV-4-3a

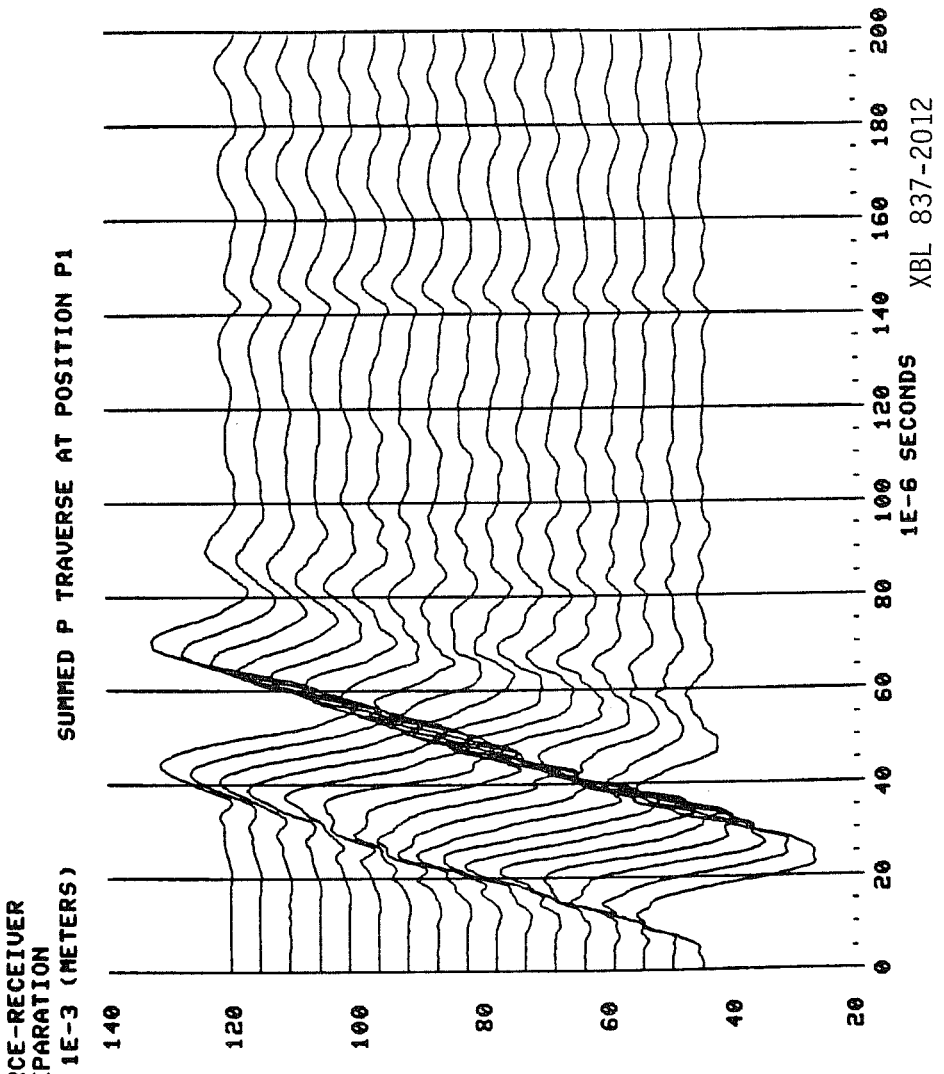

Figure IV-4-3b

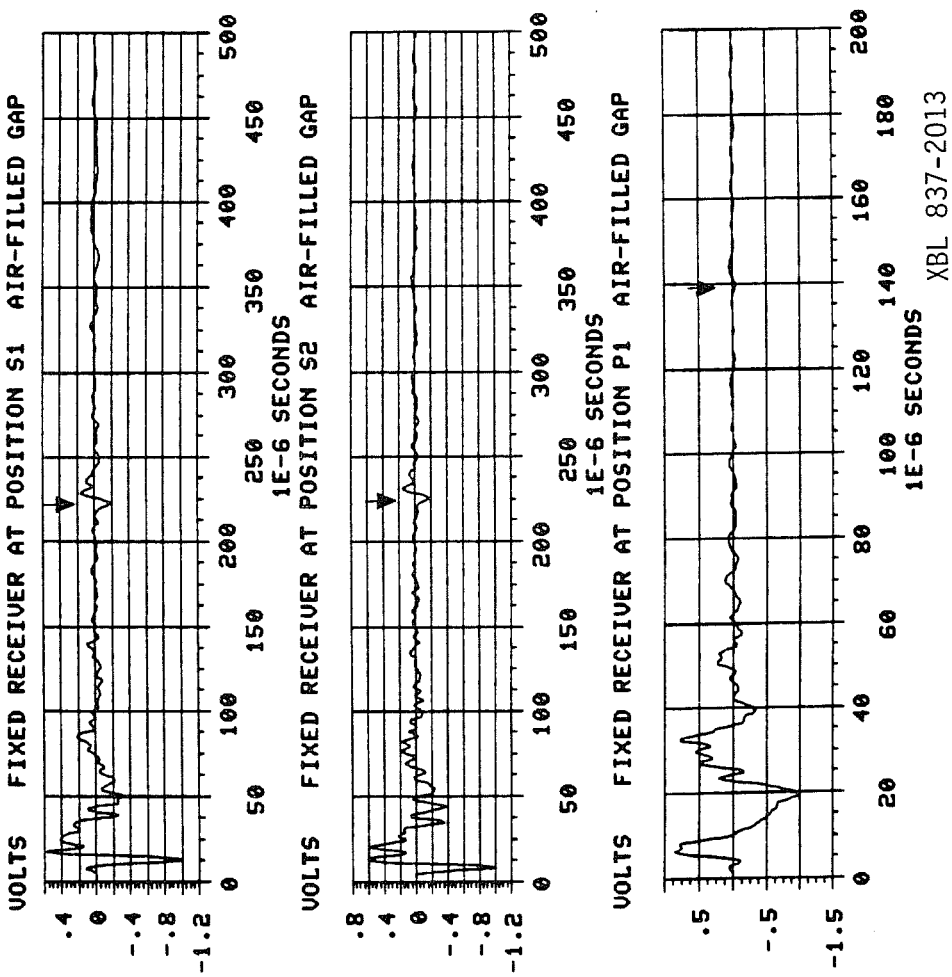
VOLTS FIXED RECEIVER AT POSITION S1 AIR-FILLED GAP
.4
0
-.4
-.8
-1.2
0 50 100 150 200 250 300 350 400 450 500
1E-6 SECONDS
VOLTS FIXED RECEIVER AT POSITION S2 AIR-FILLED GAP
.8
.4
0
-.4
-.8
-1.2
0 50 100 150 200 250 300 350 400 450 500
1E-6 SECONDS
VOLTS FIXED RECEIVER AT POSITION P1 AIR-FILLED GAP
.5
-.5
-1.5
0 20 40 60 80 100 120 140 160 180 200
1E-6 SECONDS
XBL 837-2013

Figure IV-4-4

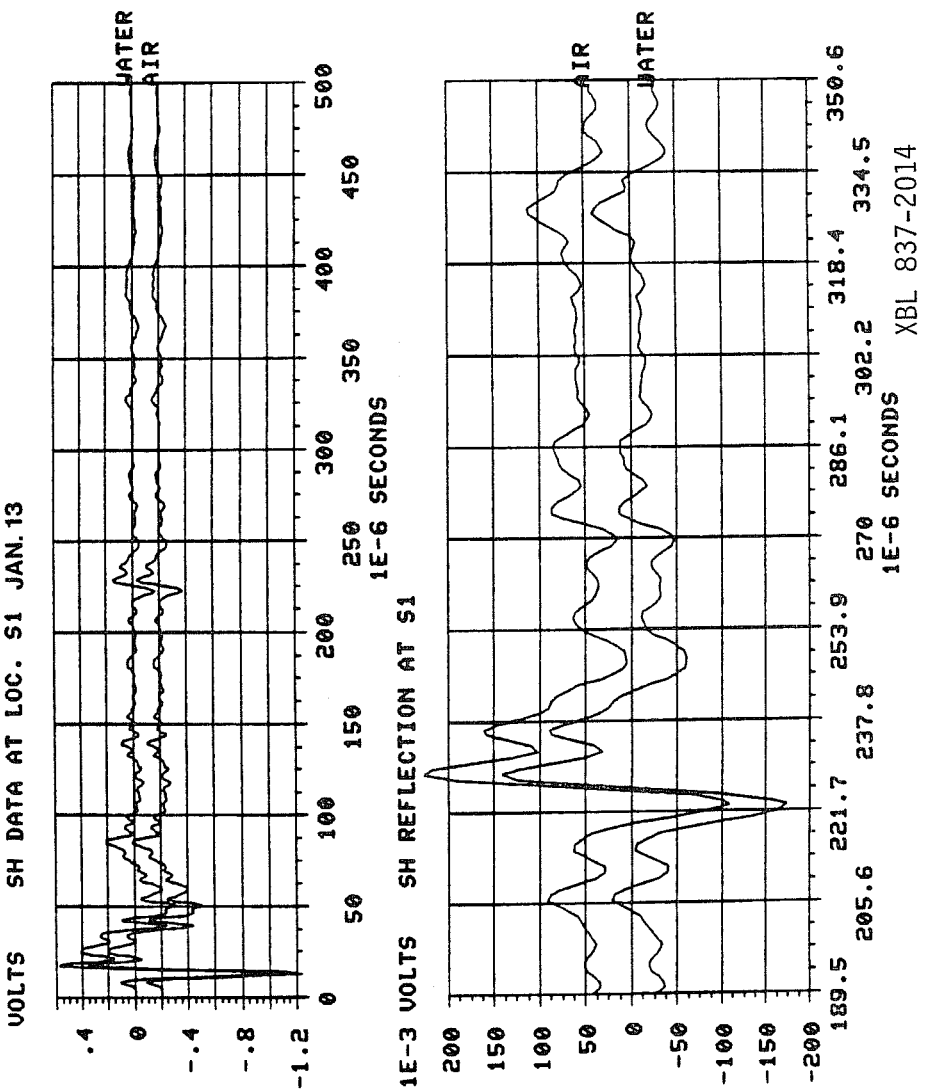

Figure IV-4-5a

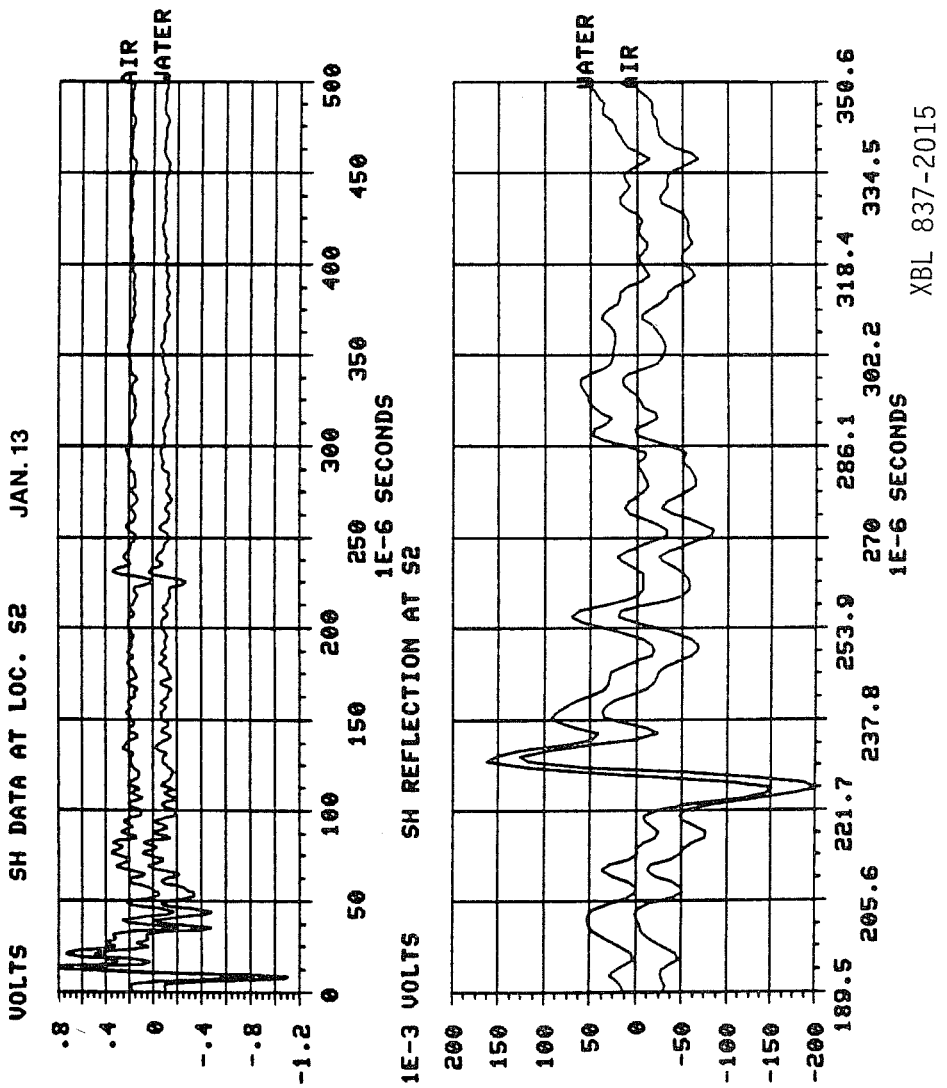

Figure IV-4-5b

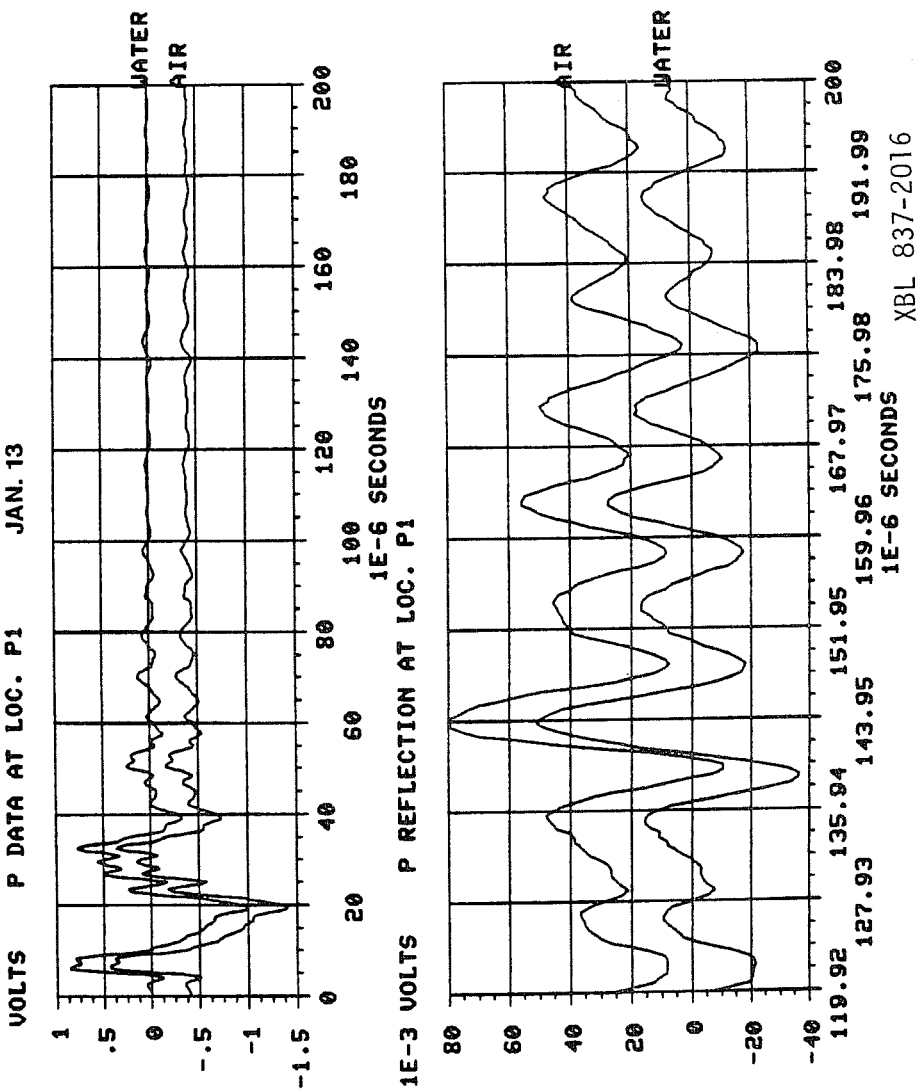

Figure IV-4-5c

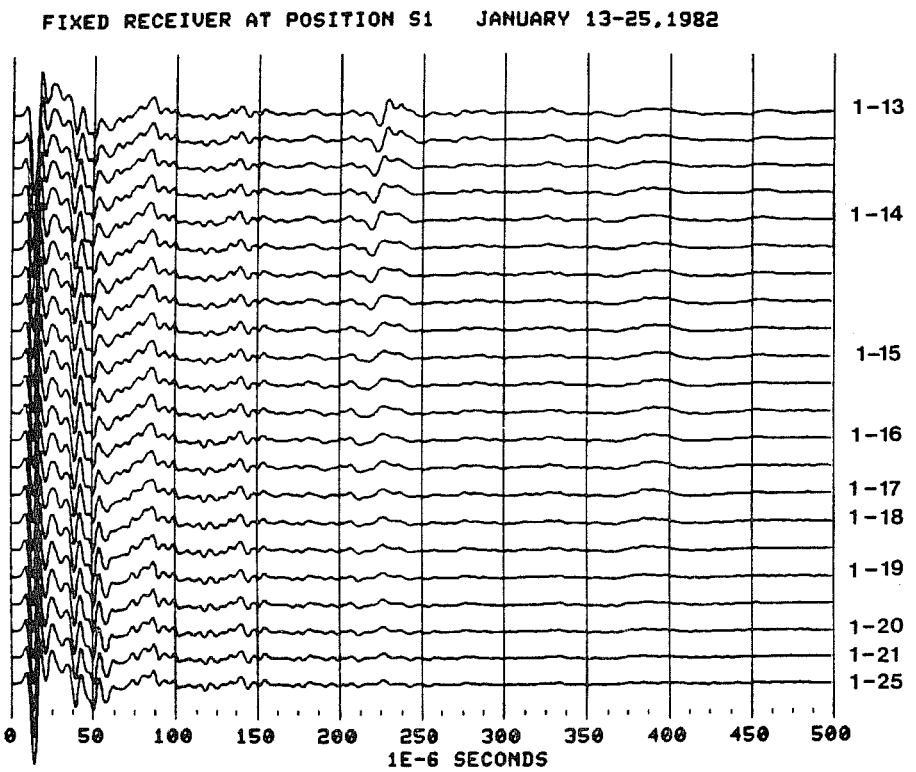

Figure IV-4-6a

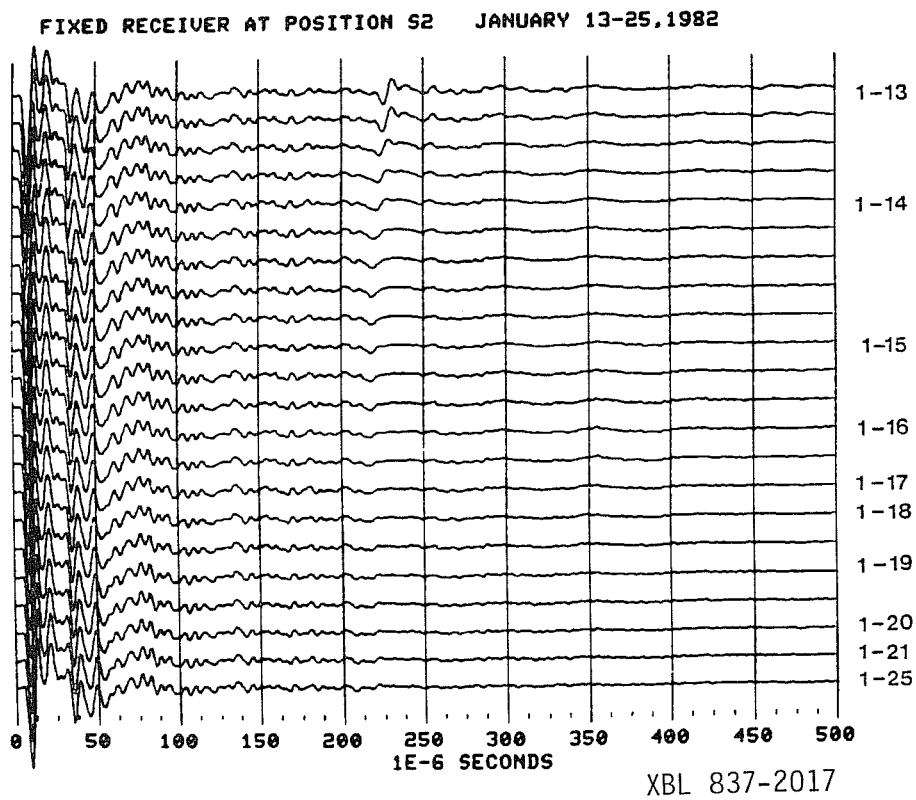

XBL 837-2017

Figure IV-4-6b

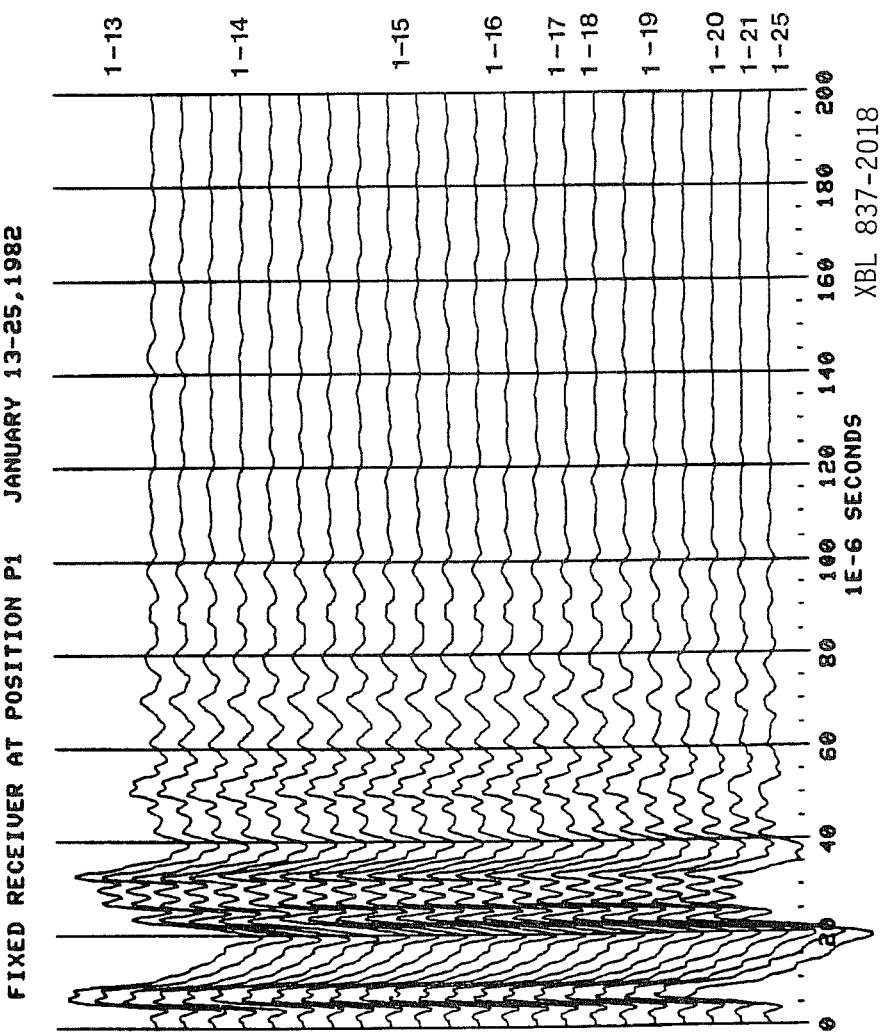
FIXED RECEIVER AT POSITION P1 JANUARY 13-25,1982
1-13
1-14
1-15
1-16
1-17
1-18
1-19
1-20
1-21
1-25
0
20
40
60
80
100
120
140
160
180
200
1E-6 SECONDS
XBL 837-2018

Figure IV-4-7

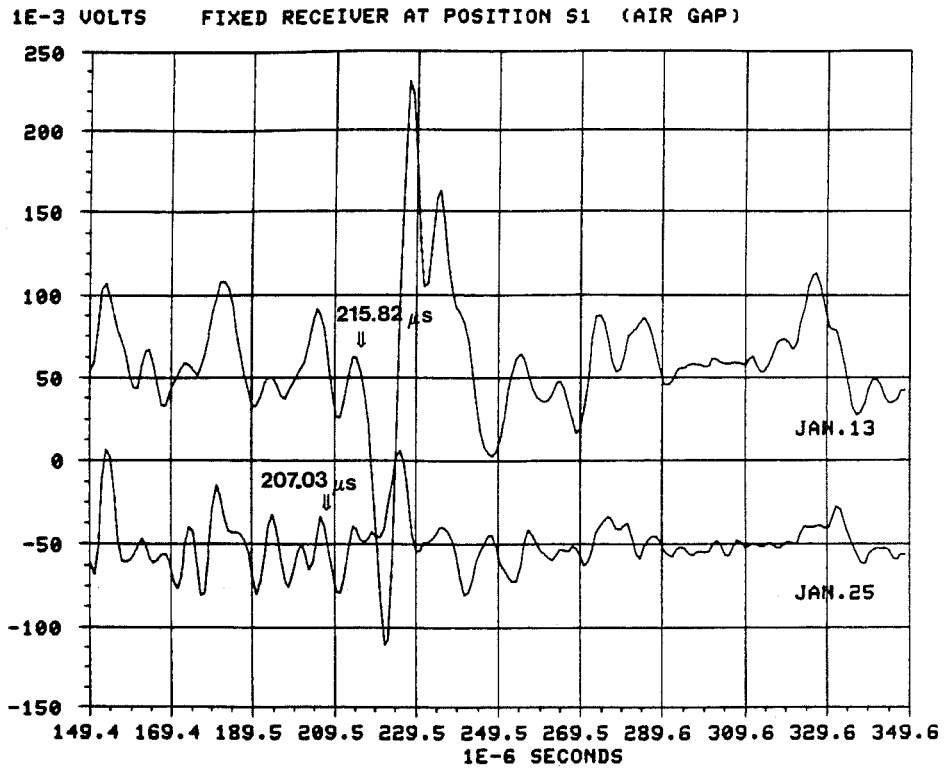

Figure IV-4-8a

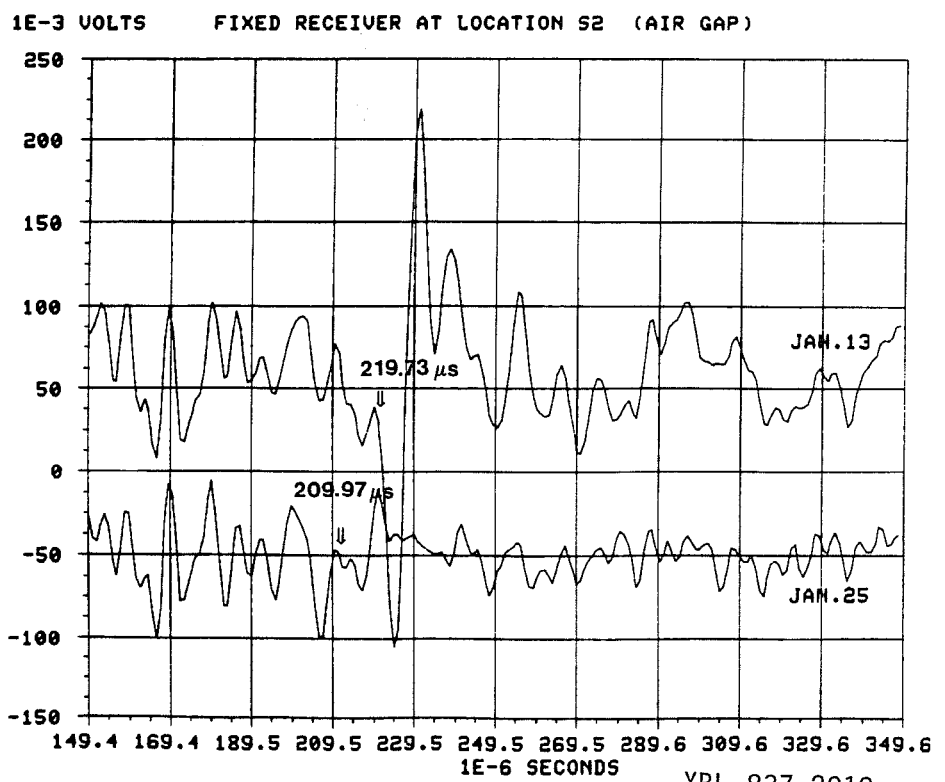

XBL 837-2019

Figure IV-4-8b

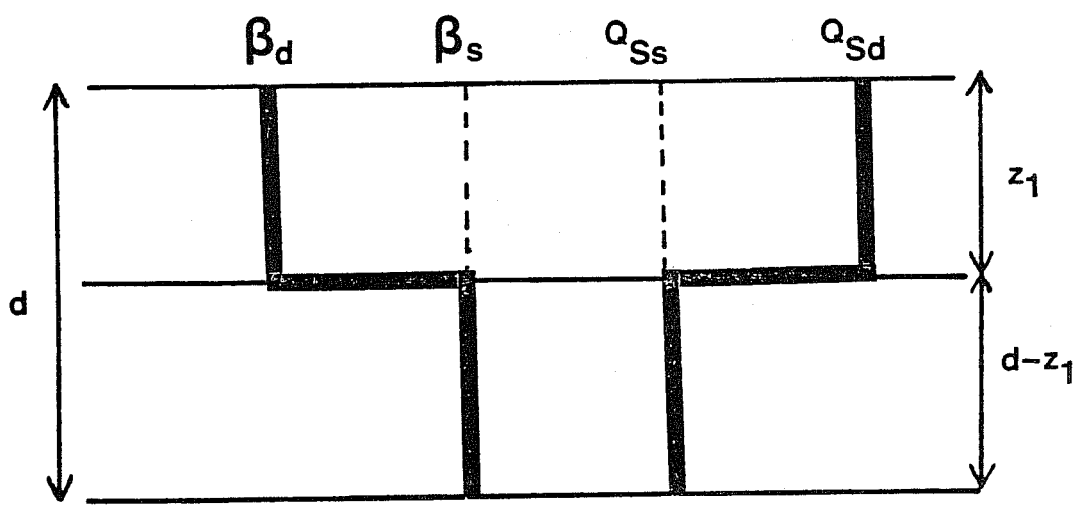

$\beta_d < \beta_s$ $\qquad$ $Q_{Ss} < Q_{Sd}$

XBL 837-2020

Figure IV-4-9

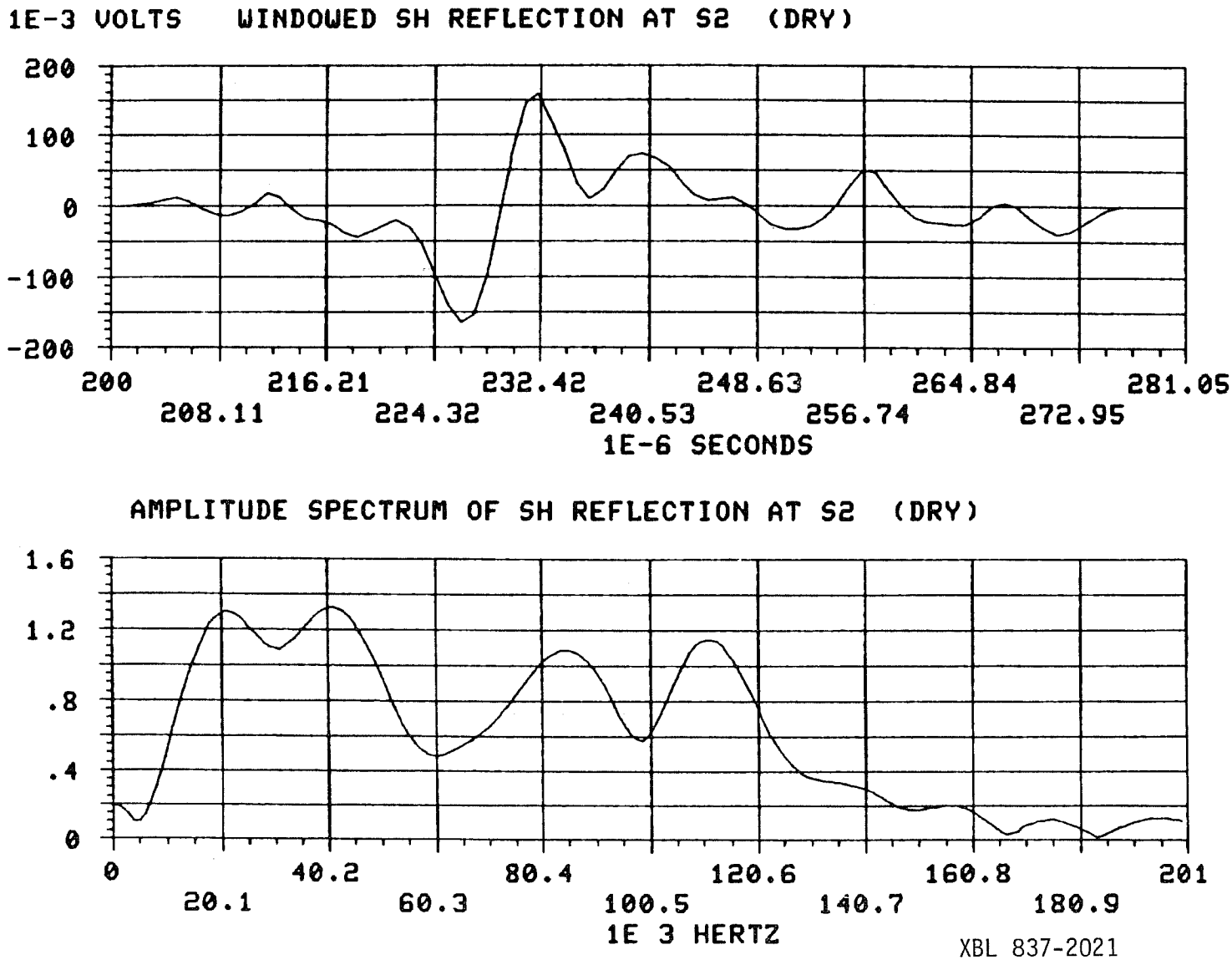

XBL 837-2021

Figure IV-4-10

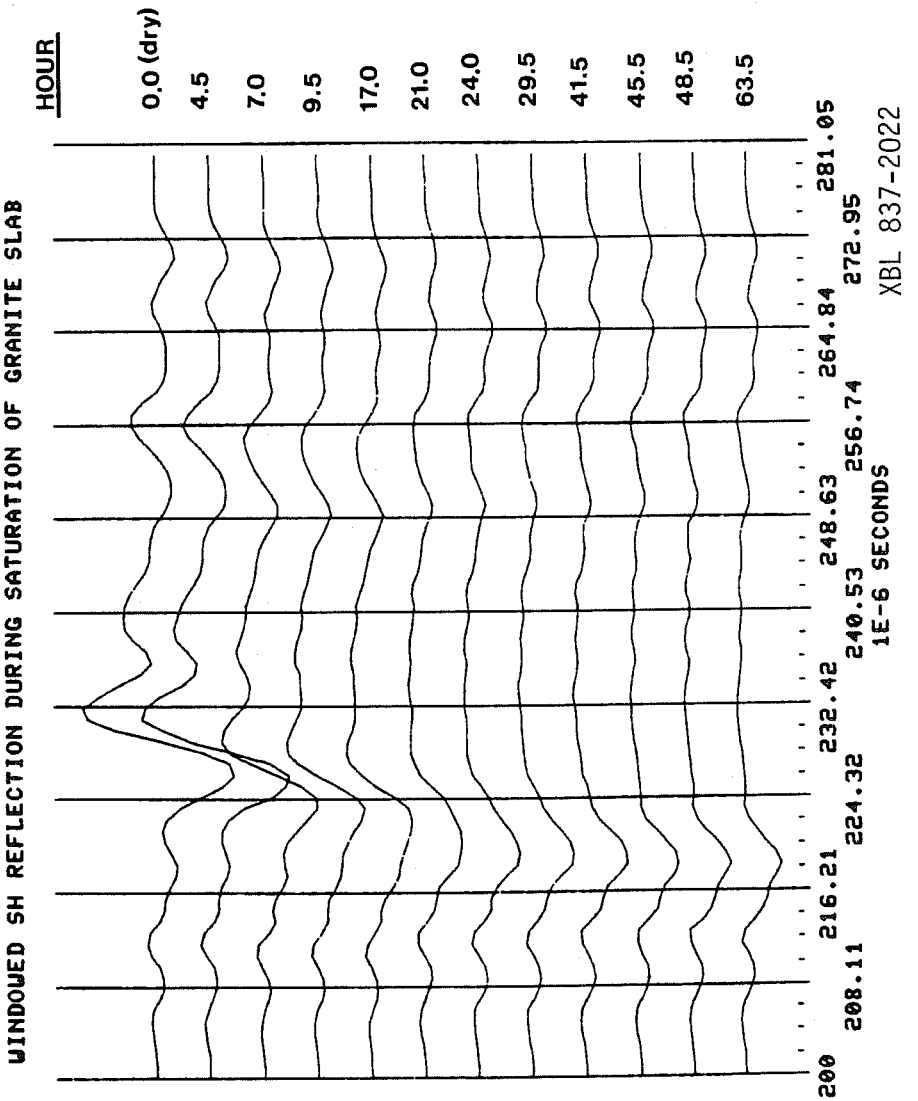

Figure IV-4-11a

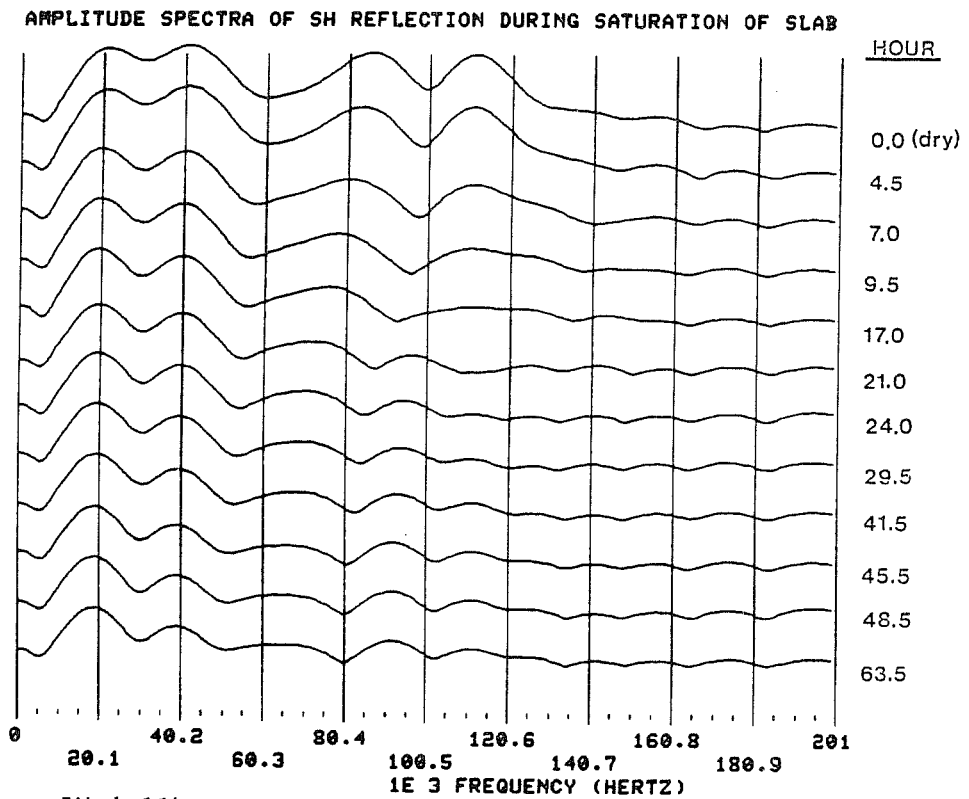

Figure IV-4-11b

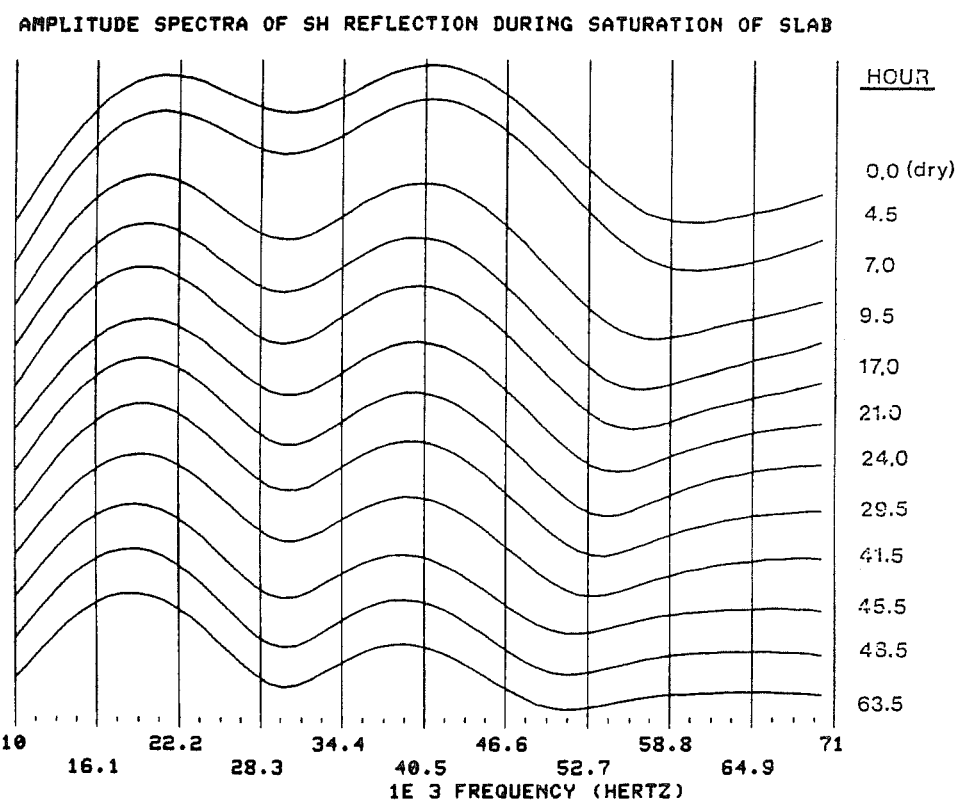

Figure IV-4-11c

XBL 837-2023

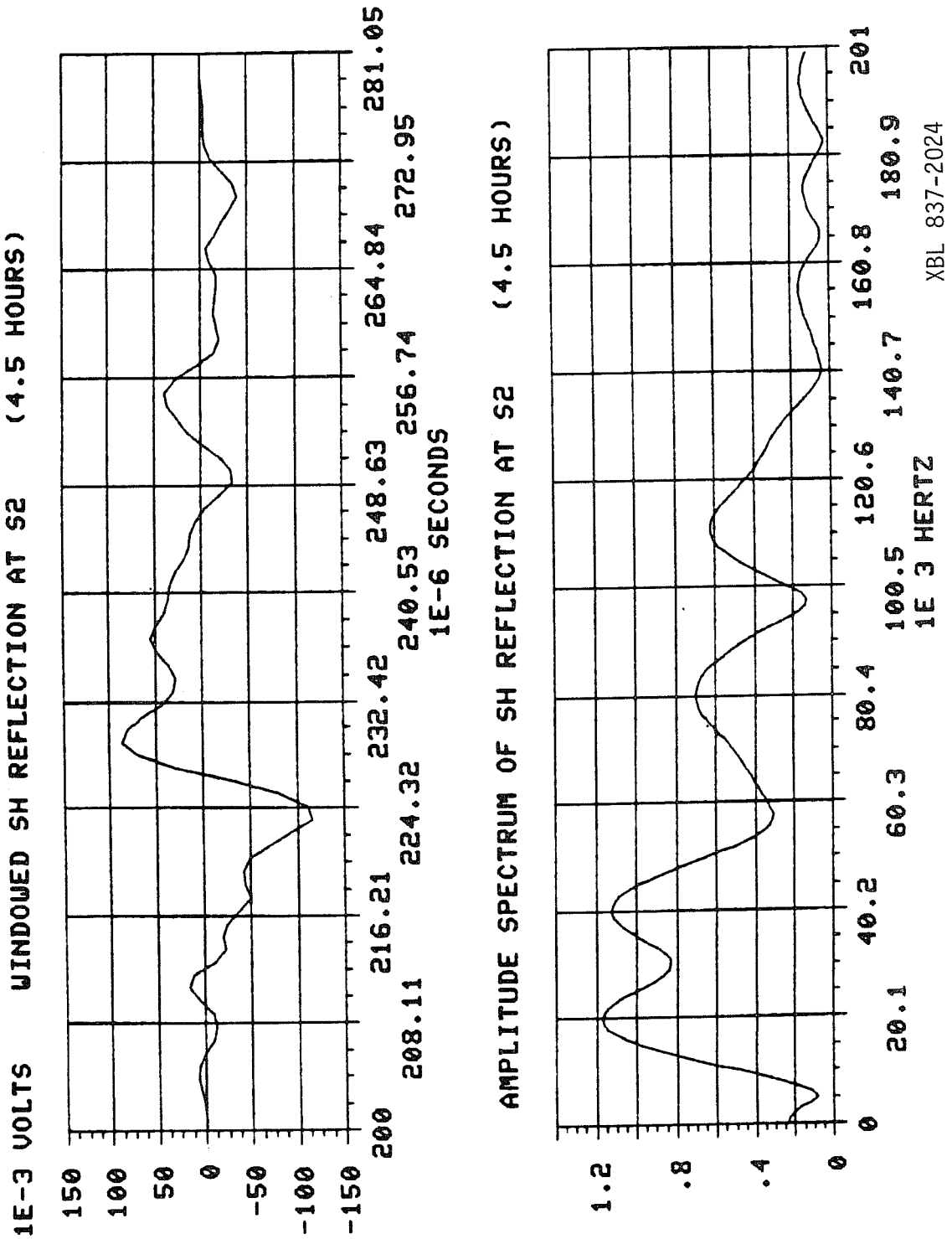

Figure IV-4-12a

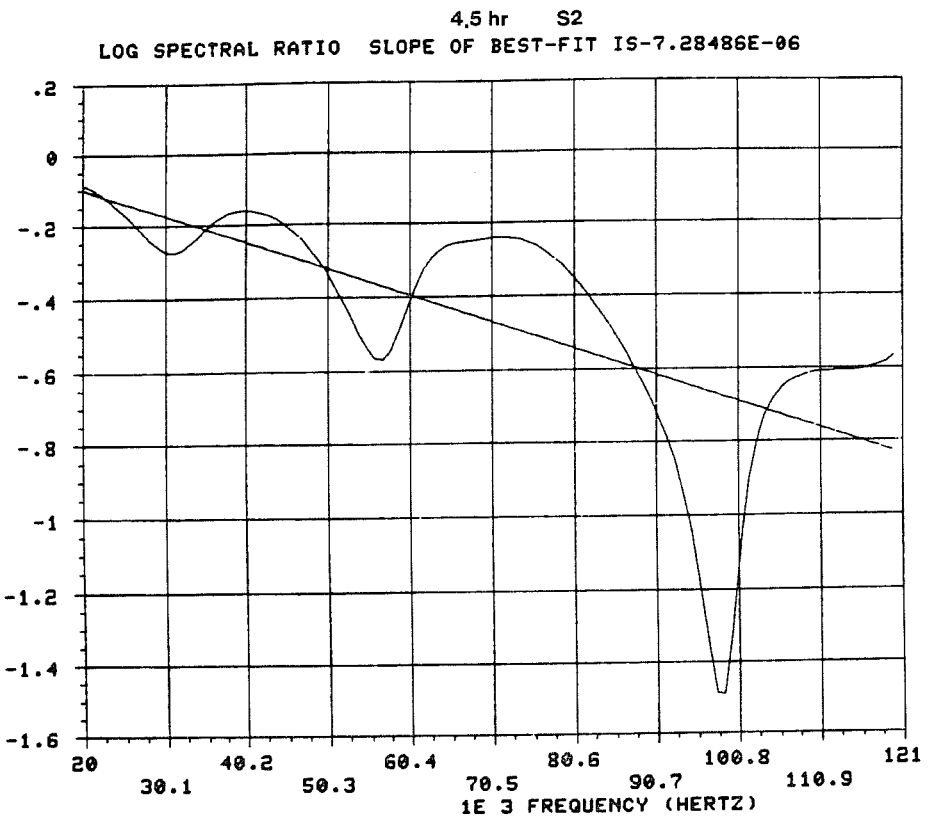

Figure IV-4-12b

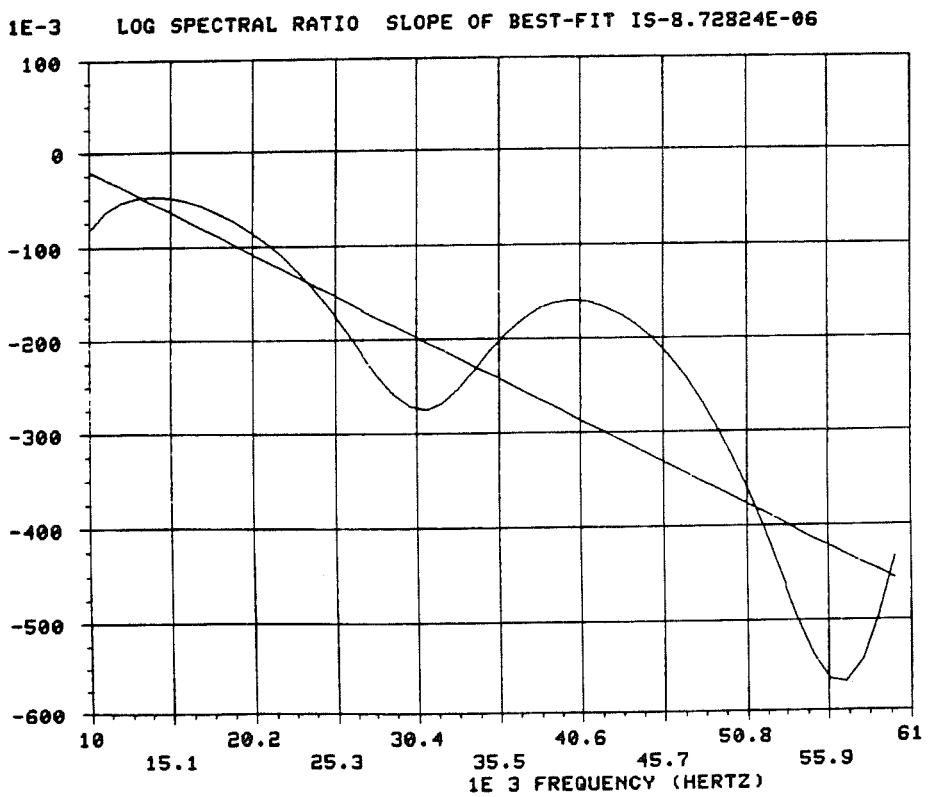

Figure IV-4-12c

XBL 837-2025

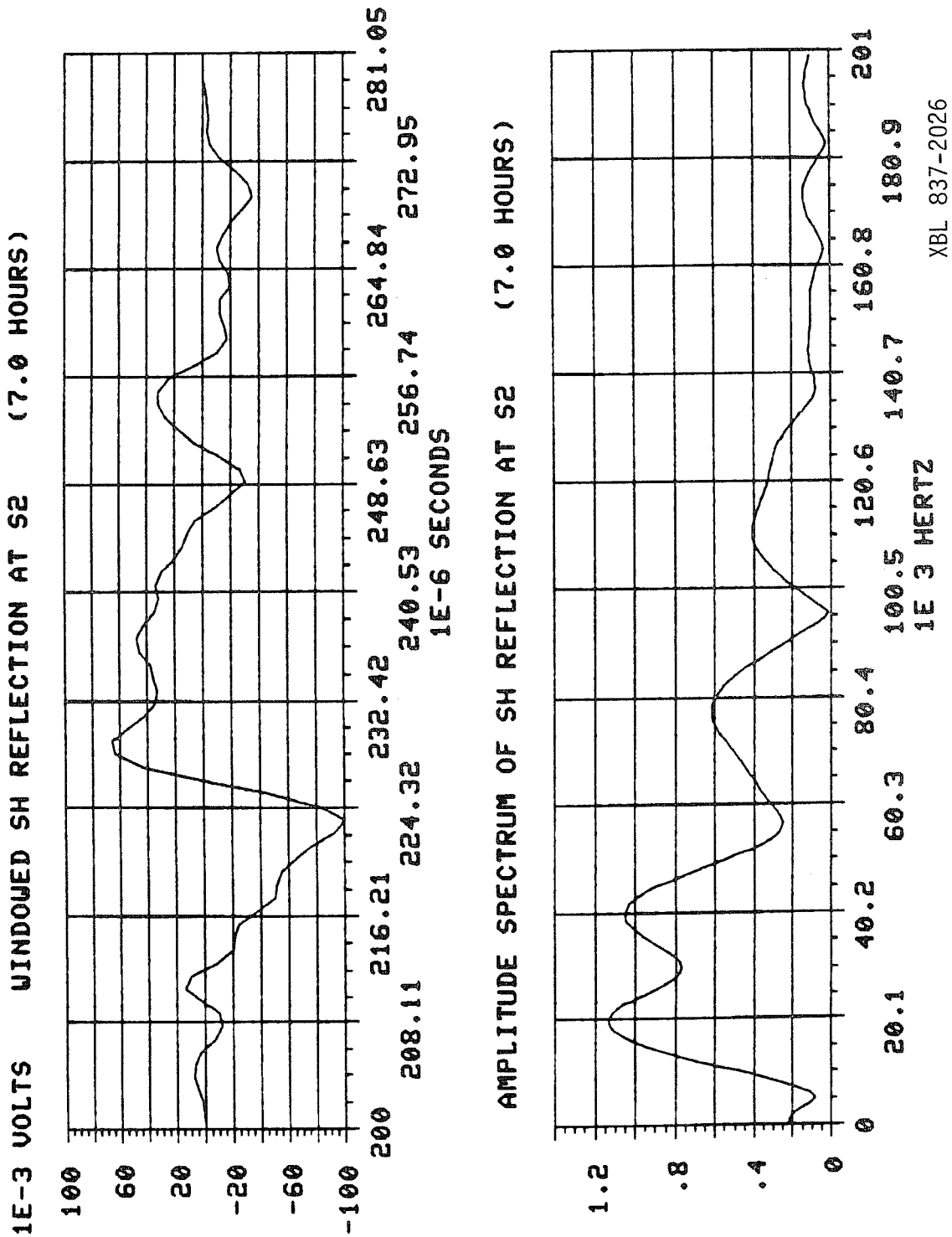

Figure IV-4-13a

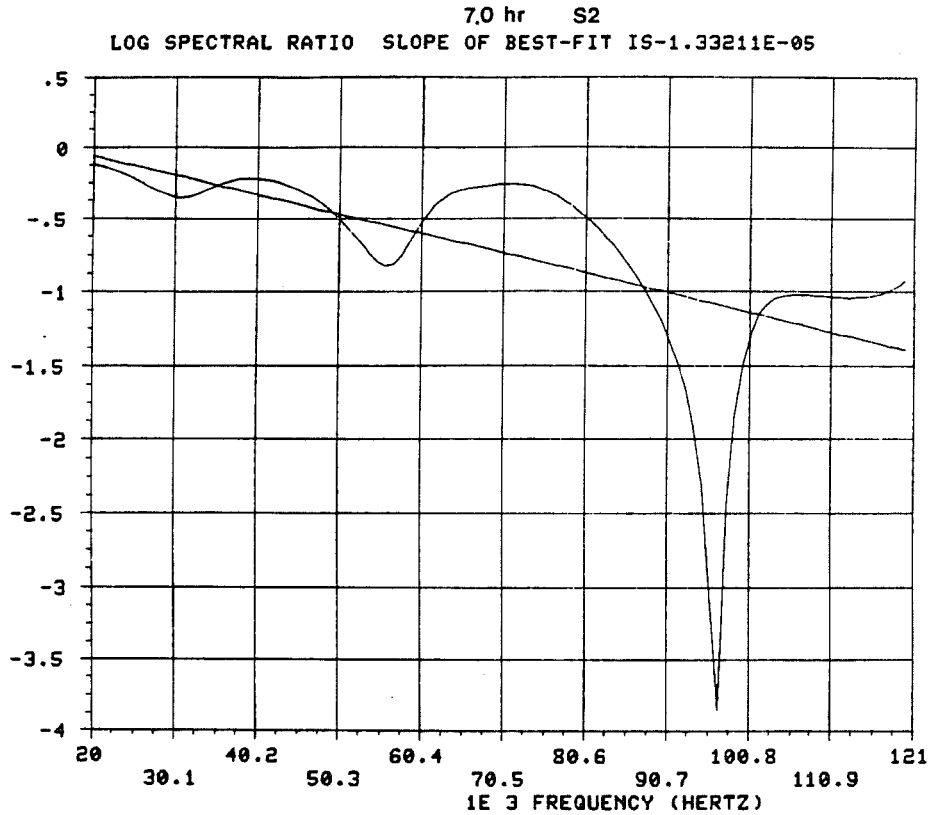

Figure IV-4-13b

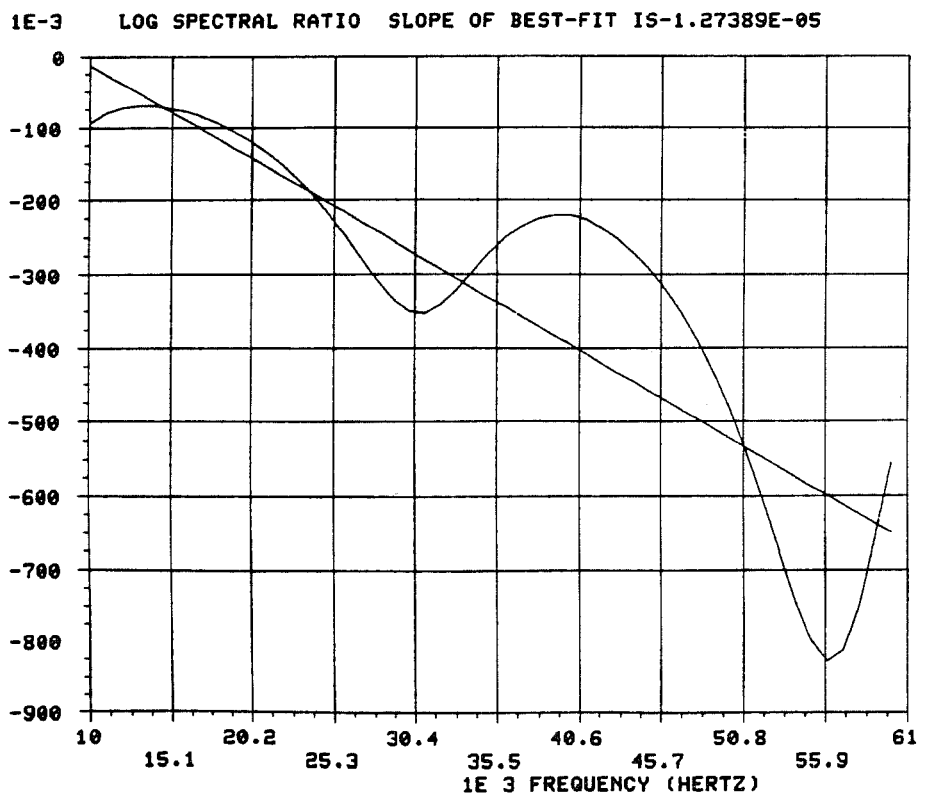

Figure IV-4-13c

XBL 837-2027

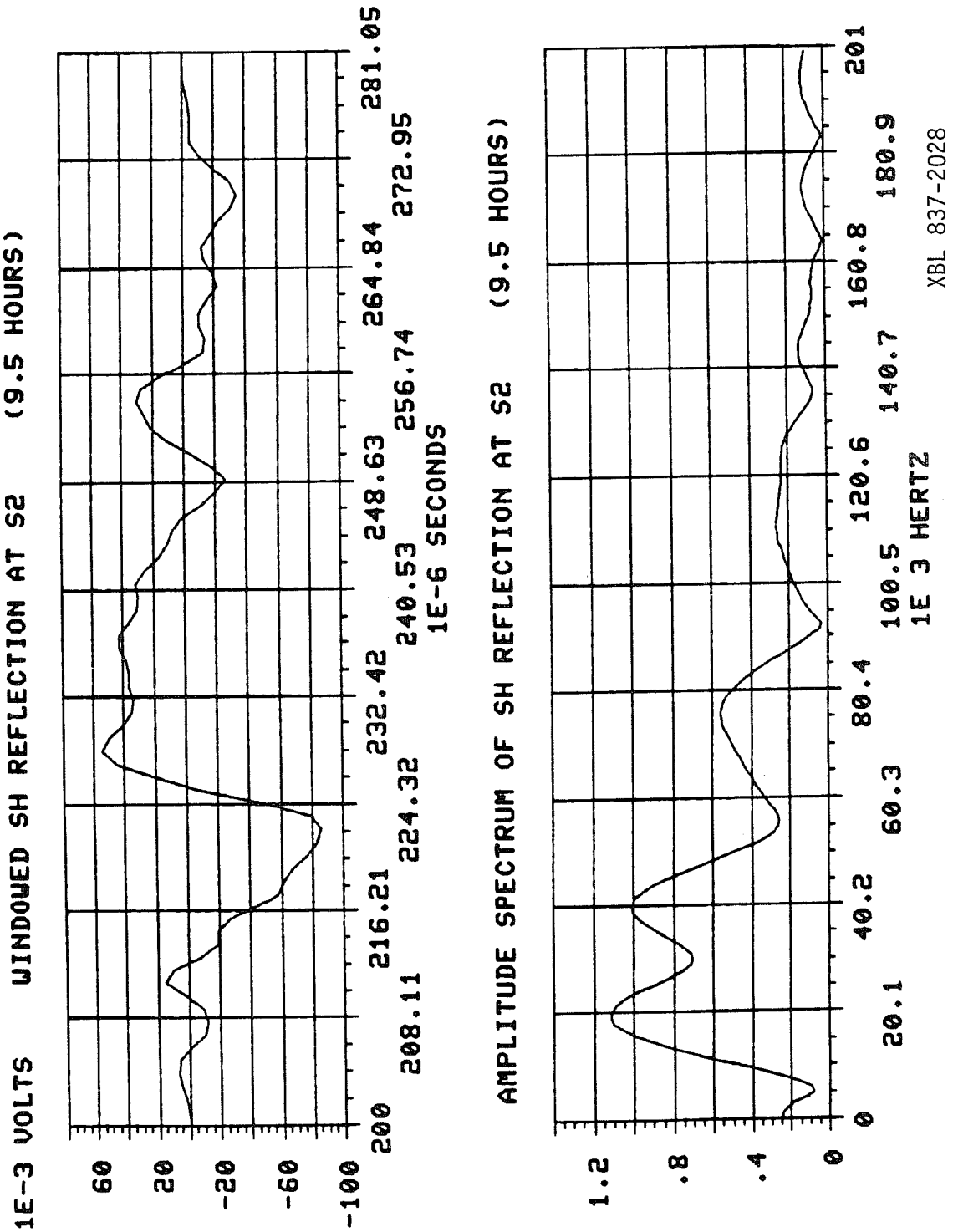

Figure IV-4-14a

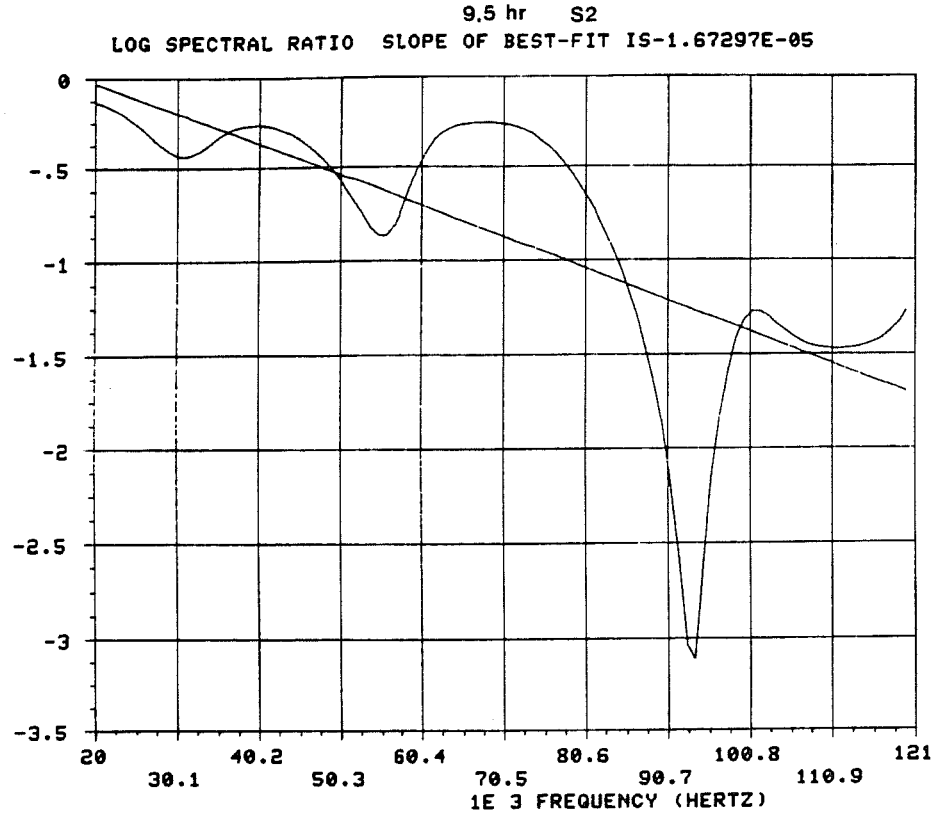

Figure IV-4-14b

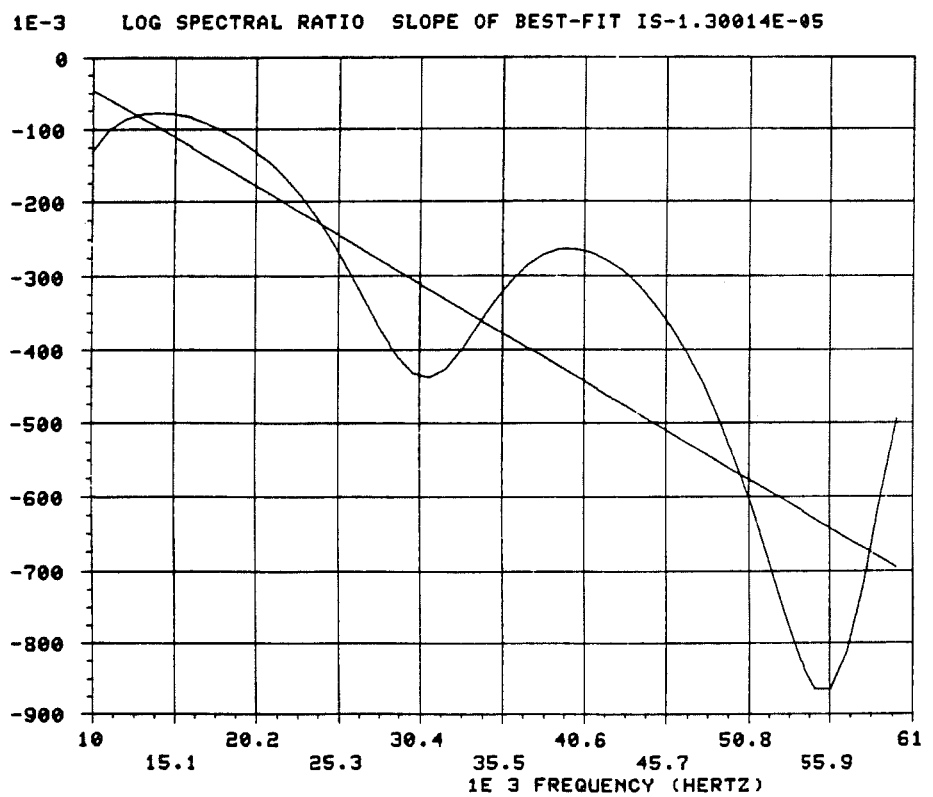

Figure IV-4-14c

XBL 837-2029

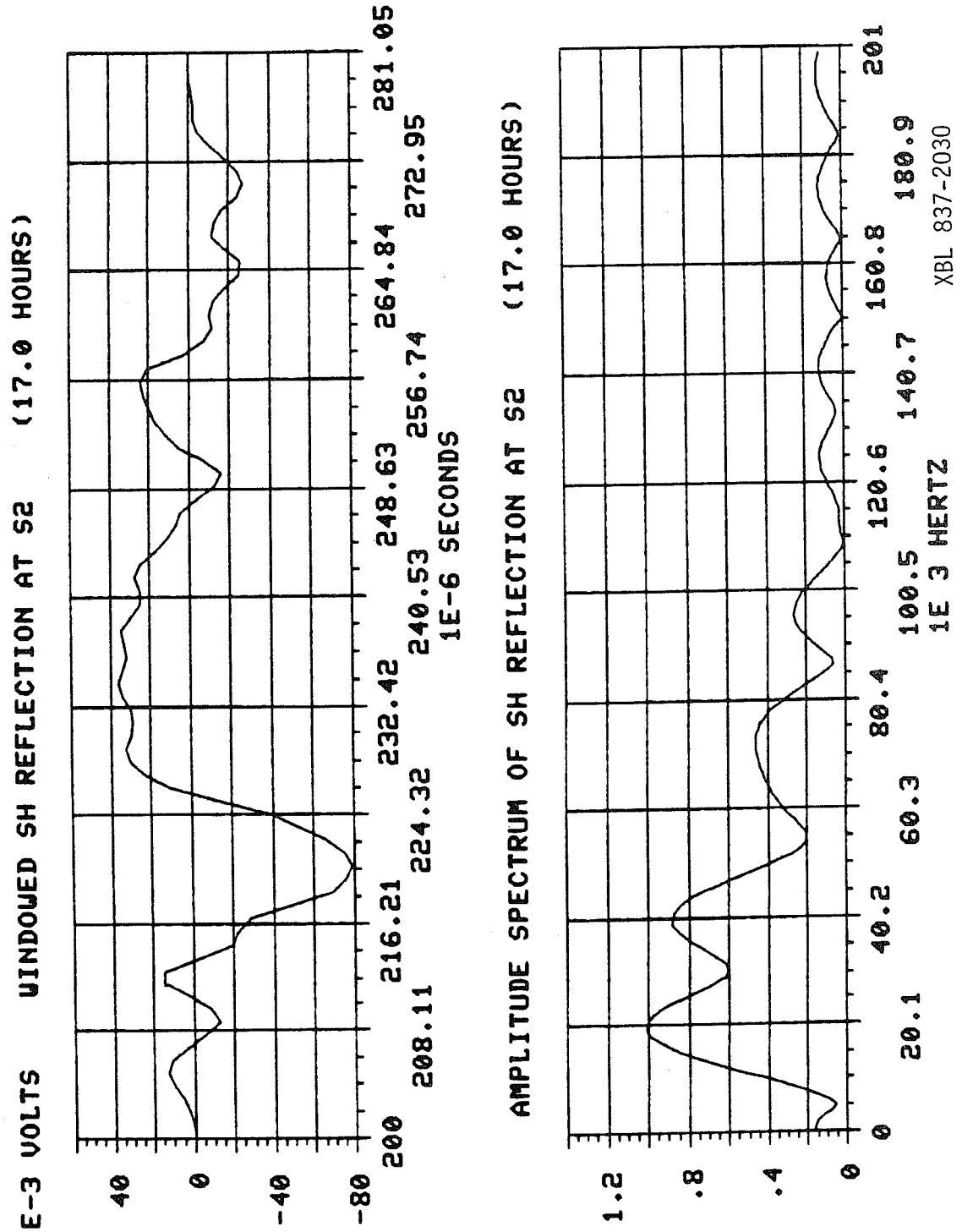

Figure IV-4-15a

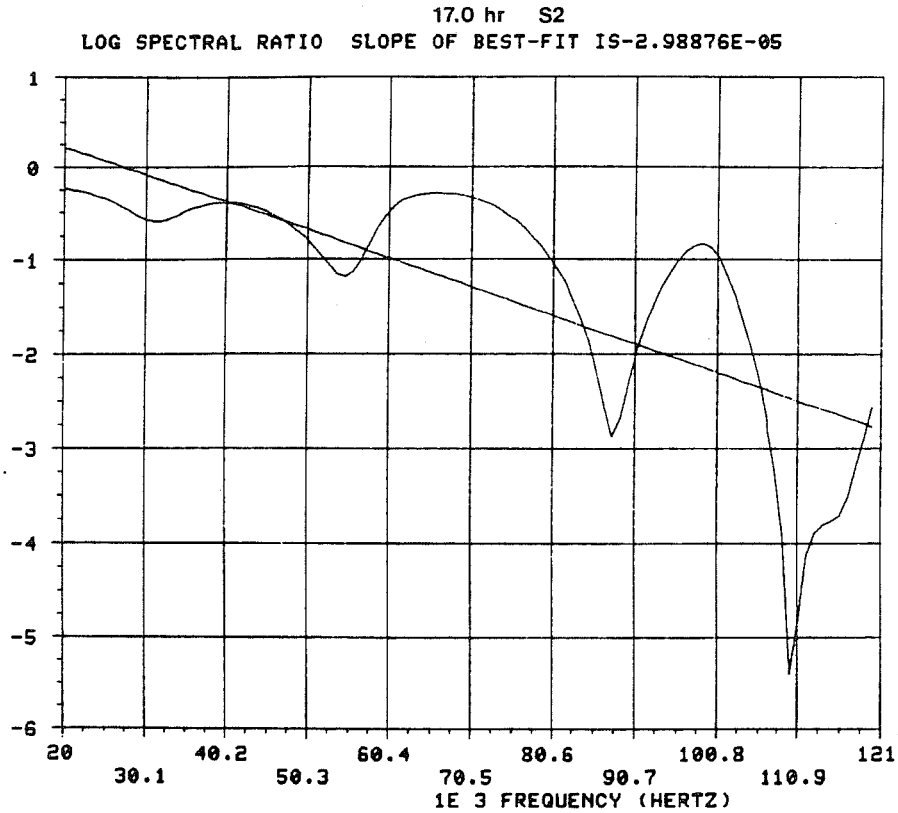

Figure IV-4-15b

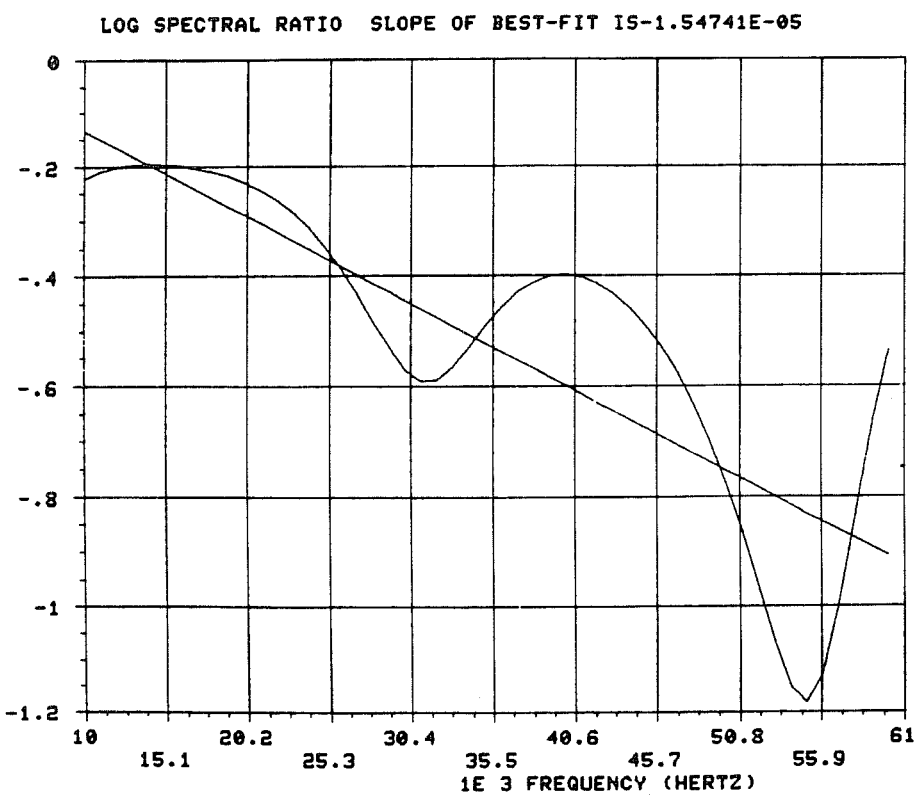

XBL 837-2031

Figure IV-4-15c

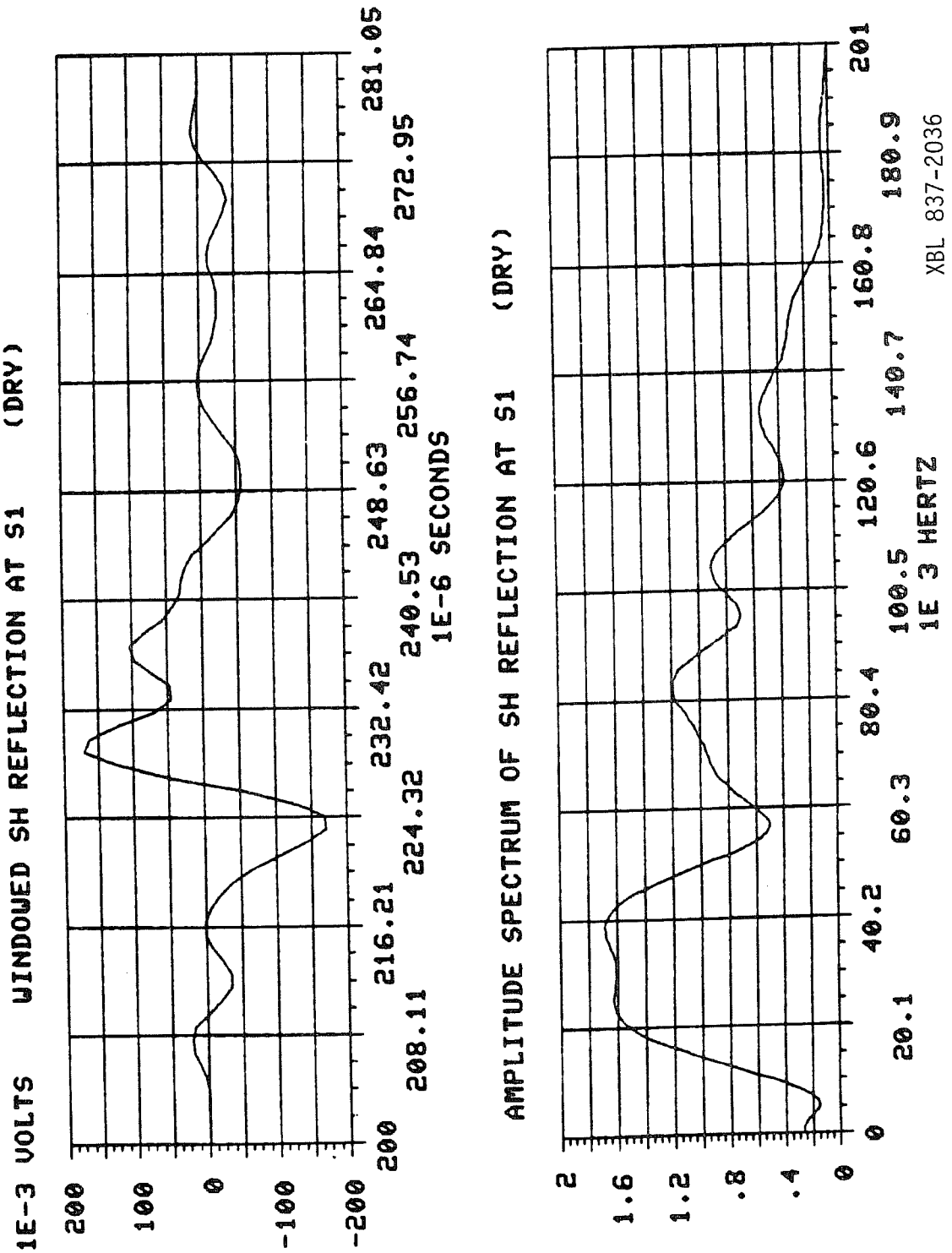

Figure IV-4-16

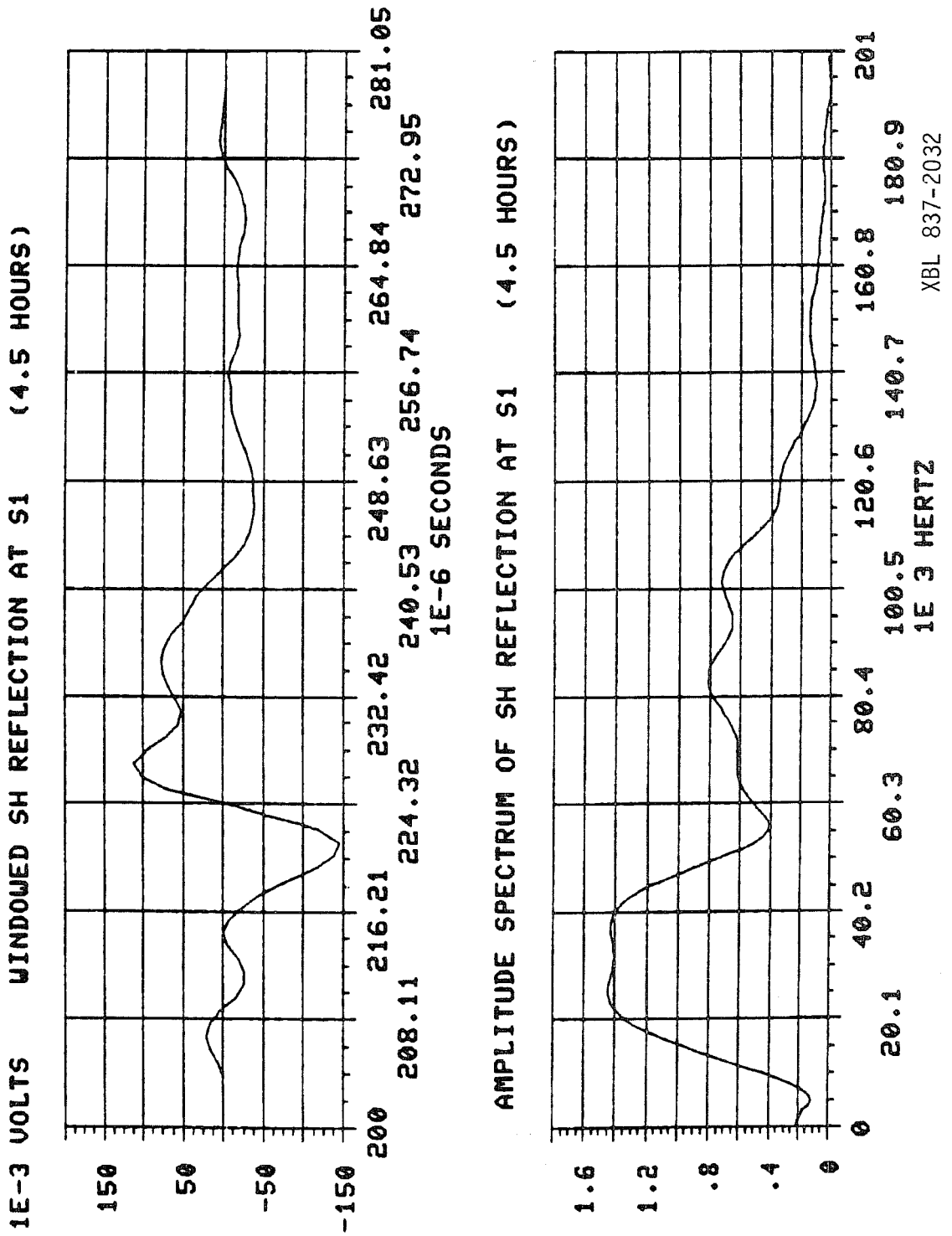

Figure IV-4-17a

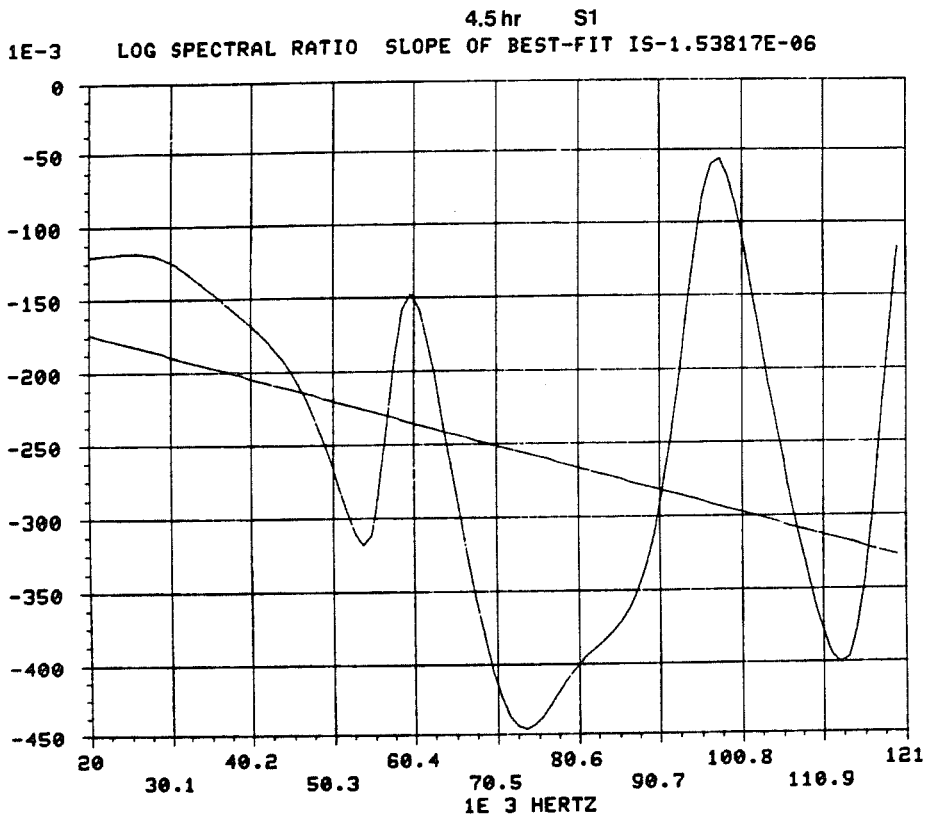

Figure IV-4-17b

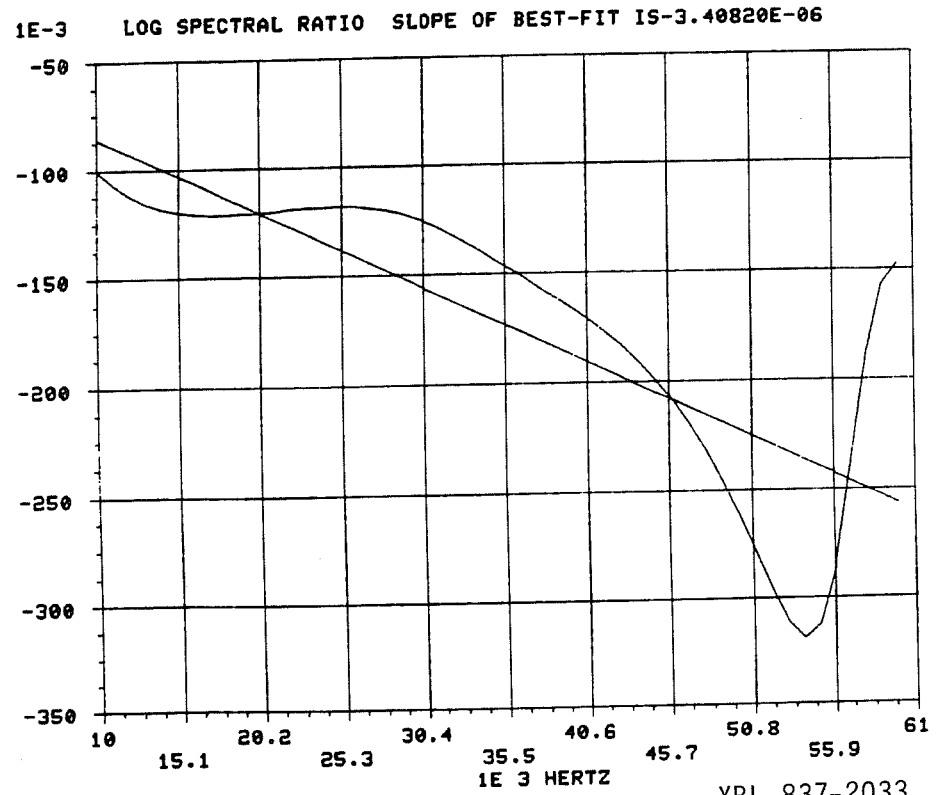

XBL 837-2033

Figure IV-4-17c

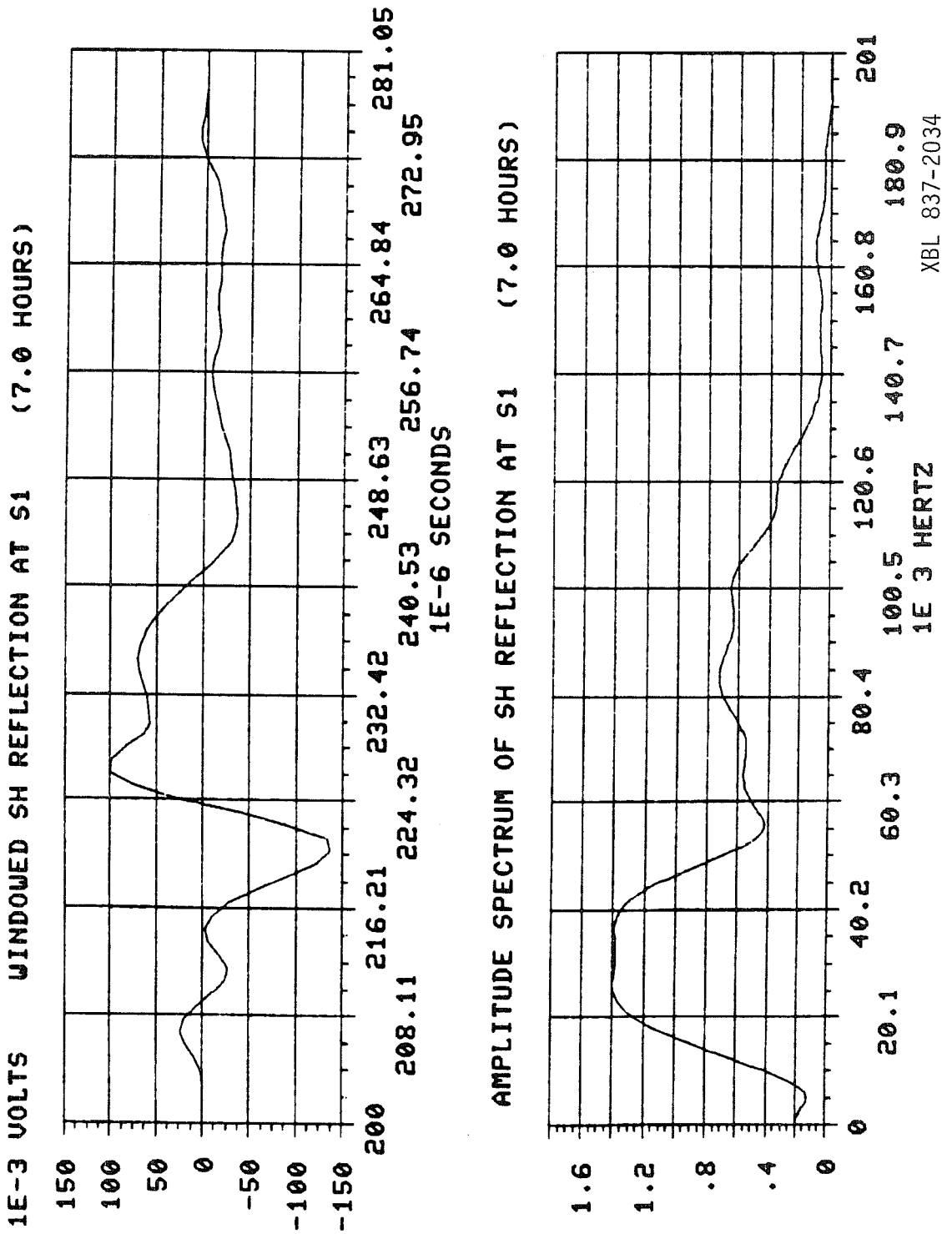

Figure IV-4-18a

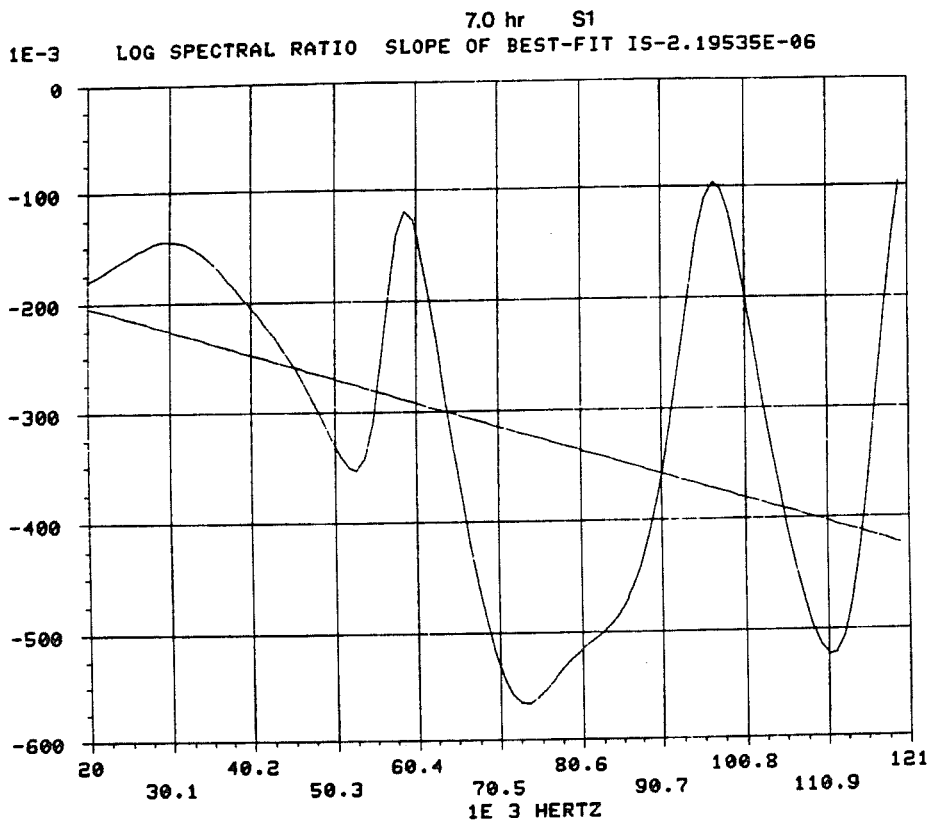

Figure IV-4-18b

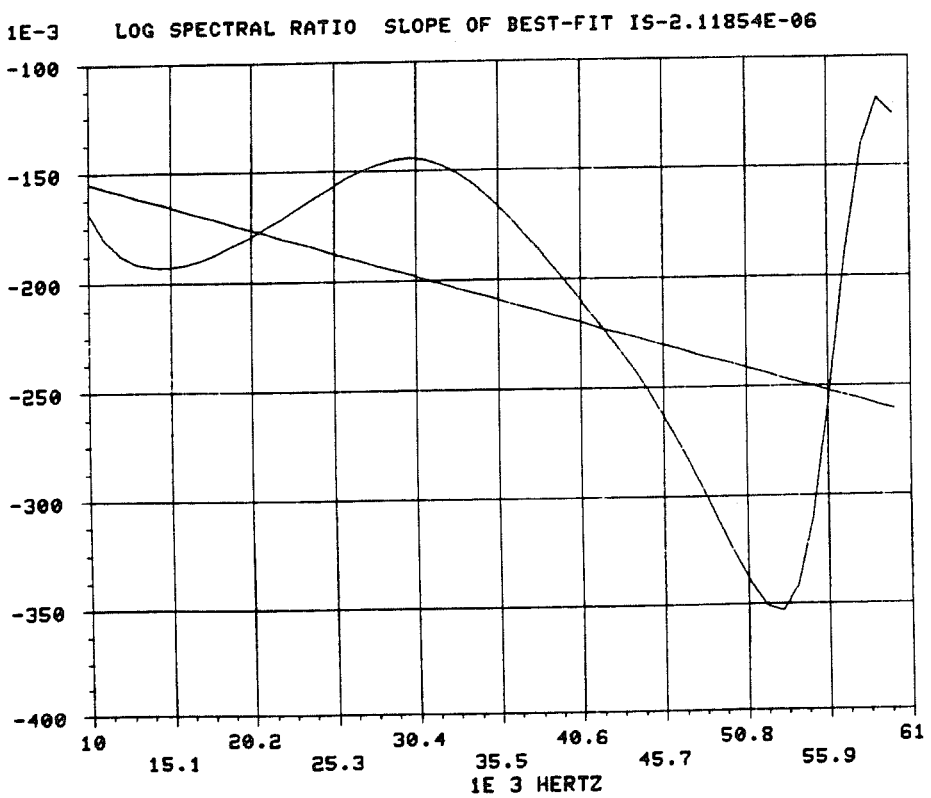

Figure IV-4-18c

XBL 837-2035

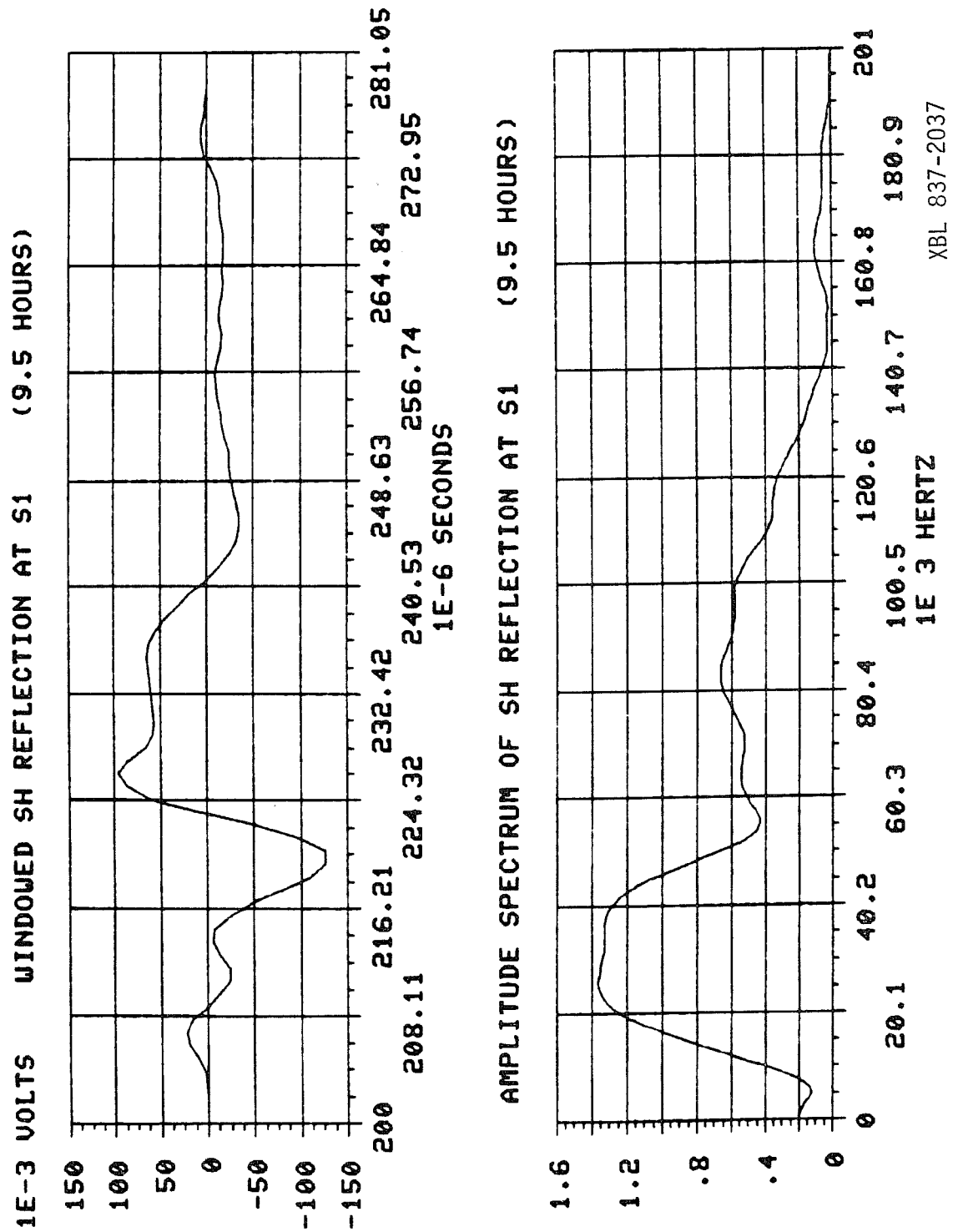

Figure IV-4-19a

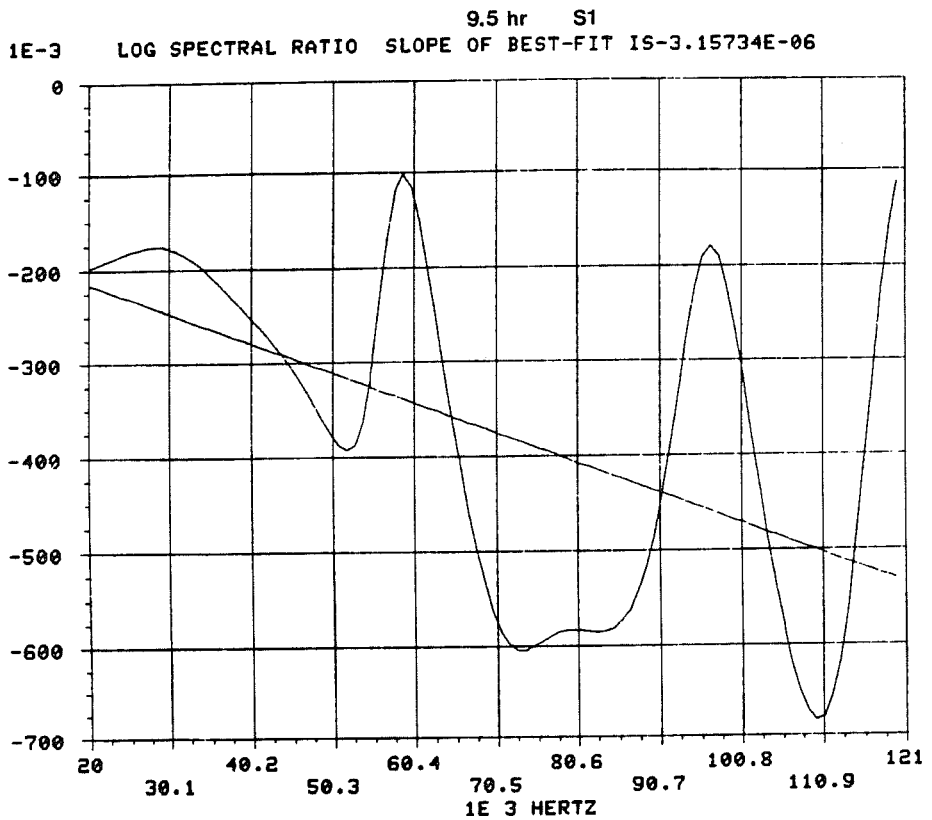

Figure IV-4-19b

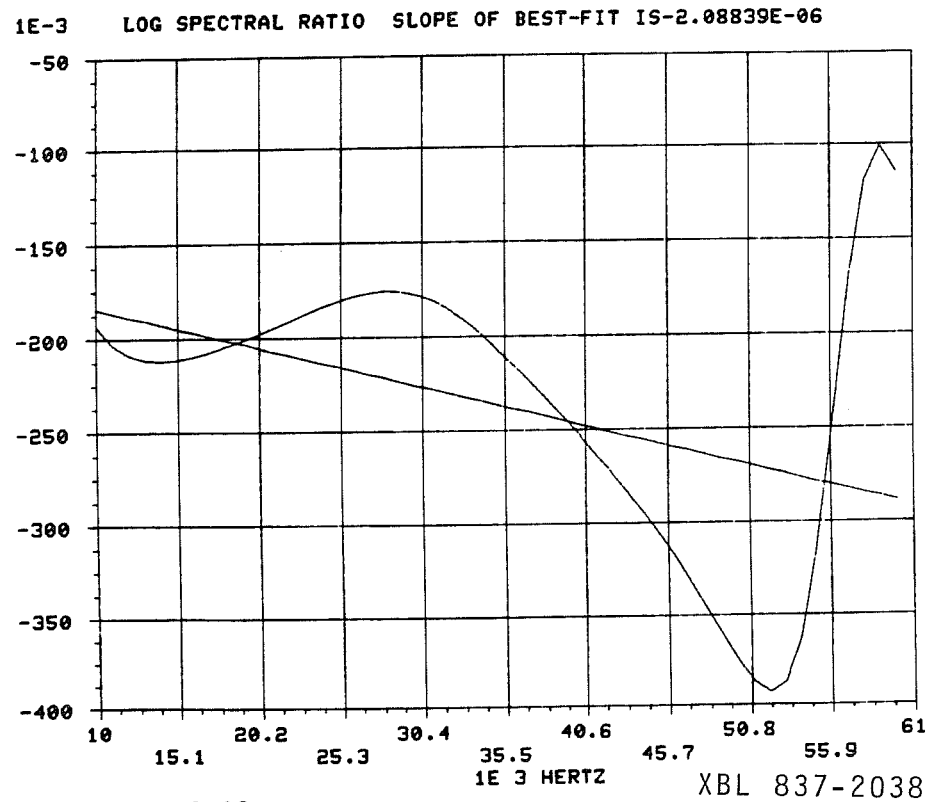

Figure IV-4-19c

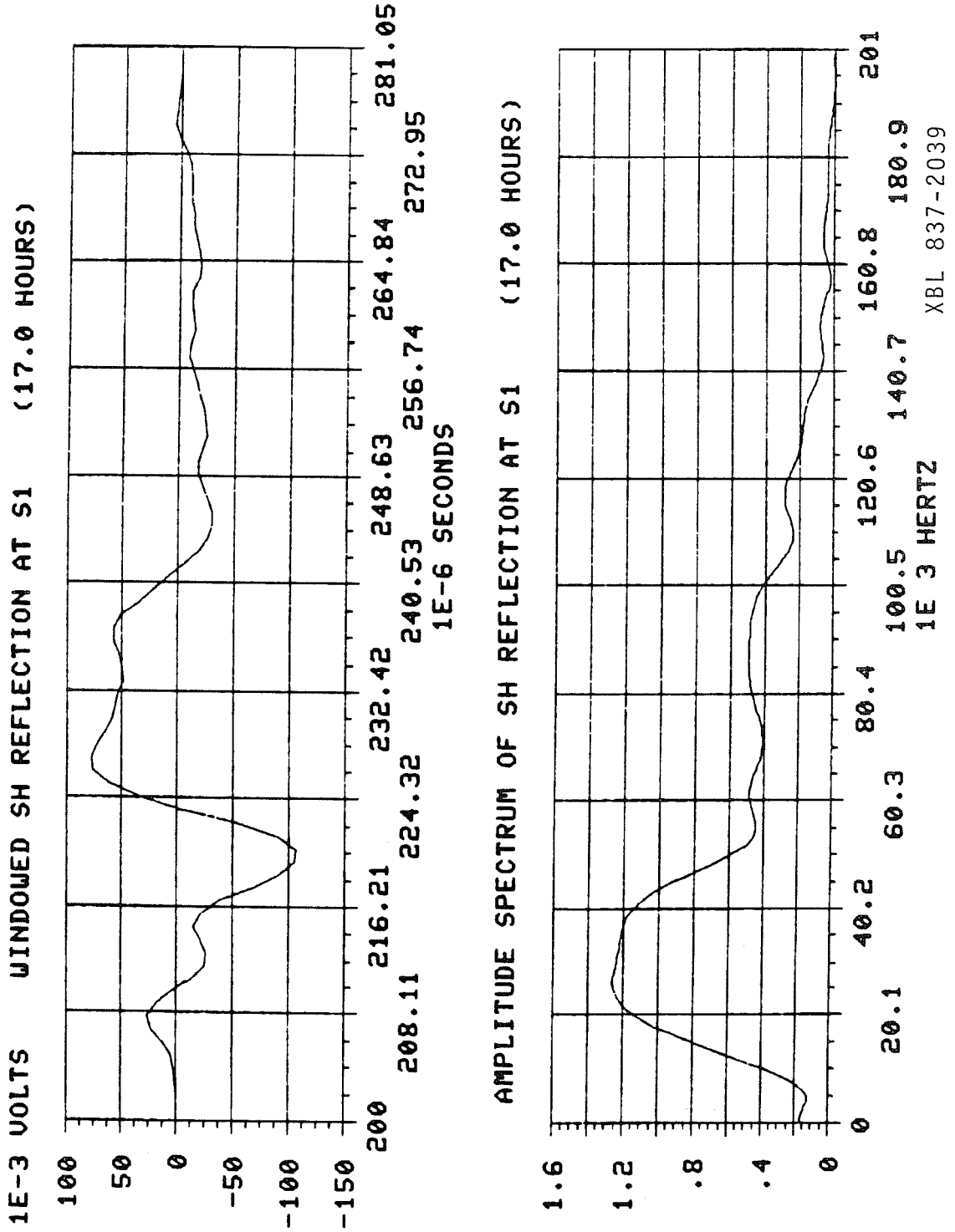

Figure IV-4-20a

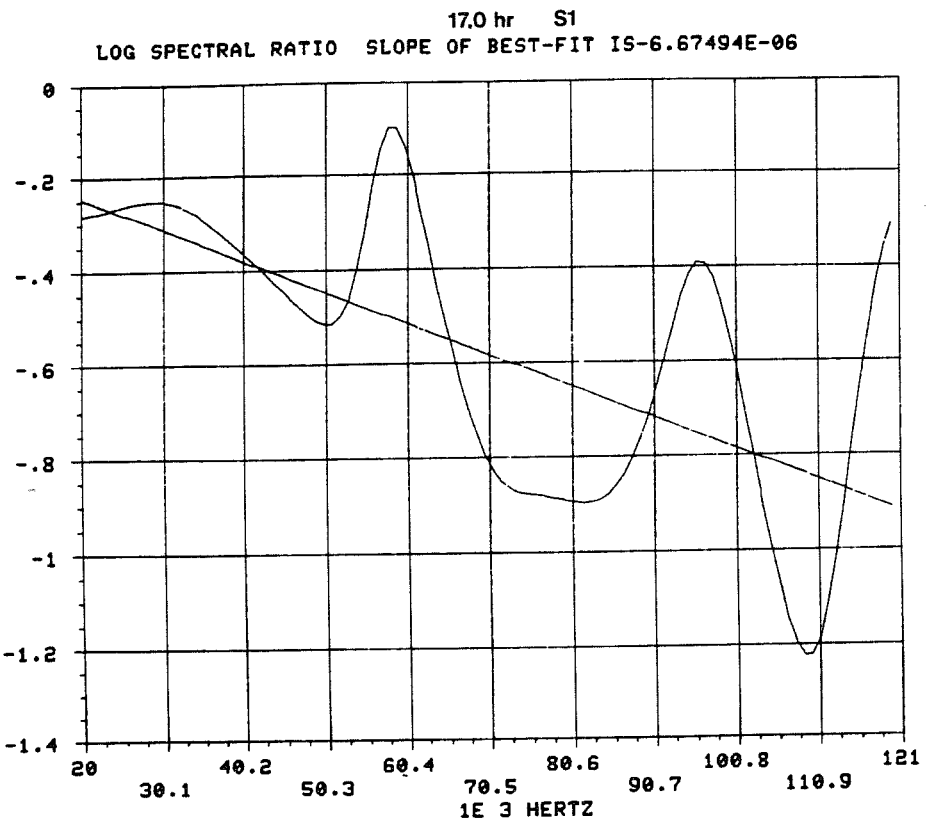

Figure IV-4-20b

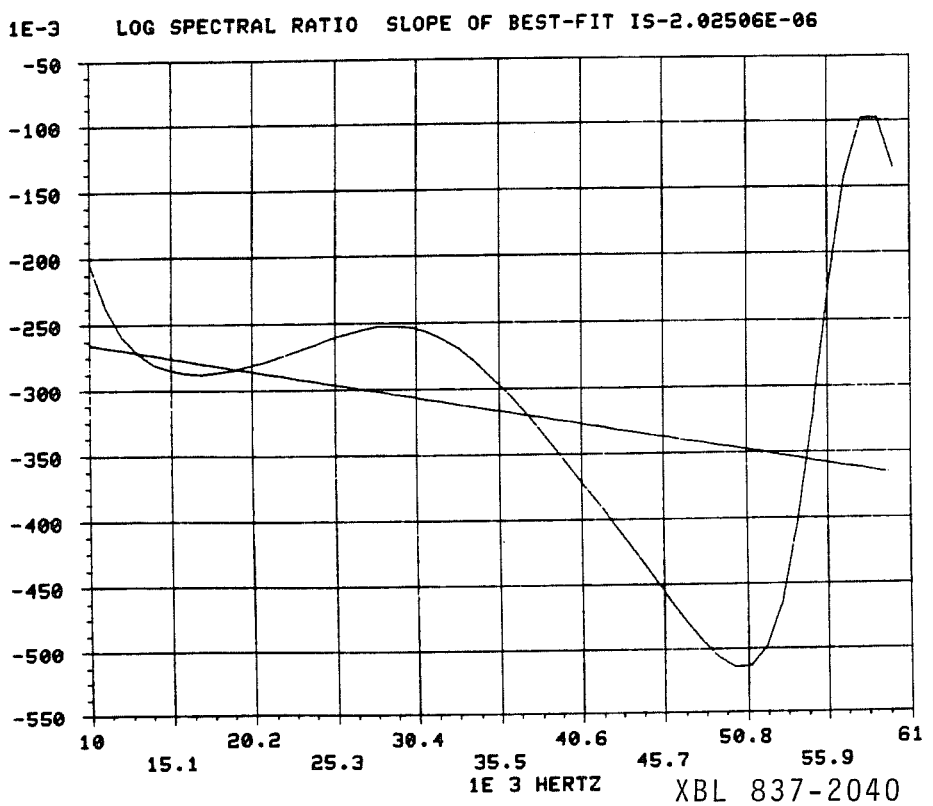

Figure IV-4-20c

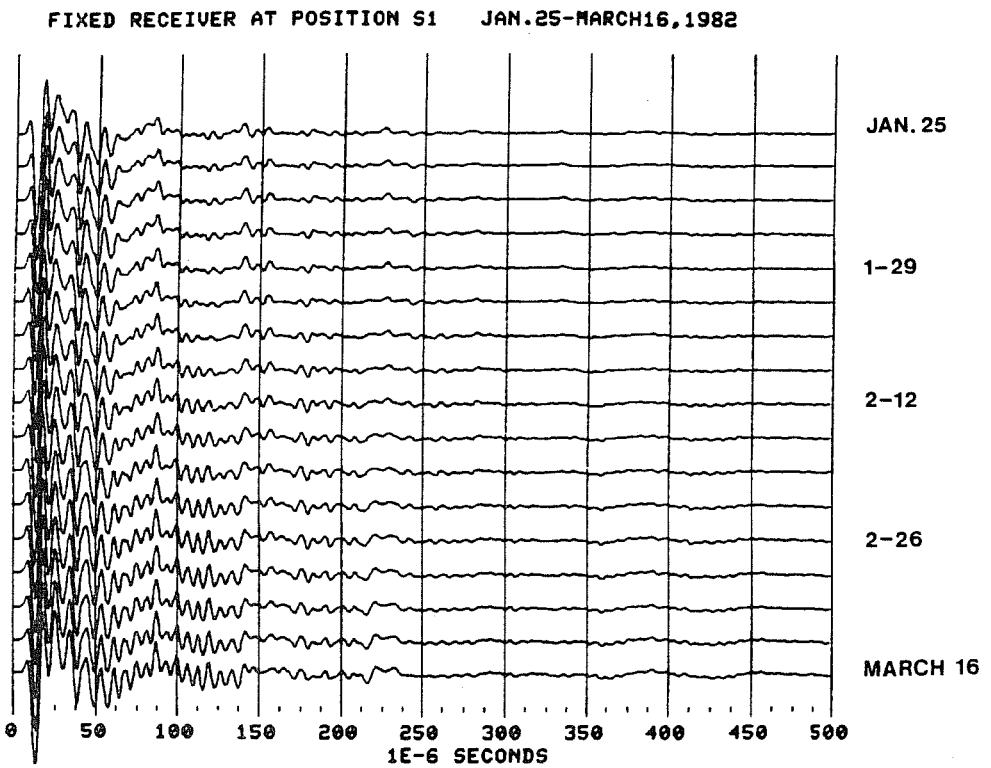

Figure IV-4-21a

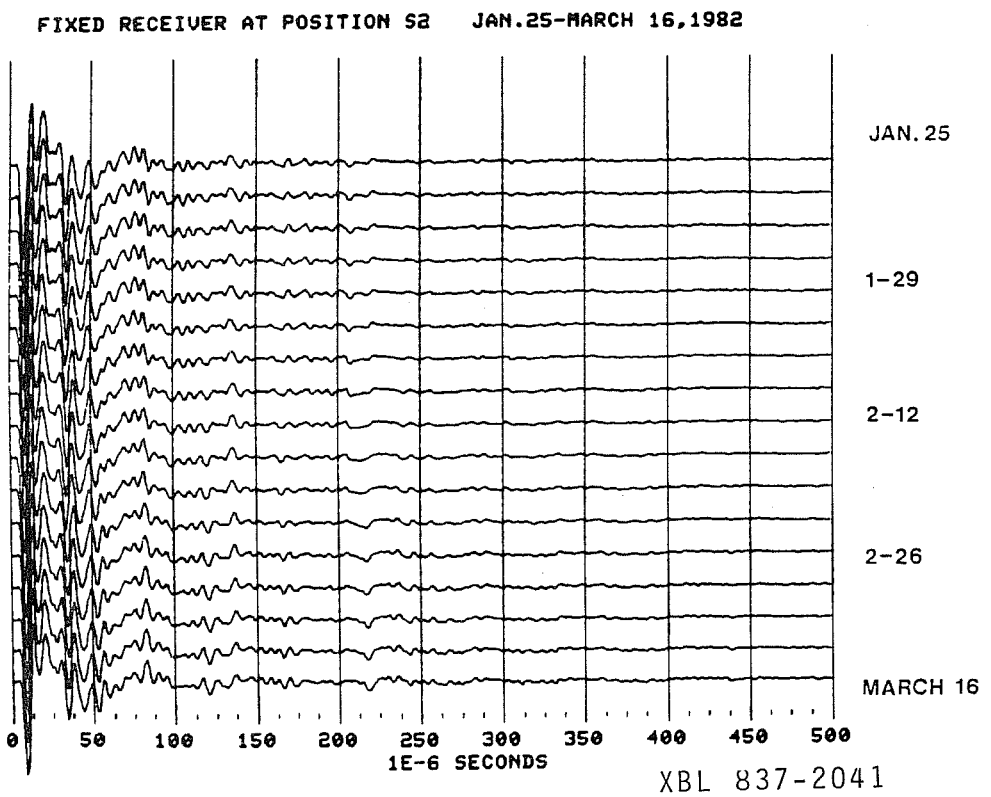

XBL 837-2041

Figure IV-4-21b

CHAPTER IV

Section 5

Phase Spectra and Arrival Time Analysis

In the previous two sections of this chapter, experiments were performed in which the arrival time of the SH reflection from an air or water gap was measured. The means of determining this arrival time was strictly manual, i.e., a human being inspected the waveform about the SH reflection and visually determined the initiation of this event. Since this may be a rather biased process, a more suitably quantitative method of measuring the relative change in arrival time of two time-windowed SH reflection wavelets was derived.

Let a time-windowed seismic event be expressed in the frequency domain as:

$$A(\omega)\ ^{-i\omega t} = A(\omega)e^{i\phi(\omega)} \qquad [IV.5.1]$$

where, $A(\omega)$ = amplitude spectrum of the time-windowed reflection

t = arrival time of the windowed event

$\phi(\omega)$ = phase angle of the windowed event.

This representation of the arrival wavelet is suitable for use with the discrete Fourier transform (DFT) used in the Tektronix computer software system. Then the phase of this wavelet is:

$$\phi(\omega) = -\omega t \qquad [IV.5.2]$$

Considering the change in phase $\delta\phi$ with the change in arrival time δt, then (letting $2\pi f = \omega$):

$$\delta\phi(f) = -2\pi f \delta t \qquad \text{[IV.5.3]}$$

Applying this result to the water gap experiment, the difference in arrival time between the dry reference SH reflection arrival time t_d and the saturated SH reflection arrival time t_s is:

$$\delta t = t_d - t_s \qquad \text{[IV.5.4]}$$

and the phase difference is:

$$\delta\phi(f) = \phi_d(f) - \phi_s(f) \qquad \text{[IV.5.5]}$$

Substituting these expressions into IV.5.3, then:

$$\phi_d(f) - \phi_s(f) = -2\pi f(t_d - t_s) \qquad \text{[IV.5.6]}$$

Differentiating these expressions with respect to frequency f gives:

$$\frac{d\phi_d(f)}{df} - \frac{d\phi_s(f)}{df} = 2\pi(t_s - t_d) \qquad \text{[IV.5.7]}$$

or

$$\Delta t = t_s - t_d = (1/2\pi)\left[\frac{d\phi_d(f)}{df} - \frac{d\phi_s(f)}{df}\right] \qquad \text{[IV.5.8]}$$

Measurement of the change in arrival time of the SH reflection event during the water gap experiment was crucial to all further analysis of these data. Equation IV.5.8 then presents a quantitative method of estimating the arrival time different $\Delta t = t_s - t_d$ (see Equation IV.3.2) from the slope of the phase curves of the dry and saturated reflection waveforms. The following example will attempt to use IV.5.8 in measuring Δt from the windowed SH reflection events used in the velocity model analysis of Section 3, and shown in Figure IV.3.10. These waveforms were recorded on July 7 (dry reference) and on August 12 (saturated) with the gap air-filled in both cases, and the arrival time difference Δt was estimated by manual determination of the arrival time data to be $\Delta t = -11.72$ μs.

The SH data recorded at location S2 (8 cm offset) on July 6, 1981, are shown in Figure IV-5-1a, and this waveform will be used as the dry reference. The SH reflection from the air gap was windowed between 200-325 μs, as shown in Figure IV-5-1b. The amplitude and phase spectra of the windowed SH reflection were obtained using the DFT, and are given in Figure IV-5-2.

In obtaining the phase spectrum shown in Figure IV-5-2b, the DFT actually returns:

$$\phi_{DFT}(f) = \phi(f) \text{ MOD } 2\pi \qquad [IV.5.9]$$

Thus, it is necessary to unwrap the phase spectrum returned by the DFT in order to determine the slope of the phase curve. The DFT phase spectrum is unwrapped by adding integer multiples of 2π to each of the

various sawtooth regions seen in Figure IV-5-2b. The resulting unwrapped phase spectrum is shown in Figure IV-5-3, and the linearity of this phase curve is much more apparent.

Returning to Equation IV.5.2, we note that if the propagation of the SH reflection event is non-dispersive (so that the arrival time t is independent of frequency), then the phase $\phi(f)$ is linearly related to the frequency f. The non-dispersive assumption was implicit in performing the differentiation of Equation IV.5.6, where the term $t_d - t_s$ is assumed to be independent of frequency. For the moment we will adopt the assumption that dispersion is negligible over the bandwidth of measurement, so that the frequency derivatives of the phase spectra in this band are constant values.

This non-dispersive relationship suggests that the frequency derivative of the unwrapped phase spectrum (Figure IV-5-3) can be esimated within a given frequency band using the least-squares linear regression described in the previous chapters. The frequency derivative of the phase spectrum is given by the best-fit slope of the regression. The uncertainty of the best-fit slope will give a measure of the validity of the negligible dispersion assumption within the frequency band of the fit. If dispersion is large, then the phase will not remain linear with frequency; instead the phase spectrum will exhibit a significant curvature due to dispersion. The degree of this curvature will be reflected in the slope uncertainty from the best-fit analysis. If the curvature is large, the uncertainty on the best-fit slope will be large, and vise-versa. Thus, this method of arrival time analysis, even though based on the assumption of negligible dispersion, will provide a quantitative test of this assumption.

The least-squares best-fit slope and corresponding uncertainty of the phase spectrum of Figure IV-5-3 were obtained in the frequency bands 20-50 kHz, and 20-100 kHz, and are presented in Table IV-5-1. The slope values determined in these two frequency bands are very similar, and indicate that any dispersion is below the significance level of these measurements.

The SH data recorded at location S2 (8 cm offset) on August 12, 1981, are shown in Figure IV-5-4a, and the windowed SH reflection is seen in Figure IV-5-4b. These data were recorded after the granite was presumably saturated, but with the gap air-filled as was the case on July 6. The purpose of this exercise will be to attempt to measure the change in arrival time Δt between the windowed SH reflections shown in Figures IV-5-(1b and 4b). The amplitude and phase spectra returned from the DFT are presented in Figure IV-5-5, and the unwrapped phase spectrum is given in Figure IV-5-6.

The best-fit slope and corresponding uncertainty of the unwrapped phase spectrum were calculated in the 20-50 kHz and 20-100 kHz bands, and the results presented in Table IV-5-2. The difference in these computed slopes in the two frequency bands suggests that dispersion is significant in the phase spectrum of this event. Indeed, the unwrapped phase spectrum shown in Figure IV-5-6 exhibits significant curvature in the 20-120 kHz band. However, the amplitude spectrum of this event (Figure IV-5-5a) shows that the signal amplitude is above the background noise level only in the band from 10-50 kHz. Thus, the distinctly steeper curvature of the phase curve above 60 kHz probably results from the background noise arriving in the time window containing the SH

Table IV-5-1

Phase Slope at S2 July 6

Dry

Frequency Band (kHz)	Slope of Phase Spectrum (radian/Hz)	Uncertainty on Slope (radian/Hz)	% Value
20- 50	-1.51896×10^{-4}	$\pm 1.68185 \times 10^{-5}$	±11.1%
20-100	-1.62583×10^{-4}	$\pm 3.1565 \times 10^{-6}$	± 1.9%

Table IV-5-2

Phase Slope at S2 August 12

Saturated

Frequency Band (kHz)	Slope of Phase Spectrum (radian/Hz)	Uncertainty on Slope (radian/Hz) % Value
20- 50	-9.17442×10^{-5}	$\pm 1.0335 \times 10^{-5}$ ±11.3%
20-100	-3.3087×10^{-4}	$\pm 1.57729 \times 10^{-5}$ ± 4.8%

reflection event. Thus, the 20-100 kHz band slope is probably an unreliable estimate, since the spectral contribution of the SH reflection above 60 kHz has fallen below the background noise level. However, since the uncertainty on the saturated 20-100 kHz band slope is fairly low (± 4.8%), then the slope uncertainty is not a very good measure of the degree of curvature of the phase spectrum.

The arrival time difference Δt is calculated for the 20-50 kHz frequency band using Equation IV.5.8 and the phase slope values given in Tables IV-5-(1 and 2). The calculated arrival time difference is Δt = -9.6 μs, and has a corresponding error of ±45%. This result shows, however, that in the 20-50 kHz band the saturated arrival time was advanced 5.3 μs to 13.9 μs with respect to the dry reference arrival time. This range of values compares favorably with the difference Δt = -11.7 μs ± 0.5 μs determined using a visual pick of the arrival times.

This phase method of estimating Δt was applied to the SH data recorded at location S2 between January 13-16, 1982. The details of this experiment were discussed in Section 4, and will not be elaborated here. The windowed SH reflection waveforms shown in Figure IV-5-7 were recorded during a 63.5 hour period after filling the air gap with water. The SH trace recorded with the gap still air-filled at 0.0 hours will be used as the dry reference phase spectrum. The arrival time difference of the saturated SH reflection data will be measured relative to the 0.0 hour dry reference trace.

The amplitude spectra of the windowed data of Figure IV-5-7 are presented in Figure IV-5-8. The visible effects of increasing attenuation on the spectra shown in this figure extend to below 20 kHz, and

are very severe on the frequency components above 50 kHz. Thus, phase data in the frequency band 10-40 kHz was used in the determination of the best-fit slope of the phase spectrum. The phase spectra components above 60 kHz were considered to be due to the effects of background seismic noise.

The unwrapped phase spectra of the windowed reflection data are shown in Figure IV-5-9. The linearity of these phase spectra is very apparent in the 10-60 kHz band, even though the amplitude of the corresponding windowed SH reflection event has been severely diminished by attenuation. Again the choice of the 10-40 kHz frequency band for the best-fit analysis seems justified by the visible linearity of phases in this band. The best-fit slopes and uncertainties in the 10-40 kHz band and the differential arrival times Δt calculated from these phase slopes using Equation IV.5.8 are given in Table IV-5-3. These phase estimates of Δt can be compared with the values of Δt determined manually in Section 4, and included in this table.

The large error on the differential arrival time at 4.5 hours ($\Delta t = -1.24\ \mu s \pm 129\%$) occurs because the difference in phase slopes is only about 8×10^{-6} rad/Hz. In fact, the uncertainty of the phase method of estimating Δt arises only in the phase slope difference. The uncertainties of the phase slopes all range from 1.5% to 3%, as seen from Table IV-5-3, but the errors on Δt decrease with increasing hours into the experiment. This apparent decrease in Δt error is due simply to the fact that the phase slope difference increases as the experiment proceeds from 0-63.5 hours. The change in phase slope corresponds to the change in the arrival time of the windowed reflection event during the saturation experiment.

Table IV-5-3

(10-40 kHz)

Hours After Saturation	Slope of Phase Curve (radian/Hz)	Arrival Time Difference Δt (μs)	Arrival Time Difference Δt from Visual Pick (Section 4) (μs)
0.0	$-3.493 \times 10^{-4} \pm 1.4\%$	———	———
4.5	$-3.415 \times 10^{-4} \pm 1.5\%$	- 1.24 ± 129%	-0.98 ± 50%
7.0	$-3.029 \times 10^{-4} \pm 1.8\%$	- 7.38 ± 22.4%	-1.96 ± 25%
9.5	$-2.907 \times 10^{-4} \pm 2.1\%$	- 9.33 ± 18.6%	-2.93 ± 16.5%
17.0	$-2.777 \times 10^{-4} \pm 2.2\%$	-11.4 ± 15.3%	-4.89 ± 10%
21.0	$-2.755 \times 10^{-4} \pm 2.3\%$	-11.7 ± 15.1%	———
24.0	$-2.684 \times 10^{-4} \pm 2.5\%$	-12.9 ± 12.7%	———
29.5	$-2.651 \times 10^{-4} \pm 2.5\%$	-13.4 ± 13.6%	———
41.5	$-2.598 \times 10^{-4} \pm 2.4\%$	-14.2 ± 12.5%	———
45.5	$-2.523 \times 10^{-4} \pm 2.8\%$	-15.4 ± 11.9%	———
48.5	$-2.482 \times 10^{-4} \pm 2.6\%$	-16.1 ± 11.7%	———
63.5	$-2.493 \times 10^{-4} \pm 2.8\%$	-15.9 ± 12.0%	———

There is significant disagreement in Table IV-5-3 between the Δt values determined using the phase slope method and those determined by manual picking. It is possible this discrepancy results from the natural tendency of visual arrival time determination to emphasize the higher frequency components of the waveform. Regardless of the reason for the difference in Δt values, the important result is that all determinations of Δt indicate that the SH reflection event decreases in arrival time during the saturation of the granite slab. The quantitative estimate of Δt obtained using the phase spectral method presents an unbiased method of determining the reality of the visually apparent change in reflection arrival time observed during the saturation experiments. The results of this phase spectral analysis conclusively show that there is a significant decrease in the arrival time of the SH reflection during the course of the saturation experiments described in Sections 3 and 4.

Although the decrease in SH reflection arrival time at S2 during the 63.5 hour period is confirmed by the phase spectral results in Table IV-5-3, completeness requires that the attenuation effects also be quantified in the 10-40 kHz frequency band. Thus, Q_{Ss} will be estimated using a step S velocity/attenuation model and the log spectral method described in Section 4 of this chapter.

First, the thickness of the saturated zone $d - z_1$ is estimated using Equation IV.3.4, and the arrival time and velocity values at S2 (see Section 4):

$\beta_d = 2735$ m/s $\pm$ 1%

$\Delta\beta = 315$ m/s $\pm$ 1.5%

$t_d = 219.73$ μs $\pm$ 0.5%

The thickness $d - z_1$ was calculated for the data recorded at 4.5, 7.0, 9.5, and 17.0 hours using the appropriate value of Δt obtained from the phase spectral analysis. These values of Δt and $d - z_1$ are detailed in Table IV-5-4. Next, a log spectral ratio of the amplitude spectra shown in Figure IV-5-8 was obtained where the spectrum at 0.0 hours was used as the reference. The log spectral ratios in the 10-40 kHz band at 4.5, 7.0, 9.5, and 17.0 hours are shown in Figure IV-5-10. The best-fit lines with slopes b are also included in these figures, and the calculated slopes and uncertainties are listed in Table IV-5-4. By assuming that $Q_{Sd} = 50 \pm 30\%$, as in Section 4, then Q_{Ss} can be calculated using Equation IV.4.14 and the parameter values listed above and in Table IV-5-4.

The values of Q_{Ss} determined in the 10-40 kHz band and given in Table IV-5-4 suggest $Q_{Ss} = 17 \pm 6$. This range of Q_{Ss} is slightly larger than the range of Q_{Ss} values determined at S2 in the 20-120 kHz and 10-60 kHz bands (see Section 4). However the poor precision of these determinations suggests that these differences are probably not statistically significant.

The fundamental purpose of this section was to quantitatively verify that the advance in arrival time of the SH reflection did indeed occur during the granite slab saturation experiments described in Sections 3 and 4. A phase spectral method of measuring the differential arrival time between two windowed SH reflection events was derived, and the SH data recorded at location S2 during the period January 13 to 16, 1982 (see Section 4) was analyzed using this technique. The results of this analysis conclusively showed that the 10-40 kHz band of the SH

Table IV-5-4

Hour Into Experiment	Arrival Time Difference Δt (μs)	Thickness of Saturated Layer $d - z_1$ (cm)	Slope b from Log Spectral Ratio ($Volt^{-1} - Hz^{-1}$)	Q_{Ss} Calculated Using $Q_{Sd} = 50$
4.5	- 1.24 ± 129%	1.90 ± 140%	-6.7824×10^{-6} ±14.9%	Not calculated because of large error on $d - z_1$
7.0	- 7.38 ± 22.4%	9.97 ± 39%	-8.1708×10^{-6} ±13.8%	18.1 ± 36%
9.5	- 9.33 ± 18.6%	12.5 ± 45%	-1.0904×10^{-5} ±14.4%	17.8 ± 38%
17.0	-11.4 ± 15.3%	15.3 ± 42%	-1.2599×10^{-5} ±13.2%	16.1 ± 36%

Position S2

reflection advanced in arrival time during the saturation of the granite slab. These results also corroborated the previous calculations using values of Δt determined manually.

Finally, the values of Q_{Ss} were determined using the log spectral ratio technique described in Section 4. The phase spectral estimates of Δt were used in calculating the saturated layer thickness $d - z_1$, which was subsequently used in determining Q_{Ss}. The results of this analysis showed that Q_{Ss} had a value of 17 ± 6 in the frequency band 10-40 kHz. The estimated error on Q_{Ss} obtained in this analysis was the smaller than those obtained in the 20-120 kHz and 10-60 kHz determinations of Q_{Ss} given in Sections 3 and 4. This suggests that the best measurements of these attenuation effects are in the lower frequency band (10-40 kHz), despite the obvious attenuation effects in the higher frequencies (> 60 kHz). In fact, attenuation of the signal wavelet (SH reflection) becomes so strong in the higher frequency band that the background spectral noise becomes dominant.

Figure Captions

Figure IV-5-1
SH data recorded at location S2 (8 cm offset) on July 6, 1981, prior to filling the gap with water.
a) Full 500 μs waveform
b) SH reflection windowed from 200-325 μs.

Figure IV-5-2
Results of DFT applied to the windowed reflection shown in Figure IV-5-1b.
a) Amplitude spectrum
b) Phase spectrum

Figure IV-5-3
Result of unwrapping phase spectrum shown in Figure IV-5-2b.

Figure IV-5-4
SH data recorded at location S2 (8 cm offset) on August 12, 1981, just after draining the water gap.
a) Full 500 μs waveform
b) SH reflection windowed from 200-325 μs

Figure IV-5-5
Results of DFT applied to the windowed reflection shown in Figure IV-5-4b.
a) Amplitude spectrum
b) Phase spectrum

Figure IV-5-6
Results of unwrapping phase spectrum shown in Figure IV-5-5b.

Figure IV-5-7
Windowed SH reflections recorded at location S2 between January 13 to 16, 1982, during the first 63.5 hours after filling the gap with water.

Figure IV-5-8
Amplitude spectra of windowed SH reflections shown in Figure IV-5-7.
a) 0-200 kHz band
b) 10-70 kHz band

Figure IV-5-9
Unwrapped phase spectra of windowed SH reflections shown in Figure IV-5-7.
a) 0-200 kHz band
b) 10-70 kHz band

Figure IV-5-10
Log spectral ratios of windowed SH reflections obtained using the amplitude spectra shown in Figure IV-5-8.
a) 4.5 hours after gap filled with water
b) 7.0 hours after gap filled
c) 9.5 hours after gap filled
d) 17.0 hours after gap filled

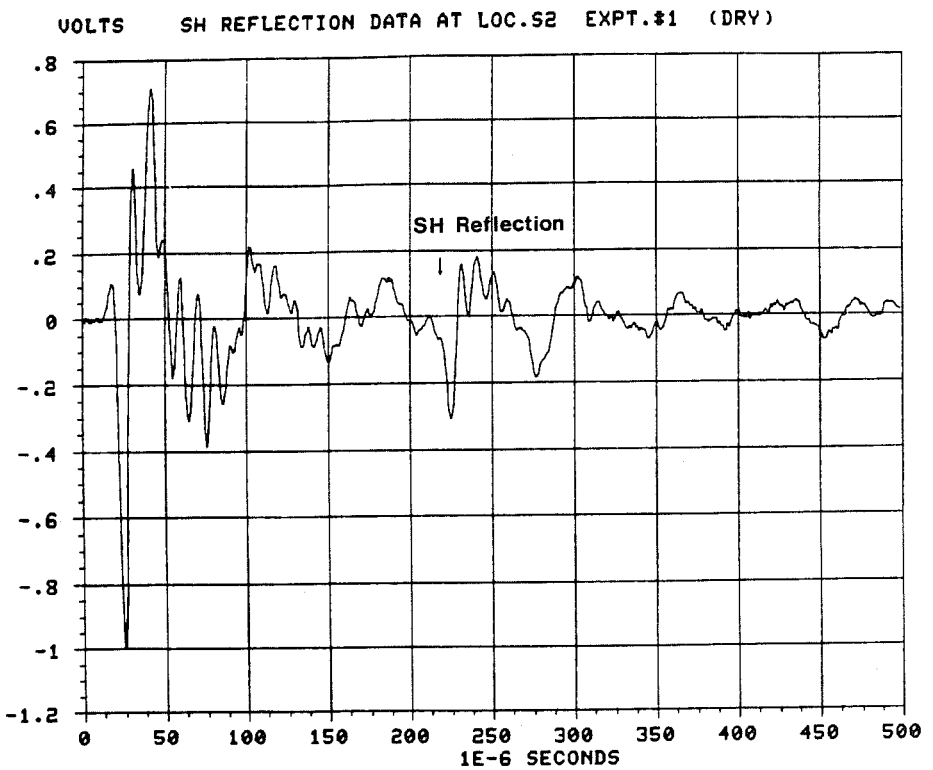

Figure IV-5-1a

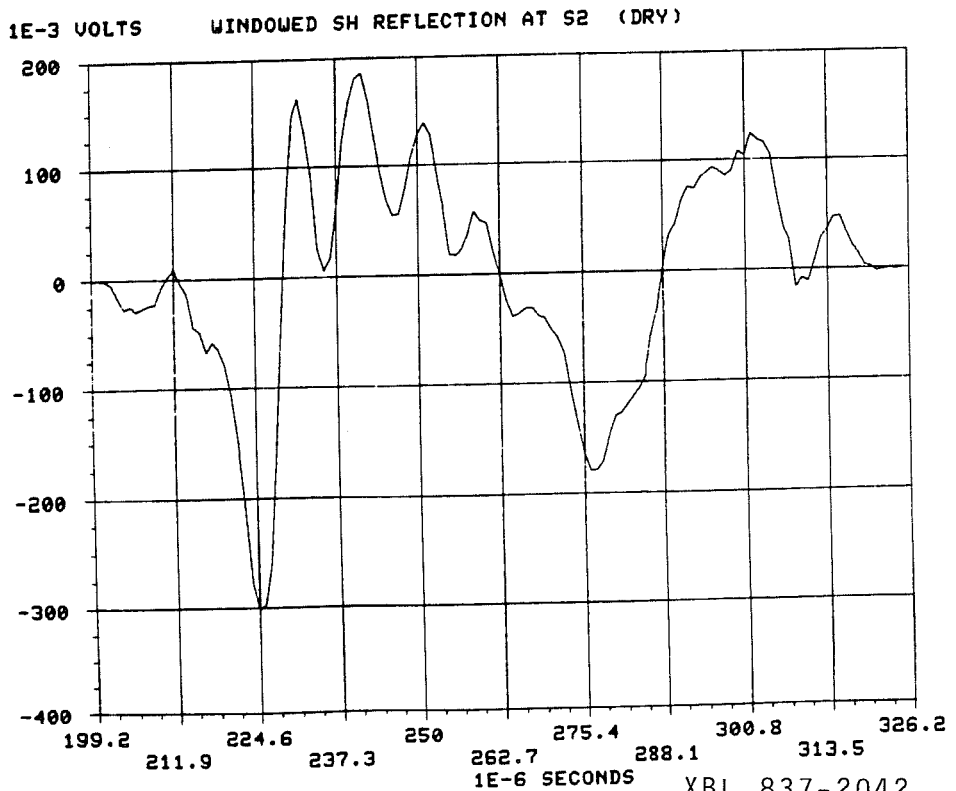

XBL 837-2042

Figure IV-5-1b

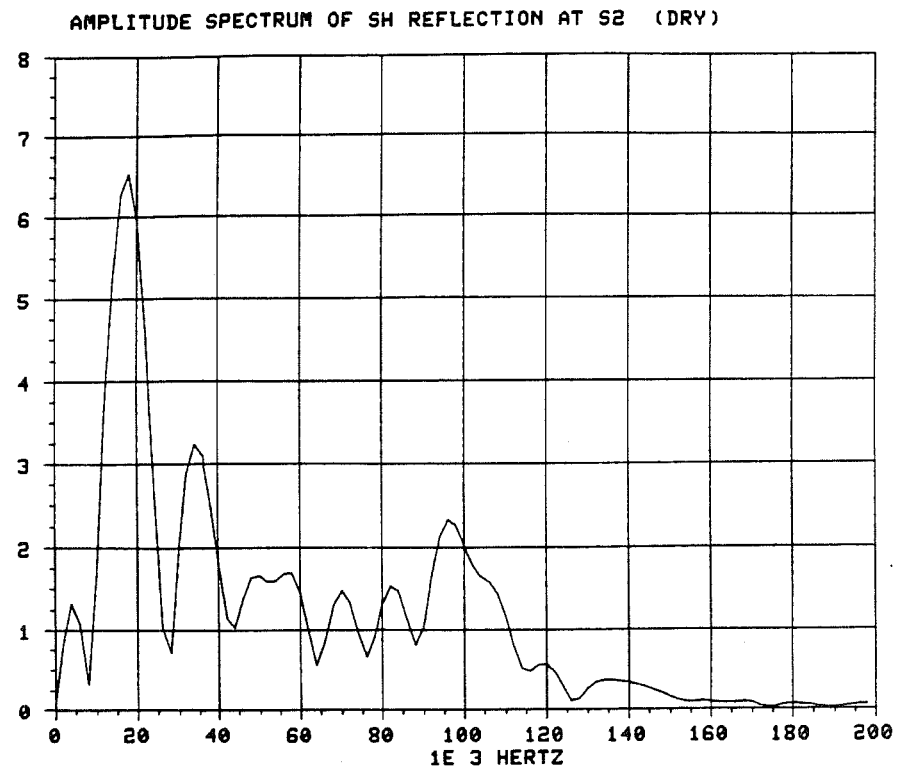

Figure IV-5-2a

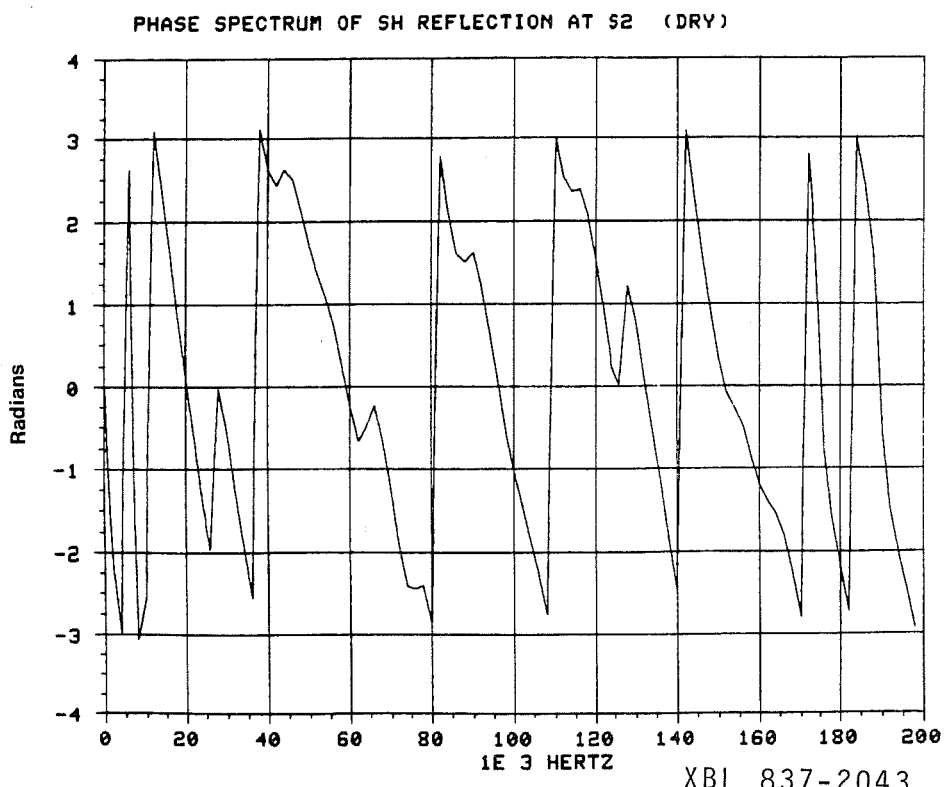

Figure IV-5-2b

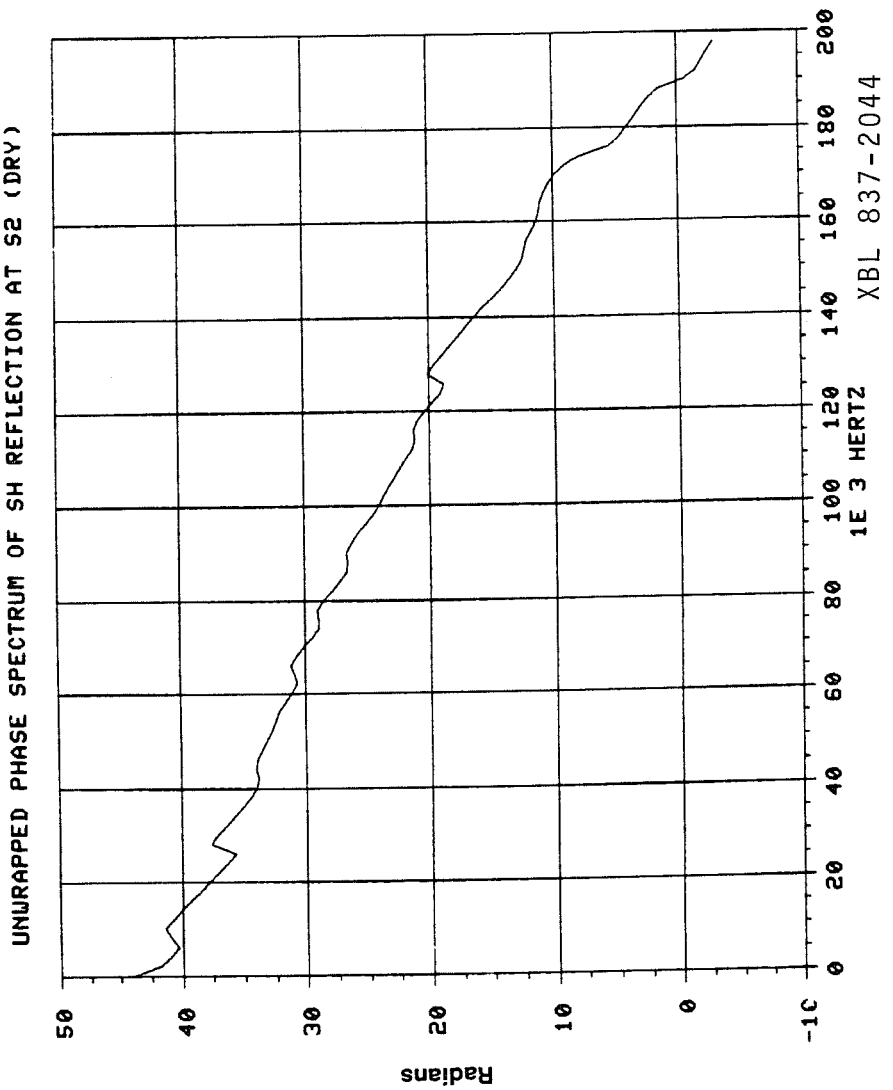
UNWRAPPED PHASE SPECTRUM OF SH REFLECTION AT S2 (DRY)
Radians
50
40
30
20
10
0
-10
0
20
40
60
80
100
120
140
160
180
200
1E 3 HERTZ
XBL 837-2044

Figure IV-5-3

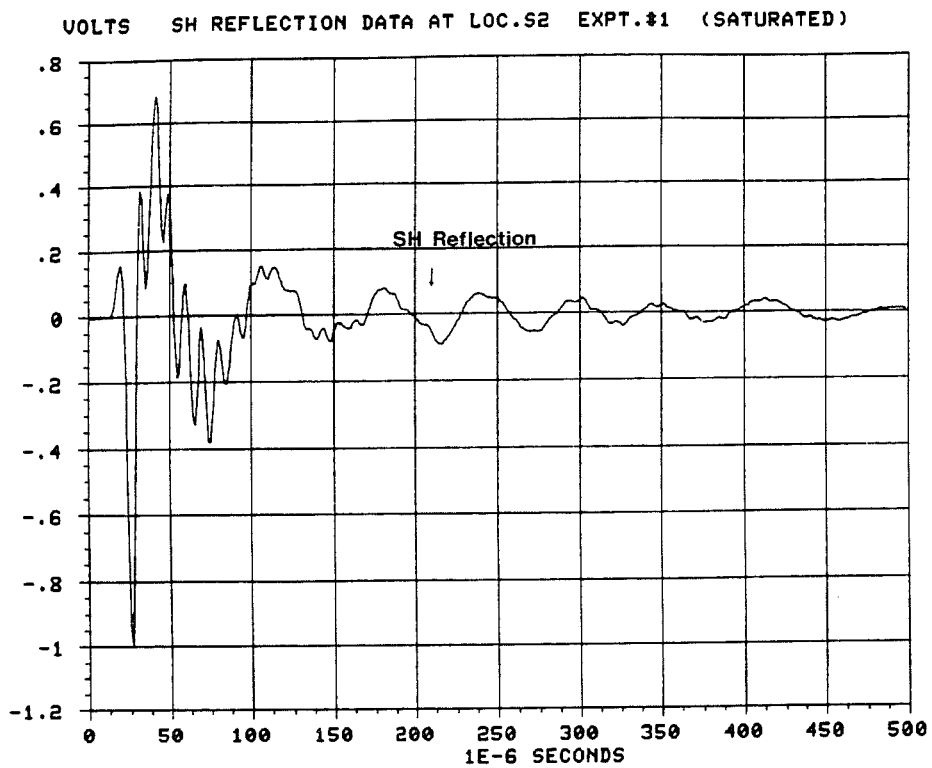

Figure IV-5-4a

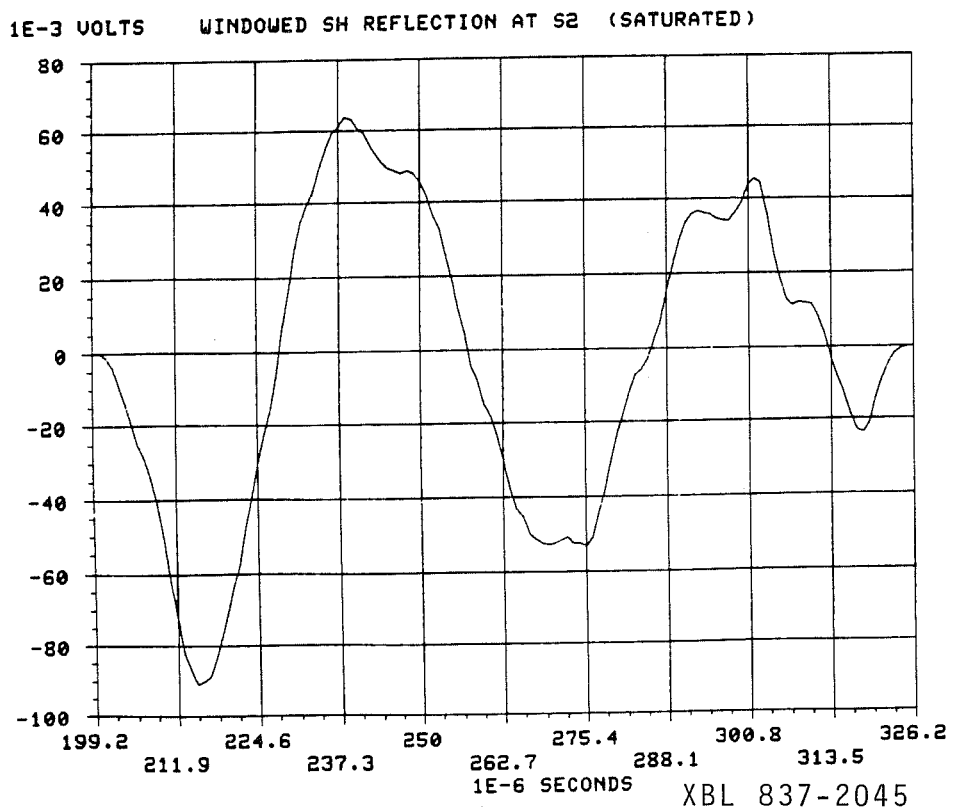

Figure IV-5-4b

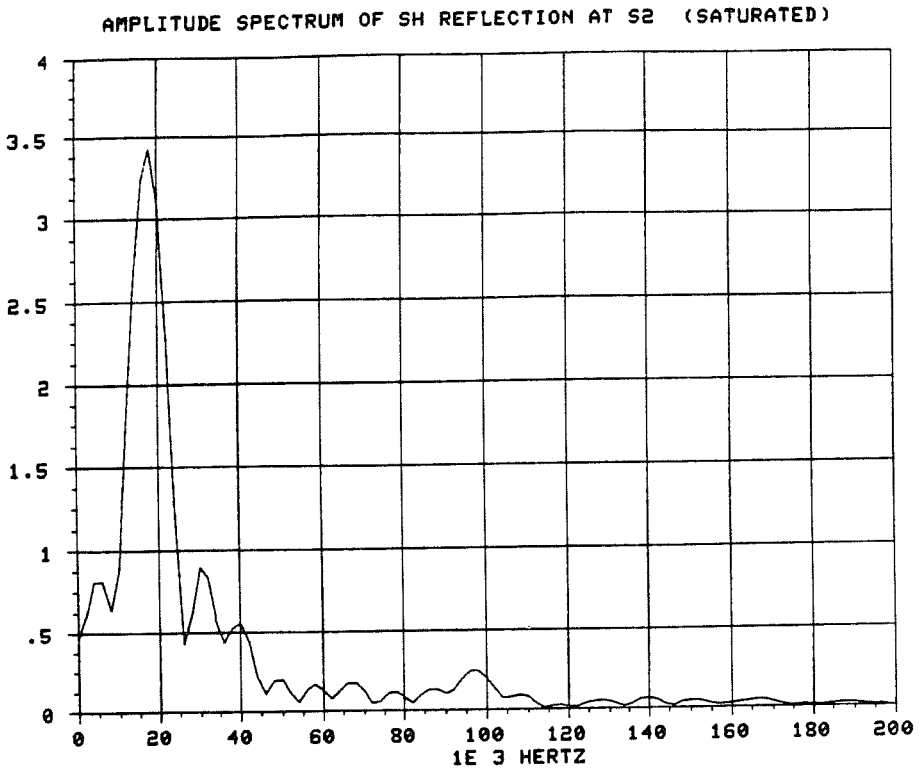

Figure IV-5-5a

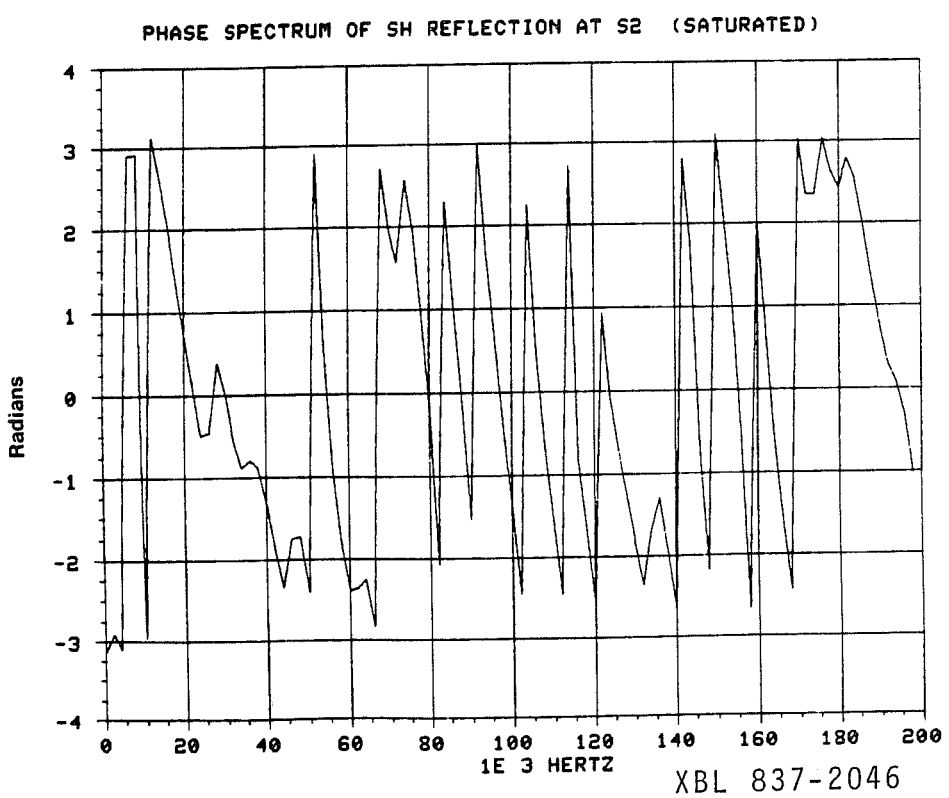

Figure IV-5-5b

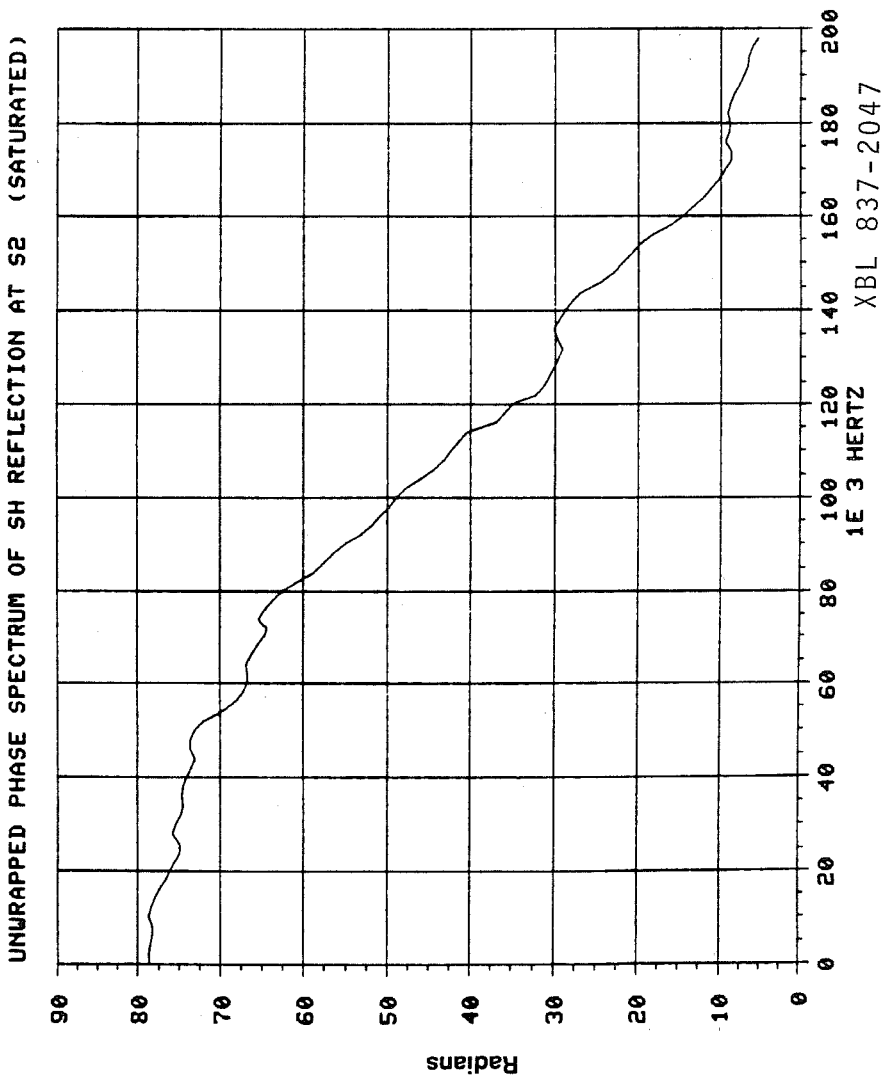
UNWRAPPED PHASE SPECTRUM OF SH REFLECTION AT S2 (SATURATED)
Radians
0
10
20
30
40
50
60
70
80
90
0
20
40
60
80
100
120
140
160
180
200
1E 3 HERTZ
XBL 837-2047

Figure IV-5-6

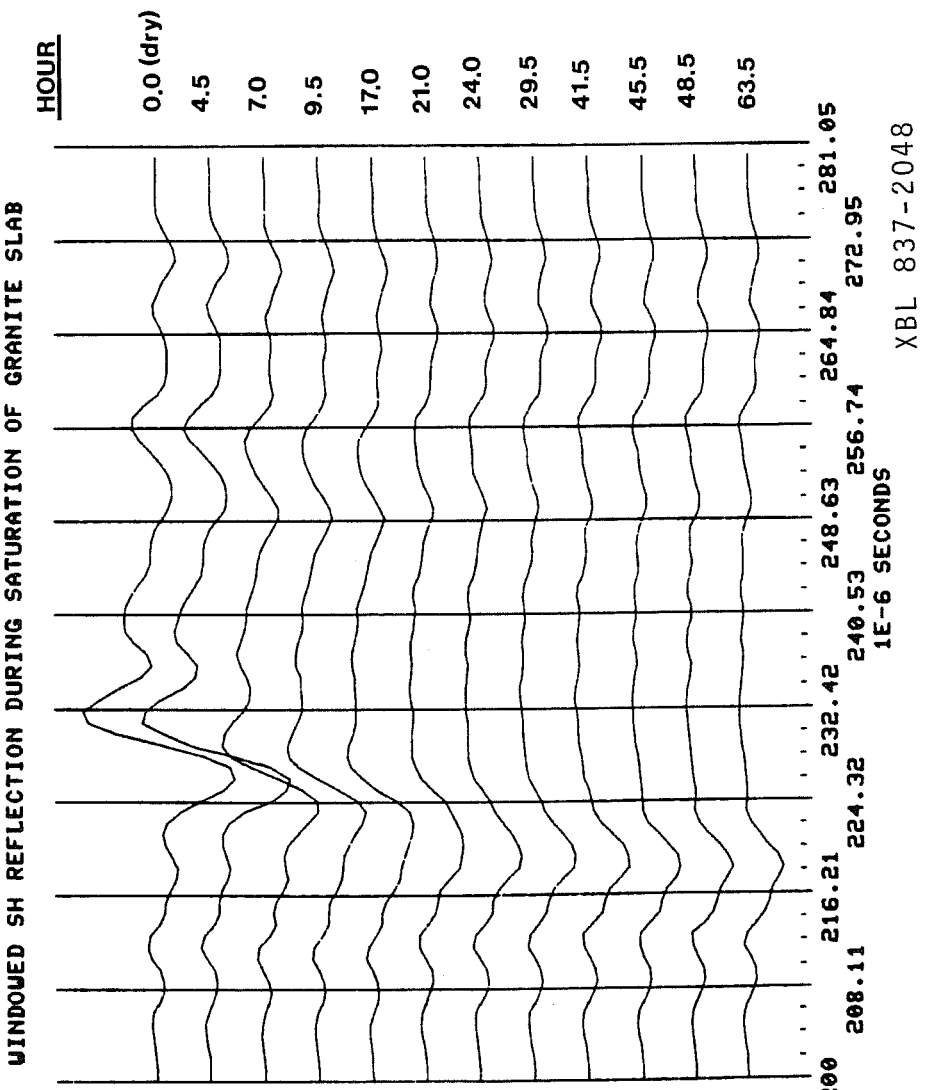
WINDOWED SH REFLECTION DURING SATURATION OF GRANITE SLAB
HOUR
0.0 (dry)
4.5
7.0
9.5
17.0
21.0
24.0
29.5
41.5
45.5
48.5
63.5
200
208.11
216.21
224.32
232.42
240.53
248.63
256.74
264.84
272.95
281.05
1E-6 SECONDS
XBL 837-2048

Figure IV-5-7

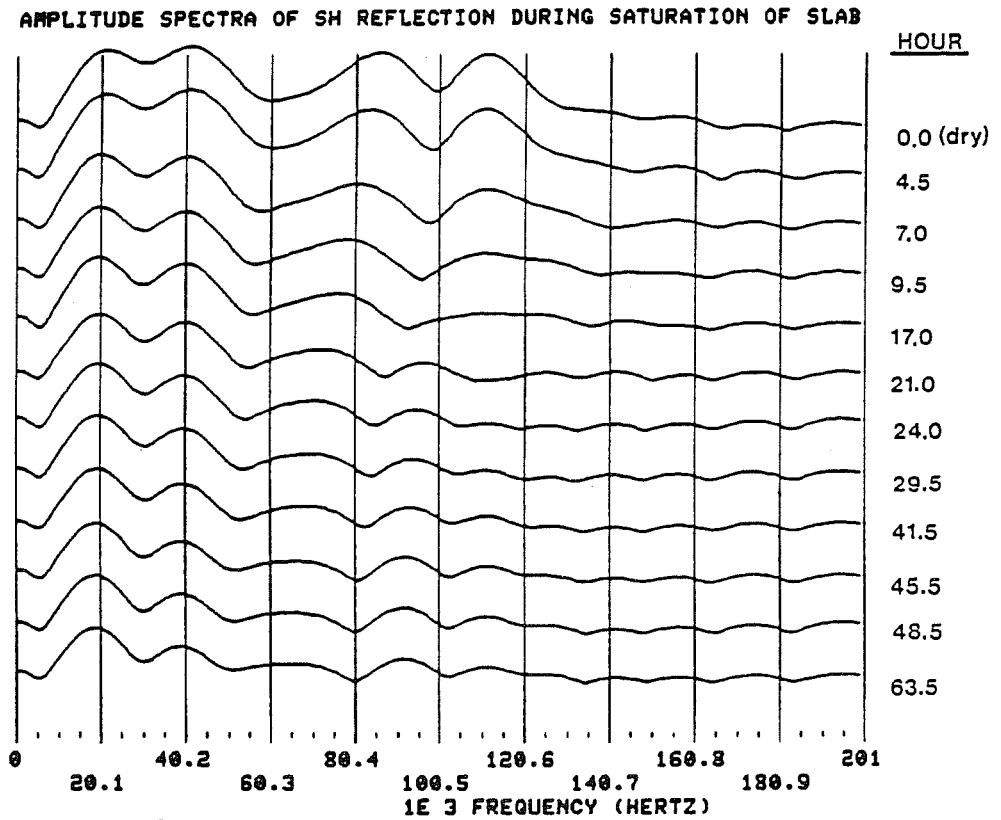

Figure IV-5-8a

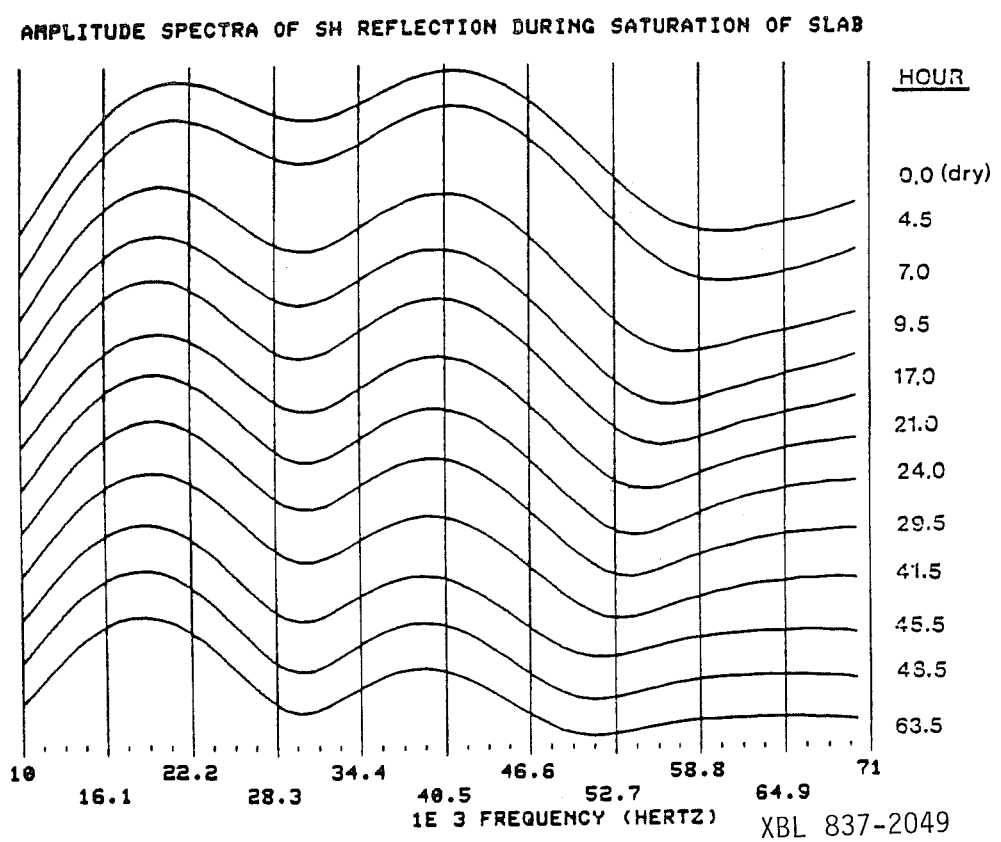

XBL 837-2049

Figure IV-5-8b

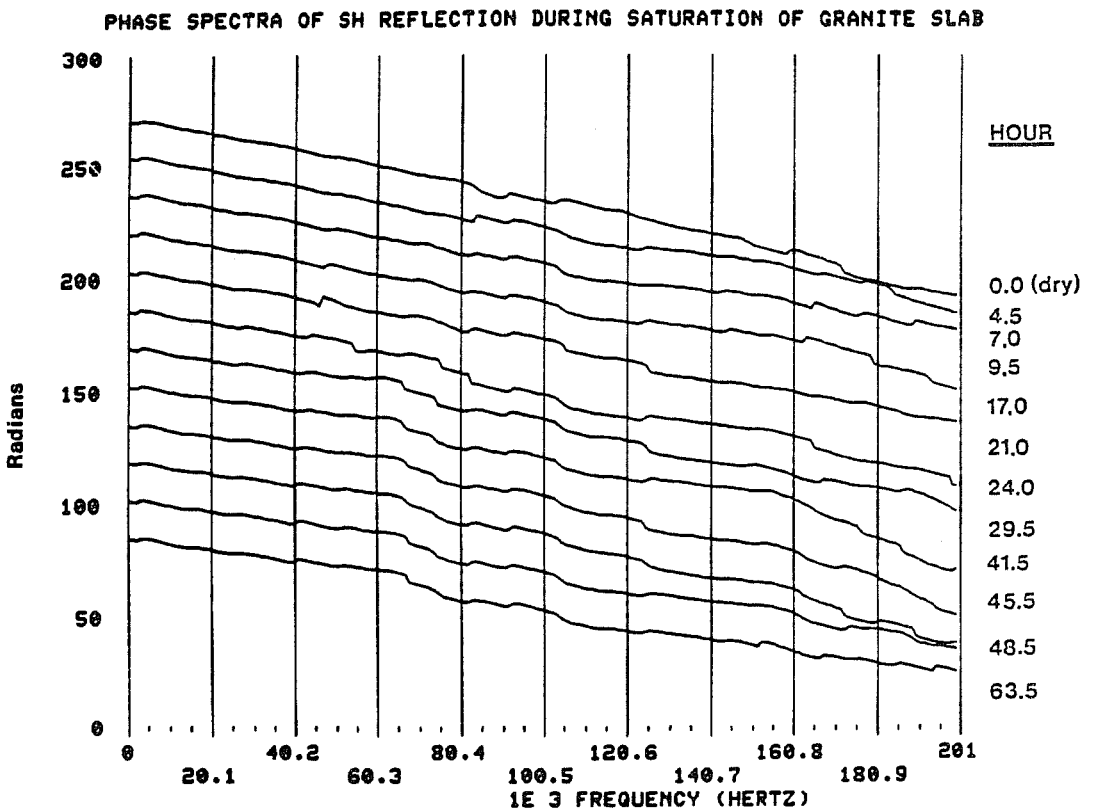

Figure IV-5-9a

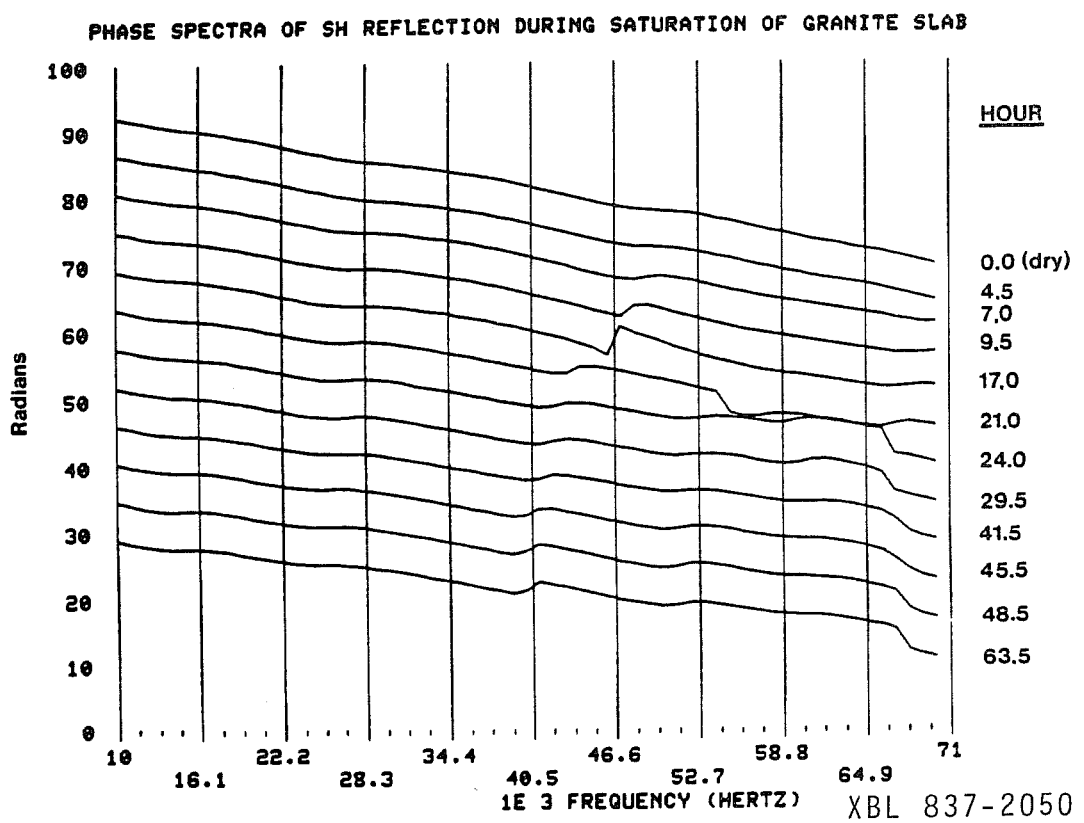

Figure IV-5-9b

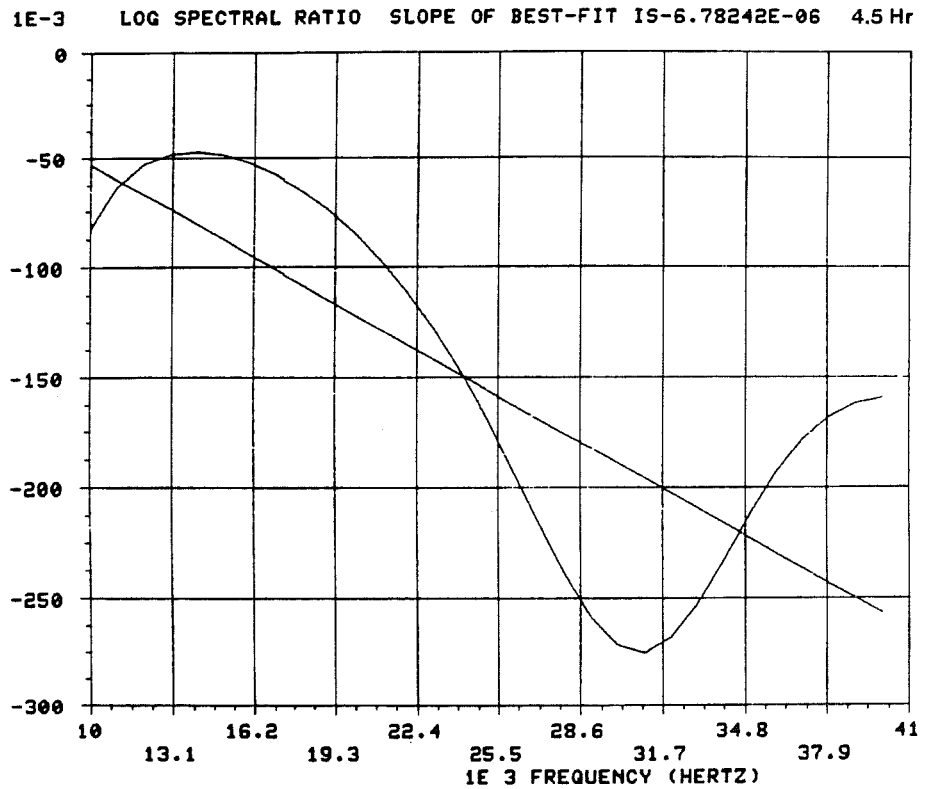

Figure IV-5-10a

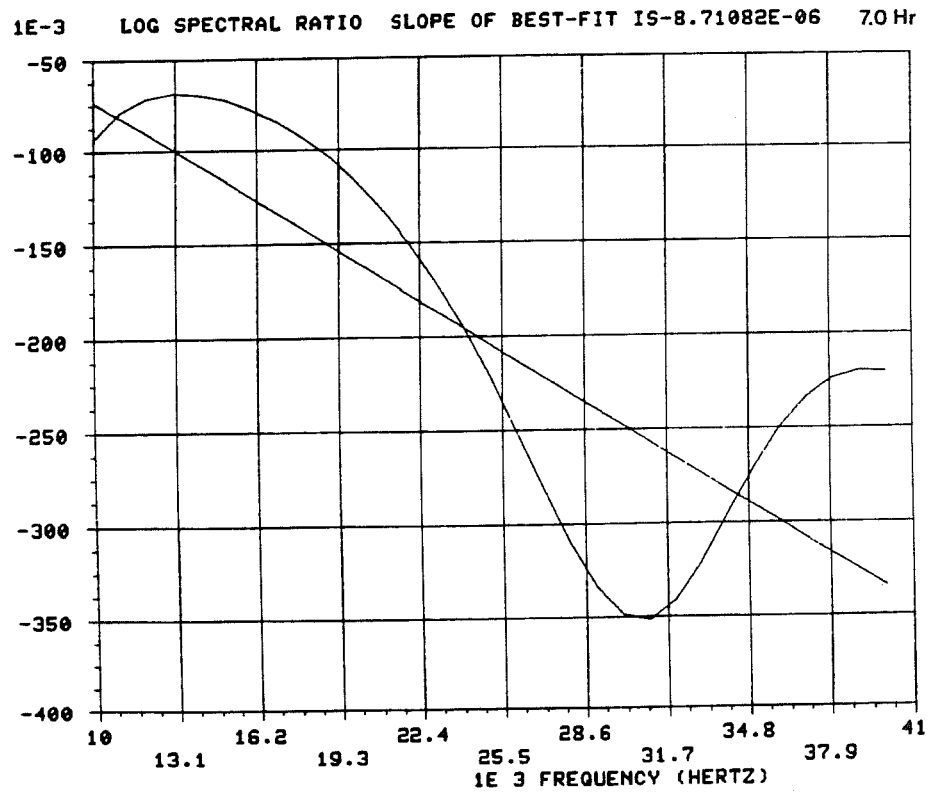

XBL 837-2051

Figure IV-5-10b

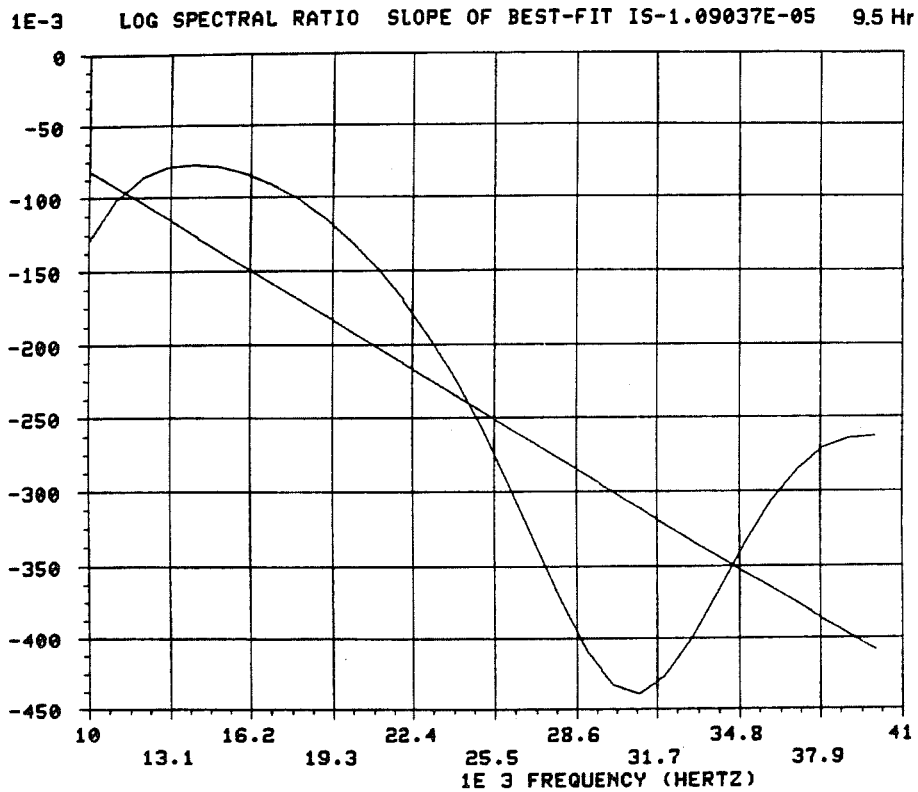

Figure IV-5-10c

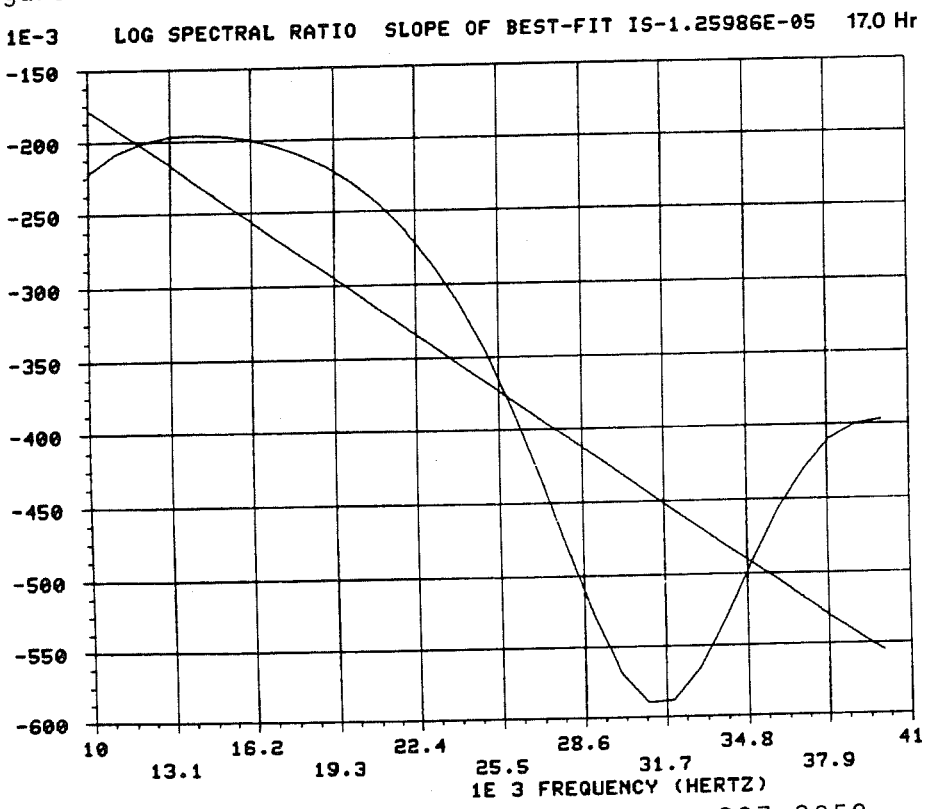

XBL 837-2052

Figure IV-5-10d

CHAPTER IV

Section 6

Conclusions

The interpretation of the SH reflection data recorded at the Shaw quarry and presented in Chapter III was based on two assumptions:

1) SH reflection from fractures at the quarry site is total, and,
2) the S velocity of the quarry granite was homogeneous beneath each survey site.

The results of a number of experiments that investigate these two assumptions were discussed in this chapter.

In the first of these experiments, the P and S velocities of small samples of Raymond granite were measured using a pulse transmission/timing method. Specimens were cored from a block of Raymond granite acquired at the Shaw quarry, and also from one of the granite slabs used as a laboratory model. S velocities measured in water-saturated specimens were found to be 10-20% faster than those measured with the specimens dry.

In another experiment a planar, air-filled fracture is simulated by shimming two 0.91 m × 0.91 m × 0.30 m granite slabs to give an air gap approximately 1.5 mm thick. Reflection data recorded along four SH profiles with the gap air-filled clearly showed the primary SH reflection from the air gap. The exterior of the air gap was filled with caulking compound, and the gap filled with water. SH profiles recorded

a week after filling the gap with water showed that the arrival time of the primary SH reflection had decreased by 5%, indicating that the average S velocity of the slab had increased by a like amount. Besides the arrival time advance, a drastic attenuation of the SH reflection wavelet was observed in this experiment. Based on the study of the effects of water-saturation on the S velocity of small granite specimens, it was concluded that water had been absorbed into the two granite slabs. This interpretation was supported by the observed increase in arrival time of the SH reflection after the water was drained from the gap and the granite slabs were dried. The changes in arrival time of the SH reflection were shown to be frequency independent in Section 5 in a quantitative analysis using the phase spectra of the reflection waveforms. The results of this analysis preclude attenuation-related dispersion as a cause of the apparent travel-time changes of the SH reflection event.

Because of the importance of these findings with regard to the field experiment, the water gap experiment was repeated. In this second experiment, one P and two S source-receiver pairs were fixed with a very small source-receiver offset (< 3 cm). The primary P and S reflections from the air gap are easily observed in the fixed receiver data, and for our purposes P and SH reflection was assumed total at the air gap. The air gap was again filled with water, and the seismic data immediately recorded at each receiver. Comparison of the air and water gap reflection data verified our previous theoretical predictions about reflection of P and SH waves at a water-filled fracture.

Although little evaporation loss to the atmosphere was possible, during the next two weeks it was necessary to add 1500 cm^3 of water in order to keep the gap totally filled. Observation of the fixed receiver data during this period showed a 5% decrease in the arrival time of the SH reflection, and a decrease in the amplitude of this event by a factor of three. Two different velocity models were used in an attempt at estimating the thickness of the saturated zone in the upper granite slab. The first model considers a step transition from ambient dry to fully saturated S velocities at some depth in the slab. This velocity step is assumed to represent the form of the saturation transition in the granite slab. The second velocity model assumes that a linear variation in the S velocity of the granite slab can be interpreted as a linear change in the degree of saturation. The results of this modeling suggest that the thickness of the saturated zone created by the absorbed water ranged from 10-30 cm, with 10 cm being the minimum thickness of this layer. This minimum thickness estimate corresponds closely to the thickness of the fully saturated layer calculated using the measured amount of absorbed water, the area of the granite slab, and an assumed porosity of 1% for the granite (estimated from measurements performed by Dr. M. S. King and presented in Section 2 of this chapter).

An attempt was made to quantify the decrease in Q_S implied by the increased attenuation of the SH reflection event observed during this experiment. The value for Q_S at ambient laboratory conditions was estimated using a spectral ratio of the primary and first multiple SH reflection wavelets. The results of this analysis, presented in Appendix II, suggest that $Q_S = 50 \pm 30\%$ is a reasonable estimate for the

granite slab at ambient dry conditions (i.e. prior to filling the gap with water).

Water absorbed into the granite during this experiment was presumed to be responsible for the observed decrease in amplitude of the SH reflection. This implied that Q_S for the Raymond granite decreased with increasing water saturation, and again spectral ratio techniques were used to estimate the change in Q_S due to saturation effects. A step transition model of Q_S based on the previous step velocity model was used to obtain an estimate of Q_S for a saturated Raymond granite. The results of this analysis suggest that Q_S = 3 - 30 for the saturated granite, although this particular model will tend to over-estimate the change in Q_S with increased saturation. We expect that Q_S for the saturated Raymond granite is more likely to have a value of Q_{Ss} = 10 to 30.

The results of the experiments discussed in this chapter have many implications with regard to the interpretation of the SH field data presented in Chapter III. The results of the work presented in this chapter confirm that SH reflection from a planar, horizontal, water-filled gap with a thickness in the range 1-2 mm is indeed total. However, the results of the experiments presented in this chapter emphatically demonstrate the significant increase in the S velocity of the Raymond granite caused by an increase in water saturation. Also, the observed decrease in Q_S of the Raymond granite with increased saturation could result in a profound decrease in the amplitude of the SH event reflected from a water-filled fracture located in a water-saturated granite. The implications of the experimental results presented in this chapter will be discussed in detail in Chapter V.

References--Chapter IV

Aki, K. and Richards, P. G.; 1980; Quantitative Seismology: Theory and Methods; W.H. Freeman and Company; San Francisco; 932 pp.

Frisillo, A. L. and Stewart, T. J.; 1980; "Effects of Partial Gas/Brine Saturation on Ultrasonic Absorption in Sandstone"; J.G.R.; Vol. 85; pp. 5209-5211.

Johnson, D. H. and Toksoz, M. Nafi; 1980; "Ultrasonic P and S Wave Attenuation in Dry and Saturated Rocks Under Pressure"; J.G.R.; Vol. 85; pp. 925-936.

King, M. S. and Paulsson, B. N. P.; 1981; "Acoustic Velocities in a Heated Block of Granite Subjected to Uniaxial Stress"; Geophys. Res. Letters; Vol. 8; No. 7; pp. 699-702.

Nur, A. and Simmons, G.; 1969; "The Effect of Saturation on Velocity in Low Porosity Rocks"; Earth and Planetary Science Letters; Vol. 7; pp. 183-193.

Nur, A.; 1971; "Viscous Phase in Rocks and the Low-Velocity Zone"; J.G.R.; Vol. 76; No. 5; pp. 1270-1277.

O'Connell, R. J. and Budiansky, B.; 1977; "Viscoelastic Properties of Fluid-Saturated Cracked Solids"; J.G.R.; Vol. 82; pp. 5719-5735.

Winkler, K. W. and Nur, A.; 1982; "Seismic Attenuation: Effects of Pore Fluids and Frictional Sliding"; Geophys.; Vol. 47; No. 1; pp. 1-15.

CHAPTER V

Section 1

Reexamination of the Field Work at the Shaw Quarry

The various laboratory results detailed in Chapter IV helped to resolve a number of assumptions used in the initial interpretation of the SH field data recorded at the Shaw quarry in Chapter III. We will list the pertinent results given in Chapter IV as a preview to the re-interpretation of the SH field data:

1) The S velocity of field and laboratory specimens of Raymond granite was found to increase from 10-20% at low stress levels after saturation of the samples with water. This increase was found to be reasonably consistent with the published results of Nur and Simmons, 1969.

2) Water in contact with an exposed surface can be quickly absorbed into an ambient dry Raymond granite slab, creating a zone of saturated granite on the order of 5-15 cm thick. Likewise, this zone can be removed (at a slower rate) by re-exposure of the granite slab to ambient dry conditions. It appears that the granite slab can attain saturation equilibrium with the surrounding dry laboratory conditions in a period of about three months.

3) There is a strong increase in shear wave attenuation in the saturated layer of the granite slab, implying that Q_S decreases in a Raymond granite. The dry and saturated values of Q_S presented in Appendix II and Chapter IV are poorly determined, but do indeed suggest

that if the dry value of Q_S is 50, then the saturated value of Q_S will lie in the range of 10-30.

As was previously stated at the conclusion of Chapter III, the interpretation of event E#1 as a SH reflection from a planar reflector segment was indecisive at best. A primary assumption in this initial interpretation was that the layer above the reflector segment had a constant S velocity; in this way the S velocity of this layer could be directly obtained from the direct SH body wave event. The results of transit-time measurements presented in Section 2, Chapter IV showed that the S velocity of a dry sample of Raymond granite is significantly lower than the S velocity of the fully-saturated specimen.

The following physical arguemnt suggests a mechanism for the creation of a low S velocity surface layer at the Shaw quarry field site. A significant amount of rain (10-20 inches) falls at the Shaw quarry during the winter months. The moss and lichen growing on the exposed granite faces, as seen in Figures III-1-(3 and 5), indicate that this surface must be very moist during the rainy season. Also, the nearly vertical target fractures seen in Figure III-1-2 apparently provide a natural conduit for water flow during the rains. Abundant moss growing in the gap of these fractures and water staining beneath these features, although not distinctly visible in this figure, are evidence of a significant flow of water. During the summer months (mid-May to mid-September) the noonday temperature averages around 100° F, and the relative humidity is typically very low (10-20%).

We hypothesize that during the winter months the entire granite layer between the observation surface and target fractures is homo-

geneously saturated by the rainfall and runoff. During the spring and summer the observation face is dried by constant exposure to the high temperatures and low humidities of these seasons. Since this region of California has essentially no summer rainfall, the existence of a dry surface layer just beneath the observation surface seems a likelihood. If such a dry surface layer does exist over a much thicker saturated layer, then consideration of the velocity measurements detailed in Chapter IV, Section 2 suggests that the S velocity distribution beneath the observation surface is not homogeneous. In fact, this physical situation would create a low S velocity surface layer above a higher S velocity half-space. This is the sort of spatial variation in S velocity that is required for the existence of Love waves, a dispersive waveguide mode of SH wave propagation.

In this section, a second model will be used to analyze the SH field data. This model will be based on the assumption that a low S velocity surface layer exists at the observation surface, and that this distinct layer is underlain by a higher S velocity half-space. If this S velocity structure did indeed exist at the quarry site, then the SH source-receiver geometry used in this study should record Love wave arrivals after the direct SH body wave. In general, models in which the S velocity increases with depth will result in Love wave propagation (Ewing, Jardetsky, and Press, 1957), regardless of the functional form of the velocity gradient. Then, this new S velocity model would suggest that event E#1 is a Love wave arrival, and not a SH reflection from a sub-surface fracture.

The assumed S velocity model used in this reinterpretation of the Shaw quarry field data is depicted in Figure V-1-1. A layer of constant S velocity β_1 and thickness h overlies a half-space of constant velocity β_2. It is required that $\beta_1 < \beta_2$ to allow for the existence of the guided Love waves. This sharp velocity boundary represents a mathematical convenience, and may not at all represent the true nature of the transition between β_1 and β_2, if indeed such a transition truly does exist in the field. However, the step S velocity model of Figure V-1-1 will be adopted in the following Love wave dispersion analysis to simplify mathematical formulations.

The following period equation for the fundamental mode Love wave is taken from Aki and Richard, 1980. In this equation, the S velocity contrast β_1--β_2 is assumed due to a contrast in shear moduli μ_1--μ_2, so that the density of the layer and half-space is assumed equal ($\rho_1 = \rho_2$). The density contrast between a dry and saturated granite with a 1% porosity is indeed negligible in this situation. The fundamental mode Love wave period equation is

$$\tan\left[\left(\frac{2\pi fh}{\beta_1}\right)\sqrt{1-(\beta_1^2/c^2)}\right] = \left(\frac{\beta_1}{\beta_2}\right)\left[\frac{\sqrt{(\beta_2^2/c^2)-1}}{\sqrt{1-(\beta_1^2/c^2)}}\right] \qquad \text{[V.1.1]}$$

where, f = frequency (Hz)

c = the horizontal phase velocity of the Love wave.

The phase velocity c obtained using Equation V.1.1 is dispersive, i.e., c varies with the choice of frequency f. This dispersion is such that lower frequency components propagate with phase velocities asymptotic to the half-space velocity β_2, and the phase velocities of the higher frequency components are asymptotic to the layer velocity β_1.

The Love wave period equation shows that the horizontal phase velocity c is dispersive, and the form of this dispersion is well defined for the one dimensional geometry shown in Figure V-1-1. The dispersion relation of event E#1 will now be calculated using the right spread receiver data at Location 1. By comparing the dispersion of event E#1 to the dispersion relation given in Equation V.1.1, it may be possible to determine if E#1 is indeed a Love wave event.

The horizontal phase velocity c of event E#1 is measured in the following manner. The horizontal phase $\phi(f,x)$ of an event received along a receiver spread is given by:

$$e^{i\phi(f,x)} = e^{\frac{i2\pi fx}{c}} \qquad [V.1.2]$$

where x is the horizontal spatial coordinate. Then, simply:

$$\phi(f,x) = x\left[\frac{2\pi f}{c}\right] \qquad [V.1.3]$$

In considering a real data set, let N receivers be located at positions x_i for i = 1, 2, ..., N. Each receiver time trace has a corresponding phase value $\phi(f_j,x_i)$ at each frequency f_j for j = 1, 2, ..., M. The phase spectra $\phi(f_j,x_i)$ for each receiver trace may be obtained using the DFT described in Section 5, Chapter IV. Rewriting Equation V.1.3, then:

$$\phi(f_j,x_i) = x_i\left[\frac{2\pi f_j}{c_j}\right] \qquad [V.1.4]$$

where there will be a particular phase velocity c_j for each frequency f_j. At a given frequency f_j Equation V.1.4 is a linear equation of the form $y_i = bx_i$, and once again the linear regression described in previous chapters may be used to estimate the slope b. In this particular case $\phi(f_j,x_i)$ is obtained from the SH field data using the DFT, so that at a given frequency f_j phase values are obtained at each offset x_i. From this offset phase data, M number of estimates of b_j are obtained, one at each frequency f_j. Using these values of b_j and Equation V.1.4, it is possible to obtain the phase velocities c_j. These values will then define the dispersion relation of the SH field data, which may then be compared to the one dimension relation given in Equation V.1.1.

The unprocessed SH field data recorded along the right receiver spread at location S1 were shown in Figure III-2-2 (Chapter III, Section 2). These traces were summed in groups of two in order to smooth the irregularities in the unprocessed data. The amplitude and phase responses of such a two element, 1 cm array are presented in Figure V-1-2. This figure shows that the amplitude effects are minimal, although significant phase shifts do occur at higher frequencies and near horizontal angles of incidence. However, since each trace in the summed data set is phase shifted by the same amount, the summation process will translate the phase $\phi(f_j,x_i)$ at a given frequency f_j by some constant value for each x_i. This translation will not affect the estimated slope values b_j, nor the subsequent calculation of phase velocities c_j.

The smoothed right spread SH data recorded at Location 1 is shown in Figure V-1-3. The direct SH event (.35-.95 msec) and event E#1 (1.1-1.7 msec) are quite distinctly observed in this record section. Event

E#1 is windowed as shown in Figure V-1-4 in preparation for the calculation of the phase spectra $\phi(f_j,x_i)$ using the DFT. The phase velocities c_j are calculated from the best-fit slopes b_j, and these values of c_j are plotted at their corresponding frequency f_j in Figure V-1-5. The error bars associated with each c_j value are determined from the uncertainties obtained in calculating the best-fit slopes b. Values of c_j with associated errors greater than 8% were not plotted in Figure V-1-5.

The phase velocity results presented in Figure V-1-5 indicate that there is significant dispersion of event E#1 in the 3-8 kHz band. Generally the phase velocities decrease with increasing frequency for this event, which is consistent with the dispersion relation predicted for the fundamental mode Love wave. For comparison, a Love wave dispersion curve was calculated using Equation V.1.1 for a 10 cm thick layer with S velocity β_1 = 2000 m/s overlying a half-space with velocity β_2 = 2500 m/s, and is denoted as Model A in Figure V-1-5. In this model β_1 = 2000 m/s was determined from the direct SH event moveout, and was considered to represent the dry S velocity of the quarry granite. The value β_2 = 2500 m/s is then the saturated S velocity given in Figure IV-2-1 (Chapter IV, Section 2) corresponding to a dry S velocity of 2000 m/s. The thickness h = 10 cm was obtained from the estimates of the saturated layer thickness using the step velocity transition model.

The correspondence between Model A and the actual dispersion curve of event E#1 is not particularly good. The phase velocities of event E#1 at lower frequencies (3-5 kHz) are faster than the theoretical maximum (2500 m/s) predicted using Model A. The agreement between the theoretical and measured phase velocities is better in the higher frequency

band (6.5-8 kHz). Again the phase velocity values in the 5-6.5 kHz band for the right spread data were not included because the uncertainties on the slopes b_j were larger than the arbitrary ±8% cut-off level used in this analysis.

Another method of viewing the dispersion of event E#1 involves the selective low or high-pass frequency filtering of the SH record section shown in Figure V-1-3. If E#1 is actually a Love wave event, then selective frequency filtering will cause the moveout of this event to vary depending on the choice of the filter band. The right spread record section is filtered using an 8-pole, zero-phase Butterworth filter. The record section given in Figure V-1-6a is obtained using such a low-pass filter with a corner frequency of 4000 Hz, and the section shown in Figure V-1-6b is obtained using a high-pass filter with a corner frequency of 6000 Hz.

An X-T fit was performed on the direct SH event and event E#1 in both of these sections, and the phase velocities obtained from these fits are presented in Table V-1-1. Again, the arrival times of these events were determined from the point of maximum (or minimum) value within the time windows bounding each event. This table shows that the phase velocities estimated from the direct SH event in each section are in statistical agreement (2180 m/s ± 60 m/s and 2090 m/s ± 30 m/s). This result indicates that the velocity of the direct SH wave does not vary significantly between these two frequency bands, and thus the direct SH event exhibits negligible dispersion. Also, these results show that the filtering operation itself does not introduce dispersion into the filtered seismic sections.

Table V-1-1

Corner Frequency	Phase Velocity of Direct SH Event	Phase Velocity of Event E#1
Low-Pass 4000 Hz	2180 m/s ± 60 m/s	2940 m/s ± 120 m/s
High-Pass 6000 Hz	2090 m/s ± 30 m/s	2240 m/s ± 75 m/s

A similar analysis shows that the phase velocity of event E#1 is distinctly different in each of the two filter bands. The low-pass filtered version of E#1 yields a phase velocity of 2940 m/s ± 120 m/s, whereas the high-pass version of E#1 propagates with a phase velocity of 2240 m/s ± 75 m/s This result indicates that the dispersion of event E#1 is statistically significant. Also, the form of this dispersion is consistent with the interpretation of E#1 as a Love wave event, as the lower frequency component of E#1 propagates with a phase velocity greater than that of the higher frequency component.

A second dispersion curve, denoted Model B, has also been plotted in Figure V-1-5. This curve is calculated using β_1 = 2000 m/s, β_2 = 2800 m/s, and h = 20 cm. The value of β_2 was chosen using the phase velocity value obtained from the low-pass filtered version of event E#1. The thickness h = 20 cm was used to give the best visual fit between Model B and the measured phase velocity curve. Indeed, the visual fit of Model B offers further support for the interpretation of E#1 as a Love wave event.

Physical observations made at the Shaw quarry field site suggested the existence of a low S velocity surface layer. This hypothetical low velocity layer was considered to result from the drying of the granite during the hot, dry summer typical of the foothills of California. A simple S velocity model (shown in Figure V-1-1) was used as a basis for the reinterpretation of the SH field data. In this reinterpretation event E#1 is postulated to be a Love wave arrival, and a dispersion analysis of this event was performed.

The results of this dispersion analysis do indeed support the interpretation of E#1 as a Love wave event. If this interpretation is correct, then the existence of a near surface low S velocity is required. Thus, the constant S velocity assumption used in the original interpretation of the field data is incorrect (see Chapter III). Indeed, the Love wave interpretation of event E#1 seems more plausible than the interpretation of this event as a SH reflection from a sub-surface fracture, as was discussed in Chapter III, Section 2.

Figure Captions

Figure V-1-1
S wave velocity model used in the Love wave analysis of the SH reflection data recorded at the Shaw quarry.

Figure V-1-2
Response of a 2 element, 1 cm linear array using a half-space velocity of 2000 m/s at frequencies of 2, 10, and 20 kHz.
a) Amplitude response
b) Phase response

Figure V-1-3
Right spread SH data recorded at field Location 1 summed in groups of two to smooth the irregularities in the unprocessed data shown in Figure III-2-2 (Chapter III).

Figure V-1-4
Event E#1 windowed from traces given in Figure V-1-3 in the time interval 1.1-1.9 msec.

Figure V-1-5
Phase velocity dispersion curve obtained from phase spectra of event E#1 recorded along right spread at Location 1. Model A corresponds to the theoretical Love wave dispersion for a 10 cm thick layer with S velocity β_1 = 2000 m/s overlying a half-space with velocity β_2 = 2500 m/s. Model B corresponds to the theoretical Love wave dispersion curve for a 20 cm thick layer with S velocity β_1 = 2000 m/s overlying a half-space with velocity β_2 = 2800 m/s.

Figure V-1-6
Smoothed right spread data at Location 1 shown in Figure V-1-3 filtered using an 8-pole, zero-phase Butterworth frequency filter.
a) Low-pass filter response with corner frequency of 4000 Hz
b) High-pass filter response with corner frequency of 6000 Hz

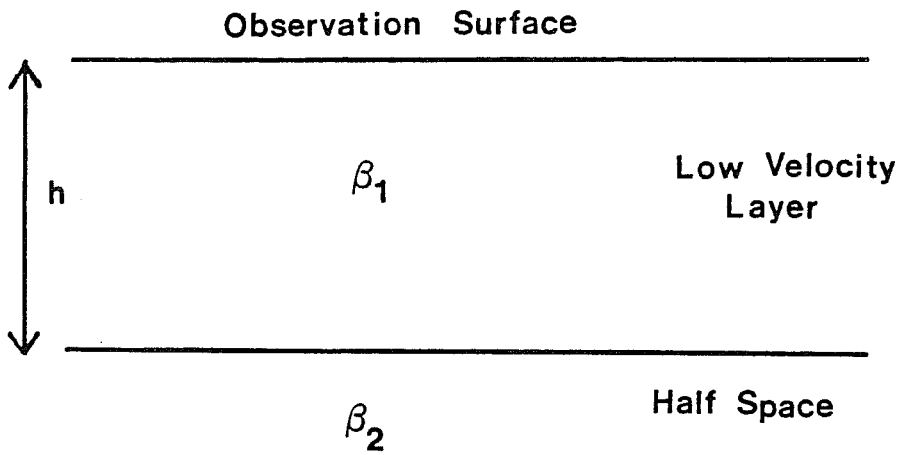

LOVE WAVE MODEL

XBL 837-2053

Figure V-1-1

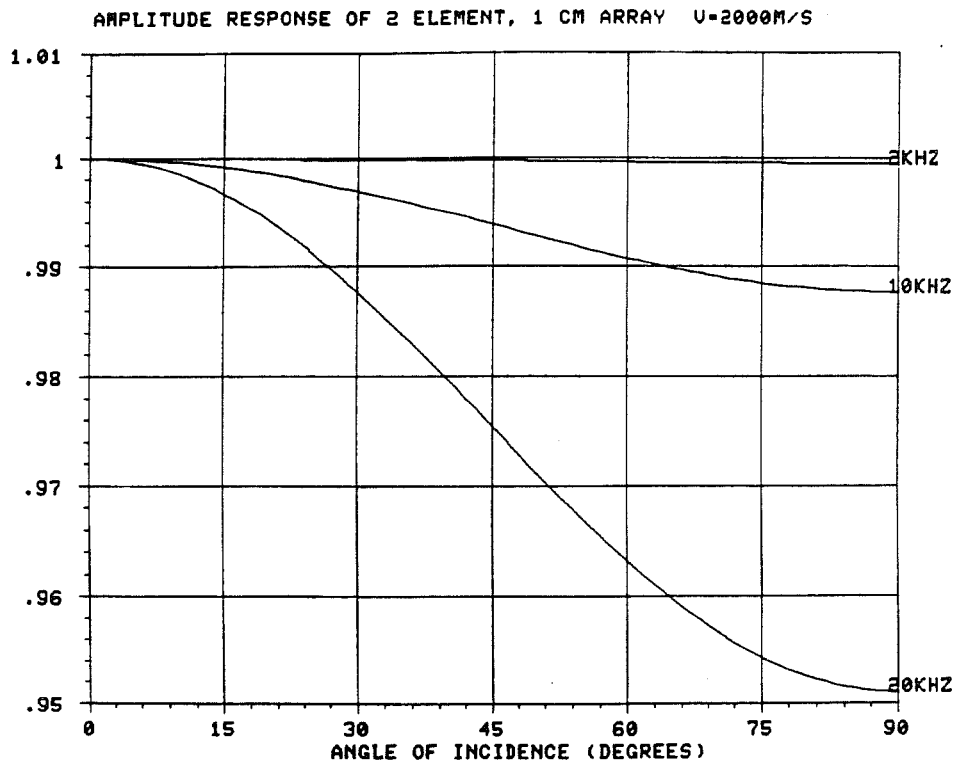

Figure V-1-2a

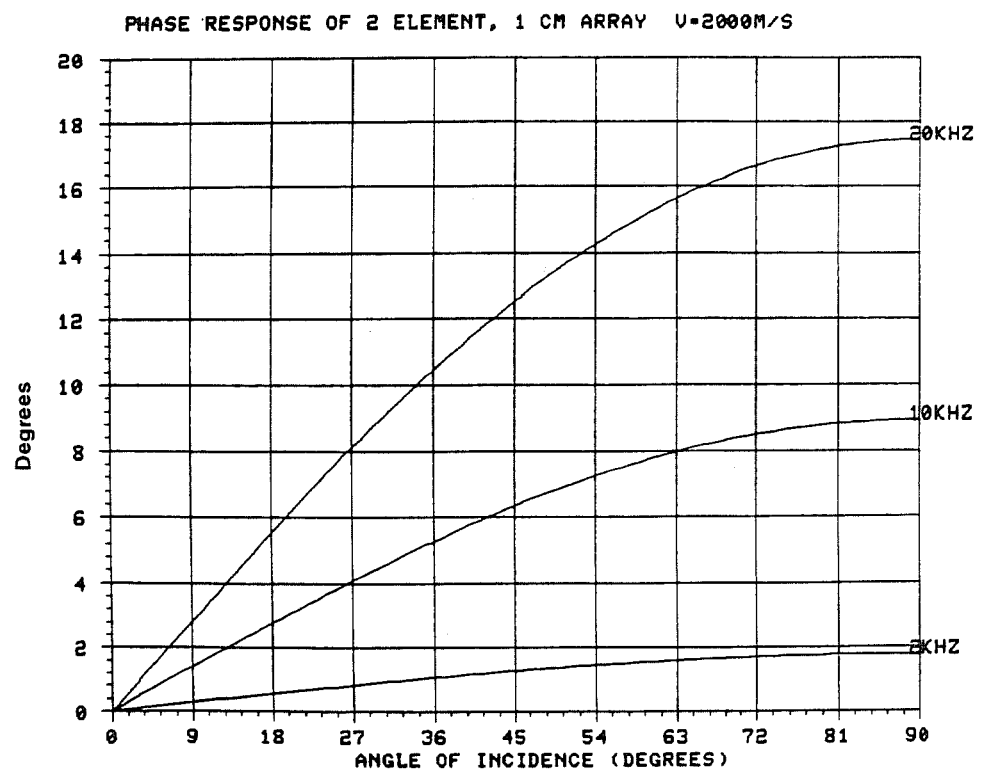

Figure V-1-2b

XBL 837-2054

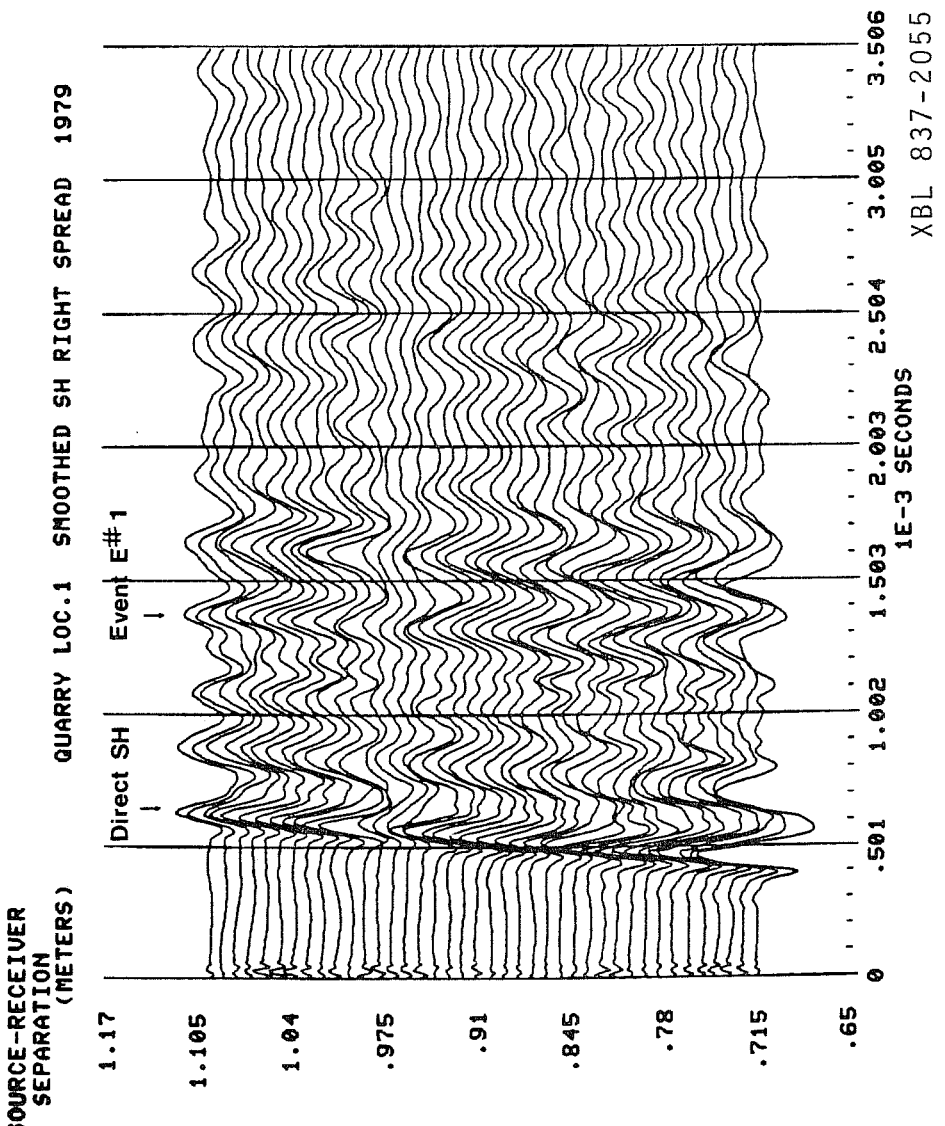
SOURCE-RECEIVER SEPARATION (METERS)
QUARRY LOC.1 SMOOTHED SH RIGHT SPREAD 1979
Direct SH
Event E#1
1.17
1.105
1.04
.975
.91
.845
.78
.715
.65
0
.501
1.002
1.503
2.003
2.504
3.005
3.506
1E-3 SECONDS
XBL 837-2055

Figure V-1-3

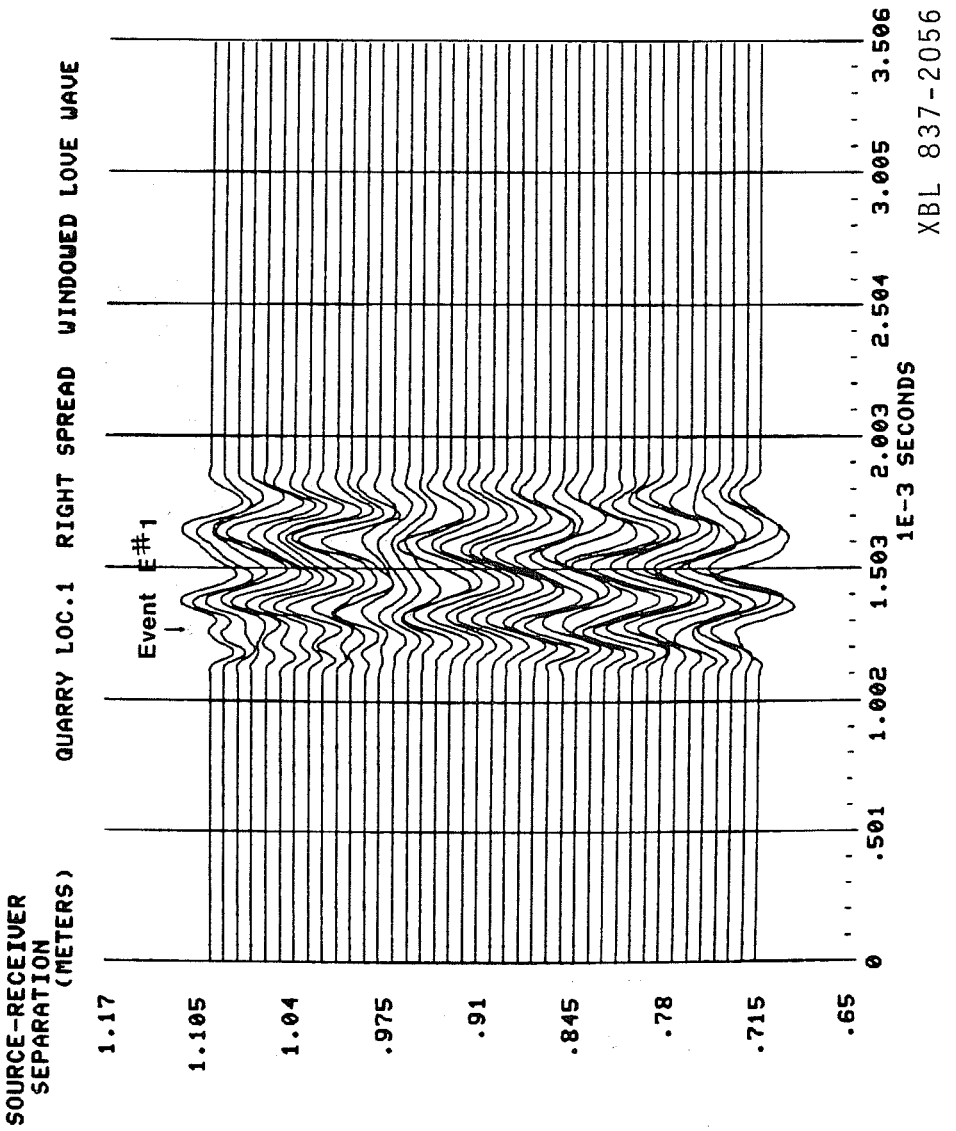
QUARRY LOC.1 RIGHT SPREAD WINDOWED LOVE WAVE
SOURCE-RECEIVER SEPARATION (METERS)
1.17
1.105
1.04
.975
.91
.845
.78
.715
.65
Event #1
0
.501
1.002
1.503
2.003
2.504
3.005
3.506
1E-3 SECONDS
XBL 837-2056

Figure V-1-4

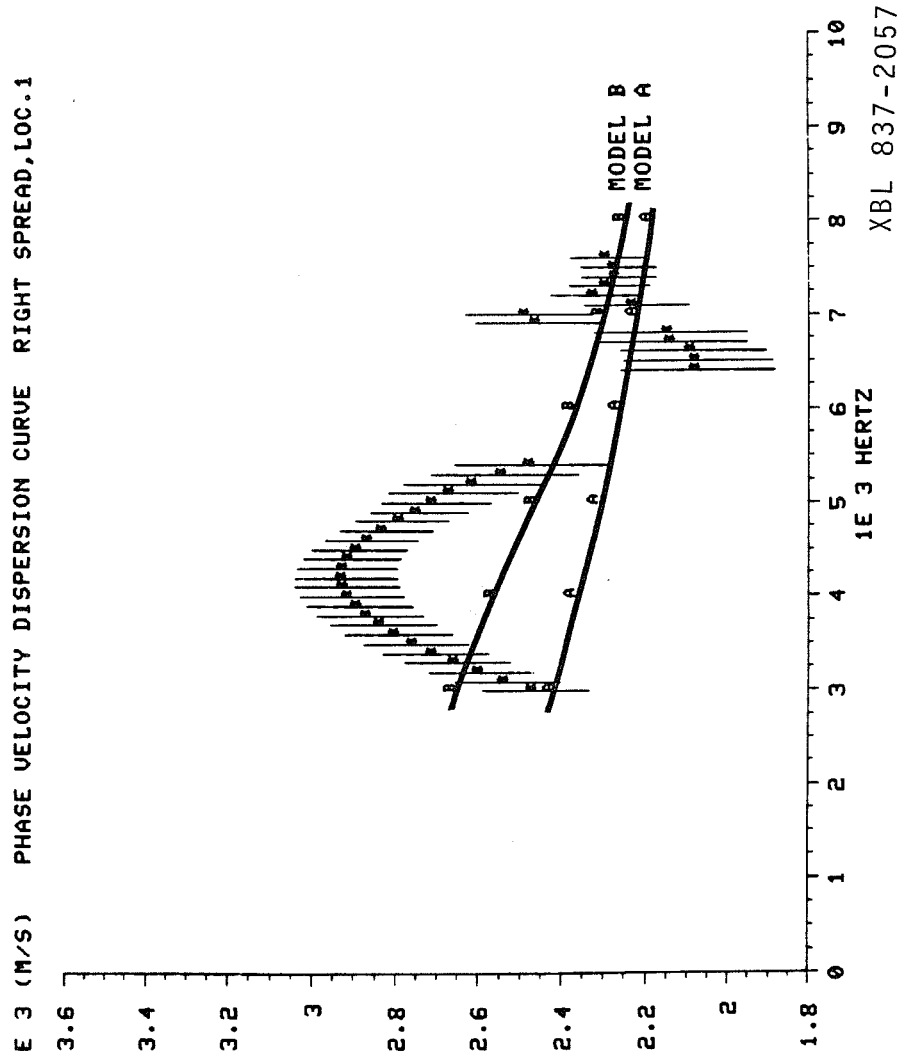
1E 3 (M/S) PHASE VELOCITY DISPERSION CURVE RIGHT SPREAD,LOC.1
3.6
3.4
3.2
3
2.8
2.6
2.4
2.2
2
1.8
0
1
2
3
4
5
6
7
8
9
10
1E 3 HERTZ
MODEL B
MODEL A
XBL 837-2057

Figure V-1-5

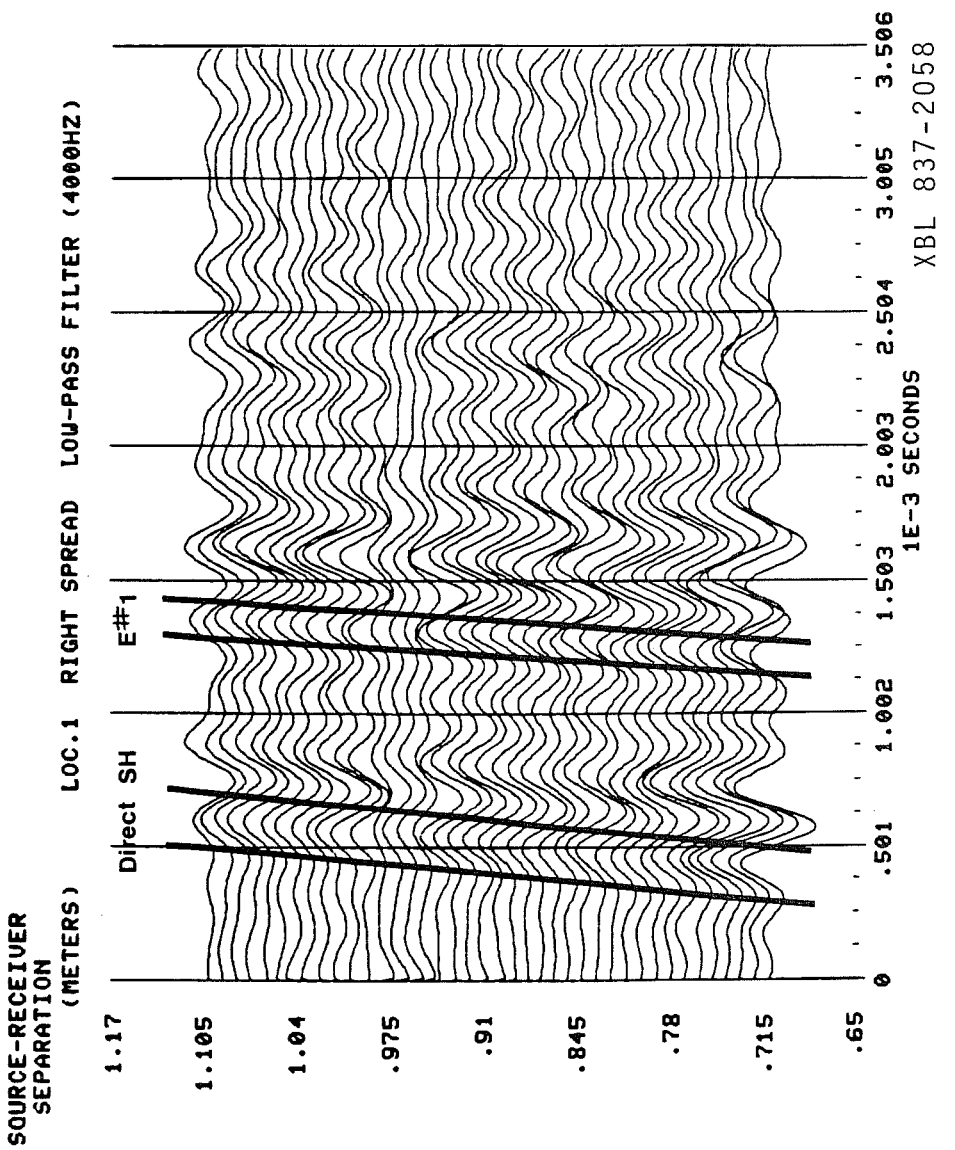
SOURCE-RECEIVER SEPARATION (METERS)
LOC.1 RIGHT SPREAD LOW-PASS FILTER (4000HZ)
Direct SH
E#1
1.17
1.105
1.04
.975
.91
.845
.78
.715
.65
0
.501
1.002
1.503
2.003
2.504
3.005
3.506
1E-3 SECONDS
XBL 837-2058

Figure V-1-6a

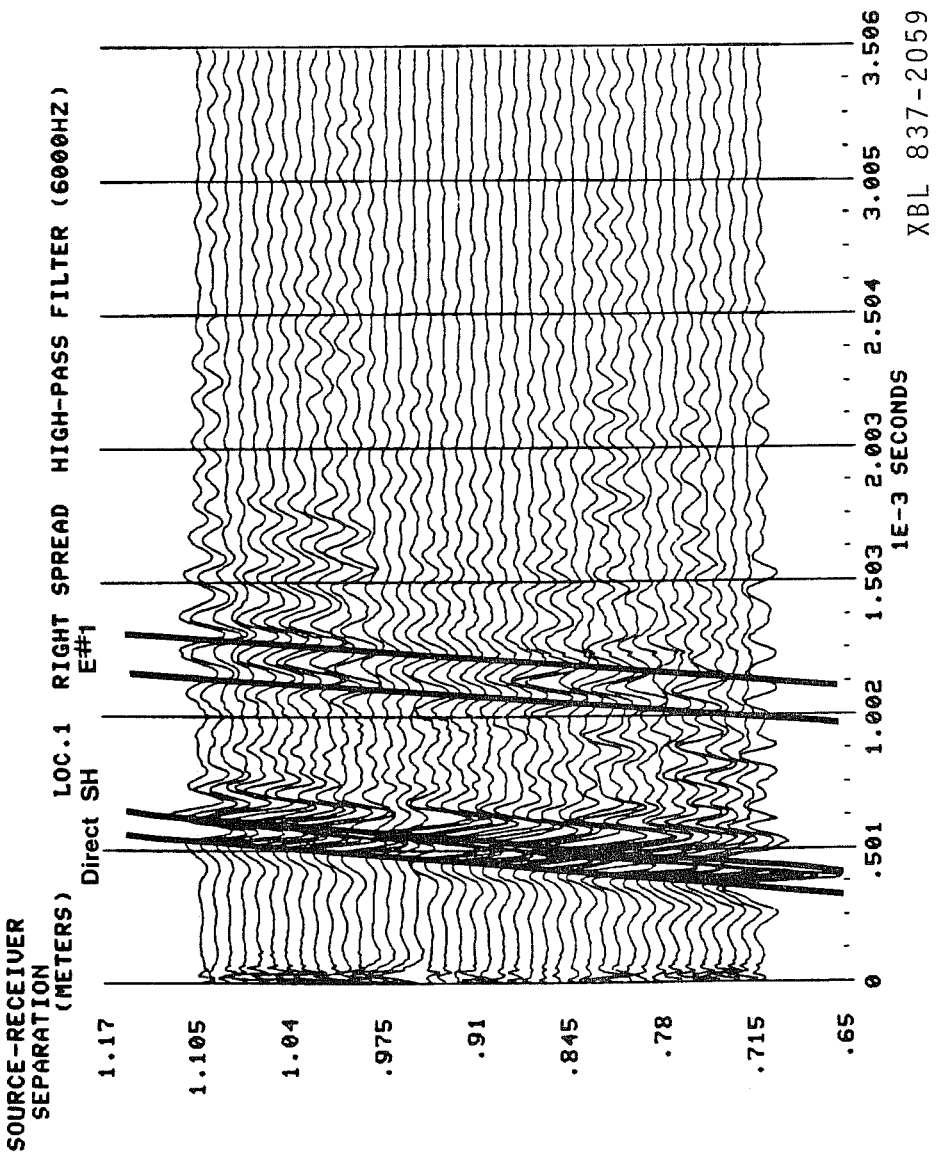
SOURCE-RECEIVER SEPARATION (METERS)
LOC.1 RIGHT SPREAD HIGH-PASS FILTER (6000HZ)
Direct SH
E#1
1.17
1.105
1.04
.975
.91
.845
.78
.715
.65
0
.501
1.002
1.503
2.003
2.504
3.005
3.506
1E-3 SECONDS
XBL 837-2059

Figure V-1-6b

CHAPTER V

Section 2

Final Statements

As seen in the last section, the most likely interpretation of the major arrival events observed in all of the SH field data (with the exception of the well defined direct SH body wave) is that these events are Love waves. Interpretation of these later-arriving events as SH reflections from dipping sub-surface fractures, as described in Chapter III, is not thought to be as plausible an explanation. In all cases, interpretation of event E#1 as a SH reflection required the rather suspicious result that the reflector always dipped downward from source to receiver.

The other piece of evidence that supports the dry surface layer model of the quarry site is the water absorption phenomenon observed in Chapter IV. These experiments showed that water absorbed by the granite slabs created a zone of saturation with a minimum thickness of 10 cm as determined using a step-velocity transition model (see Chapter IV, Section 3). If a linear velocity transition model were used, then the zone of increased saturation could have extended through the entire thickness of the granite slab. However, the saturation zone could be removed by exposure of the granite slab to ambient laboratory temperature and humidity conditions for a period of about three months. This indicates that the surface layer of the granite observation surface at the Shaw quarry had attained some degree of equilibrium with the ambient

temperature and humidity at the site, i.e., the hot, dry California summer.

The observed rate of water absorption seen in these experiments exhibits an apparently unreported rate of water transport through a dry granitic rock probably due to capillary forces. Indeed, this mechanism should be considered in analyzing the permeability of the rock around an underground opening, such as a mine. If the previous interpretation is correct, prolonged exposure to the ventilation air would create a dry surface layer around the mine opening, and concurrent pumping from adjacent boreholes could partially dry a sizeable volume of granite in the region. Water then coming into contact with this dry granite could be absorbed into the granite as well as evaporating into the air. This phenomenon is especially significant if the water coming into contact with the dry granite contains toxic or radioactive solute. Obviously, more experiments should be conducted to confirm the existence of this water absorption, and to determine the mechanism causing this phenomenon.

The increase in the shear attenuation observed in the saturated Raymond granite has important implications regarding the SH field experiments. If the low S velocity surface layer interpretation is correct, then the underlying half-space consists of saturated Raymond granite. Results given in Chapter IV show that if $Q_S = 50$ for an ambient dry Raymond granite, then the saturated value of Q_S will range from 10-30. The amplitude attenuation curves shown in Figure III-1-6 (Chapter III, Section 1) were determined using a value of $Q_S = 55$ for the granite at the Shaw quarry. This value was derived from the measurement

of Q_P of a dry Westerly granite, and is surprisingly close to the value of Q_S estimated in Appendix II for a dry Raymond granite. Then, Figure III-1-6 can be considered to represent the S attenuation at the field site if the quarry granite were in a dry condition.

The attenuation curves shown in Figure V-2-1 were calculated as in Figure III-1-6 using values of Q_S = 10, 20, and 30 and an S velocity of 2500 m/s. These figures show that the increased S attenuation caused by saturation of the granite would severely limit the ability to record SH reflection events from deep fractures. Such events would have amplitudes significantly below the -38 dB dynamic range of the analog tape recorder, and it would be impossible to record both the reflection events and direct SH event on the same recording channel.

Solution of this dynamic range problem would not present significant difficulties. Hardware solutions would include a large dynamic range recording system (either analog or digital), a larger amplitude source input, and more sensitive receivers and amplifiers (perhaps using a gain-ranging pre-amp system). Methods of recording the SH data might be used in which the direct SH event and other later-arriving events are recorded on separate channels. The amplifier gain could then be adjusted so that the maximum dynamic range was used on each channel. Also, the study of the dependence of the S wave velocity β and attenuation constant Q_S in low porosity granitic rocks with degree of saturation, frequency, severity of microfracturing, etc., might provide further enlightenment into methods of acquiring useful SH reflection data in crystalline rockmass.

The large amplitude Love waves observed in the SH field data present the greatest obstacle with regard to the dynamic range limitation of the tape recorder. The SH reflections from fractures in the field at a depth of 1-3 meters (assuming β = 2500 m/s) would have arrival times of 0.8-2.4 msec, which means that these reflections would be arriving simultaneously with the Love waves. This raises the serious dynamic range problem of recording small amplitude reflection arrivals on top of the low frequency, large amplitude Love wave events. The only hardware solution to this problem is to get an A/D converter with a very large dynamic range (> 100 dB) and a sampling rate of 10 μs or faster.

Physical receiver arrays, similar to the geophone groups used in petroleum exploration seismology, might be used prior to tape recording to decrease the amplitude of surface-travelling Love waves with respect to the vertically incident SH reflections. The resulting amplitude difference between the Love waves and SH reflections might then be reduced to within the 38 dB dynamic range of the analog tape recorder used in the field experiments.

The results of experiments performed in Chapter IV verified that near normal incidence reflection of P and SH waves from a 1-2 mm thick, air or water-filled, planar gap follows the Rayleigh thin layer response described in Chapter II, Section 1. Other experiments showed conclusively that the shear velocity β and attenuation constant Q_S vary with the degree of saturation of a Raymond granite at low stress levels. The results of these studies showed that β increases with increasing saturation, whereas Q_S was found to decrease with saturation.

The saturation effects observed in the water gap experiments described in Chapter IV, Sections 3 and 4, had important ramifications in the interpretation of the SH field studies conducted at the Shaw quarry. The results of the water gap experiments suggested that a dry, low S velocity surface layer may have existed at the field site, with this layer underlain by a saturated half-space having a higher S velocity. A dispersion analysis performed on the SH field data suggested that the later-arriving events in the field data were Love wave arrivals. This result corroborated the hypothesis of a dry, low S velocity surface layer occurring at the field site.

Future research into the application of ultrasonic reflection techniques in fracture detection in a crystalline rockmass should concentrate on:

1) the behavior of β and Q_S with the degree of saturation, stress state, and microfracture density of the rock,
2) methods of resolving the dynamic range problem caused by the existence of surface (both Love and Rayleigh) waves,
3) experimental and theoretical studies of the water absorption phenomenon observed in the research presented in this dissertation.

Figure Captions

Figure V-2-1

Amplitude attenuation curves calculated as in Chapter III, Section 1, using values of Q_S = 10, 20, and 30, and a S velocity of 2500 m/s. The -38 dB level representing the dynamic range of the analog tape recorder is also included in these figures.

a) Q_S = 10
b) Q_S = 20
c) Q_S = 30

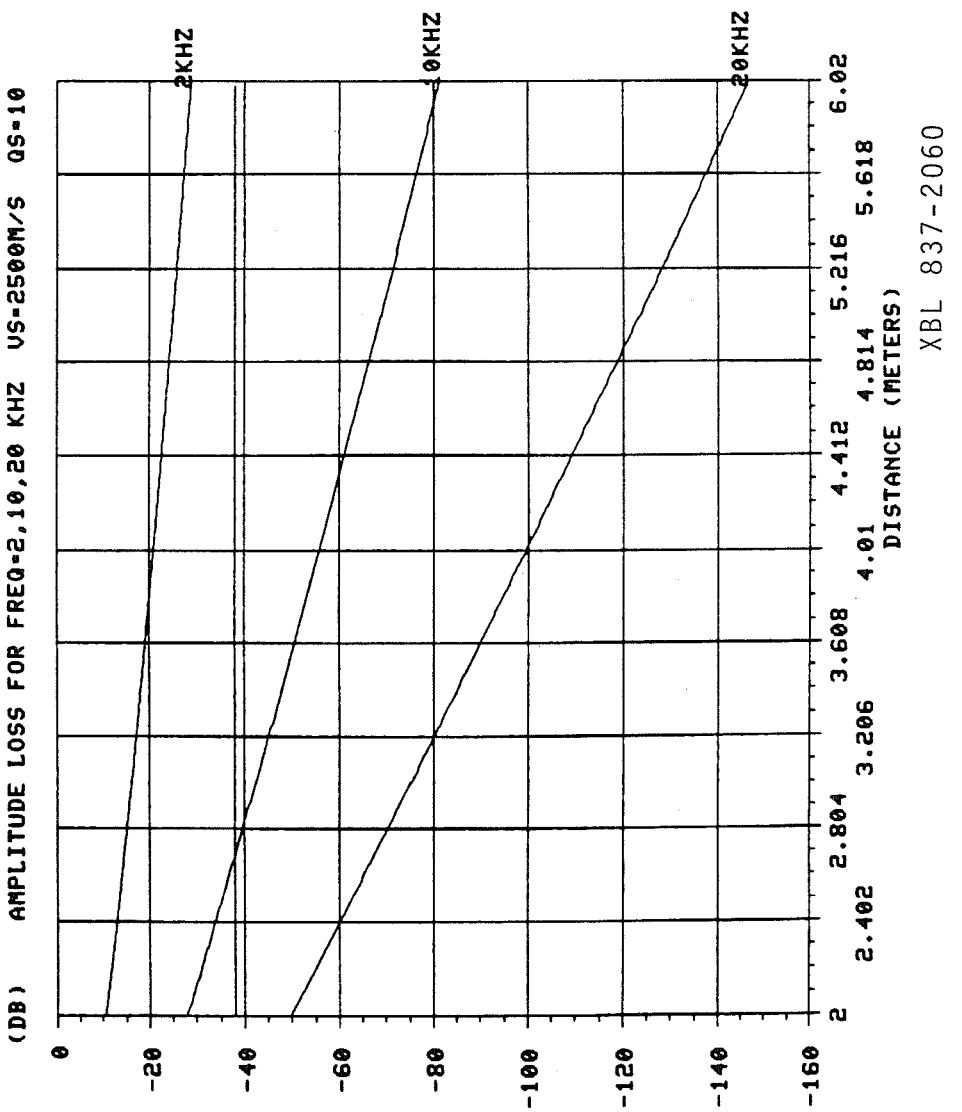
(DB) AMPLITUDE LOSS FOR FREQ=2,10,20 KHZ VS=2500M/S QS=10
2KHZ
10KHZ
20KHZ
0
-20
-40
-60
-80
-100
-120
-140
-160
2
2.402
2.804
3.206
3.608
4.01
4.412
4.814
5.216
5.618
6.02
DISTANCE (METERS)
XBL 837-2060

Figure V-2-1a

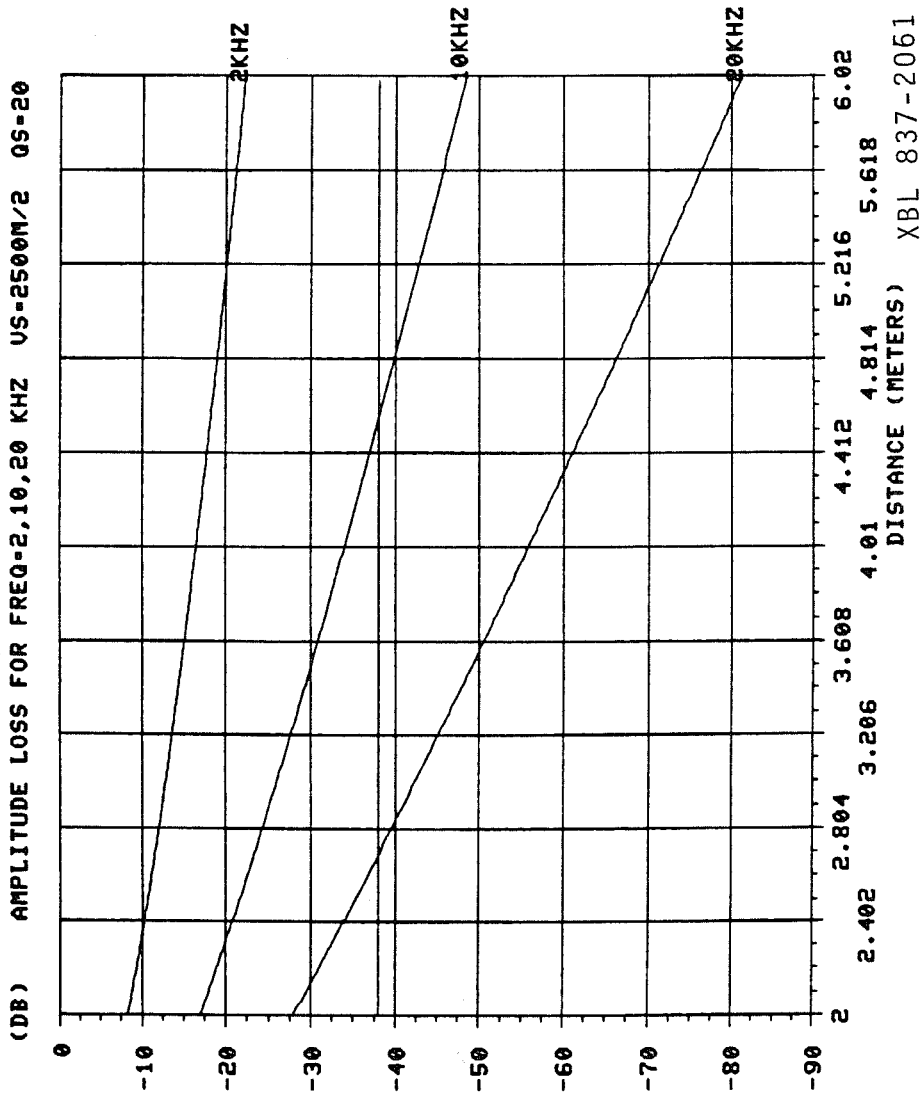
(DB) AMPLITUDE LOSS FOR FREQ=2,10,20 KHZ VS=2500M/2 QS=20
2KHZ
10KHZ
20KHZ
0
-10
-20
-30
-40
-50
-60
-70
-80
-90
2
2.402
2.804
3.206
3.608
4.01
4.412
4.814
5.216
5.618
6.02
DISTANCE (METERS)
XBL 837-2061

Figure V-2-1b

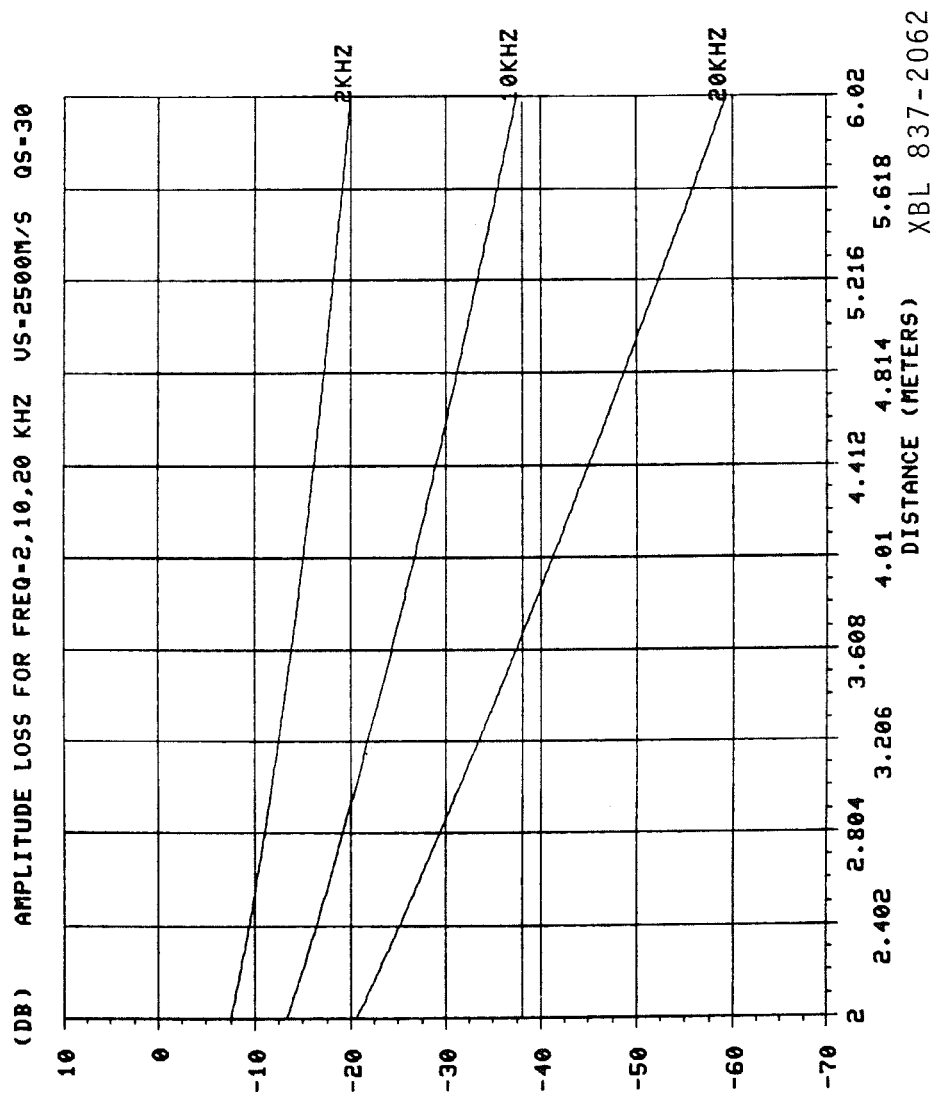
(DB) AMPLITUDE LOSS FOR FREQ=2,10,20 KHZ VS=2500M/S QS=30
10
0
-10
-20
-30
-40
-50
-60
-70
2KHZ
10KHZ
20KHZ
2
2.402
2.804
3.206
3.608
4.01
4.412
4.814
5.216
5.618
6.02
DISTANCE (METERS)
XBL 837-2062

Figure V-2-1c

References--Chapter V

Aki, K. and Richards, P. G.; 1980; Quantitative Seismology: Theory and Methods; W.H. Freeman and Company; San Francisco; 932 pp.

Ewing, W. M., Jardetsky, W. S., and Press, F.; 1957; Elastic Waves in a Layered Media; McGraw-Hill Book Company; New York; 80 pp.

Nur, A. and Simmons, G.; 1969; "The Effect of Saturation on Velocity in Low Porosity Rocks"; Earth and Planetary Science Letters; Vol. Vol. 7; pp. 183-193.

APPENDIX I

In this appendix we present the graphical method used to determine the portion of a reflector sampled by a finite length receiver spread in Chapter III. In Figure AI-1 a planar reflector (line segment $\overline{CD}$) dips at an angle θ from the horizontal, as defined by the ground surface (segment $\overline{AB}$). The reflector is located at a depth h from the source position S as measured along a line perpendicular to the reflector (segment $\overline{OS}$). The propagation velocity of the layer above the reflector ($\overline{CD}$) is assumed to have a constant value V. The position of the image source, located at point S', is determined by extending line segment $\overline{OS}$ a distance h below the reflecting surface, as shown in Figure AI-1.

Receivers are located in a densely sampled spread between points R_1 and R_2. The geometric reflection point of the source and receiver R_1 is determined by the intersection of line segments $\overline{CD}$ and $\overline{S'R_1}$, and is denoted point G_1. Likewise, the reflection point of the source and receiver R_2 is point G_2, the intersection of line segments $\overline{CD}$ and $\overline{S'R_2}$. All receivers located between points R_1 and R_2 all have corresponding reflection points that lie along the reflector (segment $\overline{CD}$) between endpoints G_1 and G_2. Thus, line segment $\overline{G_1G_2}$ is the segment of the reflector sampled by the finite length receiver spread located between points R_1 and R_2 for the given source position S. This construction can then be used in Section 2, Chapter III in the analysis if the SH field data.

Figure Captions

Figure AI-1
Depiction of a planar reflector dipping with angle θ from the horizontal ground surface in a constant velocity half-space V. Source is located at point S, and densely spaced receivers are located between points R_1 and R_2. Portion of reflector sampled by this source-receiver geometry is given by line segment $\overline{G_1 G_2}$.

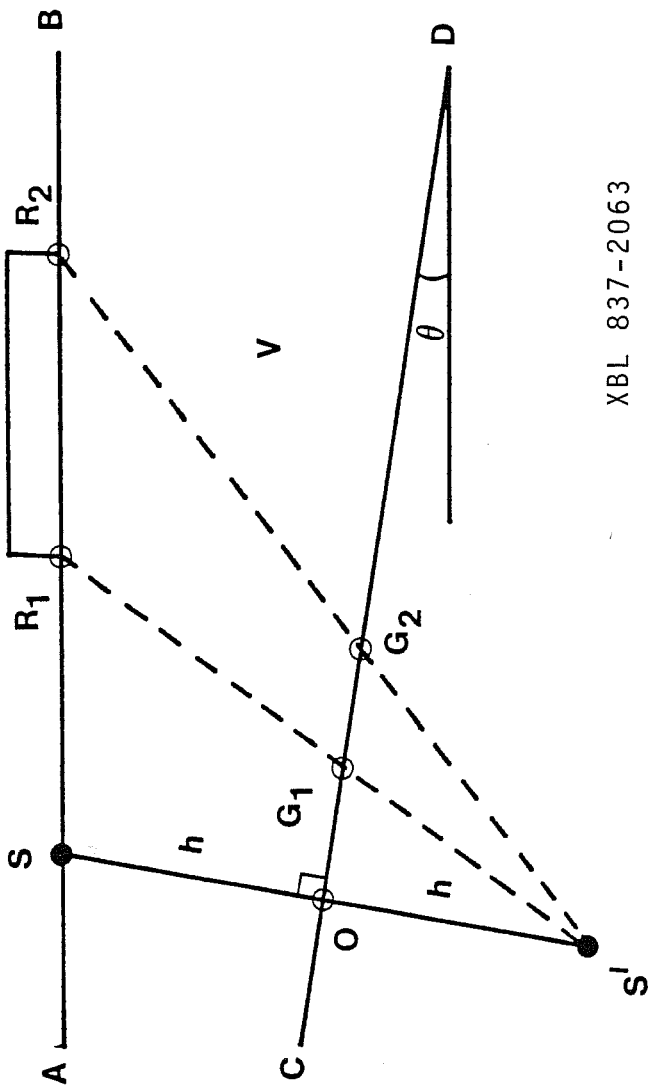

Figure AI-1

APPENDIX II

In this appendix a spectral ratio method will be used to estimate a constant Q_S value from the amplitude spectra of the primary and first multiple SH reflections from the air gap. The reflection data used in the analysis was recorded with the granite slab in an ambient dry condition, so that the calculated value of Q_S will correspond to Q_{Sd} in Section 4, Chapter IV. Q_{Sd} is determined at source positions S1 and S2 (detailed in Section 4) so that estimates of Q_{Ss} could be obtained.

The following calculations of Q_{Sd} are all based on the geometric model of the granite slab depicted in Figure AII-1. This model assumes that β_d and Q_{Sd} are homogeneously distributed in the granite slab, so that $\beta_d = 2d/t_d$, where d is the slab thickness and t_d is the arrival time of the SH reflection. Anelastic attenuation will be modeled using the plane wave constant Q results given in Equation III.1.2 (Chapter III, Section 1). In addition a geometric spreading term of $1/|x|$ must be included in the attenuation model as the propagation distances of the primary and first multiple SH reflection are quite different. It is, in fact, this difference in travel path difference that allows the calculation of Q_{Sd} from this data set. The assumption of a $1/|x|$ geometric dependence implies that the reflected SH body waves travel as spherical, rather than plane, waves.

Thus, the equation describing the amplitude loss $(A(|x_0|,f)$ of the SH reflection event at a given propagation distance $|x_0|$ and frequency f is:

$$A(|x_0|,f) = \left[\frac{A_0}{|x_0|}\right] e^{\frac{-\pi f|x_0|}{Q_{Sd}\beta_d}} \qquad [AII.1]$$

where A_0 is the amplitude at $|x_0| = 0$, and β and Q_{Sd} are the shear velocity and attenuation constants.

The primary SH reflection recorded for a near zero source-receiver offset travels a distance $|x_0| = 2d$, so that the amplitude loss of this event is, from AII.1,

$$A_P(2d,f) = \left[\frac{A_0}{2d}\right] e^{\frac{-2\pi fd}{Q_{Sd}\beta_d}} \qquad [AII.2]$$

Likewise the travel distance of the first multiple SH reflection is $|x_0| = 4d$, so the amplitude loss of this event is:

$$A_M(4d,f) = \left[\frac{A_0}{4d}\right] e^{\frac{-4\pi fd}{Q_{Sd}\beta_d}} \qquad [AII.3]$$

Dividing AII.3 by AII.2,

$$\frac{A_M(4d,f)}{A_P(2d,f)} = (1/2)e^{\frac{-2\pi fd}{Q_{Sd}\beta_d}} \qquad [AII.4]$$

Taking the log of the spectral ratio:

$$\ell n\left[\frac{2A_N(4d,f)}{A_P(2d,f)}\right] = f\left[\frac{-2\pi d}{Q_{Sd}\beta_d}\right] \qquad [AII.5]$$

Again we assume that Q_{Sd} is independent of frequency f over the band

from 10^4-10^5 Hz. The results of considerable studies suggest that Q_S is essentially independent of frequency over a limited band for dry rock (Winkler and Nur, 1982). Again, Equation AII.5 is a linear equation of the form y = bx, so that the linear regression used previously in Chapter IV, Section 4 can be applied to find the log spectra slope:

$$b = \frac{-2\pi d}{Q_{Sd}\beta_d} \qquad [AII.6]$$

Since b is determined from the log spectral data, and $\frac{2d}{\beta_d} = t_d$ then

$$Q_{Sd} = \frac{-\pi t_d}{b} \qquad [AII.7]$$

The sources of error in estimating Q_{Sd} then come from uncertainties in the slopes b and in the measurement of the arrival time t_d.

The method of estimation of Q_{Sd} was applied to SH reflection data recorded during the first week of January at positions S1 and S2. The 500 μs long traces recorded at the closest offset position (5 cm) in the SH sections shown in Figure IV-4-2 will be used as the basis for this analysis. The 5 cm offset traces at S1 and S2 are shown in Figure AII-2. The small deviation from the assumed normal incidence travel path due to the finite source-receiver offset (5 cm) will not particularly affect the final error on Q_{Sd} if the properties Q_{Sd} and β_d are indeed homogeneously distributed. The primary and first multiple SH reflections from the bottom of the slab are denoted in this figure. The primary SH reflection is quite distinct, but the multiple event is severely attenuated. In fact this event is nearly obliterated in the

background seismic noise, so that we expect a fairly large uncertainty to be associated with the log spectral slope estimate b. Since t_d is well determined (± 0.5%), then the predominant error on the calculated Q_{Sd} will be due to the slope uncertainty.

The windowed primary SH reflections at S1 and S2 are shown in Figure AII-3, and the amplitude spectra of the windowed traces are given in Figure AII-4. The time windowed multiple SH reflections at S1 and S2 are shown in Figure AII-5, and the poor signal to noise ratio of these data is obvious. The amplitude spectra of the windowed multiple reflection waveforms, given in Figure AII-6, show the limited band in which the signal component stands out above the spectral component due to the seismic background noise observed in the multiple SH reflection data.

The frequency band used in the estimate of the log spectral slope b was based on the S/N level observed in the amplitude spectra presented in Figures AII-(4 and 6). The frequency bands 30-120 kHz and 40-100 kHz were chosen at position S1, and the bands 20-120 kHz and 40-100 kHz were used in the fits at S2. The log spectral ratio data and best-fit line for the two choices of frequency band are shown in Figure AII-7 for position S1, and in Figure AII-8 for position S2. The results of the best-fit spectral analysis and the calculation of Q_{Sd} using Equation AII.7 are tabulated in Table AII-(1 and 2) for positions S1 and S2.

The results of this analysis sugest that Q_{Sd} ranges in value from 35-75, and that the errors associated with Q_{Sd} can be on the order of 10-65%. The average of the four estimates of Q_{Sd} given in Tables AII-(1 and 2) is 50. Thus, we will adopt the value $Q_{Sd} = 50 \pm 30\%$

Table AII-1

Frequency Band (kHz)	Primary Reflection Arrival Time (μs)	Log Spectral Slope b (Hz^{-1})	Calculated Q_{Sd}
30-120	223.5 ± 1%	-1.890×10^{-5} ± 28.2%	37.2 ± 28.2% (±10.5)
40-100	223.5 ± 1%	-1.565×10^{-5} ± 61.5%	44.9 ± 61.5% (±27.6)

Position S1

Table AII-2

Frequency Band (kHz)	Primary Reflection Arrival Time (μs)	Log Spectral Slope b (Hz^{-1})	Calculated Q_{Sd}
20-120	225.0 ± 1%	-9.524×10^{-6} ± 64.5%	74.2 ± 64.5% (±46.7)
40-100	225.0 ± 1%	-1.568×10^{-5} ± 38.4%	45.1 ± 38.4% (±17.3)

Position S2

(range of Q_{Sd} from 35-65) for use in the calculation of Q_{Ss} in Section 4, Chapter IV.

The large uncertainty in the slope b and corresponding estimate of Q_{Sd} for the 20-120 kHz band at S2 is due to the presence of two spectral "holes" located about 30 kHz and 105 kHz (see Figure AII-8a). It is questionable whether the presence of these spectral "holes" substantiates the theoretical predictions of Nur, 1971, and O'Connell and Budiansky, 1977, regarding the dependence of Q_S with frequency, or whether these "holes" represent noise in the log spectral ratio technique.

Figure Captions

Figure AII-1
Geometric model of granite slab used in the analysis of Q_{Sd} using the primary and first multiple SH reflection from the slab bottom. Thickness d is well determined, and S velocity β_d and attenuation constant Q_{Sd} are assumed constant throughout the slab.

Figure AII-2
500 μs SH data recorded at positions S1 and S2 during the first week of January, 1982 with small source-receiver offsets (< 5 cm).
a) Data at position S1
b) Data at position S2

Figure AII-3
Primary SH reflection shown in traces of Figure AII-2 windowed between 225-325 μs.
a) SH reflection at position S1
b) SH reflection at position S2

Figure AII-4
Amplitude spectra of windowed SH reflection shown in Figure AII-3.
a) Amplitude spectrum of primary reflection at S1
b) Ampliutde spectrum of primary reflection at S2

Figure AII-5
First multiple SH reflection shown in traces of Figure AII-2 windowed between 225-325 μs.
a) First multiple reflection at position S1
b) First multiple reflection at position S2

Figure AII-6
Amplitude spectra of windowed multiple SH reflection shown in Figure AII-5.
a) Amplitude spectrum of multiple reflection at S1
b) Amplitude spectrum of multiple reflection at S2

Figure AII-7
Log spectral ratios calculated from the amplitude spectra presented in Figures AII-(4 and 6) for location S1 in two different frequency bands.
a) 30-120 kHz band
b) 40-100 kHz band

Figure AII-8
Log spectral ratios calculated from the amplitude spectra presented in Figures AII-(4 and 6) for location S2 in two different frequency bands.
a) 20-120 kHz band
b) 40-100 kHz band

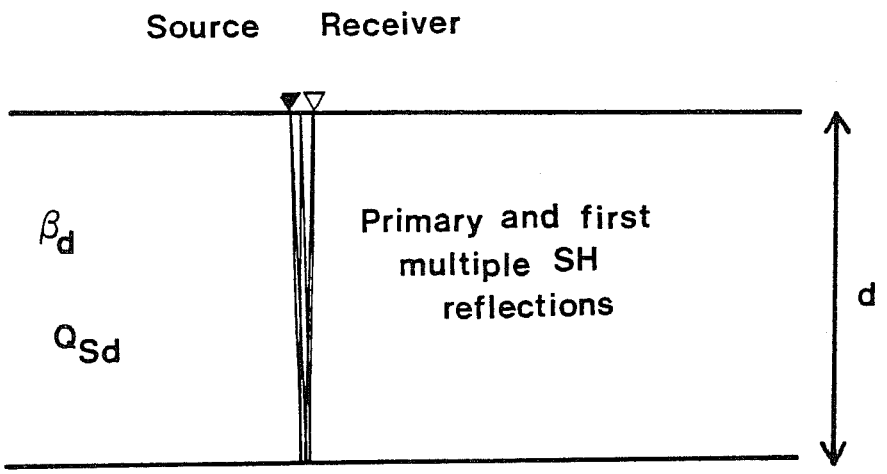

Granite slab at ambient (dry) laboratory conditions

XBL 837-2064

Figure AII-1

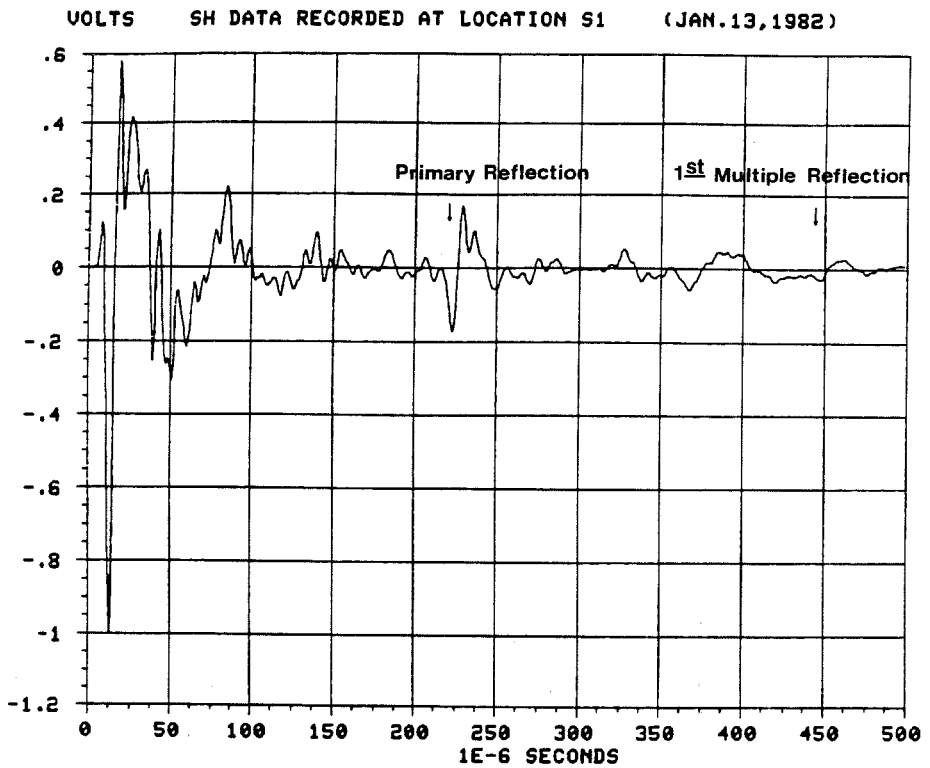

Figure AII-2a

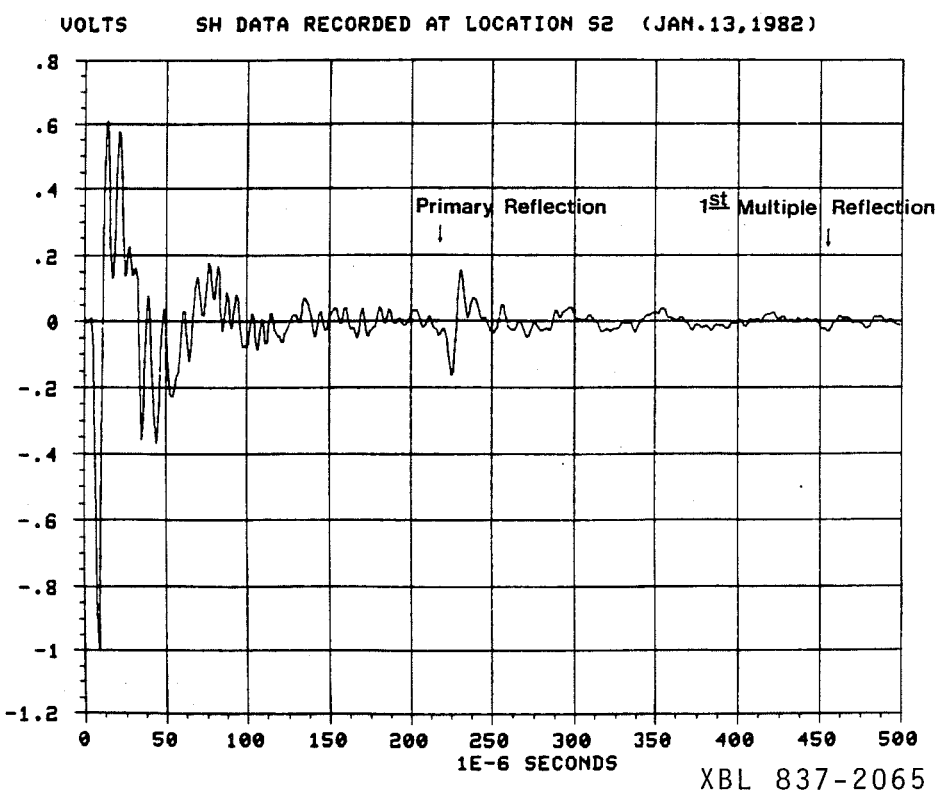

Figure AII-2b

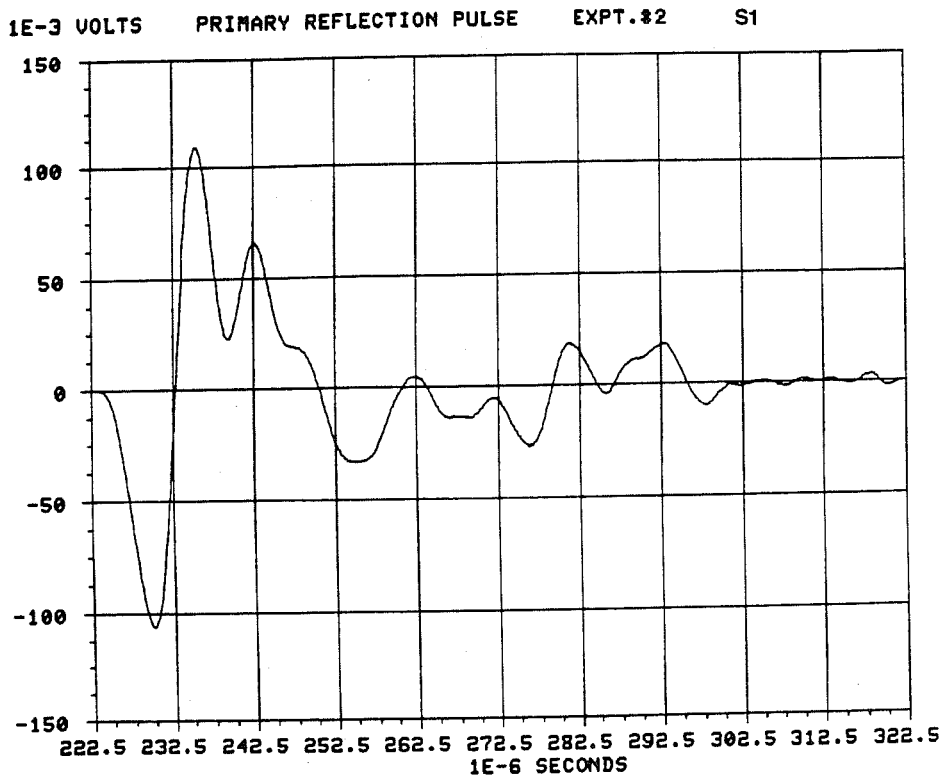

Figure AII-3a

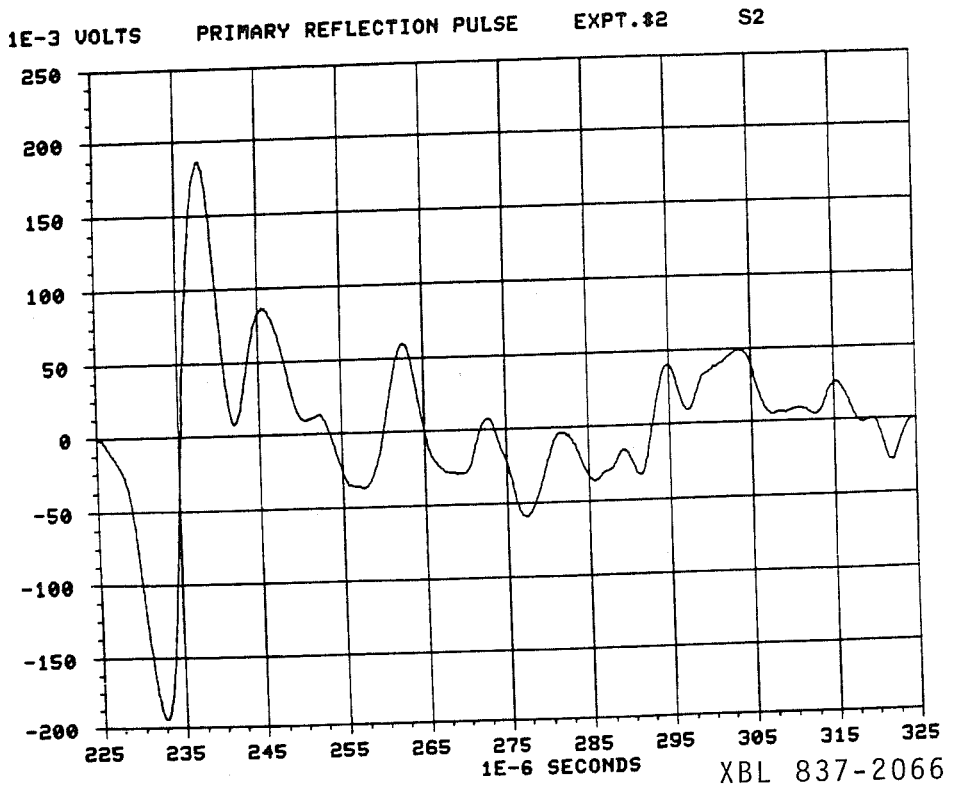

Figure AII-3b

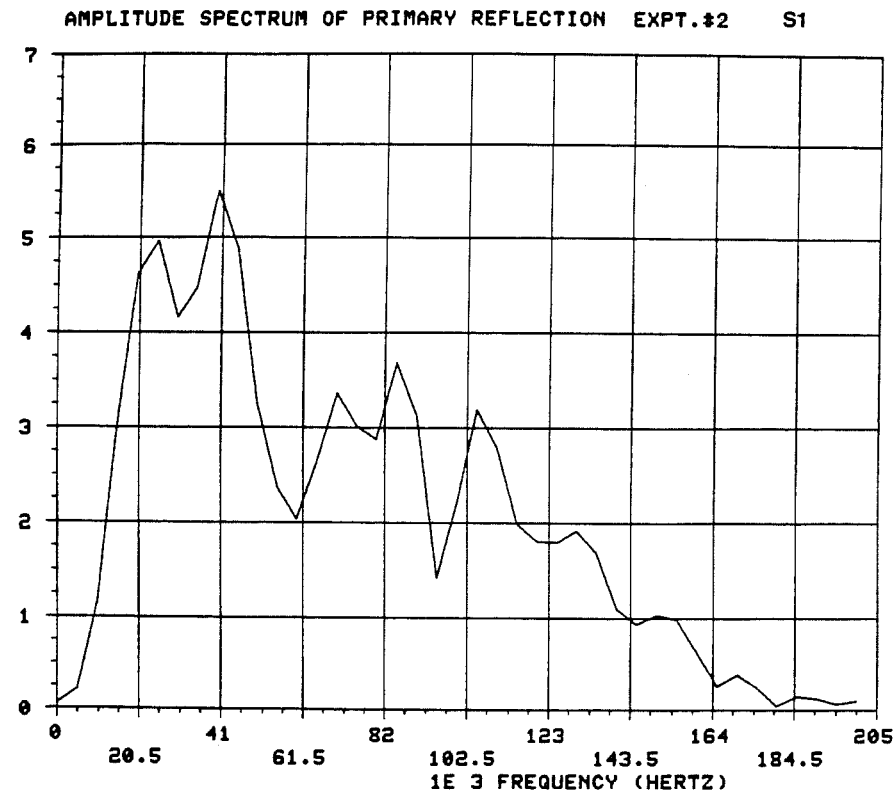

Figure AII-4a

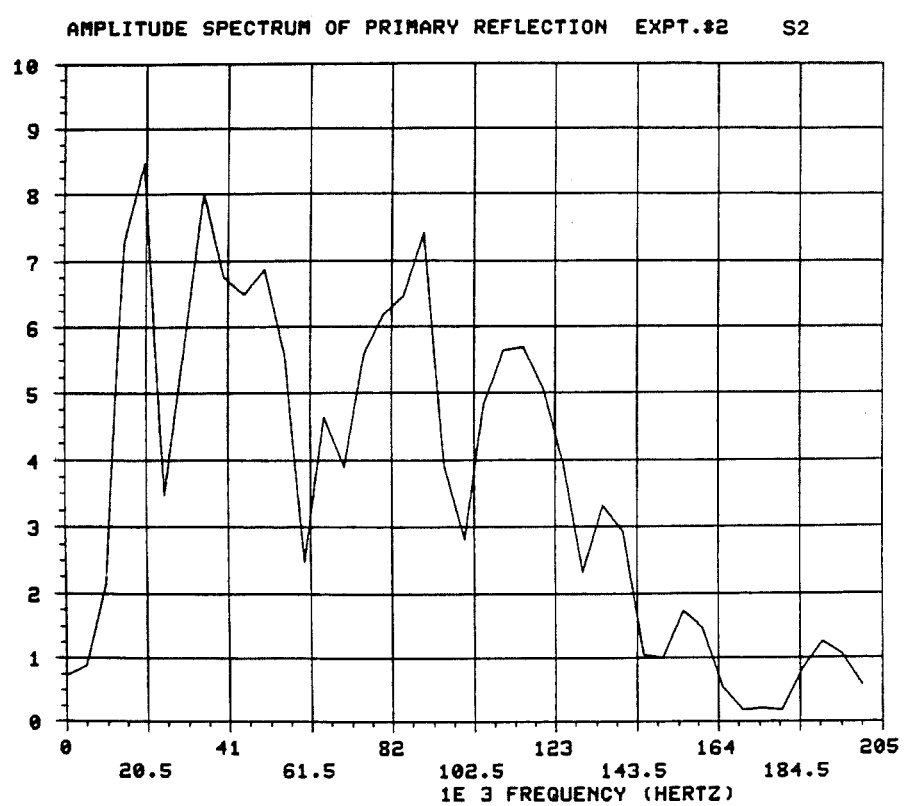

XBL 837-2067

Figure AII-4b

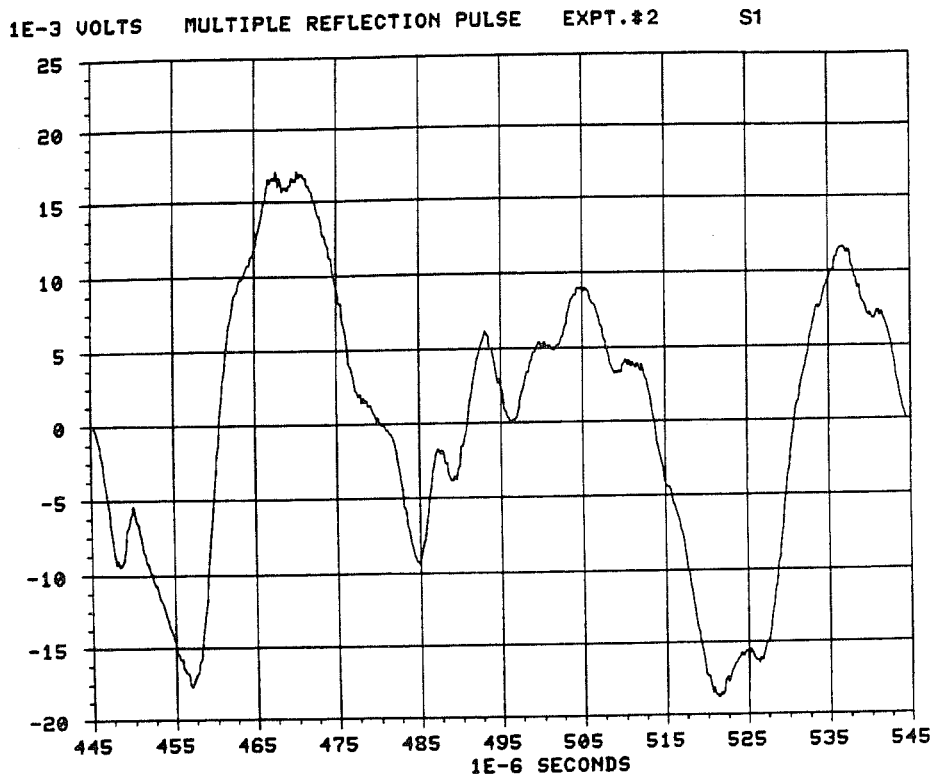

Figure AII-5a

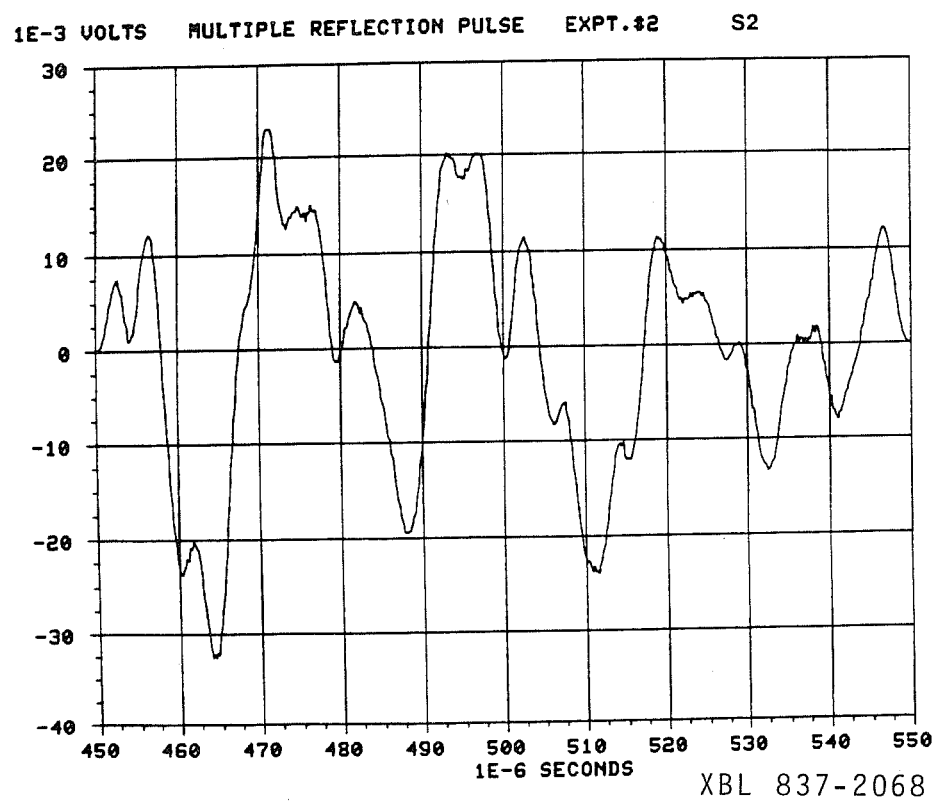

XBL 837-2068

Figure AII-5b

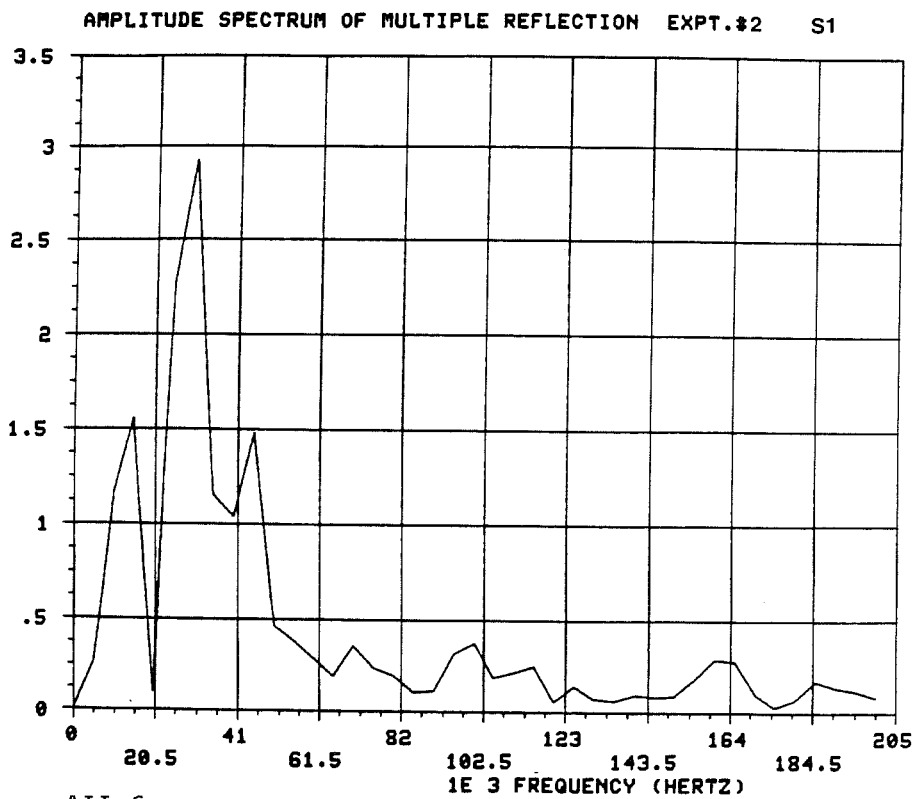

Figure AII-6a

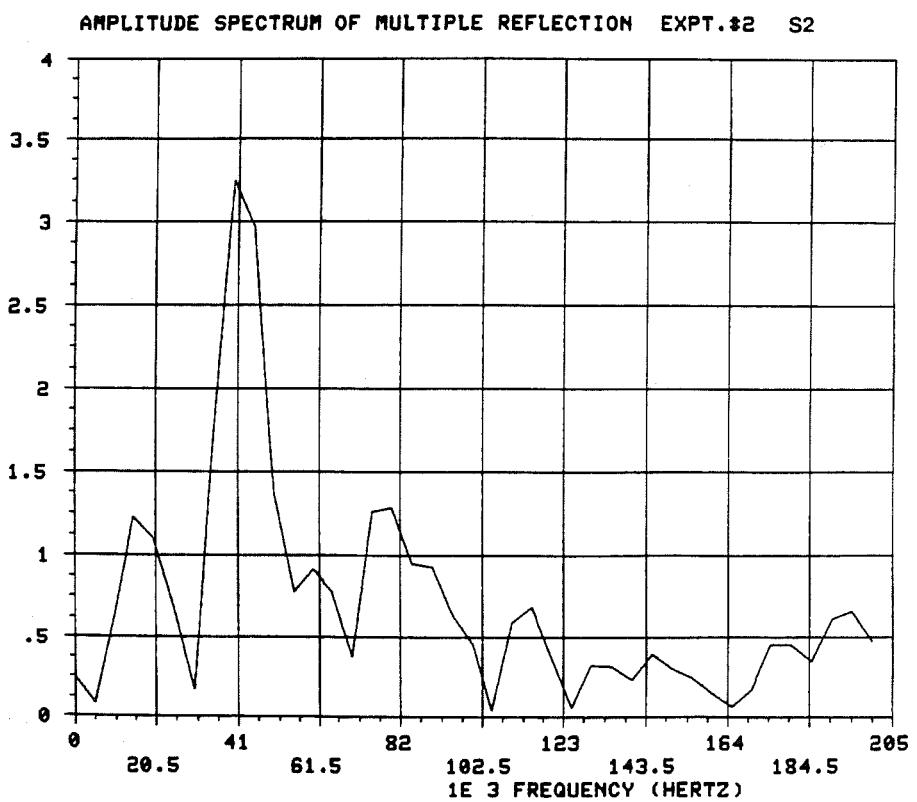

Figure AII-6b

XBL 837-2069

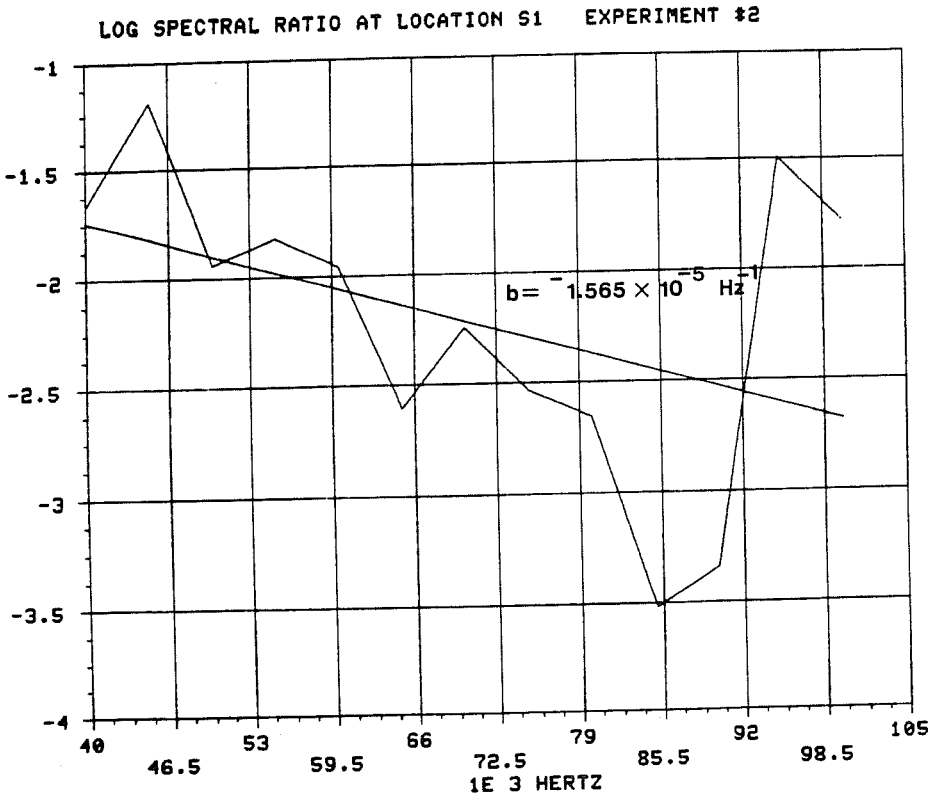

Figure AII-7a

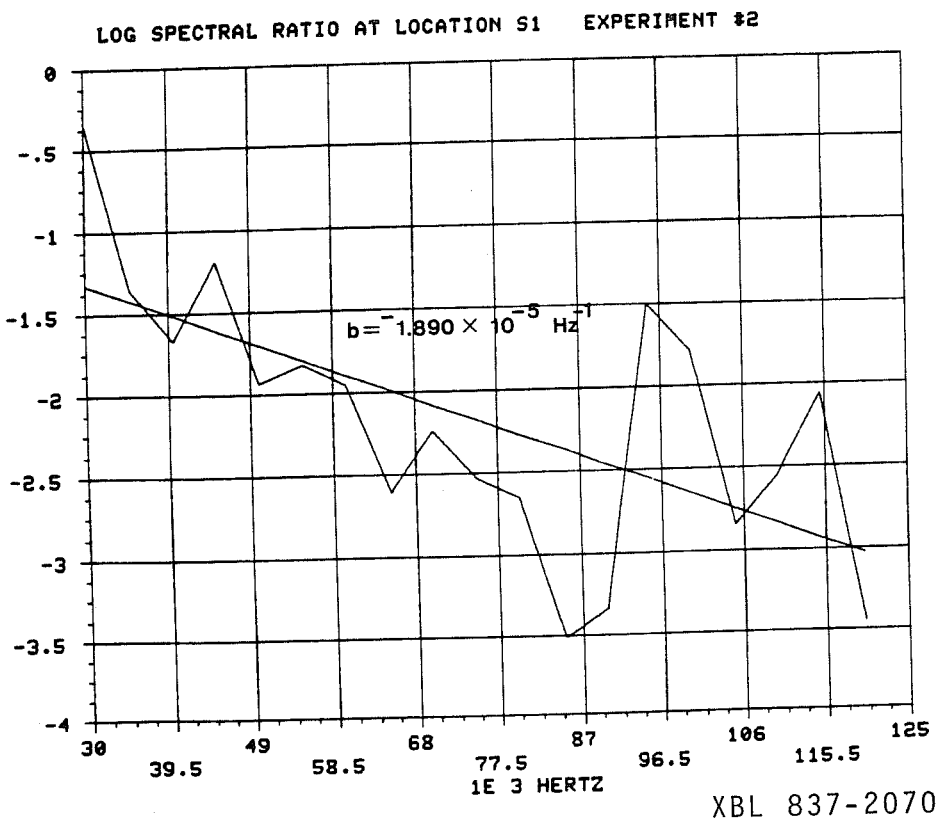

XBL 837-2070

Figure AII-7b

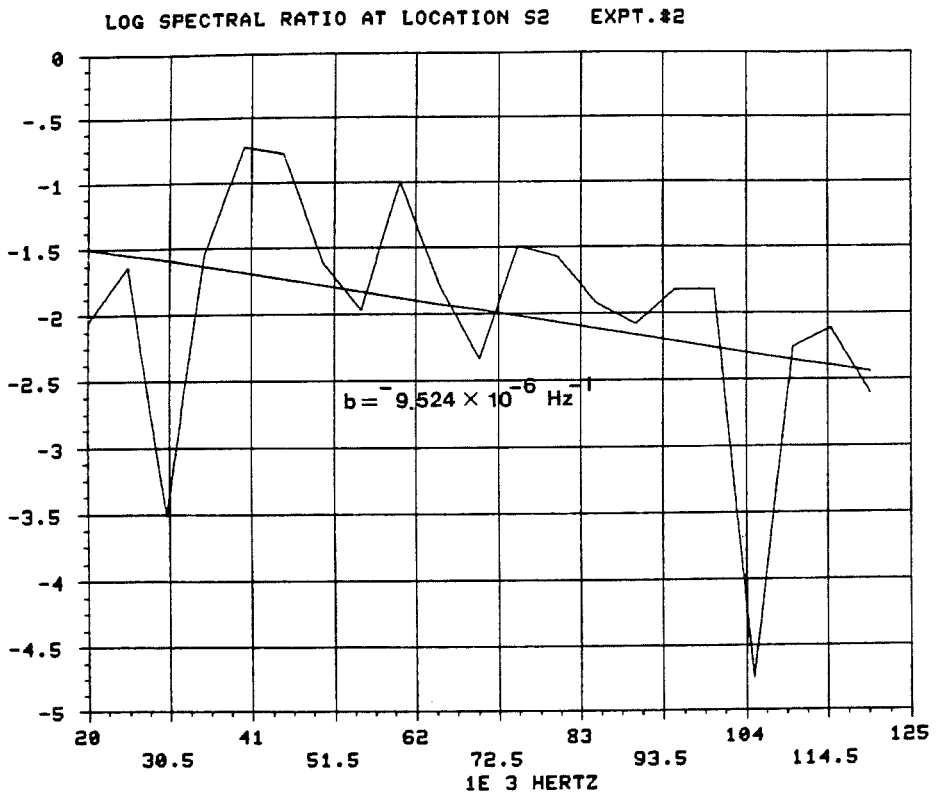

Figure AII-8a

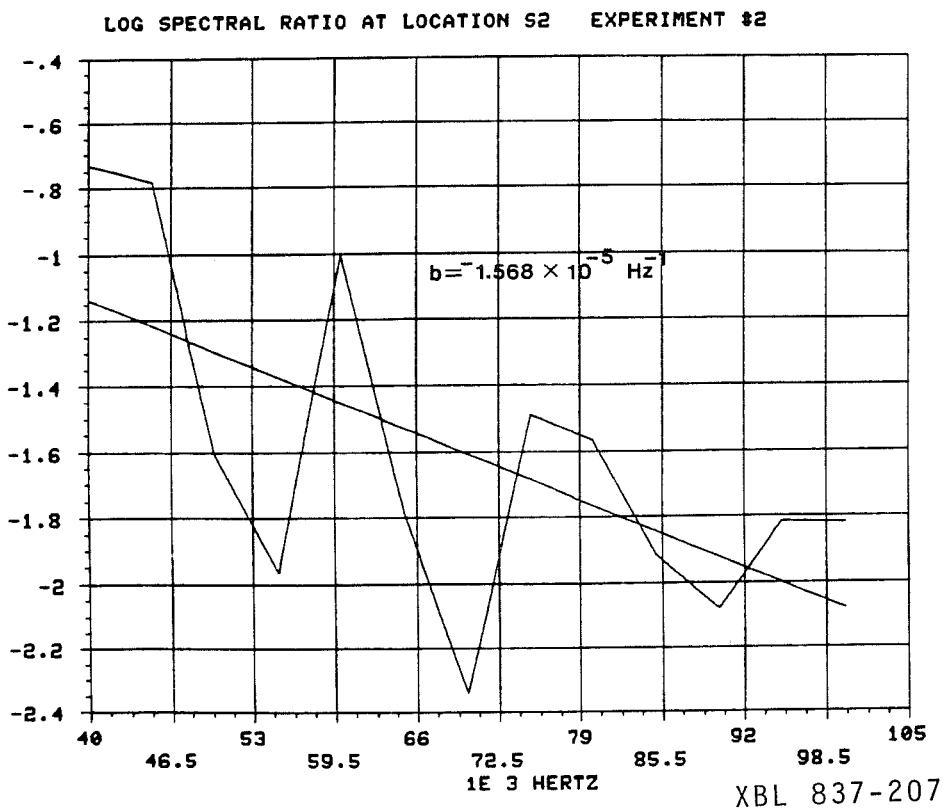

Figure AII-8b

References--Appendix II

Nur, A.; 1971; "Viscous Phase in Rocks and the Low-Velocity Zone"; J.G.R.; Vol. 76; No. 5; pp. 1270-1277.

O'Connell, R. J. and Budiansky, B.; 1977; "Viscoelastic Properties of Fluid-Saturated Cracked Solids"; J.G.R.; Vol. 82; pp. 5719-5735.

Winkler, K. W. and Nur, A.; 1982; "Seismic Attenuation: Effects of Pore Fluids and Frictional Sliding"; Geophys.; Vol. 47; No. 1; pp. 1-15.

☆USGPO: 1983 — 759-109/1649

This report is part of a cooperative Swedish-American project supported by the U.S. Department of Energy and/or the Swedish Nuclear Fuel Supply Company. Any conclusions or opinions expressed in this report represent solely those of the author(s) and not necessarily those of The Regents of the University of California, the Lawrence Berkeley Laboratory, the Department of Energy, or the Swedish Nuclear Fuel Supply Company.

TECHNICAL INFORMATION DEPARTMENT
LAWRENCE BERKELEY LABORATORY
UNIVERSITY OF CALIFORNIA
BERKELEY, CALIFORNIA 94720